Nonlinear Dynamos in Stars

Paul James Bushby

Clare College

September, 2003

This dissertation is submitted for the degree of
Doctor of Philosophy

Preface

All of the work described in this dissertation is original except where explicit reference is made to other authors. This dissertation is the result of my own work and includes nothing which is the outcome of work done in collaboration except where specifically indicated in the text. No part of this thesis has been or is being submitted for any qualification other than the degree of Doctor of Philosophy at the University of Cambridge.

Acknowledgements

I would like to thank my supervisor Nigel Weiss for his enthusiasm, guidance and support throughout my PhD. I have also benefited from discussions with Jon Dawes, Mike Proctor, Jack Thomas and Steve Tobias, who have all provided useful suggestions and ideas. In addition I would like to thank Paul Charbonneau, Mausumi Dikpati and Andrew Markiel for their assistance with the validation of my numerical codes. I would particularly like to thank Andrew Markiel for allowing me to have access to his code so that I could carry out detailed validation checks on my own code. I am also grateful to Steve Houghton for his enthusiastic proof-reading of several parts of this thesis. I would also like to thank PPARC for a research studentship.

Many people within the department have contributed towards making my three years as a PhD student more enjoyable. Besides those people mentioned above, I would particularly like to thank Claire Postlethwaite, Jennifer Siggers, Stephen Thompson and Mike Tildesley, for their enthusiasm for the occasional coffee break as well as their sense of humour.

Most importantly, I would like to thank my wife Liz, and the rest of my family, for their advice and support and for helping me to keep a sense of perspective.

Summary

Many stars are observed to possess magnetic fields, although the origin of this magnetic activity is still not fully understood. This thesis discusses the application of mean-field dynamo theory to the Sun and other late-type stars. The first chapter is introductory in nature, and discusses relevant observational details concerning stellar magnetic fields. The next chapter (which is also introductory) reviews the theoretical aspects of hydromagnetic dynamos and describes ways in which this theory has already been used to describe the solar dynamo.

Motivated by the fact that the solar magnetic field was highly asymmetric during the period known as the Maunder minimum, Chapter 3 describes a simple (one-dimensional) Cartesian model that exhibits dynamo oscillations where most of the activity is confined to one hemisphere. Such asymmetry is the result of an interaction between dynamo modes of dipolar and quadrupolar parity and, where they occur, these solutions seem to be remarkably robust.

The remainder of this thesis deals with the numerical simulation of more realistic (two-dimensional) mean-field dynamo models. Chapter 4 describes several models which incorporate different features and nonlinearities in (axisymmetric) spherical geometry. Particular emphasis is placed upon the numerical techniques and the subsequent validation of the dynamo codes. In Chapter 5, the resulting dynamo codes are used to model the solar dynamo, incorporating an analytic fit to the solar differential rotation profile. These simulations, when coupled with the solar observations, are used to discriminate between different forms of the mean-field α-effect. The constraints imposed by the observations of the (so-called) torsional oscillations are also examined in detail, in Chapter 6, with particular reference to the relationship between these oscillations and time-dependent modulational behaviour.

Finally, in Chapter 7, these ideas are applied to those (very active) late-type stars

that are rotating much more rapidly than the Sun. Unlike the Sun, such stars very often have large polar starspots. Rapid rotation suggests a Coriolis-dominated Taylor-Proudman-like differential rotation profile. Some of the observed features of these stars are reproduced; in particular, this model naturally leads to magnetic activity at high latitudes.

Contents

Chapter 1

Introduction

It has long been known that the Earth possesses a magnetic field, but it wasn't until the beginning of the last century that magnetic fields were first detected in the Sun by Hale (1908). This was the first instance of magnetic fields being found in any astrophysical body other than the Earth. Since then it has been established that the Earth and the Sun are not unique in their magnetic activity, with magnetic fields being found in other planets and stars. On a much larger scale, it is now apparent that many galaxies also possess magnetic fields. Explaining how magnetic fields arise in astrophysical systems is one of the key questions in modern astrophysics.

1.1 The solar-stellar connection

The Sun plays a major role in the study of stellar magnetic activity. As our closest star, observations of the Sun have given us very detailed information about its structure and behaviour. For more distant stars it is clearly not possible to get the same level of detail in the observations, but it seems highly plausible that stars like the Sun will behave in a very similar way. We can therefore use what we know about the Sun to predict how other solar-like stars will behave. This idea is known as the solar-stellar connection.

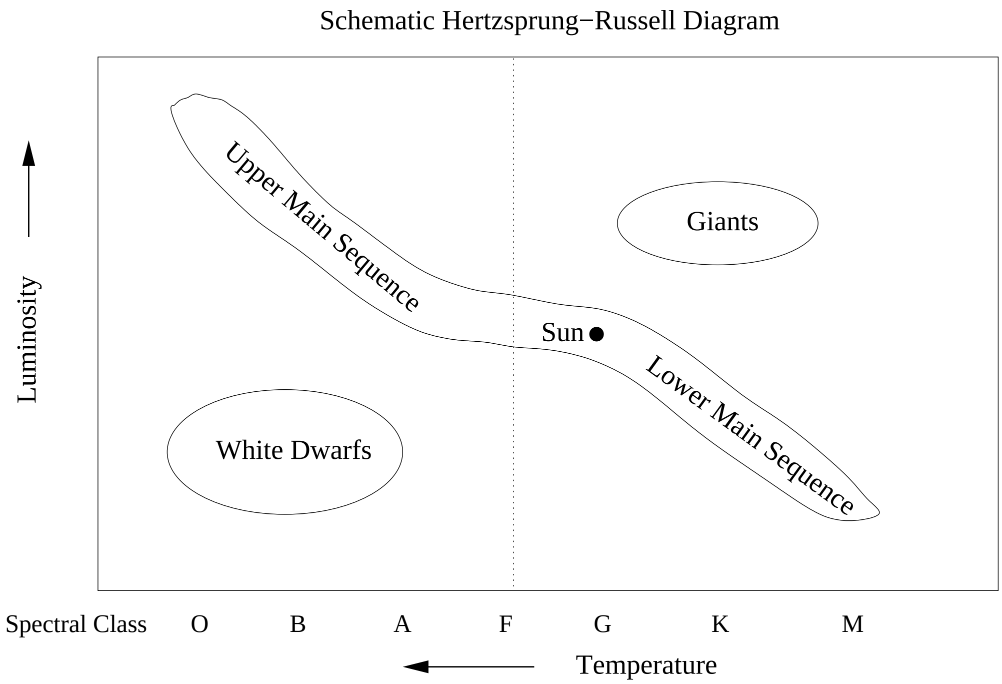

Figure 1.1: A schematic Hertzsprung-Russell diagram. The dotted line represents the approximate boundary between the hotter stars that are classified as "early-type", on the left, and the cooler "late-type" stars on the right. The locations of the different spectral classes are also indicated.

If we wish to compare observations of the Sun with those of another star, we need to know how similar the two stars actually are. It is important, therefore, to have some means of classifying different types of stars. Stars are commonly grouped according to their position on the Hertzsprung-Russell diagram (Figure 1.1), which plots the luminosity of a star against its effective surface temperature (or, equivalently, spectral type) – see, for example, Kippenhahn and Weigert (1990). Each of the spectral classifications given in Figure 1.1 is subdivided into 10 subclasses – for example, the Sun is classified as a G2 star. The main sequence is one of the most prominent features on the Hertzsprung-Russell diagram, and is of particular interest because the Sun is a main sequence star. The initial position of a star on the main sequence is determined by its mass, with very different features being observed on low-mass and high-mass stars. The upper main sequence is defined as those (so-called) early-type main sequence stars that have a mass greater than (approximately) $1.2M_{\odot}$, and such stars have a high luminosity and effective surface temperature. They also possess convective cores and radiative outer envelopes. Lower main sequence stars, such as the Sun, are late-type stars that have a lower luminosity and effective surface temperature. They also differ from upper main sequence stars in having a radiative core and an outer convective envelope. Given the fact that the Sun is a late-type star, it is with other late-type stars that the most productive solar-stellar comparisons can be made.

1.2 Magnetic activity in late-type stars

1.2.1 General trends

The direct measurement of magnetic fields in stars is achieved by analysing the Zeeman broadening of spectral lines. The analysis assumes that the stellar atmosphere is made up of radial patches of some well-defined magnetic field strength, embedded in a non-magnetic atmosphere (see, for example, Schrijver and Zwaan, 1999). It is then possible to deduce the mean magnetic field strength and the so-called filling factor (the percentage of the stellar atmosphere that contains magnetic field). Magnetic measurements carried out for a range of late-type stars (see, for example, Saar, 1996) show that the characteristic magnetic field strengths associated with these stars vary from about 1000G for moderately active stars up to about 4200G for extremely active stars. The filling factors vary even more dramatically: from a few per cent in moderately active stars up to around 60 per cent in very active stars.

It is well known that Ca^{+} H and K emission is correlated with solar magnetic activity, and these emission lines provide the best method for monitoring magnetic activity in other stars. One such survey for late-type stars has been carried out by Baliunas et al. (1995). The key result here is that for stars of a given spectral type, there is a clear correlation between magnetic activity and rotation rate. Rapidly rotating late-type stars are very active and rarely display any kind of smooth cyclic behaviour, whilst slower rotators (like the Sun) are less active but often exhibit cyclic magnetic activity. The dependence of magnetic activity upon rotation rate was first quantified by Noyes et al. (1984), who used these chromospheric emission lines to establish a close correlation between the magnetic activity of a star and its inverse Rossby number, $Ro^{-1} = \Omega\tau_c$, where Ω is the angular velocity of the star and τ_c is the star's (theoretically predicted) convective turnover time – the larger the value of Ro^{-1}, the more active the star.

In fact, it is possible to link the magnetic activity of late-type stars with the length of time that they have spent on the main sequence. The angular velocity of a star increases as it contracts onto the main sequence, due to the conservation of angular momentum (see, for example, Weiss, 1994). However, as the star evolves during its main sequence phase, the action of magnetic braking by the magnetic field associated with the stellar wind (Mestel, 1968, 1999), will cause the star to lose angular momentum. Therefore, the rotation rates of main sequence stars will decrease with time. In fact, as first noted by Skumanich (1972), the decline in rotation rates in older main sequence stars closely follows a power law with the angular velocity decaying like $t^{-1/2}$. In order to quantify the kind of rotation rates that are being discussed here: the most rapidly rotating young late-type stars have a rotational period of the order of 0.3 days, whilst the Sun (a typical slower rotator) has a sidereal rotational period of about 25 days. It is clear that there is a correlation between age and rotation rate, and therefore age and magnetic activity, with young stars generally being the most active. In some binary systems – such as the RS CVn stars – this relationship between age and rotation rate does not apply. This is because tidal interactions tend to enforce rapid rotation in these systems, and any angular momentum loss through stellar winds from either of the binary components can be replenished from the orbital angular momentum of the system (Schrijver and Zwaan, 1999). Due to their rapid rotation, these binaries tend to be highly magnetically active, regardless of their age.

Although this section is primarily concerned with activity in late-type stars, it is worth mentioning that other types of stars possess magnetic fields. Zeeman line broadening indicates that magnetic fields are also found on some early-type stars (Mestel, 1999). The strength of the fields on these magnetically active (so-called) Ap stars is typically of the order of 10^3–10^4G, although weaker fields have also been observed. Moving off the main sequence, much stronger magnetic fields have been observed on white dwarfs (Kemp et al., 1970) and on neutron stars (Mestel, 1999).

1.2.2 Solar magnetic activity

The Sun is a middle-aged lower main sequence star and, therefore, is rotating relatively slowly. The results described above would suggest that its magnetic activity should be cyclic in character, and that is precisely what is observed. It is important to understand the main observational features of magnetic activity in the Sun before formulating any theory for magnetic field generation, and I will simply summarise the main points here. Further details can be found in Tayler (1997), Stix (2002) and Tobias (2002b).

The 11 year sunspot cycle was first noted by Schwabe in 1843 (see, for example, Rüdiger, 1989; Stix, 2002). This is, historically, the first hint of cyclic magnetic behaviour in the Sun, although this was not apparent at the time because the magnetic origin of sunspots was not then understood. Schwabe did little more than count sunspot numbers, but observations subsequently carried out, independently, by Carrington and Spörer (as described by Rüdiger, 1989) soon established further patterns in the behaviour of sunspots. It was found that sunspots are confined to low latitudes – appearing at (about) $\pm 30°$ at the start of each cycle. The zones of sunspot activity then migrate equatorwards, with the number of sunspots first increasing to a maximum and then decreasing as the

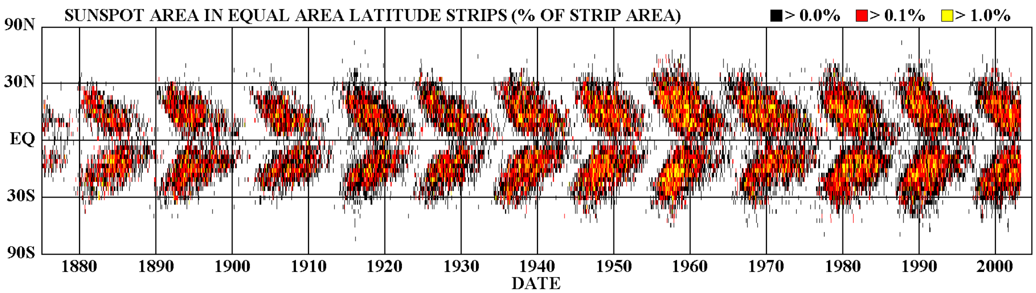

Figure 1.2: The Butterfly Diagram. Here, the sunspot number is plotted as a function of latitude (the vertical axis) and time (the horizontal axis). This image was produced by D. Hathaway.

zones of activity near the equator, until the sunspot number reaches a minimum. The cycle then repeats with a period of approximately 11 years. The sunspot cycle is often represented by the familiar butterfly diagram (Figure 1.2), which was first introduced by Maunder (1904). This diagram also demonstrates that the sunspot coverage varies from cycle to cycle, which implies that this 11 year cycle is modulated in some form. Sunspot records suggest that this modulation is aperiodic.

Since Hale (1908) used the Zeeman splitting of spectral lines to show that sunspots were magnetic, it has become clear that sunspots can provide a great deal of information about the nature of magnetic fields within the Sun. With typical field strengths of approximately 2500–3000G, sunspots are the most prominent magnetic features on the solar surface, and they are found exclusively within active regions at low latitudes. Most young active regions are bipolar in nature, and are observed on the solar surface as two adjacent patches of opposite magnetic polarity appearing at approximately the same latitude (see, for example, Schrijver and Zwaan, 1999). These active regions often contain large (bipolar) sunspot pairs. A study of the properties of these sunspot pairs was carried out by Hale et al. (1919), and regular patterns were found. Firstly, in each solar hemisphere, the leading member of a sunspot pair almost always possesses the same polarity. Secondly, sunspot pairs have opposite leading polarities in the Northern and Southern hemispheres. Finally, these polarity patterns reverse from one cycle to the next. These observations are commonly referred to as Hale's polarity laws.

An attractive explanation for the formation of bipolar active regions is that they are the result of loops of azimuthal magnetic flux breaking through the photosphere. The regular patterns of emergence – as described by Hale's laws – suggest that, if sunspots are indeed the surface manifestation of some submerged magnetic field, this subsurface magnetic field must also have regular properties. In particular, the azimuthal component of the magnetic field must be antisymmetric about the equator and, given that the sunspot polarities flip at the end of each 11 year cycle, the full magnetic cycle must be approximately 22 years. Before this theory can be accepted, it is necessary to establish a physical mechanism by which loops of magnetic flux can be transported from the site of this coherent magnetic field to the photosphere. It was Parker (1955a) and Jensen (1955) that first (independently) pointed out that an isolated, horizontal magnetic flux tube (in thermal equilibrium with the fluid around it) will be less dense than its surroundings, and therefore buoyant. It has subsequently been shown that magnetic buoyancy can also lead to the formation of rising flux tubes from a horizontal layer of magnetic fluid (see, e.g. Hughes, 1992; Matthews et al., 1995). So, magnetic buoyancy is clearly capable of explaining how magnetic flux from the solar interior could appear at the surface of the Sun.

The magnetic fields associated with sunspots, and active regions in general, provide a great deal of information concerning the nature of the azimuthal component of the subsurface field. Active regions are a low-latitude phenomenon, but magnetograms show that there are much weaker magnetic fields to be found at high latitudes (of the order of a few Gauss). Each polar cap has a clear dominance of one magnetic polarity, with opposite dominant polarities on opposite poles (Schrijver and Zwaan, 1999; Stix, 2002). Like the magnetic field associated with active regions, this polar field is observed to oscillate with a period of about 22 years. However, rather than oscillating in phase with the the low-latitude activity, the polar field is observed to reverse near sunspot maximum, and reaches its maximum extent around sunspot minimum. The sunspot field is therefore oscillating approximately 90° out of phase with the polar field. This regular behaviour suggests that the polar field is actually the radial component of the large-scale subsurface magnetic field. The symmetries of the mean solar magnetic field that have been described above seem to be relatively robust, with the equatorial antisymmetry of both the radial and azimuthal components being preserved from one cycle to the next. A magnetic field with this kind of symmetry is normally described as having dipolar parity.

The recent sunspot records (see Figure 1.2) suggest that the 11 year sunspot cycle has been remarkably persistent. However, the sunspot cycle has not always been so regular. Starting about midway through the 17$^{\text{th}}$ century, there was a period of about 70 years when very few sunspots were observed – this period of time is known as the Maunder minimum (Eddy, 1976). It is clear that the lack of sunspots was genuine and not due to deficiencies in the solar observations (Ribes and Nesme-Ribes, 1993). In fact, even though there were few sunspots observed during the Maunder minimum, they still provide us with some information concerning the large-scale subsurface field within the Sun. As shown in Figure 1.3, those sunspots that were observed during the final stages of the Maunder minimum were almost entirely confined to the Southern hemisphere (Ribes and Nesme-Ribes, 1993; Sokoloff and Nesme-Ribes, 1994), within about 20° of the equator. Such asymmetry in the appearance of sunspots strongly suggests that the underlying magnetic field had (temporarily) departed from dipolar symmetry.

In order to assess the significance of the Maunder minimum to the global picture of solar magnetic activity, we need to know whether it was a unique event or whether such "grand minimum" phases are a recurrent feature of the solar cycle. Sunspot records do not extend far enough back in time to provide this information, so other sources of

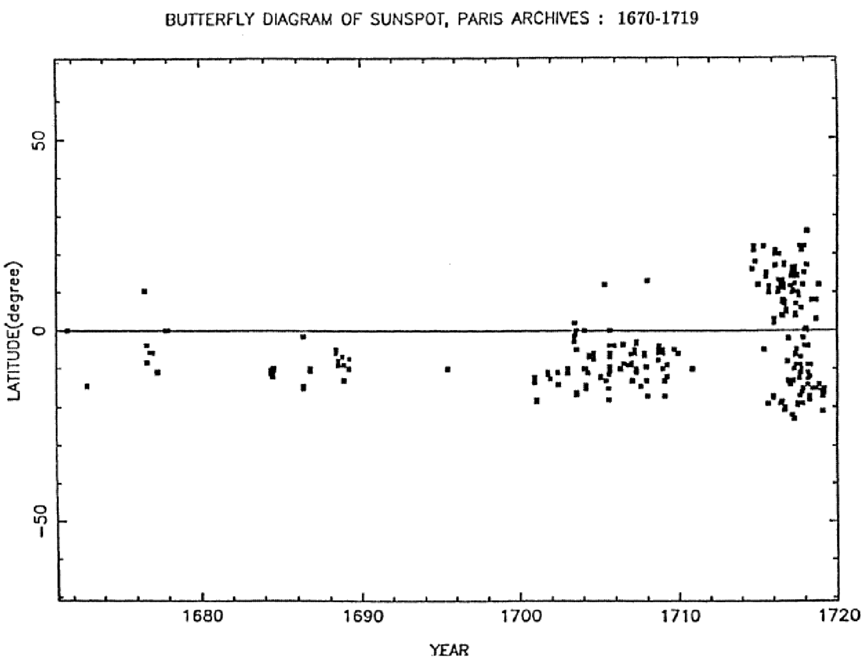

Figure 1.3: Sunspot observations during the latter stages of the Maunder minimum (taken from Sokoloff and Nesme-Ribes, 1994).

information are required. Perhaps surprisingly, much can be learnt about solar magnetic activity from the study of terrestrial deposits of ^{10}Be in ice cores, and ^{14}C in tree rings (see, for example, Beer et al., 1991; Wagner et al., 2001). These isotopes are generated as the result of cosmic rays entering the Earth's atmosphere. The magnetic fields that are associated with the solar wind tend to deflect these cosmic rays away from the Earth, therefore the abundance of these terrestrial isotopes is anti-correlated with solar magnetic activity. Studies of ^{10}Be and ^{14}C have shown that grand minimum phases – similar to the Maunder minimum – are a regular feature of the solar magnetic cycle, with a grand minimum occurring (on average) about every 200 years. Interestingly, it is still possible to observe cyclic behaviour in the ^{10}Be records during the Maunder minimum (Beer et al., 1998). This suggests that some kind of cyclic magnetic activity was occurring in the Sun during this period, but not at a high enough level to produce many sunspots. The solar-stellar connection suggests that "solar-like" late-type stars should also experience grand minimum phases, and behaviour of this type seems to have been found (Baliunas and Jastrow, 1990; Baliunas et al., 1995).

1.2.3 Activity in rapidly rotating late-type stars

As described above, rapidly rotating late-type stars show different patterns of magnetic activity to that found in older late-type stars. So, it is unclear how much the Sun can tell us about magnetic activity in rapid rotators. As such detailed observation of more distant stars is clearly not possible, information about the distribution of magnetic fields on the surface of these stars can only be provided by indirect imaging techniques. Photometric techniques (see, e.g., Oláh and Strassmeier, 2002) can be used to provide qualitative information regarding the starspot coverage. Light curves for highly spotted stars can show a great deal of modulation as the star rotates – Byrne (1992) found modulation of the order of 40 per cent for the RS CVn binary II Peg. This level of modulation can only occur if a very large fraction of the stellar surface is covered by starspots. Having said that, the analysis of light curves cannot provide detailed information about the surface distribution of starspots. The most commonly used technique for surface imaging is Doppler imaging (Rice, 1996, 2002). The latitudinal distribution of starspots can be deduced by the speed at which "bumps" travel across the rotationally-broadened spectral line profiles as the star rotates. Many Doppler imaging surveys have been carried out for rapidly rotating stars (for a recent survey, see Strassmeier, 2002).

The most surprising finding from Doppler imaging surveys is that rapidly rotating late-type stars often have surface magnetic fields at all latitudes, with a high proportion of such stars showing features at high latitudes or even covering their rotational poles (Strassmeier, 2002). Polar magnetic features produce a characteristic bump in the spectral line profile that shows little (or no) variation in position as the star rotates. Polar spots have never been observed on the Sun, and this has led to some people to question the reality of these features on rapid rotators. Byrne (1992) points out that the accurate determination of the "unspotted" line profile for rapid rotators is not straightforward – any inaccuracies here could lead to a spurious polar spot. Byrne also proposed that the flat-bottomed line-profile that is diagnostic of a polar spot could also be caused by chromospheric emission in very active stars. Bruls et al. (1998) have subsequently demonstrated that chromospheric activity is not capable of producing this effect in all the commonly used Doppler-imaging lines (although it is effective for some of them), and it is therefore unlikely that it gives rise to false observations of polar spots. Many other error sensitivity tests have been carried out on the various image reconstruction techniques (see, for example, Rice, 2002), and the reality of polar spots is now generally accepted (Schrijver and Title, 2001; Strassmeier, 2002).

One of the most widely studied rapidly rotating late-type stars is the K0 dwarf AB Doradus (Collier Cameron and Unruh, 1994; Donati and Collier Cameron, 1997; Collier Cameron and Donati, 2002), and it might reasonably be supposed to be a typical "rapid rotator". As a late-type star that has only just arrived on the main sequence, AB Doradus has a very high rotation rate – its rotational period of about 0.5 days means that it is rotating approximately 50 times faster than the Sun. Early Doppler imaging studies (Collier Cameron and Unruh, 1994) found that AB Doradus did, indeed, have high-latitude magnetic features as well as weaker features at lower latitudes. Subsequent studies have found that (in qualitative terms), the surface distribution of magnetic field on AB Doradus is relatively robust.

1.3 Differential rotation in late-type stars

Modern theories of magnetic field generation in late-type stars suggest that differential rotation plays a key role. Before discussing such theories, it is important to understand the key observational facts concerning differential rotation. This section describes observations of solar and stellar differential rotation, as well as observations of other large-scale flows in the solar convection zone.

1.3.1 Solar differential rotation

It was Carrington (during the 1860s) who first detected differential rotation on the surface of the Sun (see, for example, Rüdiger, 1989). He carefully measured the relative motions of sunspots and discovered that spots at lower latitudes seem to move across the solar disk faster than those at higher latitudes. In fact, we now know that the equatorial regions at the solar surface rotate (approximately) 40 per cent faster than the polar regions. Of course, surface feature tracking can tell us nothing about the internal distribution of angular velocity within the Sun. Early theoretical models (see, for example, Gilman, 1974) predicted that the angular velocity should be constant along cylindrical surfaces whose axes are aligned with the rotational axis – a consequence of the Taylor-Proudman constraint for rapidly rotating fluids (Proudman, 1916; Taylor, 1921).

With the advent of helioseismology, it became possible to put theories of solar differential rotation to the test. A wide spectrum of pressure driven (p-mode) oscillations are found in the Sun, the frequencies of which depend closely upon the properties of the medium through which they are propagating. By observing the behaviour of these modes of oscillation, conclusions can be drawn regarding the internal structure of the Sun (see, for example, Schou et al., 1998; Chitre and Antia, 2003). In particular, the fact that rotation causes splitting of the frequencies of these p-modes means that helioseismology can be used to determine the spatial dependence of the internal angular velocity of the Sun. Figure 1.4 shows the solar rotation profile according to a recent inversion carried out by Schou et al. (1998). Regions at high latitudes and regions at small radii are not included in the plot shown in Figure 1.4, because the rotation profile

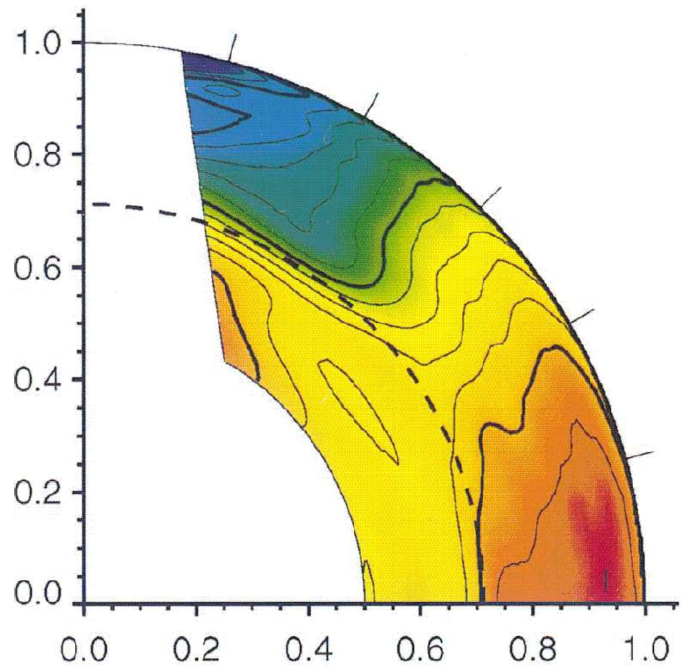

Figure 1.4: The spatial dependence of angular velocity within the Sun, as determined from helioseismology. Contours with red shading correspond to faster rotation rates, blue shading corresponds to slower rotation rates. Taken from Schou et al. (1998).

there is not well-constrained by the helioseismic data. The first thing to notice is that the internal angular velocity of the Sun is not constant on cylindrical surfaces. Rather than varying according to distance from the rotation axis, the angular velocity within the convection zone is, in fact, approximately constant along lines of constant latitude. The second surprising result from helioseismology is the presence of a sharp transition region at the base of the convection zone, now commonly referred to as the tachocline (Spiegel and Zahn, 1992). The tachocline is the site of strong radial gradients in the angular velocity profile, with a steep negative gradient at high latitudes and a slightly weaker positive gradient closer to the equator. The core appears to be rotating virtually as a solid body.

1.3.2 Trends in stellar differential rotation

With the use of helioseismology, we can probe the distribution of angular velocity within the Sun. Unfortunately, this is not possible with more distant stars, and the best that we can hope for is an understanding of the surface differential rotation. One of the most extensive studies of stellar differential rotation was carried out by Hall (1991). This photometric study relied on the analysis of long-term light curve records and the rotation periods that can be deduced from them. The variation in the determined rotation period is interpreted as being due to starspots forming at different latitudes, and therefore the scatter in rotation periods is interpreted as being due to differential rotation. The sample of stars that was analysed by Hall (1991) possessed a wide range of rotation periods, which spanned about 3 orders of magnitude. What Hall found was that the "lap-time" (the time taken for the equator to lap the poles) was nearly independent of rotation period for the stars within the sample. More precisely, if $\Delta\Omega$ is the angular velocity difference between the pole and the equator in these stars, then $\Delta\Omega$ does not vary a great deal from star to star. Therefore, $\Delta\Omega/\Omega$ is small in rapidly rotating stars. The consequence of this is that very rapidly rotating stars are rotating much more like a rigid body than stars like the Sun. The long-term variations in chromospheric emission can also be used as a means of studying differential rotation (see, for example, Donahue et al., 1996). This study sampled stars with a smaller range of rotation rates than those studied by Hall (1991), but (although there were slight differences in the observed trends) they also came to the conclusion that the value of $\Delta\Omega$ depends only weakly upon the rotation rate.

For rapidly rotating late-type stars, Doppler imaging techniques provide us with a surface map of magnetic features, so it is possible to use surface tracking as a means of measuring surface differential rotation (see, for example, Collier Cameron, 2002). Donati and Collier Cameron (1997) used the technique of surface feature tracking to measure the differential rotation on the surface of AB Doradus – as AB Doradus has magnetic features at all latitudes, this technique can provide a reasonable picture of the differential rotation. They found that AB Doradus shows only very small surface differential rotation, with the equator rotating slightly faster than the poles. The lap-time found by Donati and Collier Cameron (1997) is about 110 days, which implies that it takes about 220 rotational periods for the equator to lap the poles. By way of comparison with the Sun, the solar lap time is about 120 days, which only corresponds to $4-5$ rotational periods. This all agrees with the qualitative statements about differential rotation made by Hall (1991).

1.3.3 Torsional oscillations and meridional flows

Although this section is primarily concerned with stellar differential rotation, there are other large-scale flows observed in the Sun. Howard and LaBonte (1980) carried out Doppler velocity measurements of the solar surface rotation, and they discovered an oscillatory pattern that is superimposed on the surface differential rotation profile. They found a pattern consisting of alternating bands of slower and faster rotation, which migrate towards the equator. These oscillations, which have the appearance of travelling waves with an 11 year period were referred to as torsional oscillations. This 11-year periodic behaviour is highly suggestive of a link between the magnetic activity cycle and these torsional oscillations – a fact also noted by Howard and LaBonte (1980). These torsional oscillations have been the subject of numerous subsequent studies (see, for example, Ulrich et al., 1988; Hathaway et al., 1996), but it is only very recently that it has become possible to examine the distribution of these oscillations throughout the convection zone. Recent observations (Vorontsov et al., 2002), based on an improved method of data analysis, indicate that torsional oscillations are not confined to the surface regions of the Sun. Figure 1.5 is a plot taken from Vorontsov et al. (2002), which shows how the torsional oscillations vary according to latitude and radius – a harmonic function has been fitted to six year's worth of data in such a way as to give the oscillations an 11 year period. The observations clearly suggest a double-banded structure for the torsional oscillations, with the high-latitude band migrating polewards and the low-latitude band migrating equatorwards. Also notable is the fact that the torsional oscillations penetrate well below the surface so that a large part of the convection zone is involved in this oscillatory behaviour, particularly at high latitudes. Interestingly, there is preliminary evidence for similar oscillations in the rotation profile of AB Doradus (Collier Cameron and Donati, 2002).

Torsional oscillations represent an azimuthal perturbation to the solar differential rotation profile. Meridional flows have also been observed in the Sun – Doppler measurements (Hathaway, 1996) can be used to show that typical meridional flows at the surface of the Sun are polewards with a small mean velocity of approximately 10-20ms^{-1}. Although this flow is very weak, it is possible to use the techniques of helioseismology to deduce the subsurface distribution of this meridional flow. Giles et al. (1997) found that the observed surface flow is approximately constant throughout the outer layers of the Sun (4 per cent of the solar radius). This finding was confirmed by Braun and Fan (1998), who showed that the poleward flow extends down throughout the top half of the convection zone, with no evidence of a returning (equatorward) flow in this region. This does not rule out the possibility of an equatorial (returning) flow in the lower portion of the convection zone, although the effects of compressibility mean that this flow should be very weak.

1.4 Magnetic field generation in stars

In the context of the Earth, the need for a theory of magnetic field generation is clear. As will be shown in the next chapter, magnetic fields decay away if there is nothing to sustain them. The decay time for a fossil field within the Earth is of the order of 8×10^4 years (see, for example, Jones, 2000), which is inconsistent with the idea that

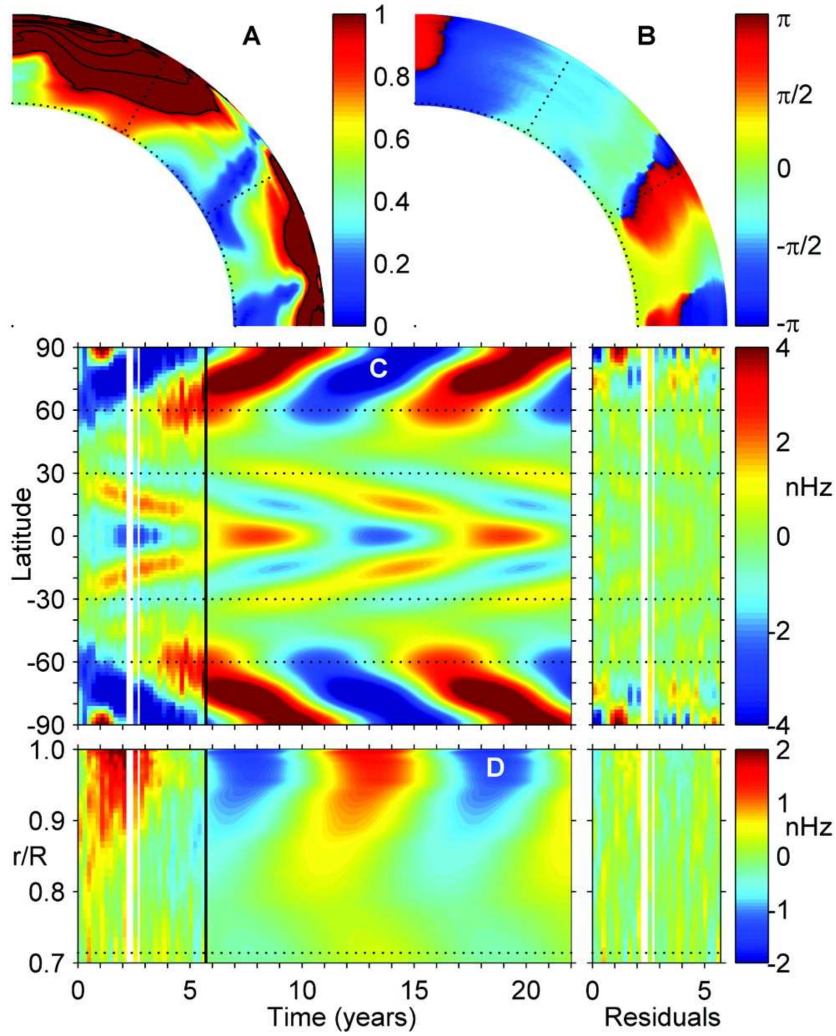

Figure 1.5: Torsional oscillations in the solar convection zone. A harmonic function with an 11 year period has been postulated on the basis of 6 years worth of data. Plot A shows the amplitude of this function; plot B shows the phase; plot C shows a plot at constant radius (r=0.98R$_\odot$), showing the rotational variation as a function of latitude and time; plot D shows the rotational variation as a function of radius and time at a constant latitude of 20°. Taken from Vorontsov et al. (2002).

the Earth's magnetic field could be a relic field. So, there must be some mechanism that is responsible for regenerating the terrestrial magnetic field. In the case of the Sun, this ohmic decay time is of the order of 10^{10} years – this is comparable with the length of time that the Sun has spent on the main sequence, so we need more than a simple comparison of time-scales to rule out the possibility of a fossil magnetic field (Tobias, 2002b). Having said that, it is very difficult to reconcile the idea of a relic field explanation with all the time-dependent features described in Section 1.2.2. Some alternative explanation is therefore required.

Two mechanisms have been proposed for the generation of a cyclic magnetic field within the Sun (see, for example, Tobias, 2002b). The first suggestion is the idea that there is some kind of hydromagnetic oscillator within the Sun. The basic idea is that there is a fixed magnetic field lying in meridional planes within the Sun. If this field is then subject to cyclic perturbations in the azimuthal direction, this will result in a azimuthal field that varies with the appropriate periodicity. There are two main objections to this idea. Firstly, this kind of situation will give rise to a stationary radial field, and is therefore incompatible with the observed cyclic reversals of the field at the solar poles. More importantly, in order that the correct (22 year) period be obtained for the solar cycle, the oscillator must also have a 22 year period. However, the torsional oscillations (described in Section 1.3.3) are observed to have an 11 year period and are therefore inconsistent with the oscillator theory. A rather more likely scenario is that these oscillations are actually driven by the magnetic field (through the action of the Lorentz force) rather than being, in some way, responsible for its the generation. The Lorentz force is quadratic in the magnetic field, so a 22 year magnetic cycle should lead to an 11 year period for the torsional oscillations. Given these objections, it seems unlikely that a hydromagnetic oscillator is responsible for magnetic field generation within the Sun. The general consensus is that solar magnetic activity is due to a hydromagnetic dynamo, and this is the subject of the next chapter.

Chapter 2

Dynamo Theory

It was Larmor (1919) who first suggested that some sort of hydromagnetic dynamo may be responsible for the generation of magnetic fields within the Sun. The essence of Larmor's idea is that the motion of an electrically conducting fluid across a magnetic field will induce a current, which in turn will generate more magnetic field. If this process works in such a way as to amplify the net magnetic field, then we have a dynamo. Dynamo theory has become a vast area of research in its own right, and has been the subject of many books and review articles (for example, Moffatt, 1978; Parker, 1979; Krause and Rädler, 1980; Cowling, 1981; Weiss, 1994; Tobias, 2002b; Ossendrijver, 2003). In this chapter, I review the current status of dynamo theory, with particular reference to its application to solar and stellar dynamos.

2.1 Introducing the dynamo problem

2.1.1 The induction equation

Before the dynamo problem can be discussed, it is important to be able to describe the evolution of magnetic fields quantitatively. Maxwell's equations (see, for example, Priest, 1982) describe the behaviour of electromagnetic fields:

$$\nabla \cdot \mathbf{E} = \frac{\rho_c}{\epsilon_o}, \tag{2.1}$$

$$\nabla \cdot \mathbf{B} = 0, \tag{2.2}$$

$$\nabla \times \mathbf{E} = -\frac{\partial \mathbf{B}}{\partial t}, \tag{2.3}$$

$$\nabla \times \mathbf{B} = \mu_o \mathbf{j} + \frac{1}{c^2}\frac{\partial \mathbf{E}}{\partial t}, \tag{2.4}$$

where $\mathbf{E}$ represents the electric field, $\mathbf{B}$ represents the magnetic field, ρ_c is the charge density, $\mathbf{j}$ is the current density, μ_o is the permeability of free space, ϵ_o is the permittivity of free space, and c is the speed of light (SI units have been used). Given that we are interested in magnetic fields in non-relativistic plasmas, it is possible to simplify these equations. If l_o is a typical length-scale and t_o a typical time-scale, then it is possible to define a characteristic velocity $u_o = l_o/t_o$. For non-relativistic fluids, $u_o \ll c$. Balancing terms in equation (2.3) gives

$$\frac{E}{l_o} \sim \frac{B}{t_o}, \tag{2.5}$$

which, in turn implies that

$$\left|\frac{1}{\nabla \times \mathbf{B}}\right| \left|\frac{1}{c^2}\frac{\partial \mathbf{E}}{\partial t}\right| \sim \frac{E l_o}{c^2 t_o B} \sim \frac{l_o^2}{t_o^2 c^2} \sim \frac{u_o^2}{c^2} \ll 1. \tag{2.6}$$

For a non-relativistic fluid, we can therefore approximate equation (2.4) by

$$\nabla \times \mathbf{B} = \mu_o \mathbf{j}. \tag{2.7}$$

We need an equation linking $\mathbf{j}$, $\mathbf{E}$ and $\mathbf{B}$ in order to derive an evolution equation for $\mathbf{B}$. Ohm's law for a moving conductor provides an approximate relationship between these quantities:

$$\mathbf{j} = \sigma(\mathbf{E} + \mathbf{u} \times \mathbf{B}), \tag{2.8}$$

where $\mathbf{u}$ is the fluid velocity and σ is the electrical conductivity. It should be stressed that equation (2.8) is an approximate relationship that is only valid in certain circumstances. Choudhuri (1998) derives a generalised Ohm's law, assuming that the fluid is fully ionised and is purely made up of electrons and ions (see also Cowling, 1976). It turns out that, provided the gas is sufficiently dense that the time between electron-ion collisions is small, equation (2.8) is a good approximation. This is certainly true within stellar interiors.

Assuming that Ohm's law is valid in all cases to be considered, it can be used to substitute for $\mathbf{j}$ in equation (2.7):

$$\nabla \times \mathbf{B} = \mu_o \sigma (\mathbf{E} + \mathbf{u} \times \mathbf{B}). \tag{2.9}$$

Taking the curl of this expression and then making use of equation (2.3) gives:

$$\frac{\partial \mathbf{B}}{\partial t} = \nabla \times (\mathbf{u} \times \mathbf{B}) - \nabla \times (\eta \nabla \times \mathbf{B}), \tag{2.10}$$

where $\eta = 1/\mu_o \sigma$ is the magnetic diffusivity. Equation (2.10) is known as the induction equation, and is one of the fundamental equations of magnetohydrodynamics (see, for example, Roberts, 1967; Moffatt, 1978; Parker, 1979). If the magnetic diffusivity, η, is constant, equation (2.10) becomes

$$\frac{\partial \mathbf{B}}{\partial t} = \nabla \times (\mathbf{u} \times \mathbf{B}) + \eta \nabla^2 \mathbf{B}. \tag{2.11}$$

The two terms on the right hand side of equation (2.11) have obvious physical interpretations: the first term represents advection by the fluid flow, the second term represents diffusion. Clearly, in the absence of any fluid flow, the magnetic field will simply decay. In order to get amplification of the net magnetic field, the inductive effects due to the fluid motions must outweigh the dissipative effects of diffusion. In a perfect conductor there is no dissipation and the magnetic field acts as though it is "frozen in" to the fluid

– this was a result first derived by Alfvén (see, for example, Choudhuri, 1998). In astrophysics, it is commonly the case that the advection term in equation (2.11) dominates over diffusion. In such a situation, we would expect the magnetic flux to be (effectively) frozen into the plasma.

2.1.2 The dynamo process

Solving the dynamo problem self-consistently is a formidable problem. Equation (2.10) tells us that one requirement is to have a velocity field that is capable of maintaining a magnetic field against dissipative effects. Finding such a velocity field is the essence of the kinematic dynamo problem, which is discussed below. However, in order to be self-consistent, it is also important that the velocity field can be sustained by the forces acting on it.

In an electrically conducting fluid, the evolution of the velocity field in an inertial frame of reference is governed by the magnetically-modified Navier-Stokes equation (see, for example, Rüdiger, 1989),

$$\rho \frac{D\mathbf{u}}{Dt} = -\nabla p + \rho \mathbf{g} + \mathbf{j} \times \mathbf{B} + \nabla \cdot \mathbf{T}, \tag{2.12}$$

where ρ is the fluid density, p is the pressure, $\mathbf{g}$ is the gravitational acceleration, and $\mathbf{T}$ represents the viscosity tensor:

$$\mathbf{T}_{ij} = \rho\nu \left[\left(\frac{\partial u_i}{\partial x_j} + \frac{\partial u_j}{\partial x_i} \right) - \frac{2}{3} \frac{\partial u_k}{\partial x_k} \delta_{ij} \right], \tag{2.13}$$

where ν is the kinematic viscosity. In equation (2.12), electrostatic effects have been neglected, as they are negligible when compared to magnetic effects. The key point to notice is that the magnetic field plays a dynamical role in the evolution of the velocity field, via the Lorentz force, $\mathbf{j} \times \mathbf{B}$, which, by equation (2.7), is equal to $(1/\mu_o)(\nabla \times \mathbf{B}) \times \mathbf{B}$. Strictly speaking, we must therefore solve equation (2.10) and equation (2.12) simultaneously in order to find a self-consistent solution to the dynamo problem.

2.2 Kinematic dynamos

2.2.1 Preliminary ideas

Given the complexity of the problem described in the previous section, much of the work on dynamo theory has focused on (linear) kinematic dynamos. The induction equation – equation (2.10) – describes the competition between magnetic induction and diffusion. For a kinematic dynamo, the idea is to find a velocity field, $\mathbf{u}$, such that the magnetic field generation due to the inductive term is more efficient than the dissipation due to the diffusive term. Such a velocity field is taken to be prescribed, so there is no back-reaction on $\mathbf{u}$ due to the magnetic field.

Because $\mathbf{B}$ is divergence free (see equation 2.2), in spherical geometry it is often convenient to decompose the magnetic field into toroidal and poloidal parts (see, e.g., Roberts, 1994):

$$\begin{aligned} \mathbf{B} &= \nabla \times (T\mathbf{r}) + \nabla \times \nabla \times (S\mathbf{r}) \\ &\equiv \mathbf{B_T} + \mathbf{B_P}, \end{aligned} \tag{2.14}$$

where T and S are scalar functions of position and time, and $\mathbf{r}$ is the usual radial vector. In spherical geometry this is a particularly convenient way of representing axisymmetric fields because, since T and S are independent of the azimuthal angle, ϕ, equation (2.14) becomes:

$$\mathbf{B} = B\mathbf{e}_\phi + \nabla \times (A\mathbf{e}_\phi), \tag{2.15}$$

where $\mathbf{e}_\phi$ is the unit vector in the ϕ direction,

$$B = -\frac{\partial T}{\partial \theta} \tag{2.16}$$

represents the toroidal component, and

$$A = -\frac{\partial S}{\partial \theta} \tag{2.17}$$

represents the poloidal part of the magnetic field. For an axisymmetric field, we can attach simple physical meanings to the poloidal and toroidal components: the toroidal field is purely azimuthal, whilst the poloidal field lies in the meridional plane. Many approaches to the kinematic dynamo problem are based on the idea of a poloidal-toroidal decomposition, so this is an important concept.

2.2.2 Antidynamo theorems

The induction equation looks deceptively simple – as $\mathbf{u}$ is a prescribed quantity, the equation is linear in $\mathbf{B}$. We would expect, therefore, that there might be a relatively simple solution to the problem. Unfortunately, this does not appear to be the case. Following Larmor's proposal of dynamo theory, it soon became clear that there were certain simple magnetic field configurations and velocity fields that were not possible solutions of the kinematic dynamo problem. The most famous of these (so-called) antidynamo theorems was a result demonstrated by Cowling (1934).

The basic statement of Cowling's theorem is that a hydromagnetic dynamo is incapable of maintaining a steady axisymmetric magnetic field. The proof of Cowling's theorem (see, for example, Moffatt, 1978) relies upon the idea of a neutral point: In each meridional plane there exists at least one point (the neutral point) on each side of the symmetry axis about which the poloidal field lines form closed loops. At this neutral point the magnetic field is purely toroidal. By integrating Ohm's law over a small neighbourhood containing a neutral point, in the meridional plane, it is straightforward to show that an axisymmetric steady field is (at least locally) unsustainable. The impossibility of a steady axisymmetric field was also demonstrated by Braginsky (1964), using an alternative argument. Hide and Palmer (1982) have since generalised Cowling's theorem to show that unsteady axisymmetric magnetic fields are also not sustainable by dynamo action. Cowling's theorem and other such antidynamo theorems suggest that it is not possible to obtain solutions of the kinematic dynamo problem using over-simplified geometries.

2.2.3 Physical considerations

From a mathematical perspective, it has been established that the kinematic dynamo problem is highly complex. Antidynamo theorems provide information about things that don't work, but they don't tell us much about what will. In order that we might make an informed choice for the velocity field, $\mathbf{u}$, it is sensible to establish whether there are any particularly desirable characteristics that $\mathbf{u}$ may possess.

The relevance of differential rotation to the dynamo process has long been understood (Bullard and Gellman, 1954, were amongst the first people to realise this). Differential rotation, like that found in the Sun, provides an efficient means by which toroidal field (that is frozen into the plasma) can be regenerated by stretching out the poloidal field in the direction of flow. This process is shown schematically in Figure 2.1(a), and is often referred to as the "ω-effect". As the ω-effect provides a mechanism by which poloidal field can be converted into toroidal field, a dynamo could feasibly operate if a sustainable mechanism for the reverse process could be found – ie. something that can regenerate poloidal magnetic field from toroidal field.

It was Parker (1955b) who first proposed a mechanism for the completion of this dynamo cycle. Parker's idea was based upon the fact that convective upwellings within a rotating astrophysical body, such as the Sun, will stretch the associated toroidal field lines upwards. These rising pockets of fluid will then expand due to the effects of stratification and, in order to conserve angular momentum, they also twist. This leads to a twisting of the associated field lines. This process is illustrated in Figure 2.1(b). The resulting loop of magnetic field will then drive a current in the toroidal direction which,

(a)

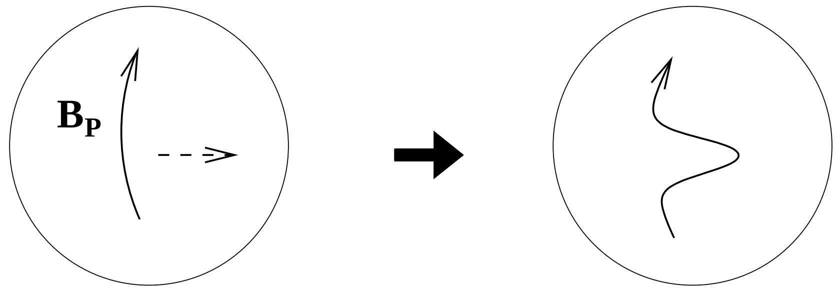

(b)

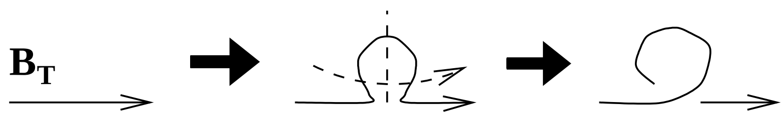

Figure 2.1: A schematic illustration of two aspects of the dynamo process. Figure (a) demonstrates the action of differential rotation (direction indicated by the dashed line) on a poloidal magnetic field line (solid line). Figure (b) illustrates Parker's idea (described in the text) that the action of cyclonic convection could lead to the regeneration of poloidal magnetic field from toroidal field: the solid line is the magnetic field line and the dashed line represents the twisting effect.

when averaged over a large number of these cyclonic events will lead to a net generation of poloidal field. This effect has since become known as the α-effect. As convective downwellings will produce a net poloidal magnetic field in the opposite direction, it is important that there is an asymmetry (due to compressibility) between upwellings and downwellings in order that we might get a net poloidal field (see, for example, Priest, 1982).

Having completed the dynamo cycle, Parker immediately managed to find a solution to the kinematic dynamo problem. This was achieved by artificially adding a source term (corresponding to the α-effect) to the poloidal field equation. This source term represented the net effect of the non-axisymmetric cyclonic events and, in fact, this additional source term gets round Cowling's theorem and enabled Parker to look for axisymmetric solutions. Parker then simplified the dynamo equations by moving to a local Cartesian co-ordinate system, (x, y, z), where the x-axis points southwards (equatorwards), y points in the azimuthal direction and z points radially outwards. Axisymmetry implies that we can use the Cartesian analogue of the poloidal-toroidal decomposition given by equation (2.15):

$$\mathbf{B} = B\mathbf{e_y} + \nabla \times (A\mathbf{e_y}), \tag{2.18}$$

where A and B are independent of y. The velocity field was taken to be that of a uniform shear, so that

$$\mathbf{u} = Gz\mathbf{e_y}, \tag{2.19}$$

where G is constant. Substituting expressions (2.18) and (2.19) into equation (2.11) – the induction equation with constant magnetic diffusivity – leads to the following evolution equations for A and B:

$$\frac{\partial A}{\partial t} = \alpha B + \eta \nabla^2 A \tag{2.20}$$

$$\frac{\partial B}{\partial t} = G\frac{\partial A}{\partial x} + \eta \nabla^2 B, \tag{2.21}$$

where the αB term on the right hand side of equation (2.20) is the additional source term due to the α-effect (α is taken to be constant). It is easily shown (Parker, 1955b) that (for an appropriate choice of parameters) these equations have solutions that take the form of exponentially growing migratory dynamo waves, which propagate in the x (North-South) direction. The direction of migration depends upon the sign of the product "αG" – a positive value leads to polewards propagation, whilst a negative value leads to equatorwards propagation. This clearly has parallels with the observed migration of sunspots during the solar cycle, although it is a local solution to the problem rather than a global one, and therefore ignores the boundary effects of the poles and the equator (where α would be expected to vanish). Tobias et al. (1997) showed that a more realistic treatment of the problem, where the boundaries are included, leads to the suppression of the (so-called) convectively unstable solutions found by Parker. The oscillations that are found in this model require stronger driving and (close to onset) take the form of wall modes concentrated around the equator. These results suggest that boundary conditions play a key role in the form of the dynamo oscillations, regardless of the horizontal scale of the domain. Having said that, both Parker's model and that of Tobias et al. (1997) do confirm that this α-effect does enable the operation of a dynamo.

Although these results are encouraging from the point of view of the viability of the dynamo idea, it is based upon physical arguments as opposed to mathematical ones. The next section is concerned, at least partially, with the mathematical justification of Parker's ideas.

2.3 Mean-field electrodynamics

2.3.1 The derivation of the equations

One way of expressing Parker's ideas in a more mathematical fashion is through the ideas of mean-field electrodynamics (Steenbeck et al., 1966; Moffatt, 1978; Krause and Rädler, 1980; Moffatt, 2002). This theory is based upon the assumption that, in a turbulent conducting fluid, it is possible to decompose the magnetic field and the imposed velocity field into mean and fluctuating parts. If this is to be done in a meaningful way, there must be a spatial separation of scales between the mean and fluctuating parts. So, the mean parts of $\mathbf{u}$ and $\mathbf{B}$ are assumed to vary over a length-scale L, whilst the fluctuating parts vary over a length-scale l. The separation of scales implies that $L \gg l$. Spatial averages are taken over some intermediate length-scale and are denoted by angled brackets: $\langle\ \rangle$. Although only spatial averages are used here, it should be noted that it is equally valid to develop the theory in terms of temporal averages. So, we can write

$$\mathbf{u} = \langle \mathbf{u} \rangle + \mathbf{u}' \equiv \mathbf{U_0} + \mathbf{u}', \tag{2.22}$$

and

$$\mathbf{B} = \langle \mathbf{B} \rangle + \mathbf{b}' \equiv \mathbf{B_0} + \mathbf{b}', \tag{2.23}$$

where $\mathbf{B_0}$ and $\mathbf{U_0}$ are the mean parts of (respectively) the magnetic field and the fluid velocity, and $\mathbf{b}'$ and $\mathbf{u}'$ are the fluctuating parts. It is easy to see that the fluctuating quantities are defined in such a way as to ensure that

$$\langle \mathbf{b}' \rangle = \langle \mathbf{u}' \rangle = 0. \tag{2.24}$$

Following the approach described in Moffatt (1978), we now substitute the expressions (2.22) and (2.23) into equation (2.11). Taking the spatial average gives an evolution equation for the mean magnetic field:

$$\frac{\partial \mathbf{B_0}}{\partial t} = \nabla \times \mathcal{E} + \nabla \times (\mathbf{U_0} \times \mathbf{B_0}) + \eta \nabla^2 \mathbf{B_0}, \tag{2.25}$$

where $\mathcal{E} = \langle \mathbf{u}' \times \mathbf{b}' \rangle$ can be interpreted as a mean electromotive force. Subtracting equation (2.25) from equation (2.11) yields an equation governing the evolution for the fluctuating magnetic field:

$$\frac{\partial \mathbf{b}'}{\partial t} = \nabla \times (\mathbf{U_0} \times \mathbf{b}') + \nabla \times (\mathbf{u}' \times \mathbf{B_0}) + \nabla \times (\mathbf{u}' \times \mathbf{b}' - \mathcal{E}) + \eta \nabla^2 \mathbf{b}'. \tag{2.26}$$

From equation (2.26) it is clear that, since $\mathbf{u}$ is a prescribed velocity field in this kinematic theory, $\mathbf{B_0}$ is linearly related to $\mathbf{b}'$ (assuming that there is no small-scale dynamo action) and therefore $\mathcal{E}$ is also linearly related to $\mathbf{B_0}$. This linear relationship may be represented (see, for example Moffatt, 2002) by an expression of the form

$$\mathcal{E}_i = \alpha_{ij} B_{0j} + \beta_{ijk} \frac{\partial B_{0j}}{\partial x_k} + ..., \tag{2.27}$$

where the dots indicate that the series can be extended to include higher order derivatives. These terms have been neglected because, since $\mathbf{B_0}$ varies over a long length-scale when compared to the turbulence, this series should be rapidly convergent (Moffatt, 1978). In theory, $\mathcal{E}_i$ should also depend upon time derivatives of $\mathbf{B_0}$, but these can be eliminated by making use of equation (2.25).

2.3.2 The properties of α and β

The coefficients which appear in equation (2.27) – namely α_{ij} and β_{ijk} – are actually components of pseudo-tensors (see, for example, Moffatt, 1978). This is because the mean electromotive force, $\mathcal{E}$, is what is known as a polar vector (its components change sign when we switch between a right-handed and a left-handed co-ordinate system), whilst $\mathbf{B_0}$ is an axial vector (its components stay the same under the same transformation). Equation (2.26) implies that these pseudo-tensors are determined by the mean flow, the properties of the fluctuating component of the velocity field and the magnetic diffusivity.

The properties of α and β are discussed extensively in Moffatt (1978), and only the main properties are summarised here. The leading term in the series defining $\mathcal{E}$ is

$$\mathcal{E}_i = \alpha_{ij} B_{0j}. \tag{2.28}$$

In order to analyse the properties of α_{ij}, it helps to split it up into symmetric and anti-symmetric parts:

$$\alpha_{ij} = \alpha_{ij}^{(s)} + \alpha_{ij}^{(a)}. \tag{2.29}$$

The antisymmetric part of this expression can be written in the form

$$\alpha_{ij}^{(a)} = -\epsilon_{ijk}\gamma_k \tag{2.30}$$

for some vector γ. So the contribution due to antisymmetric part of α in the mean-field equation is given by $\nabla \times (\gamma \times \mathbf{B_0})$, which can be interpreted physically as an effective mean ("pumping") velocity due to the turbulence. If the turbulence is isotropic, then α_{ij} takes a simpler form:

$$\alpha_{ij} = \alpha \delta_{ij}. \tag{2.31}$$

Now α_{ij} possesses no antisymmetric part and α is a pseudo-scalar, which means that it must change sign when the co-ordinate system is changed from a right-handed set to a left-handed set. It can therefore only be non-zero if the underlying turbulence (upon which α depends) lacks reflectional symmetry.

For isotropic turbulence, β_{ijk} can also be expressed in terms of an isotropic tensor:

$$\beta_{ijk} = \beta \epsilon_{ijk}, \tag{2.32}$$

where β is a true scalar. Substituting expressions (2.31) and (2.32) into equation (2.27) gives

$$\mathcal{E} = \alpha \mathbf{B_0} - \beta(\nabla \times \mathbf{B_0}), \tag{2.33}$$

and combining this expression for the mean electromotive force with the mean-field equation (2.25) gives

$$\frac{\partial \mathbf{B_0}}{\partial t} = \nabla \times [\alpha \mathbf{B_0} - \beta(\nabla \times \mathbf{B_0})] + \nabla \times (\mathbf{U_0} \times \mathbf{B_0}) + \eta \nabla^2 \mathbf{B_0}. \tag{2.34}$$

Equation (2.34) is known as the mean-field dynamo equation and, provided U_0, α, β and η are known, it can be solved for the mean field.

The physical significance of the "α-term" is that it represents an average current that is parallel to the mean magnetic field (this is easy to show from Ohm's law). It is worth remembering that the cyclonic events proposed by Parker would lead to such a current, so this is (in essence) a mathematical description of his idea. The significance of the "β-term" becomes clearer when β is taken to be constant. Since the magnetic field is solenoidal, the β-term can be written as $\beta\nabla^2\mathbf{B_0}$. It can therefore be interpreted as an eddy diffusivity – turbulent motions enhance the dissipation of magnetic fields. In practise, β and η are often combined into a single effective magnetic diffusivity (see, for example, Roberts, 1994),

$$\eta_t = \eta + \beta, \tag{2.35}$$

where the turbulent diffusivity, η_t, is generally much greater than η. This is due to the fact that the turbulence mixes the magnetic field up in such a way as to reduce its effective characteristic length-scale down to diffusive scales, leading to greatly enhanced diffusion (see, for example, Vainshtein and Cattaneo, 1992).

Nothing so far has been said about the calculation of α and β. In theory, α can be calculated by solving equation (2.26) with a uniform mean field (since α is assumed to be independent of $\mathbf{B_0}$). However, this is a complicated process notably due to the presence of the $\nabla \times (\mathbf{u}' \times \mathbf{b}' - \mathcal{E})$ term. If u_o is a representative value for the turbulent flow, then it is possible to define a magnetic Reynolds number

$$R_m = \frac{u_o l}{\eta}. \tag{2.36}$$

If R_m is small (not a good assumption for the Sun – $R_m \sim 10^6$ at the solar surface) then the $\nabla \times (\mathbf{u}' \times \mathbf{b}' - \mathcal{E})$ term in equation (2.26) is negligible when compared to the other terms on the right hand side of that equation, and so can be ignored. This is known as the first-order smoothing approximation. Assuming zero mean flow and a uniform magnetic field, equation (2.26) becomes (see, for example, Moffatt, 2002)

$$\frac{\partial \mathbf{b}'}{\partial t} = (\mathbf{B_0} \cdot \nabla)\mathbf{v}' + \eta\nabla^2\mathbf{b}'. \tag{2.37}$$

This equation is now amenable to Fourier techniques, and it can be shown that there is a direct relationship between α and the helicity of the turbulent velocity field (Moffatt, 1978). A similar relationship can be derived that links β with the kinetic energy of the turbulent flow. Whilst these precise relationships are dependent upon R_m being small, it is likely that there is still going to be some connection between α and the fluid helicity even when R_m is large. This is because α and the mean helicity for a fluid are both pseudo-scalars and so both will tend to be associated with a lack of reflectional symmetry (see, for example, Moffatt, 2002).

2.3.3 The nonlinear saturation of α and β

The description of mean-field theory that has been presented above is kinematic – there is an imposed turbulent velocity field, whose statistical properties are known, which is taken to be unaffected by the magnetic fields that it is responsible for generating. Whilst this may be a valid assumption for weak fields, for stronger magnetic fields the Lorentz force (see equation 2.12) must play a dynamical role. The α and β coefficients must therefore depend upon the magnetic field in some way.

The α-effect is associated with the small-scale advection of magnetic field lines, and we might expect that strong magnetic fields will tend to resist these motions. In mean-field dynamo simulations, this effect is often modelled in a somewhat arbitrary parameterised fashion (see, for example, Stix, 1972; Jepps, 1975; Yoshimura, 1978b,a; Brandenburg et al., 1989; Jennings and Weiss, 1991; Brandenburg, 1994; Charbonneau and MacGregor, 1996; Markiel and Thomas, 1999), with

$$\alpha \propto \frac{1}{(1 + \alpha_B |\langle \mathbf{B} \rangle|^2)} \tag{2.38}$$

being a commonly used expression. The coefficient α_B controls the strength of magnetic field at which α-quenching becomes significant, and the magnitude of this coefficient has been the source of much debate. We might expect that α-quenching would become important when the energy in the mean magnetic field is comparable to the mean kinetic energy of the turbulence. Vainshtein and Cattaneo (1992) argued that it is actually the small-scale magnetic fields that play the dominant role in α-quenching, and for large values of R_m (as found in the Sun) the energy in the small-scale field greatly exceeds that of the mean field. It is proposed that the mean magnetic energy is related to the magnetic energy of the mean field by an expression of the form:

$$\langle|\mathbf{B}|^2\rangle = R_m^n|\langle\mathbf{B}\rangle|^2, \tag{2.39}$$

with $n \geq 1$. The consequence of this result may be severe: the α-effect may be quenched long before equipartition mean magnetic fields can be established. In numerical simulations, Gilbert et al. (1993) found a slightly weaker dependence upon R_m, with $n \sim 0.3$, although this is still clearly significant for large values of R_m. Further evidence for this strong suppression of the α-effect comes from numerical simulations carried out by Tau et al. (1993) and Cattaneo and Hughes (1996), who carried out simulations of helically forced turbulence in a periodic box with an imposed, uniform, mean magnetic field. Blackman and Field (2000) suggest that the magnitude of the α-quenching may depend crucially upon the boundary conditions imposed – they argue that the use of non-periodic boxes would allow larger mean magnetic fields to develop in their turbulence model. This whole issue is still controversial. Another possible way of modelling α-quenching is to actually solve an evolution equation for α (see, for example Brandenburg, 1994; Covas et al., 1998), although this approach still features undetermined parameters.

As discussed earlier, β can be interpreted as a diffusive contribution from the turbulence to the mean-field dynamo equation. However, since the Lorentz force acts back upon the turbulent fluid motions, this enhanced diffusivity should also be quenched in the same way as the alpha effect (Roberts and Soward, 1975). With a few exceptions (for example, Tobias, 1996a), this effect has largely been ignored in mean-field dynamo simulations, in favour of α-quenching. Given the somewhat arbitrary nature of these parameterised quenching mechanisms, it is perhaps best simply to think of them as a convenient means of saturating the dynamo in mean-field simulations, rather than an accurate representation of the physical quenching mechanism.

2.4 The solar dynamo

2.4.1 The $\alpha\omega$ dynamo model

With non-constant effective magnetic diffusivity, η_t (see equation 2.35), the mean-field dynamo equation (equation 2.34) becomes

$$\frac{\partial \mathbf{B}}{\partial t} = \nabla \times (\alpha \mathbf{B}) + \nabla \times (\mathbf{U} \times \mathbf{B}) - \nabla \times (\eta_t \nabla \times \mathbf{B}), \tag{2.40}$$

where the "0" subscripts have been dropped from the mean-field quantities. Most of the progress that has been made in modelling solar and stellar dynamos has been based upon mean-field theory, and this approach has proved to be relatively successful (see, for example, Weiss, 1994; Tobias, 2002a,b, for some recent reviews). It should be noted that there is no separation in length-scales between the mean and fluctuating parts of the magnetic field in the Sun (Cowling, 1981), therefore, the application of equation (2.40) to the solar dynamo cannot be rigorously justified. However, its success in reproducing many of the qualitative features of the solar dynamo suggest that it is a useful approach that contains the important physical ideas.

The relative importance of the physical processes contained within the mean-field dynamo equation are probably best illustrated by considering a simple axisymmetric model in spherical geometry. The imposed velocity field is taken to be purely azimuthal, so that

$$\mathbf{U} = r \sin\theta \Omega(r, \theta) \mathbf{e}_\phi, \tag{2.41}$$

where $\Omega(r, \theta)$ is the local angular velocity. We can then make the standard decomposition of the magnetic field into poloidal and toroidal parts (equation 2.15) to obtain evolution equations for the scalars A and B (see, for example, Markiel, 1999):

$$\frac{\partial A}{\partial t} = \alpha B + \frac{\eta_t}{r^2}\frac{\partial}{\partial r}\left[r^2\frac{\partial A}{\partial r}\right] + \frac{\eta_t}{r^2\sin\theta}\frac{\partial}{\partial\theta}\left[\sin\theta\frac{\partial A}{\partial\theta}\right] - \frac{\eta_t A}{r^2\sin^2\theta} \tag{2.42}$$

$$\begin{aligned}\frac{\partial B}{\partial t} = {} & \frac{\partial(A\sin\theta)}{\partial\theta}\frac{\partial\Omega}{\partial r} - \frac{\sin\theta}{r}\frac{\partial(Ar)}{\partial r}\frac{\partial\Omega}{\partial\theta} - \frac{1}{r}\frac{\partial}{\partial r}\left[\alpha\frac{\partial(Ar)}{\partial r}\right] \\ & - \frac{1}{r^2}\frac{\partial}{\partial\theta}\left[\frac{\alpha}{\sin\theta}\frac{\partial(A\sin\theta)}{\partial\theta}\right] + \frac{1}{r}\frac{\partial}{\partial r}\left[\eta_t\frac{\partial(Br)}{\partial r}\right] + \frac{1}{r^2}\frac{\partial}{\partial\theta}\left[\frac{\eta_t}{\sin\theta}\frac{\partial(B\sin\theta)}{\partial\theta}\right].\end{aligned} \tag{2.43}$$

From equation (2.42), it is clear that the only physical mechanism that is capable of generating poloidal field from toroidal field (in this axisymmetric mean-field model) is the α-effect. Both the α-effect and the ω-effect (due to the differential rotation, $\nabla\Omega$) appear in the toroidal field equation. This type of dynamo model is commonly referred to as an $\alpha^2\omega$ model. If the ω term is the dominant source term in equation (2.43), which will be the case when differential rotation is strong, then it is reasonable to ignore the α term in that equation:

$$\frac{\partial A}{\partial t} = \alpha B + \frac{\eta_t}{r^2}\frac{\partial}{\partial r}\left[r^2\frac{\partial A}{\partial r}\right] + \frac{\eta_t}{r^2\sin\theta}\frac{\partial}{\partial\theta}\left[\sin\theta\frac{\partial A}{\partial\theta}\right] - \frac{\eta_t A}{r^2\sin^2\theta} \tag{2.44}$$

$$\begin{aligned}\frac{\partial B}{\partial t} = {} & \frac{\partial(A\sin\theta)}{\partial\theta}\frac{\partial\Omega}{\partial r} - \frac{\sin\theta}{r}\frac{\partial(Ar)}{\partial r}\frac{\partial\Omega}{\partial\theta} + \frac{1}{r}\frac{\partial}{\partial r}\left[\eta_t\frac{\partial(Br)}{\partial r}\right] \\ & + \frac{1}{r^2}\frac{\partial}{\partial\theta}\left[\frac{\eta_t}{\sin\theta}\frac{\partial(B\sin\theta)}{\partial\theta}\right].\end{aligned} \tag{2.45}$$

This is known as the $\alpha\omega$ approximation (see, for example, Moffatt, 1978), and these equations are qualitatively similar to those proposed by Parker (equations 2.20 and 2.21). The operation of the $\alpha\omega$ dynamo is shown schematically in Figure 2.2. Due to the fact that differential rotation converts poloidal magnetic field into toroidal field very efficiently, the dominant component of magnetic field in an $\alpha\omega$ dynamo will be the toroidal component.

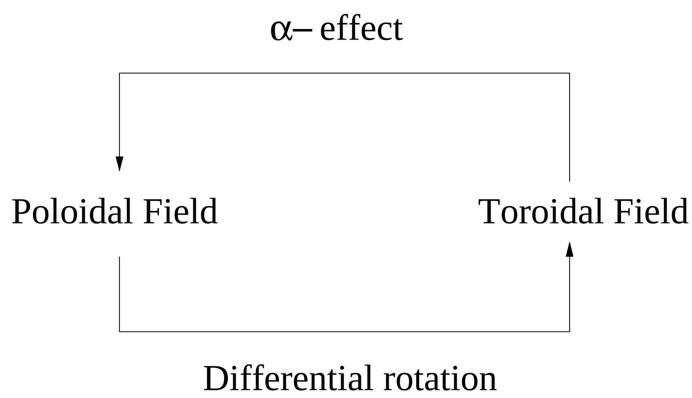

Figure 2.2: A schematic diagram showing the operation of the $\alpha\omega$ dynamo.

2.4.2 The location of the solar dynamo

As the magnetic fields found in sunspots are much more intense than the radial magnetic field component (observed at the poles), this suggests that the toroidal component of magnetic field in the Sun is very much greater than the poloidal component. This is certainly consistent with the idea that the solar dynamo may be of $\alpha\omega$ type. However, in order to decide whether or not this is the case, we need to know a bit more about the solar dynamo – in particular, where it is located.

It is difficult to see how the solar dynamo could be operating wholly within the convection zone itself. The magnetic flux tubes responsible for the bipolar active regions at the photosphere are very strong. Magnetic flux within the convection zone will tend to rise buoyantly up to the photosphere long before it can be amplified to the required strength (Parker, 1979). In addition, simulations of rising magnetic flux tubes (for example, Caligari et al., 1995, 1998) suggest that the strength of the subsurface azimuthal field must be of the order of 10^5G in order to be compatible with the observed features of active regions (including the small tilt angles of the bipolar regions and the restriction to low latitudes). Parker (1993) estimates that the equipartition field strength at the base of the convection zone is of the order of $10^3 - 10^4$G, so it seems likely that the

α-effect would be quenched long before magnetic fields of the order of 10^5G could be produced.

The general consensus is that the solar dynamo is operating in a region straddling the base of the convection zone (Spiegel and Weiss, 1980; Galloway and Weiss, 1981; van Ballegooijen, 1982). Convective motions will tend to sweep magnetic flux out of the convection zone and concentrate it into a thin overshoot layer just below the base of the convection zone (Spiegel and Weiss, 1980). Magnetic flux within this stably stratified region will not be as susceptible to buoyancy instabilities, thus allowing the possibility for stronger fields to develop. Given that this is also the site of the tachocline, there is also strong differential rotation, which is a crucial element in the production of strong toroidal fields. If the dynamo is operating in the same area as the tachocline, the $\alpha\omega$ approximation seems highly reasonable. These physical considerations led to theorists constructing (so-called) "interface" dynamo models (Deluca and Gilman, 1986).

Parker (1993) developed a two-layer Cartesian dynamo model that was based around this interface idea. The lower layer of Parker's model represents the overshoot layer and features strong differential rotation. The upper layer corresponds to the base of the convection zone, and it is assumed that the α-effect is restricted to this region. There is no overlap between these layers and they are coupled purely by diffusion. Parker argues that the strong toroidal field generated by the differential rotation within the lower layer will tend to suppress the eddy diffusivity, as discussed in Section 2.3.3, and therefore the diffusivity in the lower layer is assumed to be smaller than that in the upper layer. Presumably the fact that the turbulence is less vigorous in the overshoot layer should also imply that the (turbulent) magnetic diffusivity should be reduced there. The advantage of this model is that the strong fields are largely separate from the region where the α-effect is operating – this reduces the effects of the "α-quenching problem". The linear analysis carried out by Parker shows that this model yields dynamo wave solutions.

2.4.3 The dynamo parameters

Having established that the solar dynamo is likely to be of $\alpha\omega$-type, we must now focus upon what α and ω actually are in the Sun. The results from helioseismology (discussed in Section 1.3.1) mean that the form of the differential rotation, leading to the ω-effect, is well known. The spatial distribution of the α-effect is less well understood. As the first-order smoothing approximation is not valid for the high R_m conditions found in the Sun, numerical simulations provide the most feasible means of determining α. The most advanced calculations so far were carried out by Ossendrijver et al. (2001). These compressible simulations were carried out in a rotating Cartesian domain, the stratification of which is chosen to represent the lower part of the convection zone and the overshoot layer. A weak horizontal magnetic field is initially imposed across the box. Although only modest values of R_m were reached in these simulations ($R_m \sim 30$), this is well beyond the region of validity for the first-order smoothing approximation. It was found that the component of α in the direction of the imposed field changed sign within the convection zone, just above the transition to the stably stratified overshoot region, taking positive values at the base of the convection zone in the southern hemisphere. Interestingly a direct relationship between this component of α and the kinetic helicity is found (in agreement with the first-order smoothing calculations) – they change sign at the same depth, and the sign of the kinetic helicity is always opposite that of the α coefficient.

So far, attention has been focused upon an α-effect driven by turbulent convection in a rotating fluid. As discussed in Section 2.3.3, this process is subject to quenching by equipartition (or weaker) magnetic fields, and this may have serious consequences for the operation of the dynamo. There are other ways of generating an α-effect within the Sun. As discussed above, it is likely that there is a region of strong toroidal field in the sub-adiabatically stratified overshoot region. Where the field decreases rapidly with height – ie. at the top of the layer – magnetic buoyancy instabilities can occur. In the presence of rotation, this instability takes the form of growing magnetostrophic waves which are capable of generating an α-effect (Moffatt, 1978; Schmitt, 1987; Thelen, 2000a). Thelen (2000b) has incorporated this idea into a nonlinear $\alpha\omega$ model and demonstrated that this kind of α-effect is capable of producing dynamo waves. As noted by (for example) Thelen, this dynamic α-effect actually requires strong fields to operate, so is not subject to the same quenching problems as the turbulent α-effect (and is therefore also not truly self-excited). Another issue to consider is that the toroidal magnetic field layer is subject to a strong (radial) shear. There is evidence to suggest that a strong shear may suppress non-axisymmetric modes of the magnetic buoyancy instability in a magnetic layer (Tobias and Hughes, 2004). Non-axisymmetric modes are crucial for an α-effect, so the strong shear within the tachocline may play an important role here.

Based on the assumption that the tachocline toroidal field is a collection of magnetic flux tubes, Ferriz-Mas et al. (1994) find a similar α-effect based upon the undular instabilities of these flux tubes. The linear analysis of the instabilities of thin flux tubes is a simpler problem than the magnetic layer, and Ferriz-Mas et al. (1994) were able to use an analytic fit to the solar rotation profile to deduce how an instability of this type may depend upon the position of the flux tube within the Sun. It was found that the non-axisymmetric modes of the instability (necessary for an α-effect) generally favour low latitudes. Perhaps this is a consequence of the fact that the strongest shear in the tachocline is to be found at high latitudes, and this suppresses the instability there.

A final possibility for a tachocline-based α-effect comes from so-called "shallow-water" models (Dikpati and Gilman, 2001a,b). These models suggest that the latitudinal differential rotation within the solar tachocline, coupled with the effects of the sub-adiabatic stratification, could lead to a hydrodynamic instability. A net helicity is associated with the growing (longitudinally propagating) unstable modes, which can therefore drive an α-effect. Dikpati and Gilman (2001b) proposed a dynamo model based on this idea, which reproduces several of the main features of the solar cycle.

Away from the tachocline, it has been proposed that the decay of bipolar active regions could lead to the production of a net poloidal field, so taking the role of a surface α-effect (see, for example, Babcock, 1961; Leighton, 1969). In these dynamo models, the weak meridional circulation observed at the solar surface is used as a means of coupling the (now very separate) α and ω layers (Choudhuri et al., 1995; Dikpati and Charbonneau, 1999). Like the dynamo models where the α-effect is located around the tachocline, these models reproduce many of the features of the solar cycle. Having said that, they are open to several criticisms, in particular they ignore the possibility of a tachocline α-effect (see, for example, Tobias, 2002a). Mason et al. (2002) have shown that (in the absence of a meridional flow) even a weak α-effect operating around the tachocline will lead to the surface α-effect becoming insignificant.

2.4.4 Solar dynamo models

Direct numerical simulations

Before discussing the solar dynamo, in this context, it seems worthwhile to mention some results concerning the geodynamo. In the theory of the geodynamo (recently reviewed by Fearn, 1998; Jones, 2000), direct numerical simulations have played a key role. Although the parameter regime that is attainable in these simulations is not at all close to being "realistic", they have been remarkably successful in reproducing physically observed phenomena (see, for example, Jones, 2000). Simulations suggest that the behaviour of the geodynamo may be strongly influenced by rapid rotation – angular velocity contours within the (simulated) fluid outer core are nearly cylindrical (Taylor-Proudman-like). One consequence of this is that the solid inner core plays an important role in the dynamics of the fluid within the so-called tangent cylinder (see, for example, Weiss, 2002). One of the most ambitious calculations so far is a fully three-dimensional simulation carried out by Glatzmaier and Roberts (1995), which took about a year's worth of super-computer processor time. This was a particularly successful model in terms of reproducing the main features of the Earth's magnetic field, and even managed to simulate a geomagnetic reversal (where the sign of the radial field at the magnetic poles flips).

Given the apparent success of direct numerical simulations in terms of the geodynamo, we might expect that this would be a productive avenue of research for the solar dynamo. The problem with this is that the range of scales (both spatial and temporal) which need to be resolved in order to model the solar dynamo is vast (as discussed by, for example, Tobias, 2002b). In fact, some simulations have been carried out for the solar dynamo (see, for example, Gilman and Miller, 1981; Gilman, 1983; Glatzmaier, 1985). The main features of the results from these simulations are that the rotational profile is roughly Taylor-Proudman-like (which is inconsistent with helioseismological observations) and the dynamo waves that are produced migrate polewards rather than equatorwards. This strongly suggests that progress towards understanding the solar dynamo is not (yet) going to be made by direct numerical simulations. A simpler approach that contains the important physics is therefore needed – the obvious candidate is mean-field dynamo theory.

Mean-field models

Early dynamo models (see, for example, Steenbeck and Krause, 1969; Roberts and Stix, 1972; Köhler, 1973; Yoshimura, 1975; Stix, 1976), although successful in reproducing migratory dynamo waves, were hindered by a lack of knowledge concerning the differential rotation within the Sun. One of the first models to make use of the differential rotation profile inferred from helioseismology was studied by Prautzsch (1993), and (although this is only a very brief paper) he makes several important findings. Various different formulations for the α-effect were used in an attempt to establish how a dynamo with a realistic rotation profile depends upon α. For an α-effect driven by cyclonic convection it is natural to assume that α operates throughout the convection zone, and that it is antisymmetric about the equator. A commonly used expression (see, for example, Köhler, 1973; Stix, 1976) is $\alpha \propto \cos\theta$, which reflects equatorial antisymmetry and the fact that we would expect the twisting due to the Coriolis force to be greatest at the poles. Prautzsch (1993) found that an α-effect of this form favoured magnetic activity at mid to high latitudes, with oscillatory features only being found for a positive α-effect in the northern hemisphere. An α-effect that was restricted to the overshoot region and low latitudes (justified by being due to magnetic buoyancy) produced low-latitude oscillatory features. In keeping with the "sign" rule found by Parker (see Section 2.2.3), the dynamo waves migrate towards the equator for an α-effect that is negative in the northern hemisphere. This work strongly suggests that, in order to be compatible with observations, a tachocline α-effect may be of prime importance to the solar dynamo.

A model of the solar dynamo in the overshoot layer was put forward by Rüdiger and Brandenburg (1995). They made use of anisotropic expressions for α and the magnetic diffusivity, η_T, where the anisotropy is due to the influence of rotation. These expressions were derived from a model of Rüdiger and Kichatinov (1993), which in turn is based upon the first order smoothing approximation. Like Prautzsch (1993), they found that a solar-like rotation profile promotes activity at high latitudes. The resulting dynamo waves are mostly confined to the overshoot region and migrate polewards. Low-latitude oscillations, which migrate towards the equator are again found when α is restricted to low latitudes.

The idea of an interface dynamo (Parker, 1993) has also been extended to more realistic solar dynamo models. Treating the interface between the convection zone and the overshoot layer as a discontinuity, Charbonneau and MacGregor (1996, 1997) have looked at kinematic (and α-quenched) axisymmetric dynamos in spherical geometry with a realistic rotation profile. The α-effect is concentrated into a narrow band above the interface, the diffusivity in the overshoot layer is one or two orders of magnitude smaller than that in the convection zone, and these two regions are coupled by diffusion. A $\cos\theta$ α-profile (as would be expected) yields an oscillatory interface mode concentrated round the poles. They also find a curious (so-called) hybrid mode, which is driven by the latitudinal shear, and shows migration towards the equator at low latitudes. A very similar system was studied by Markiel and Thomas (1999), who looked at an idealised interface system with α-quenching. They did not find this hybrid mode, and in fact argued that this solution was a consequence of the fact that Charbonneau and MacGregor used an unphysical boundary condition which allowed the tangential electric field to be discontinuous at the interface (Markiel, 1999; Markiel and Thomas, 1999).

The model considered by Markiel (1999) and Markiel and Thomas (1999) yielded many interesting results. The strength of the driving of the dynamo in this $\alpha\omega$ model is characterised by a single dimensionless parameter – the dynamo number. For a large enough magnitude of the dynamo number, they found radially propagating dynamo waves driven by the latitudinal shear within the convection zone. These modes are not likely to be important in the solar dynamo. For moderately supercritical dynamo numbers, the convection zone plays less of a role in the dynamo. For a sharp contrast in diffusivities (a factor of 10^{-2}) between the two layers either side of the interface, steady modes were found for negative dynamo numbers. These steady modes are actually driven by the latitudinal shear (Markiel and Thomas, 1999). For a less pronounced (10^{-1}) diffusivity contrast, oscillatory modes with features at high and low latitudes were found for moderately large positive dynamo numbers, whilst a steady mode was again found for negative dynamo numbers. A solar-like butterfly diagram was again produced by considering an α-effect that was restricted to low latitudes. In his thesis, Markiel (1999) considered non-idealised interfaces, where the diffusivity now varied smoothly (as an error function) between the convection zone and the overshoot layer. Markiel found that the width of the transition layer was an important factor – a sharp transition region tends to favour (unwanted) steady modes for negative dynamo numbers, whilst a wide transition region favoured oscillatory features with equatorially-migrating weak low-latitude waves and polewards-migrating high-latitude oscillations.

Another dynamo model incorporating a realistic rotation profile was considered by Ossendrijver (2000). In this model two competing α-effects were operating – a turbulent α within the convection zone and a (buoyancy driven) α operating in the overshoot layer. The buoyant α was confined to low latitudes within the overshoot layer and, since the magnetic buoyancy instability requires strong fields, was assumed to "switch on" at field strengths of 10^5G. The turbulent α had a $\cos\theta$ dependence, as well as a random fluctuating term. The only nonlinearity involved is α-quenching. In many respects, this is one of the most complicated mean-field dynamo models that have been considered so far, and it readily produces highly modulated solutions with marked, but irregular, grand minima-type phases.

The modulation in Ossendrijver's model is really due to the presence of the randomly fluctuating source term. It is, however, possible to generate modulational effects without resorting to stochastic effects. Yoshimura (1978a) analysed a spherical dynamo model with parameterised quenching mechanisms which incorporated a time lag. This readily produced multi-periodic dynamo oscillations. Another way of producing modulated dynamo oscillations is by considering a different nonlinear mechanism, namely the back-reaction of the azimuthal component of the Lorentz force on the velocity field (Malkus and Proctor, 1975). Tobias (1996b, 1997b) derived a simplified Cartesian model representing the dynamo region within the Sun, using this nonlinear mechanism. It was found that it is possible to obtain modulated dynamo waves with this model, with the time-scale of the modulation being controlled by the ratio of the viscous to the magnetic diffusivity (the magnetic Prandtl number, τ). The time-scale for the modulation scales as $\tau^{-\frac{1}{2}}$. Two types of modulation can be found: categorised as Type 1 and Type 2 (Tobias, 1997b). Type 1 modulation is simply an interaction between dynamo modes of different symmetries – this can result in a dynamo wave that is asymmetric about the equator. Type 2 modulation involves changes in the magnetic energy without significant changes in the symmetry of the solution, and is brought about by an exchange of energy between the magnetic field and the velocity perturbation. Type 1 modulation is often associated with periods of reduced activity. The modulation in this model is a consequence of the separation of diffusive time-scales (achieved by varying τ away from unity). The Cartesian model described by Tobias has subsequently been extended by Phillips et al. (2002), who argued that the results are sensitive to changes in the overall structure of the model.

Moss and Brooke (2000) have combined this macrodynamic nonlinearity with a realistic rotation law in spherical geometry. Their α-effect was chosen to occupy the lower part of the convection zone and was given a $\cos\theta\sin^2\theta$ dependence. In keeping with other models incorporating a realistic rotation law, they found strong oscillatory features at both high and low latitudes. Values of τ less than unity led to more interesting time-dependent behaviour, with both the magnetic energy and parity showing strong modulation. The model of Moss and Brooke has also been extensively used as a tool for investigating torsional oscillations, which are a byproduct of this nonlinearity (Covas et al., 2000a,b, 2001a; Tavakol et al., 2002). This model has successfully reproduced some of the main features of the observed torsional oscillations, although the lack of stratification means that it doesn't reproduce the observed variation of these oscillations with depth (as discussed in Chapter 1). In their Cartesian model, Brooke et al. (2002) do not find torsional oscillations. They argue that the appearance of torsional oscillations is incompatible with the low values of τ that are required in order to get modulated solutions. This is something that merits further investigation.

Other approaches to the solar dynamo problem should also be mentioned. Apart from the Babcock-Leighton models, meridional flows have largely been ignored in solar dynamo calculations. As discussed in Section 2.2.3, Parker showed that an α-effect that is positive in the Northern hemisphere, coupled with a positive radial shear should lead to the polewards migration of dynamo waves. Küker et al. (2002) and Bonanno et al. (2002) have shown, using an imposed solar rotation law, that a meridional flow that is directed equatorwards at the base of the convection zone can reverse this migration, leading to dynamo waves that are reminiscent of the solar butterfly diagram.

All the models so far have made use of some kind of imposed differential rotation. By using the so-called Λ-effect (Rüdiger, 1989), which is a parameterisation of the non-diffusive Reynolds stresses in a rotating fluid, Küker et al. (1993) and Kitchatinov and Rüdiger (1995) have succeeded in reproducing a moderately solar-like rotation law in a hydrodynamic model. There have been several successful dynamo models produced that use this idea as a means of generating the underlying differential rotation (see, for example, Kitchatinov et al., 1994; Küker et al., 1996, 1999; Kitchatinov et al., 1999; Pipin, 1999). The nonlinear quenching mechanism used in most of these models was the quenching of the Λ-effect due to the suppression of turbulent eddies by the magnetic field. Küker et al. (1999) investigated the modulational effects that Λ-quenching can cause when combined with the macrodynamic nonlinearity discussed by Malkus and Proctor (1975). It was shown that this readily produces strongly time-dependent behaviour.

Illustrative models

A final approach to the dynamo problem is to consider illustrative models. All mean-field models are (to a certain extent) qualitative, however it is sometimes useful to simplify these equations further to investigate particular aspects of the model. Although it is clear that radial structure is important in dynamo models (Jennings et al., 1990), many one-dimensional models have been studied. One such model is that of Jennings (1991) and Jennings and Weiss (1991), who looked at a simple one-dimensional model with parameterised quenching mechanisms for the α and ω effects. Solutions of this model in the linear regime were either of dipolar or quadrupolar parity, although it produced some very complicated parity interactions in the nonlinear regime. Mixed parity dynamo modes were found (see also, for example, Brandenburg et al., 1989) which exhibited asymmetry about the equator. The advantage of a simple model like this is that it is possible to analyse the full bifurcation structure of the problem, in detail. Other notable one-dimensional models include those of Schmitt et al. (1996) and Schüssler et al. (1997), which model the interaction of an α-effect that is due to unstable magnetic flux tubes with an additional (randomly fluctuating) source term, which can be taken as being due to the turbulent α-effect operating within the convection zone. The dynamo oscillations that are found in these models show strong time-dependent amplitude variations, including periods of prolonged reduced activity.

Low-order models consisting of a set of differential equations provide even more extreme examples of illustrative models. Weiss et al. (1984) derived a low-order model by considering single Fourier modes in an $\alpha\omega$ model. Simple quenching mechanisms are considered together with the macrodynamic back-reaction of the Lorentz force on the velocity field. In this model, the Lorentz force has two Fourier components: if the one that is independent of the spatial co-ordinate is neglected, and all parameterised quenching mechanisms are removed, this results in a sixth-order system of ordinary differential equations. This system shows successive oscillatory (Hopf) bifurcations, and progresses from simply periodic, to quasi-periodic to aperiodically modulated solutions. This modulation is reminiscent of that found in the solar cycle. The disadvantage of the low-order model derived by Weiss et al. (1984) is that it is sensitive to the number of Fourier modes that are used in the truncation. A slightly different approach is to construct a low-order model of ordinary differential equations, based upon normal form equations. The bifurcation structure of these normal forms is robust, and their properties are generic in the sense that they describe the behaviour that is found in a wide range of nonlinear systems. Tobias et al. (1995) produced a set of three ordinary differential equations that modelled the transition from periodic dynamo waves to (Type 2) modulated solutions. With the same kind of idea, Knobloch and Landsberg (1996) produced a fourth-order model capable of describing Type 1 (parity) modulation and the transition from pure parity to mixed parity modes. Both forms of modulation were exhibited by a sixth-order model derived by Knobloch et al. (1998). These low-order models reproduced many of the modulational effects that have been found in deterministic mean-field dynamo simulations (see, for example, Yoshimura, 1978a; Tobias, 1996b, 1997b).

Chapter 3

Strong Asymmetry in Stellar Dynamos

The asymmetry that was observed in the sunspot observations, at the end of the Maunder minimum, was described in Section 1.2.2. Such asymmetry may have occurred during other grand minima phases of the Sun and this may also be the case in other solar-type stars. In this chapter, a simple, illustrative, $\alpha\omega$ mean-field dynamo model is analysed in order to investigate the occurrence of such asymmetry. Direct numerical integration of the resulting partial differential equations shows that highly asymmetric dynamo modes exist in a large region of parameter space and, where they do occur, they are surprisingly robust. This model is then used as the basis for the derivation of a low-order model which displays the simplest possible interaction between dipolar and quadrupolar components of magnetic field. This chapter concludes with a discussion of the implications of this work for dynamos in late-type stars. The work described in this chapter forms the basis for a recently published paper (Bushby, 2003b), where it is presented in a similar form.

3.1 Motivation

As described in Chapter 1, the Sun's magnetic field is approximately dipolar in nature. In terms of the poloidal-toroidal decomposition given in equation (2.15), dipolar symmetry implies that B (the toroidal field) is antisymmetric about the equator, whilst A (which represents the poloidal field) is symmetric. Although the solar magnetic field only makes relatively small departures from dipolar symmetry, they are measurable (see, for example, Sokoloff and Nesme-Ribes, 1994; Brooke et al., 2002). For example, a new magnetic cycle may begin slightly earlier in one hemisphere than in the other, or (at some point later on in the cycle) there may be a significant difference in the number of sunspots in each hemisphere. This (slight) asymmetry is probably due to the fact that the solar magnetic field is actually of mixed-parity (Jennings and Weiss, 1991; Sokoloff and Nesme-Ribes, 1994), so that, in addition to the dominant dipolar component, there is also a weak quadrupolar component present. For a quadrupolar dynamo mode, A is antisymmetric about the equator, whilst B is symmetric. The superposition of these two modes in the nonlinear regime leads to an overall asymmetry about the equator. Mixed-parity modes have been found in numerous simplified mean-field dynamo models (see, for example, Brandenburg et al., 1989; Jennings and Weiss, 1991).

The sunspot observations during the latter stages of the Maunder minimum (see Section 1.2.2) suggest that the underlying magnetic field was both weak and highly asymmetric (Ribes and Nesme-Ribes, 1993; Sokoloff and Nesme-Ribes, 1994). If this is due to a mixed-parity mode, as proposed by Sokoloff and Nesme-Ribes (1994), then the quadrupolar and dipolar components must now be of a comparable magnitude. As the Maunder minimum is the only grand minimum phase for which detailed sunspot records exist, it is not possible to say categorically that parity fluctuations are associated with such phases, although simulations do suggest that this may be the case (Tobias, 1997b; Beer et al., 1998). In Figure 3.1(a), we see a modulated, predominantly dipolar, dynamo wave, that undergoes grand minimum phases. As it enters and (more particularly) comes

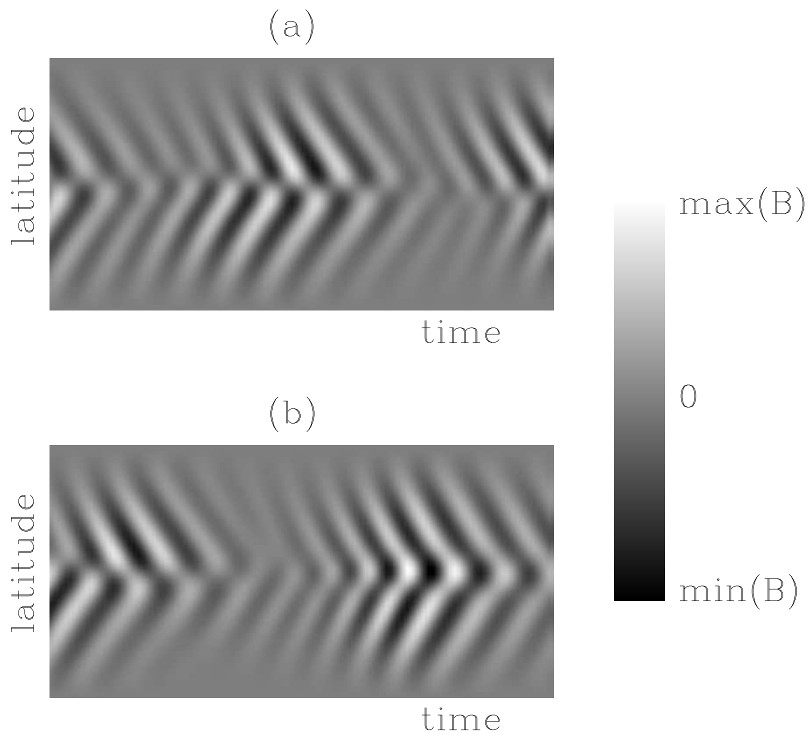

Figure 3.1: Contours of toroidal field plotted against latitude and time. These show mixed parity dynamo modes in a Cartesian model – (a) shows modulation without significant parity changes, (b) shows modulation with parity changes. Note the asymmetry in (a) as the solution emerges from a minimum period. Taken from Beer et al. (1998).

out of these periods of reduced activity, it is more active on one side of the equator than the other. After about one cycle, symmetry is restored. This is rather reminiscent of the asymmetric sunspot observations from the latter stages of the Maunder minimum. Figure 3.1(b) suggests another interesting possibility: the dynamo emerges from a minimum period with quadrupolar symmetry after entering with dipolar symmetry. It is not known whether or not such parity flipping has occurred following previous grand minima in the Sun, but if so, it could mean that the solar magnetic field has spent periods of time away from having nearly dipolar symmetry.

All the mixed-parity modes found in these simulations display fluctuations in parity. In three-dimensional simulations of a convectively driven dynamo in a rotating spherical shell, Busse (2000) found stable magnetic field configurations, of constant parity, that were highly asymmetric, with almost no magnetic field in one hemisphere. This extreme asymmetry was termed “hemispherical”, and Busse speculated that this hemispherical behaviour was due to a mixed-parity mode. One of the mixed-parity modes found by Jennings (1991) was similarly asymmetric; however, in this simple model this solution seemed to be unstable. The sort of asymmetric mixed-parity mode found by Busse may have been responsible for the confinement of sunspots to the southern hemisphere of the Sun during the latter stages of the Maunder minimum.

It seems remarkable that such extreme asymmetry should occur so readily as the result of dipole-quadrupole interactions, but from the point of view of mean-field theory this asymmetry is physically reasonable. Due to its dependence upon the Coriolis force, the α-effect is antisymmetric about the equator, and must therefore also vanish there. As this important physical feature of the dynamo vanishes at the equator, it then seems plausible that it should be possible for the two hemispheres to decouple, with dynamo action occurring in one hemisphere, but not the other. Having said all that, from a mathematical point of view, given the equatorial symmetry (or antisymmetry) of the linear eigenfunctions of this problem (see, Jennings, 1991; Jennings and Weiss, 1991), the fact that such extreme asymmetry appears to occur so naturally in nonlinear dynamo models is actually rather surprising and this requires further investigation.

The aim of this chapter is to investigate the possible occurrence of highly asymmetric (or hemispherical) mixed-parity modes in the context of stellar dynamos. The basis for the investigation will be a highly simplified illustrative $\alpha\omega$ mean-field dynamo model, and this is derived in the next section.

3.2 The idealised model

The aim of this illustrative model is to demonstrate the possibility of highly asymmetric mixed-parity modes in a mean-field dynamo model. This model will be based on the assumption that in a star such as the Sun, an $\alpha\omega$ dynamo operates in a thin spherical shell at (or near) the base of the convection zone. Fluid density and magnetic diffusivity are assumed to be constant for the purposes of this simplified calculation. The magnetic field will be assumed to be axisymmetric.

The model used here is based on that used by Tobias (1996b,c, 1997b), which is in itself an extension of Parker's model (discussed in Section 2.2.3). In that model, the thin shell domain for the dynamo is flattened out to form a Cartesian box: y corresponds to the azimuthal direction (axisymmetry implies that the resulting equations are independent of y); x corresponds to the latitudinal direction ($x = 0$ and $x = 2L$ are the locations of the north and south poles respectively, whilst the equator is at $x = L$); z corresponds to the direction of increasing radius ($z = 0$ is taken to be the midpoint of the layer). The standard decomposition of the magnetic field into toroidal and poloidal parts is made. Following the ideas used by Jennings and Weiss (1991), the α-effect is chosen to be antisymmetric about the equator and, in order to mimic curvature effects in this Cartesian model, the ω-effect must vanish at the poles. Here this corresponds to setting the velocity field and the α term to be $V(z)\sin(\pi x/2L)$ and $\alpha(z)\cos(\pi x/2L)$

respectively. The nonlinearity in this set of equations is taken to be the back-reaction of the azimuthal component of the Lorentz force on the velocity field, and the resulting perturbation is denoted by u. The equations used by Tobias (1996b,c, 1997b) are:

$$\begin{aligned}
\frac{\partial A}{\partial t} &= \alpha(z)\cos\left(\frac{\pi x}{2L}\right) B + \eta_t \left(\frac{\partial^2 A}{\partial x^2} + \frac{\partial^2 A}{\partial z^2}\right) && (3.1)\\
\frac{\partial B}{\partial t} &= \left[V'(z)\sin\left(\frac{\pi x}{2L}\right) + \frac{\partial u}{\partial z}\right]\frac{\partial A}{\partial x} && (3.2)\\
&\quad - \left[\frac{\pi}{2L}V(z)\cos\left(\frac{\pi x}{2L}\right) + \frac{\partial u}{\partial x}\right]\frac{\partial A}{\partial z} + \eta_t\left(\frac{\partial^2 B}{\partial x^2} + \frac{\partial^2 B}{\partial z^2}\right)\\
\frac{\partial u}{\partial t} &= \frac{1}{\rho\mu_o}\left(\frac{\partial A}{\partial x}\frac{\partial B}{\partial z} - \frac{\partial B}{\partial x}\frac{\partial A}{\partial z}\right) + \tau\eta_t\left(\frac{\partial^2 u}{\partial x^2} + \frac{\partial^2 u}{\partial z^2}\right). && (3.3)
\end{aligned}$$

Here (as usual), η_t is the (turbulent) magnetic diffusivity, ρ is the fluid density, μ_o is the permeability of free space, τ is the magnetic Prandtl number and $'$ denotes differentiation with respect to z.

In order to simplify this system, the z-dependence of these equations is now removed by an averaging process following the method of Belvedere et al. (1990). Tobias solved these equations in a shallow Cartesian box, whereas the model to be used here differs in that the only condition that will be imposed on A, B and u in the z-direction is that they all decay to zero as $|z|$ gets large. Physically, this corresponds to removing the top and bottom of the box and treating the dynamo as being localised in z around $z = 0$. Provided A, B and u decay in the z direction on a length-scale that is small when compared to L, this should still give physically realistic field configurations.

Firstly, in order to separate out the z dependence of the variables, we look for separable solutions of the form

$$A(x,z,t) = f(z)\hat{A}(x,t) \tag{3.4}$$

$$B(x,z,t) = g(z)\hat{B}(x,t) \tag{3.5}$$

$$u(x,z,t) = h(z)\hat{u}(x,t). \tag{3.6}$$

Clearly, by looking for solutions of this form, we are placing certain constraints on the system and it is likely that any solutions found will not be the preferred modes in the fully two-dimensional system. Having said that, this is an illustrative model and it should still be possible (after making this simplifying assumption) to use it to investigate mixed-parity dynamo modes in a meaningful way. Besides reducing the complexity of the system, the other advantage that this approach has is to introduce a set of parameters into the equations, as will be seen below. These parameters can be varied widely in order to capture the main patterns of behaviour.

The z-dependence of A, B and u is now contained in the functions $f(z)$, $g(z)$ and $h(z)$. In order to be consistent with the assumption that A, B and u all decay to zero as $|z|$ gets large, the same must be true for $f(z)$, $g(z)$ and $h(z)$. There are clearly other ways of approaching this problem, for example boundary conditions could be imposed at finite values of z, corresponding to solving these equations in a box. This would, however, complicate the analysis and, in any case, for a dynamo that is operating in a localised region it is to be expected that, in the absence of any external sources, the magnetic field should decay away to zero as we move away from this region. Therefore the assumption that $f(z)$, $g(z)$ and $h(z)$ decay with increasing $|z|$ seems reasonable.

Having made this separation of variables, the next step is to average these equations over z. Following the general method described by Belvedere et al. (1990), equations (3.1), (3.2) and (3.3) are first multiplied up by $f(z)$, $g(z)$ and $h(z)$ respectively. The equations are then integrated with respect to z over its whole range (formally $\pm\infty$, although most of the activity is confined to the region of $z = 0$). The parameters resulting from this integration now contain the only z-dependence of these equations, and these parameters are dependent upon the functional forms of $f(z)$, $g(z)$ and $h(z)$. An important feature of this simplification, as noted by Belvedere et al. (1990), is that it preserves the property of the original set of equations, that the nonlinear terms make no net contribution to the total energy of the system. Given the restrictions on $f(z)$, $g(z)$

and $h(z)$ described above, it is straightforward to verify that this "energy property" is preserved here.

One further modification to the model is made. In an attempt to try and promote asymmetric solutions, the $\alpha(z)\cos(\pi x/2L)$ term in equation (3.1) is replaced by $\alpha(z)\cos^3(\pi x/2L)$. This causes the contribution to the α-effect to be smaller around the equator and should hopefully lead to less coupling between the two regions on either side, thus leading to asymmetric solutions far more readily. This substitution maintains the equatorial antisymmetry of the α-effect and the fact that the α-effect is strongest at the "poles". The effects of this substitution will be discussed briefly later in the chapter. The equations are now non-dimensionalised using scalings similar to those used by Tobias (1996b,c, 1997b), with the only difference being that the characteristic length-scale is taken to be the distance between the equator and one of the poles, in the x direction, rather than some length in the z direction. The scalings used are as follows:

$$
\begin{array}{lll}
x \rightarrow L\tilde{x} & z \rightarrow L\tilde{z} & t \rightarrow (L^2/\eta_o)\tilde{t} \\
B \rightarrow B_o\tilde{B} & A \rightarrow (\alpha_o L^2 B_o/\eta_o)\tilde{A} & \\
\alpha \rightarrow \alpha_o\tilde{\alpha}(\tilde{z}) & V' \rightarrow V'_o\tilde{V}'(\tilde{z}) & V \rightarrow V'_o L\tilde{V}(\tilde{z}) \\
\eta_t \rightarrow \eta_o\tilde{\eta} & u \rightarrow V'_o L\tilde{u} & \rho \rightarrow \rho_o\tilde{\rho}.
\end{array}
\tag{3.7}
$$

Here L, B_o, α_o, V'_o, ρ_o and η_o are characteristic values of x, B, α, V', ρ and η_t respectively. The fact that the density and the magnetic diffusivity are assumed to be constant implies that it is possible to set $\tilde{\rho}$ and $\tilde{\eta}$ equal to unity.

Dropping the tildes, the equations become:

$$k_f \frac{\partial A}{\partial t} = k_\alpha \cos^3\left(\frac{\pi x}{2}\right) B + k_f \frac{\partial^2 A}{\partial x^2} + \eta_A A \tag{3.8}$$

$$\begin{aligned} k_g \frac{\partial B}{\partial t} &= D\left[k_{V'} \sin\left(\frac{\pi x}{2}\right) + k_3 u\right] \frac{\partial A}{\partial x} \\ &\quad - D\left[k_V \frac{\pi}{2} \cos\left(\frac{\pi x}{2}\right) + k_1 \frac{\partial u}{\partial x}\right] A + k_g \frac{\partial^2 B}{\partial x^2} + \eta_B B \end{aligned} \tag{3.9}$$

$$k_h \frac{\partial u}{\partial t} = \left[\frac{B_o^2 \alpha_o L}{\rho_o \mu_o V_o' \eta_o^2}\right] \left[k_2 \frac{\partial A}{\partial x} B - k_1 \frac{\partial B}{\partial x} A\right] + \tau k_h \frac{\partial^2 u}{\partial x^2} + \tau \eta_u u, \tag{3.10}$$

where

$$\begin{aligned} k_f &= \int_{-\infty}^{\infty} f^2 \, \mathrm{d}z, \quad k_g = \int_{-\infty}^{\infty} g^2 \, \mathrm{d}z, \quad k_h = \int_{-\infty}^{\infty} h^2 \, \mathrm{d}z, \\ k_1 &= \int_{-\infty}^{\infty} f' g h \, \mathrm{d}z, \quad k_2 = \int_{-\infty}^{\infty} f g' h \, \mathrm{d}z, \quad k_3 = \int_{-\infty}^{\infty} f g h' \, \mathrm{d}z, \\ k_\alpha &= \int_{-\infty}^{\infty} f g \alpha \, \mathrm{d}z, \quad k_{V'} = \int_{-\infty}^{\infty} f g V' \, \mathrm{d}z, \quad k_V = \int_{-\infty}^{\infty} f' g V \, \mathrm{d}z, \\ \eta_A &= \int_{-\infty}^{\infty} f f'' \, \mathrm{d}z, \quad \eta_B = \int_{-\infty}^{\infty} g g'' \, \mathrm{d}z, \quad \eta_u = \int_{-\infty}^{\infty} h h'' \, \mathrm{d}z. \end{aligned} \tag{3.11}$$

The non-dimensional parameters in the above equations are the dynamo number, $D = (\alpha_o V_o' L^3)/(\eta_o^2)$, and τ, the magnetic Prandtl number. It is straightforward to verify using integration by parts that, provided $f(z)$, $g(z)$ and $h(z)$ decay away as $|z|$ tends to ∞,

$$k_2 = -k_3 - k_1, \tag{3.12}$$

which can be shown to imply that the nonlinear terms make no net contribution to the total energy of the system. There are therefore only two independent parameters corresponding to the nonlinear terms in these equations. Given that $f(z)$, $g(z)$ and $h(z)$ tend to zero as $|z|$ tends to ∞, integration by parts also trivially implies that η_A, η_B and η_u are all negative (as would be expected for diffusive terms). The constant in front of the nonlinear terms in equation (3.10) is also non-dimensional and it can be removed simply by rescaling B_o. Equation (3.10) then becomes:

$$k_h \frac{\partial u}{\partial t} = \mathrm{sign}(D) \left[k_2 \frac{\partial A}{\partial x} B - k_1 \frac{\partial B}{\partial x} A \right] + \tau k_h \frac{\partial^2 u}{\partial x^2} + \tau \eta_u u, \tag{3.13}$$

where the sign(D) term arises from the fact that the constant in front of the nonlinear terms in equation (3.10) must take the same sign as the dynamo number (see, for example, Tobias, 1996c). It is worth mentioning that it is possible to remove this sign(D) term by rescaling u by D and then rescaling A and B by $|D|^{\frac{1}{2}}$, although this has not been done here. In terms of boundary conditions for these equations, A, B and u are chosen to vanish at the poles (ie. $A = B = u = 0$ at $x = 0$ and $x = 2$).

Equation (3.8), (3.9) and (3.13) are the model equations in their final forms. All that remains is to pick suitable profiles for $f(z)$, $g(z)$, $h(z)$, $\alpha(z)$ and $V(z)$. Gaussian profiles are adopted for $f(z)$ and $g(z)$, ie.

$$f(z) = e^{[-(z-a)^2]/\sigma^2} \tag{3.14}$$

$$g(z) = e^{[-(z-b)^2]/\sigma^2}, \tag{3.15}$$

where a and b are chosen in order that these might represent physically plausible profiles. In an interface model for a stellar dynamo the α-effect might be assumed to be dominant above $z = 0$, where convection is at its strongest, whilst the ω-effect dominates just below the base of the convection zone. A positive value for a will therefore imply that the poloidal component (which is regenerated by α) reaches its maximum above $z = 0$, whilst a negative value for b implies that the bulk of the toroidal field coincides with the region of strong radial shear that is needed to generate it. The spread, σ, is taken to be the same in these profiles. In a model where density and magnetic diffusivity vary with depth, the assumption of simple gaussian profiles with equal spread would be less applicable, but it is adequate for this illustrative model. The value of σ^2 must be chosen to be substantially less than unity to ensure that the fields are localised around $z = 0$. It should be noted that these profiles for $f(z)$ and $g(z)$ imply that $k_f = k_g$ and

$\eta_A = \eta_B$, which means that the diffusive terms in equations (3.8) and (3.9) have the same coefficients.

The Lorentz force term in equation (3.13) suggests a functional form for $h(z)$. This term suggests that $h(z)$ should behave like $f'(z)g(z)$ or $f(z)g'(z)$, therefore profiles of the form

$$h(z) = (z - v)e^{-[(z-a)^2+(z-b)^2]/\sigma^2} \tag{3.16}$$

are considered. It should be noted that in this expression for $h(z)$, the same spread, σ, arises. This is only a reasonable assumption if the magnetic Prandtl number, τ, is equal to unity. In this piece of work, we are predominantly interested in parity modulation and not amplitude modulation, so restricting the variation of τ should not be a problem. Henceforth, τ shall be set equal to unity. The other thing to note is the appearance of the $(z - v)$ term in this expression – in general v will be non-zero in order to prevent $h(z)$ from vanishing at $z = 0$, which would only be expected to occur in particularly symmetric systems.

Having set up this model, different values of a, b, v and σ can now be considered, and these will generate a wide range of parameter values in the model equations. In an illustrative model such as this one, it is important to verify that the behaviour of this set of equations is relatively insensitive to the specific values of the parameters, so it is necessary to perform a wide survey of parameter space. It is, however, assumed without loss of generality that it is possible to scale $\alpha(z)$ and $V(z)$ such that $k_\alpha = 1$ and $k_{V'} = 1$. As this is a simple rescaling, it will have no qualitative affect on the solutions obtained. In principle, it is also possible to normalise $f(z)$, $g(z)$ and $h(z)$ such that $k_f = k_g = k_h = 1$, also without affecting the solutions. This would be desirable from the point of view of reducing the number of parameters in the equations, however the required normalisation will vary with a, b, v and σ. Since this will further complicate the evaluation of the other constants in equation (3.11), the functions $f(z)$, $g(z)$ and

$h(z)$ are left as they are.

3.3 Numerical results

Before integrating the full set of partial differential equations, the linear problem was analysed in order to investigate the dependence of the initial bifurcation on the parameters D, k_V and σ. The linearised equations were expanded as Fourier sine series,

$$A(x,t) = \sum_{n=1}^{N} A_n(t)\sin(n\pi x/2) \tag{3.17}$$

$$B(x,t) = \sum_{n=1}^{N} B_n(t)\sin(n\pi x/2) \tag{3.18}$$

$$u(x,t) = \sum_{n=1}^{N} u_n(t)\sin(n\pi x/2). \tag{3.19}$$

When these expressions are substituted into the model equations the result is a set of $3N$ linear ordinary differential equations. In this linear regime, the u_n equations decouple from the rest and all the u_n modes decay to zero exponentially with time. The $2N$ equations involving A_n and B_n can then be analysed in order to find the critical dynamo numbers for the problem. This process is equivalent to finding the eigenvalues of a $2N \times 2N$ matrix and this can easily be accomplished for any relatively small value of N.

In order to achieve the correct direction of migration for the dynamo waves (i.e. equatorwards) the dynamo number must be restricted to negative values, so the linear analysis concentrated on finding critical dynamo numbers that were less than zero. As the Sun's magnetic field is currently dipolar, using the results from the linear analysis, the parameters are adjusted so that the first non-trivial solution to be observed as D is decreased from zero is an oscillatory dipolar solution. It turns out that the form of this initial solution depends closely upon the value of σ. As σ is decreased from about unity, the initial bifurcation goes from being stationary quadrupolar to oscillatory dipolar to oscillatory quadrupolar. The stationary mode that is preferred for larger values of σ vanishes at around $\sigma = 0.4$ – a quadrupolar stationary mode still exists for smaller values of σ although the critical dynamo number is much larger. The range of values of σ for which the dipolar solution is preferred is actually quite small, however $\sigma = 1/3$ is at the centre of this range, so that is the value used throughout the simulations.This value of σ is sufficiently small that the solutions decay in the z-direction on a length-scale that is short when compared to the horizontal scale which, as discussed in Section 3.2, is a necessary feature of the model. In order to reduce the number of free parameters, k_V is initially set to zero – this parameter can be varied later, if this is subsequently found to be too restrictive. As stated in the previous section, the magnetic Prandtl number, τ, is set to equal unity throughout these simulations.

The numerical method, for solving the full nonlinear partial differential equations, is a one-dimensional finite differencing scheme with centred spatial derivatives and a 2nd-order Adams-Bashforth time-stepping method. The number of grid-points in the spatial direction is typically taken to be 300 – higher resolution checks confirmed the adequacy of this resolution. The model was found to be insensitive to the initial conditions used provided that the initial condition was not of pure parity (initial conditions of pure parity would restrict the solution to either the dipolar or quadrupolar invariant subspaces). Small linear combinations of the first four Fourier modes were used as initial conditions for each of the three variables.

The behaviour of the solutions observed depended on the coupling between the dipolar and quadrupolar modes. This is determined by the values of a, b and v, so these were varied widely in an attempt to capture the main patterns of behaviour. For all sets of parameters investigated, the initial bifurcation from the trivial state occurred at around $D = -2700$. This is a Hopf bifurcation and the resulting oscillatory dipolar dynamo waves migrate towards the equator, as shown in Figure 3.2.

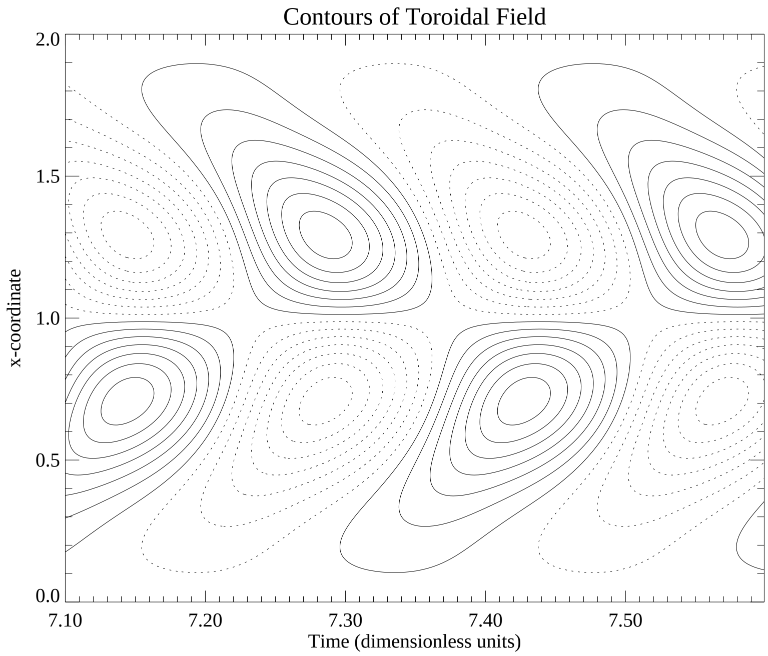

Figure 3.2: Contours of toroidal magnetic field for a dipolar dynamo wave migrating towards the equator, plotted against x and t. Dashed lines correspond to negative contours, solid lines correspond to positive ones. The parameters used are $a = 0.1$, $b = -0.05$ and $v = 1.5$. The dynamo number is -3000.

As D is decreased from here, the subsequent preferred solutions then depend on the parameters used. There is a wide range of parameters for which the next mode to appear is an oscillatory stable mixed-parity mode. Two types of stable mixed-parity mode seem to occur readily. An example of the first type of mixed-parity mode is plotted in Figure 3.3. The asymmetry here is mainly seen as a time-lag between the two hemispheres and, over any given period, each hemisphere is as active as the other. These mixed-parity modes generally revert to being purely oscillatory quadrupolar in nature as $|D|$ increases. The other type of stable oscillatory mixed-parity mode is a new solution. An example of this type of mode is plotted in Figure 3.4. It can easily be seen that this solution is highly asymmetric about the equator with one hemisphere

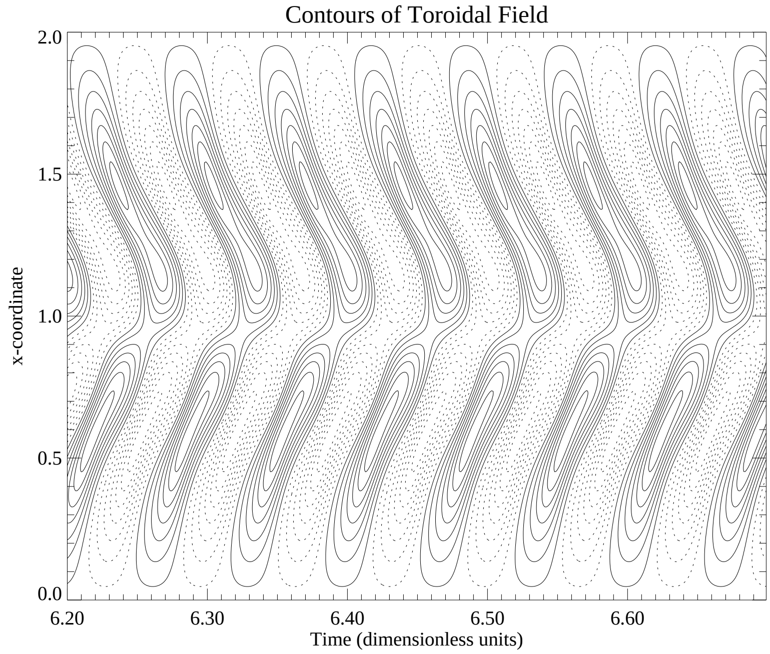

Figure 3.3: As Figure 3.2, but now for a mildly asymmetric mixed-parity mode. The parameters used are $a = 0.1$, $b = -0.05$ and $v = -1.0$. The dynamo number is -12600.

(in this case $x > 1$) being far more active than the other. It is interesting to note that not only is the activity mainly confined to the one hemisphere, but also most of the magnetic energy is concentrated in a narrow band of latitude close to the equator. This has distinct parallels with the latitudinal distribution of sunspots that were observed during the Maunder minimum. This form of highly asymmetric, stable mixed-parity mode seems to occur for a wide range of parameter values.

Possibly the most surprising fact about these particular mixed-parity solutions is that they remain stable up to very large values of $|D|$. It is only when D is less than about -25000 that this mixed-parity mode ceases to be the dominant solution. The favoured form of solution now becomes a stationary quadrupolar mode that is concentrated about the equator. The only way that this kind of hemispherical mode can arise, with continuous large-scale cancellation in one hemisphere, is through a mixed-parity

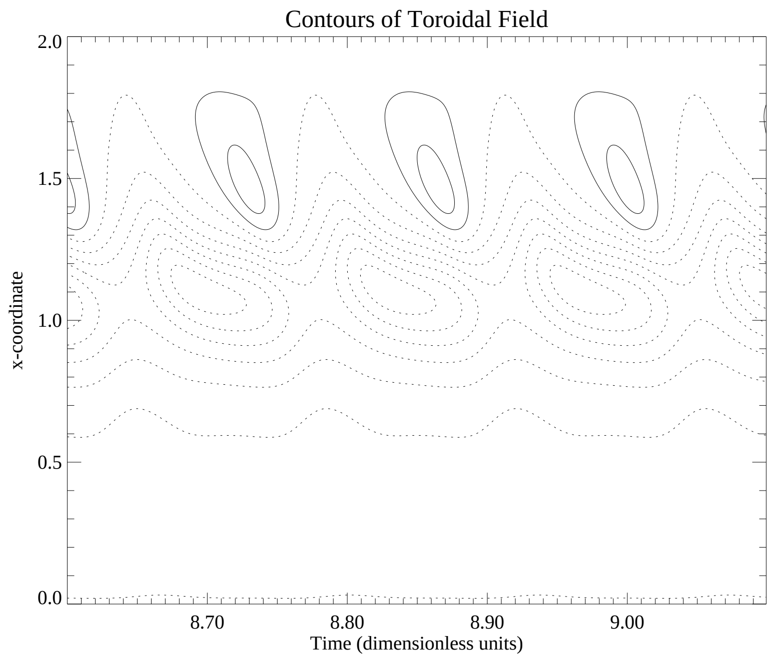

Figure 3.4: A highly asymmetric mixed-parity mode. The parameters used are $a = 0.1$, $b = -0.05$ and $v = 1.5$. The dynamo number is -7000.

mode that contains roughly equal quantities of its dipolar and quadrupolar components. For this kind of situation to hold over many time periods these two components must be oscillating in phase with each other with virtually identical time periods. If they oscillated with different time periods, that would imply that the solution would flip between looking predominantly dipolar and predominantly quadrupolar, and there is no parity flipping observed here.

Now that hemispherical mixed-parity modes have been found it is worth briefly investigating the effect of varying the latitudinal dependence of α. In order to assess the effect of altering the α-profile from $\cos(\pi x/2)$ to $\cos^3(\pi x/2)$, a few numerical runs were carried out for a $\cos(\pi x/2)$ α-profile. It was found that although there were quantitative differences (eg. lower critical dynamo numbers), qualitatively, the same kind of solutions were found. Again, it was easy to find parameters that were capable of generating

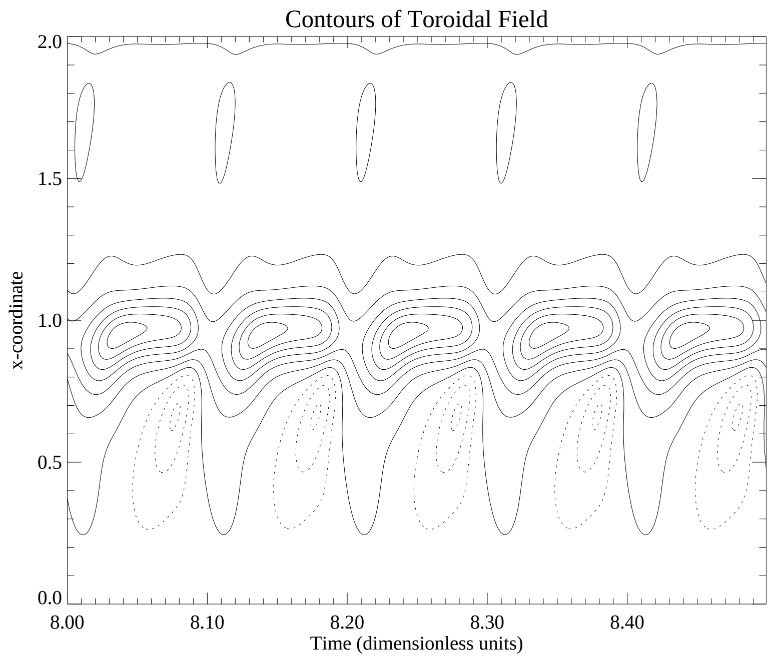

Figure 3.5: A highly asymmetric mixed-parity mode for the $\cos(\pi x/2)$ α-profile. The parameters used are $a = 0.1$, $b = -0.05$ and $v = 1.5$. The dynamo number is -6000.

hemispherical mixed-parity modes, as shown in Figure 3.5. This implies that this solution is not in fact sensitive to the form of the α-profile.

These simulations show that highly asymmetric mixed-parity modes do arise in this simple dynamo model provided that the parameters are chosen appropriately. The relative insensitivity to the precise choice of the parameters is encouraging, as it suggests that such modes are quite natural. Although these modes clearly do arise from dipolar modes interacting with quadrupolar modes in a specific way, it is very difficult to say exactly how this situation arises in a dynamo model. The next section deals with a different approach to the problem.

3.4 A low-order model

3.4.1 The derivation of the equations

In order to understand the simplest possible mixed-parity mode, work has been carried out on a low-order model. The aim behind this was to demonstrate in a fairly simple (and analytically tractable) way that dipolar and quadrupolar modes can interact in such a way as to produce extreme asymmetry, even in a simple model. As mentioned in Chapter 2, low-order models of ordinary differential equations have been very successful in reproducing many of the key aspects of stellar dynamos, so this approach seems to be a useful one.

In order to reduce this system of partial differential equations down to a series of ordinary differential equations, the Fourier series representations for A, B and u (equations 3.17, 3.18 and 3.19) were substituted into the full nonlinear equations. These series representations naturally obey the boundary conditions imposed on the variables at $x = 0, 2$. The resulting set of ordinary differential equations, which represent the evolution of each of the Fourier amplitudes, can now be truncated and analysed. The difference between this and the linear analysis described in the previous section is that the u_n equations no longer decouple from the others due to the presence of the nonlinear terms, so all of the resulting $3N$ equations must be analysed. The simplest non-trivial case that can give rise to the interaction of the dipolar and quadrupolar modes is the case of $N = 2$. This will only produce stationary (pitchfork) bifurcations but it is necessary to take $N \geq 4$ in order to produce oscillatory bifurcations and a system where $N = 4$ is too large to be algebraically tractable. The $N = 2$ case is therefore analysed in detail and hopefully, as this represents the simplest possible interaction, this can tell us something about highly asymmetric mixed parity-modes.

As the preferred modes here are stationary, we don't need to worry about getting the direction of migration of the dynamo waves correct. In contrast to the previous section, attention is restricted to the case of positive dynamo number, purely owing to the fact that in this highly truncated model, this ensures that the initial bifurcation is to a dipolar state. Exactly the same analysis can be carried out for negative dynamo numbers, the only difference being that the initial bifurcation is to a quadrupolar solution. The equations for this simple system can be expressed as:

$$\begin{aligned}
\dot{A}_1 &= B_2 - \eta_1 A_1 && (3.20)\\
\dot{A}_2 &= B_1 - \eta_2 A_2 && (3.21)\\
\dot{B}_1 &= -D\omega_1 A_2 - \eta_1 B_1 + DC_1 u_2 A_1 - DC_2 u_1 A_2 && (3.22)\\
\dot{B}_2 &= -D\omega_2 A_1 - \eta_2 B_2 + D(C_2 - C_1) u_1 A_1 && (3.23)\\
\dot{u}_1 &= -\tau\eta_3 u_1 + C_3 B_2 A_1 - C_4 B_1 A_2 && (3.24)\\
\dot{u}_2 &= -\tau\eta_4 u_2 + (C_4 - C_3) B_1 A_1, && (3.25)
\end{aligned}$$

where B_1 and B_2 have been rescaled to remove unnecessary numerical factors and the constants have been redefined, making use of equation (3.12) and the fact that $\eta_A = \eta_B$ and $k_f = k_g$:

$$\begin{aligned}
\eta_1 &= \left(\frac{\pi^2}{4} - \frac{\eta_A}{k_f}\right) \quad \eta_2 = \left(\pi^2 - \frac{\eta_A}{k_f}\right) && (3.26)\\
\eta_3 &= \left(\frac{\pi^2}{4} - \frac{\eta_u}{k_h}\right) \quad \eta_4 = \left(\pi^2 - \frac{\eta_u}{k_h}\right)\\
\omega_1 &= \frac{(2 + k_V)\pi}{16} \quad \omega_2 = \frac{(-1 + k_V)\pi}{16} < \omega_1\\
C_1 &= \frac{(k_3 + 2k_1)\pi}{16k_f} \quad C_2 = \frac{(2k_3 + k_1)\pi}{16k_f}\\
C_3 &= \frac{(k_1 - k_3)\pi}{k_h} \quad C_4 = \frac{(-k_1 - 2k_3)\pi}{k_h}.
\end{aligned}$$

Analysis of this set of equations shows that the system may possess four fixed points. These are the trivial solution $(0, 0, 0, 0, 0, 0)$; the dipolar solution $(A_{1d}, 0, 0, B_{2d}, u_{1d}, 0)$;

the quadrupolar solution $(0, A_{2q}, B_{1q}, 0, u_{1q}, 0)$; and, finally, the mixed-parity solution $(A_{1m}, A_{2m}, B_{1m}, B_{2m}, u_{1m}, u_{2m})$. The naming of these fixed points follows naturally from the symmetries of the relevant Fourier eigenfunctions. It can be seen that a pure parity dipolar or quadrupolar mode can only drive a symmetric velocity perturbation (u_1), as noted by Knobloch et al. (1998). It is clear that these equations govern the simplest interaction between dipolar and quadrupolar components that can be derived from the model.

3.4.2 Stability analysis

Elementary stability analysis about the trivial fixed point shows that the trivial solution loses stability to a dipolar mode if $D\omega_2+\eta_1\eta_2 < 0$, or a quadrupolar mode if $D\omega_1+\eta_1\eta_2 < 0$. Since we have restricted attention to the case of positive D, ω_1 and ω_2 must be negative in order to get both these bifurcations to occur in this region. This, in turn, implies that k_V must be non-zero (in fact $k_V < -2$). The fact that it is necessary to set k_V to be non-zero here, in contrast to the numerical simulations described in Section 3.3, is a reflection of the fact that this model is heavily truncated. The result of these assumptions is that the dipolar mode has the smallest critical dynamo number ($D = -\eta_1\eta_2/\omega_2$). In the negative D regime, the same arguments would lead to positive values for ω_1 and ω_2 and the quadrupolar mode being the first to bifurcate from the trivial solution. Since we are interested in the occurrence of mixed-parity modes, it makes sense to investigate a system where the initial bifurcations to dipolar and quadrupolar states are close together. The more negative the values of ω_1 and ω_2, the closer these bifurcations are.

Now, the dipolar fixed point has $B_1 = A_2 = u_2 = 0$. The equations imply that these variables will be zero for all time. Because this point is a fixed point, it is easily seen that:

$$A_1 = \frac{B_2}{\eta_1} \text{ and } u_1 = \frac{C_3 B_2^2}{\eta_1\eta_3\tau} \tag{3.27}$$

$$\implies -\left(\frac{D\omega_2}{\eta_1} + \eta_2\right) B_2 + \frac{D(C_2 - C_1)C_3}{\eta_1^2\eta_3\tau} B_2^3 = 0 \tag{3.28}$$

$$\implies B_2 = 0 \text{ or } \pm\sqrt{\frac{(D\omega_2 + \eta_1\eta_2)\tau\eta_1\eta_3}{D(C_2 - C_1)C_3}}. \tag{3.29}$$

Now, if $B_2 = 0$ that would imply that everything else would decay to zero which would take us back to the trivial state. So the non-trivial values of B_2 are the ones that are of interest here. The fact that the trivial state is only unstable if $(D\omega_2 + \eta_1\eta_2) < 0$ means that (as η_1, η_2, η_3, τ and D are all positive) we require

$$(C_2 - C_1)C_3 < 0, \tag{3.30}$$

to hold for the existence of the dipolar solution. Similar analysis holds for the quadrupolar fixed point, which implies:

$$C_2C_4 < 0. \tag{3.31}$$

These conditions are actually automatically satisfied due to the definitions of C_1, C_2, C_3 and C_4 – see equation (3.26).

So by elementary considerations in linear theory it has been shown that both dipolar and quadrupolar fixed points may exist in this system. Although the dipolar instability from the trivial state is the first to occur as D is increased from zero, it is not yet known whether this state is unstable to "quadrupolar" perturbations. More analysis is needed before any conclusions can be drawn about the global stability picture. In principle this analysis is possible without any further manipulation of the equations, however it is simpler (after a suitable change of variables) to perform a centre manifold reduction to reduce this system of 6 ordinary differential equations down to a smaller set of equations.

3.4.3 The centre manifold reduction

With the aim of clarifying which of the variables are associated with dipolar modes and which are associated with quadrupolar ones, a change of variables is employed:

$$x_1 = \frac{-\eta_2 A_1 - B_2}{(\eta_1 + \eta_2)} \text{ and } x_2 = \frac{-\eta_1 A_1 + B_2}{(\eta_1 + \eta_2)} \tag{3.32}$$

$$y_1 = \frac{-\eta_1 A_2 - B_1}{(\eta_1 + \eta_2)} \text{ and } y_2 = \frac{-\eta_2 A_2 + B_1}{(\eta_1 + \eta_2)}. \tag{3.33}$$

The x variables now correspond to the dipolar terms, whilst the y variables correspond to the quadrupolar terms. At this stage, two parameters are introduced: $\mu_1 = -(D\omega_2 + \eta_1\eta_2)$ and $\mu_2 = -(D\omega_1 + \eta_1\eta_2)$. For the purposes of the extended centre manifold reduction, these will be treated as independent variables, satisfying the equations $\dot{\mu_1} = 0$ and $\dot{\mu_2} = 0$. Varying D will then correspond to following a path through $\mu_1\mu_2$-space, and since we are interested in values of ω_1 and ω_2 that are both large and negative, this path will (at least locally) correspond to $\mu_1 \approx \mu_2$. After rescaling time by a (positive) factor of $(\eta_1 + \eta_2)$, equations (3.20)–(3.25) become

$$\dot{x}_1 = \mu_1(x_1 + x_2) - \left[\frac{\mu_1 + \eta_1\eta_2}{\omega_2}\right](C_2 - C_1)u_1(x_1 + x_2) \tag{3.34}$$

$$\begin{aligned} \dot{x}_2 = {} & -(\eta_1 + \eta_2)^2 x_2 - \mu_1(x_1 + x_2) \\ & + \left[\frac{\mu_1 + \eta_1\eta_2}{\omega_2}\right](C_2 - C_1)u_1(x_1 + x_2) \end{aligned} \tag{3.35}$$

$$\begin{aligned} \dot{y}_1 = {} & \mu_2(y_1 + y_2) - \left[\frac{\mu_1 + \eta_1\eta_2}{\omega_2}\right] C_1 u_2(x_1 + x_2) \\ & + \left[\frac{\mu_1 + \eta_1\eta_2}{\omega_2}\right] C_2 u_1(y_1 + y_2) \end{aligned} \tag{3.36}$$

$$\begin{aligned} \dot{y}_2 = {} & -(\eta_1 + \eta_2)^2 y_2 - \mu_2(y_1 + y_2) + \left[\frac{\mu_1 + \eta_1\eta_2}{\omega_2}\right] C_1 u_2(x_1 + x_2) \\ & - \left[\frac{\mu_1 + \eta_1\eta_2}{\omega_2}\right] C_2 u_1(y_1 + y_2) \end{aligned} \tag{3.37}$$

$$\begin{aligned} \dot{u}_1 = {} & -(\eta_1 + \eta_2)\tau\eta_3 u_1 - C_3(\eta_1 + \eta_2)(\eta_2 x_2 - \eta_1 x_1)(x_1 + x_2) \\ & + C_4(\eta_1 + \eta_2)(\eta_1 y_2 - \eta_2 y_1)(y_1 + y_2) \end{aligned} \tag{3.38}$$

$$\begin{aligned} \dot{u}_2 = {} & -(\eta_1 + \eta_2)\tau\eta_4 u_2 \\ & -(\eta_1 + \eta_2)(C_4 - C_3)(x_1 + x_2)(\eta_1 y_2 - \eta_2 y_1). \end{aligned} \tag{3.39}$$

The way in which the parameters μ_1 and μ_2 have been used to substitute in for D is (to a certain extent) arbitrary, although it is natural to use μ_1 for the linear terms in the x equations and μ_2 for the linear terms in the y equations. This gives the equations the form of a codimension-two bifurcation problem. For the nonlinear terms, μ_1 was used to eliminate D.

Looking at the original equations, they are unaltered by the transformations

$$(x_1, x_2, y_1, y_2, u_1, u_2) \rightarrow (-x_1, -x_2, y_1, y_2, u_1, -u_2) \tag{3.40}$$

and

$$(x_1, x_2, y_1, y_2, u_1, u_2) \rightarrow (x_1, x_2, -y_1, -y_2, u_1, -u_2). \tag{3.41}$$

The equations for x_1, y_1, μ_1 and μ_2 contain no linear terms, so the dynamics on the centre manifold are governed by these (so-called) slow variables. On the centre manifold, the other variables can therefore be expressed in terms of these slow variables. At quadratic order, the symmetries of the system (described by equations 3.40 and 3.41) restrict the possible quadratic combinations of x_1, y_1, μ_1 and μ_2 that can appear in these expressions. It is easy to see that, to this order,

$$u_1 = (C_3\eta_1 x_1^2 - C_4\eta_2 y_1^2)/\tau\eta_3 \tag{3.42}$$

$$u_2 = (C_4 - C_3)\eta_2 x_1 y_1/\tau\eta_4 \tag{3.43}$$

$$x_2 = -\mu_1 x_1/(\eta_1 + \eta_2)^2 \tag{3.44}$$

$$y_2 = -\mu_2 y_1/(\eta_1 + \eta_2)^2. \tag{3.45}$$

When these expressions are substituted into the x_1 and y_1 equations, the resulting equations can be used to determine the dynamics on the centre manifold. These are given by

$$\begin{aligned}
\dot{x}_1 &= \mu_1 x_1 - \frac{\mu_1^2 x_1}{(\eta_1+\eta_2)^2} \\
&\quad -\frac{\eta_1\eta_2}{\omega_2}(C_2 - C_1)\left[(C_3\eta_1 x_1^2 - C_4\eta_2 y_1^2)/\tau\eta_3\right] x_1 \qquad (3.46)\\
\dot{y}_1 &= \mu_2 y_1 - \frac{\mu_2^2}{(\eta_1+\eta_2)^2} y_1 - \frac{\eta_1\eta_2^2 C_1(C_4 - C_3)}{\omega_2\tau\eta_4} x_1^2 y_1 \qquad (3.47)\\
&\quad +\frac{\eta_1\eta_2 C_2}{\omega_2} y_1\left[(C_3\eta_1 x_1^2 - C_4\eta_2 y_1^2)/\tau\eta_3\right].
\end{aligned}$$

Rewriting $\mu_1' = \mu_1 - \mu_1^2/(\eta_1+\eta_2)^2$ and $\mu_2' = \mu_2 - \mu_2^2/(\eta_1+\eta_2)^2$ and then dropping the primes gives a further simplification. As these two parameters are small near the region of interest, this will have very little effect on the local straight line path through parameter space. The variables can also be rescaled to remove some of the extra constants: making use of the fact that ω_1 and ω_2 are negative, and the constraints given by equations (3.30) and (3.31), these equations can be substantially simplified be rescaling x_1 and y_1. Dropping the subscripts on x_1 and y_1, the centre manifold equations become

$$\dot{x} = \mu_1 x + \delta y^2 x - x^3 \qquad (3.48)$$

$$\dot{y} = \mu_2 y + \gamma y x^2 - y^3, \qquad (3.49)$$

where two new coefficients have been defined:

$$\delta = (C_2 - C_1)/C_2 \qquad (3.50)$$

and

$$\gamma = [C_2/(C_2 - C_1)] - [\eta_2\eta_3 C_1(C_4 - C_3)/\eta_1\eta_4 C_3(C_2 - C_1)]. \qquad (3.51)$$

This is precisely the form of the double pitchfork bifurcation (Guckenheimer and Holmes, 1986) and is exactly the result that would be expected for a system that undergoes stationary bifurcations from a basic state possessing equatorial symmetry.

The Jacobian matrix for equations (3.48) and (3.49) can easily be evaluated:

$$\begin{pmatrix} \mu_1 + \delta y^2 - 3x^2 & 2\delta xy \\ 2\gamma xy & \mu_2 + \gamma x^2 - 3y^2 \end{pmatrix}. \tag{3.52}$$

This can be used to evaluate the stability properties of the fixed points of the system. As expected, the trivial solution $(x, y) = (0, 0)$ has a Jacobian with eigenvalues μ_1 and μ_2, which implies that it is unstable if either μ_1 or μ_2 are positive. This had already been guaranteed from the previous stability analysis.

The dipolar fixed point $(x, y) = (\pm\sqrt{\mu_1}, 0)$ has a Jacobian with eigenvalues $-2\mu_1$ and $\gamma\mu_1 + \mu_2$. So, for the existence of this solution, it is required that μ_1 be positive (which coincides with the region of instability of the trivial solution). This dipole solution would always be stable if the dynamics were restricted to the x-axis but it requires $\gamma\mu_1+\mu_2 < 0$ for it to be a stable node. Otherwise it is a saddle point. Similarly, the quadrupolar fixed point $(x, y) = (0, \pm\sqrt{\mu_2})$ will exist provided μ_2 is positive. The Jacobian evaluated at this fixed point has got eigenvalues of $-2\mu_2$ and $\mu_1 + \delta\mu_2$. So it is always stable if the dynamics are restricted to the quadrupolar (y) direction. If $\mu_1 + \delta\mu_2 < 0$ then it is a stable node and it is a saddle otherwise.

The mixed-parity fixed point is located by solving:

$$\mu_1 + \delta y^2 - x^2 = 0 \tag{3.53}$$

$$\mu_2 + \gamma x^2 - y^2 = 0. \tag{3.54}$$

This has solutions:

$$(x, y) = \left(\pm\sqrt{\frac{\delta\mu_2 + \mu_1}{1 - \delta\gamma}}, \pm\sqrt{\frac{\mu_2 + \gamma\mu_1}{1 - \delta\gamma}} \right). \tag{3.55}$$

So, if this solution is going to exist when the dipolar and quadrupolar solutions are saddle points, then it is required that $\delta\gamma < 1$. This implies that:

$$C_1(C_4 - C_3)/C_3C_2 > 0, \tag{3.56}$$

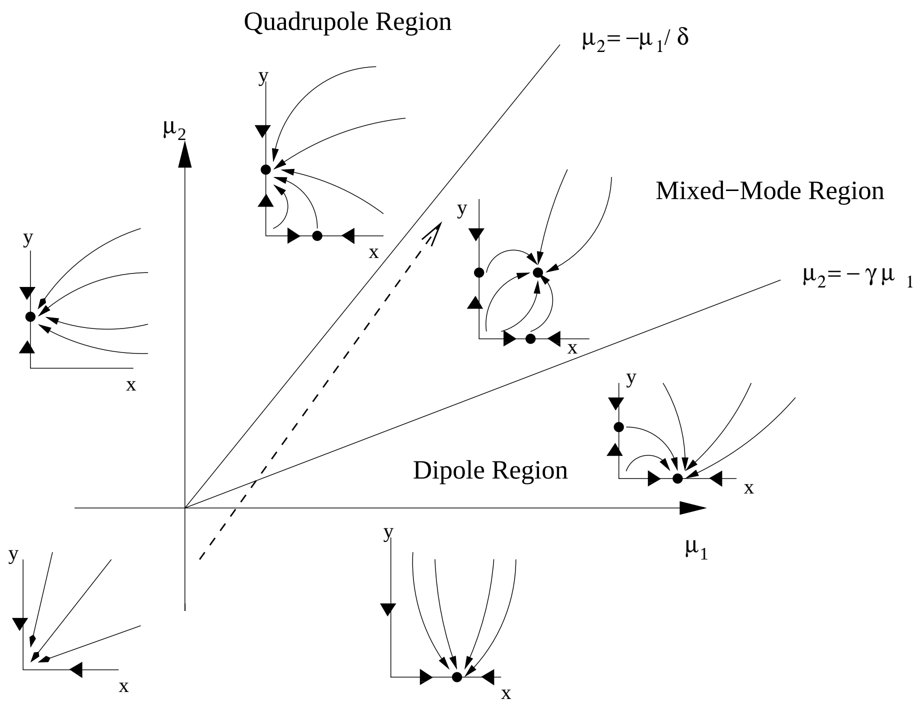

Figure 3.6: A bifurcation diagram summarising the parameter dependence of the phase portraits. The positions of the lines of bifurcation will vary with the parameters – this is a representative example. The dashed line shows an example of a path through parameter space that can be obtained by increasing the magnitude of the dynamo number

which is the final criterion that needs to be satisfied in order to ensure the existence of mixed-parity modes – it is straightforward to verify that this mode is stable where it occurs. In this low-order model, it is difficult to interpret this condition physically, but (from a mathematical point of view) it has been shown to be necessary in order to allow the system to produce mixed-parity modes. These results are summarised in Figure 3.6, which displays the stability of the fixed points depending upon their position in the (μ_1, μ_2) plane. The precise nature of this diagram depends upon the location of the lines $\mu_2 = -\mu_1/\delta$ and $\mu_2 = -\gamma\mu_1$, however this picture gives the general idea.

It should be emphasised that the original problem was a one-parameter problem. The

μ_1 and μ_2 variables were introduced in order to provide a convenient way of reducing this system down to lower order. Increasing D from zero corresponds to following a line through parameter space. The more negative the value of k_V (and hence ω_1 and ω_2), the closer to the origin of $\mu_1\mu_2$-space the path will pass, with it always entering the region of dipole stability first. In other words, the critical dynamo numbers for the dipolar and quadrupolar modes get closer as k_V gets more negative. Provided condition (3.56) is satisfied, this stationary dipolar solution can then lose stability to a stationary mixed-parity mode.

3.4.4 Results

Now that the stability criteria for a mixed-parity mode have been established, it is possible to integrate equations (3.20)–(3.25) numerically with parameters chosen in such a way as to give such a solution. This has been done using a simple 4th order Runge-Kutta scheme. The integrals that form the constants in this system are evaluated using a computer algebra package, and it was discovered that it was easy to find values for a, b and v that satisfy condition (3.56). The value of σ seems to have very little qualitative effect on the solutions, but in order to be consistent with the numerical simulations, this was set to be 1/3. As before τ is set to be equal to unity. The precise value of k_V was also shown to have very little effect on the form of the solutions provided it was sufficiently negative, and here k_V is set to be -30. For the results presented here: $a = 0.1$, $b = -0.05$, $v = -0.08$.

As D is increased from zero, the trivial solution persists until about $D = 35.6$, when a dipolar stationary mode is observed, as shown in Figure 3.7. This is characterised by a toroidal component that is antisymmetric about the equator, whilst the poloidal component is symmetric there. Since the critical dynamo number for the stationary quadrupolar mode is approximately 39.4, it is to be expected that the preferred mode would be dipolar in these simulations. This dipolar mode gives way to a stationary

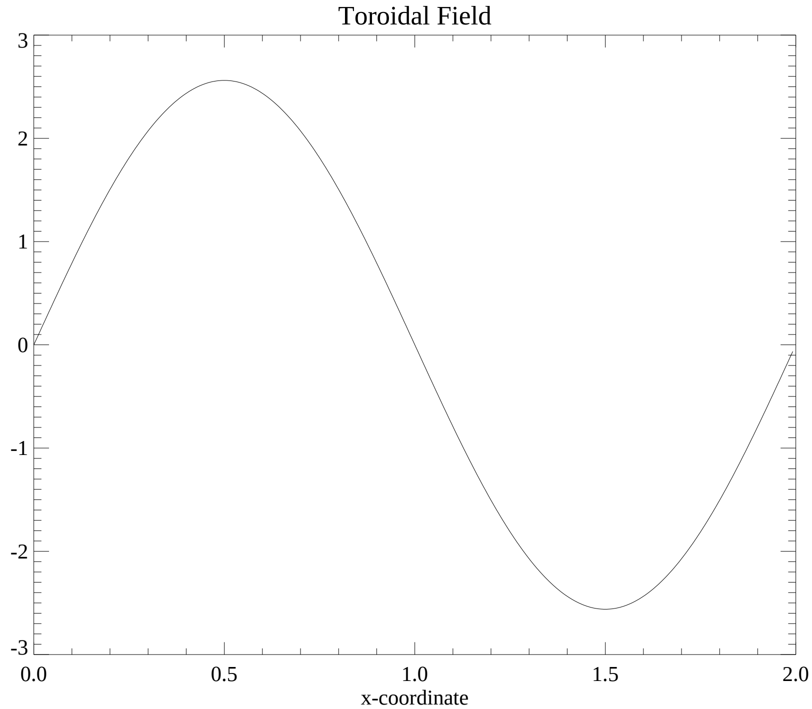

Figure 3.7: A dipolar toroidal field, B, at $D = 36$. Note the antisymmetry about the equator ($x = 1$).

mixed-parity mode at about $D = 37.3$, an example of which is shown in Figure 3.8. The toroidal field now looks strikingly asymmetric, and this asymmetry persists as the dynamo number is increased.

As a representation for a stellar dynamo, this low-order model has only limited application. This model yields stationary solutions rather than oscillatory ones and only contains two Fourier modes, so any asymmetry is clearly going to be limited. The purpose of this illustrative calculation was to give an insight into the simplest possible dipole-quadrupole interaction. In theory, by taking more Fourier modes in the truncation, it should be possible to analyse a more realistic system in this way although it becomes rapidly more and more algebraically intractable as N increases. From an analytic point of

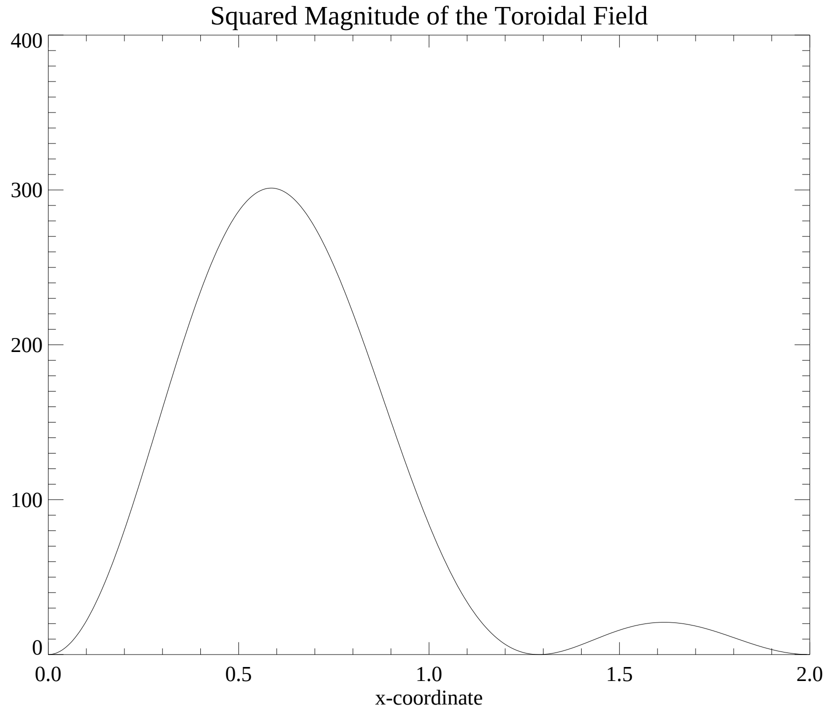

Figure 3.8: The square of the toroidal field, B, at $D = 38$. Note the asymmetry about the equator ($x = 1$).

view, it should be noted (see, Guckenheimer and Holmes, 1986) that the equations for the double pitchfork bifurcation are very similar to the amplitude equations for the double Hopf bifurcation, so the oscillatory and stationary cases may well be closely related to each other. This analogy is important, because if we can explain how asymmetry arises in the amplitudes of the oscillatory dynamo modes, that is half the picture. The surprising feature of the numerical simulations is the robustness of the hemispherical modes – that is, of course, a feature that can not be explained by this simple model and a much higher order of truncation might be necessary before such behaviour is observed. At this order, a reduction of the form that has been carried out will become much more difficult.

3.5 Summary and discussion

It has been demonstrated in this chapter that it is possible for highly asymmetric mixed-parity modes to arise in a simple, one-dimensional mean-field $\alpha\omega$ dynamo model. This model was derived from a model developed by Tobias (1996b,c, 1997b) and it was reduced to one spatial dimension by an averaging process in the z direction. This led to nonlinear terms, with coefficients that could be adjusted without altering the fact that the nonlinear terms make no net contribution to the total energy of the system. This one-dimensional system of partial differential equations was numerically integrated. Mixed-parity modes of two types were found to be stable in a large region of parameter space. The second of these types shows extreme north-south asymmetry and is the kind of solution that Busse (2000) found in some large-scale numerical simulations. This type of mode can only arise if it contains dipolar and quadrupolar components in roughly equal quantities, oscillating in phase with each other, and it was found to be surprisingly robust. As an illustrative calculation, a low-order model was derived which has been shown to give the simplest interaction of stationary dipolar and quadrupolar modes. An extended centre manifold reduction was performed in order to reduce this low-order model down to a 2nd order system. As a model for a stellar dynamo, this low-order model clearly has limited application, although the similarity of the 2nd order system to the amplitude equations for the oscillatory case (Guckenheimer and Holmes, 1986), suggests that this approach has captured some of the essential ideas. In theory, therefore, it should be possible to use the same technique on a system that is truncated at higher order in order to produce equations that govern the interaction of two oscillating modes. Unfortunately, the smallest system that will give two oscillating modes consists of twelve ordinary differential equations, and it may be necessary to go to even higher order to produce the appropriate behaviour. As this is algebraically very intractable, a system of this order was not investigated.

Ideally, it would be desirable to write down a set of criteria to establish whether or not a stellar dynamo is going to be highly asymmetric, but this is undoubtedly very difficult. What this piece of work has done is to show that given "suitable" values of the parameters in this model, highly asymmetric modes do indeed arise, and their occurrence seems to be relatively insensitive to the precise parameter values. This means that we should not be surprised that they do exist in reality. Having said that, these modes arise as secondary bifurcations from a pure parity state, and their precise form is governed by a complicated set of nonlinear partial differential equations. This means that it will probably be extremely difficult to find a simple set of criteria that establish whether or not such a dynamo is going to be highly asymmetric.

Although modulational effects (see, for example, Tobias, 2002a) must be taken into account when modelling the solar dynamo, it seems highly plausible that this is the kind of mixed-parity mode that could have given rise to the asymmetric sunspot observations that were taken during the latter stages of the Maunder minimum. A particularly appealing feature of the mixed-parity modes shown in Figure 3.4 and Figure 3.5 is that the bulk of the magnetic field in the active hemisphere is confined to a narrow band close to the equator. This compares favourably with the narrow latitudinal band of sunspots that were observed during the last stages of the Maunder minimum (Sokoloff and Nesme-Ribes, 1994). As sunspots are just indicators of the subsurface field, it should be noted that it is not necessary to have complete cancellation in one hemisphere in order to produce asymmetric sunspot observations. If the activity in one hemisphere is sufficiently reduced, then it will be less prone to the buoyancy instabilities which carry flux up towards the surface of the Sun (see, for example Hughes, 1992). In addition, any flux that does travel up through the convection zone will be weaker and therefore far more prone towards disruption by the turbulent convective motions that it will encounter. The convection zone can therefore act as a filter, only allowing the strongest magnetic flux to reach the photosphere. This implies that weaker subsurface flux will not tend to give rise to large-scale active regions. Due to the simplified nature of this model it is dangerous to try and relate the results too closely to the solar dynamo, however it does seem to capture the essential ideas. It is reasonable to suppose that these ideas should also be applicable to other solar-type stars.

As a final note, it is interesting to compare these results with the results of Bennett et al. (2002) on the so-called “Huygens clock” experiment. They looked at a system of two pendula mounted side by side on a wooden beam and the motion of this common support provides coupling between the pendula. The weight of this support was adjusted so as to alter its response to the oscillatory motion of the swinging pendula. For strong enough coupling, a state which was referred to as “beating death” resulted. This consisted of one pendulum swinging while the other remained stationary. This asymmetric behaviour is strikingly similar to the hemispherical magnetic activity observed in the dynamo model given above and in the simulations of Busse. Although this is a different problem, it is suggestive of the fact that highly asymmetric states could be a general feature of symmetric, coupled, nonlinear systems.

Chapter 4

Stellar Mean-Field Dynamo Models

In the previous chapter, an illustrative model was used in order to investigate one particular aspect of solar and stellar dynamos. Whilst this one-dimensional model provides a useful means of investigating mixed-parity modes, it is too simplistic to be regarded as a "realistic" dynamo model. As described in Section 2.4.4, recent simulations have made significant progress towards more realistic mean-field dynamo models. Various dynamo models are described in this chapter, along with the numerical schemes that are used in their simulation. The simplest model, which is based upon that of Markiel (1999) and Markiel and Thomas (1999), is described in the next section. This model then forms the basis for more ambitious models which include various new effects, such as the nonlinear back-reaction of the Lorentz force upon the angular velocity, a prescribed meridional flow and an extension of the model to $\alpha^2\omega$ dynamos.

The implementation of the numerical schemes was a lengthy process, and the resulting codes often need to run for several hours of computing time. The validation process for these codes (which is also described in this chapter) proved to be rather complicated. The simplest way to verify that a new code is operating correctly is by attempting to reproduce previously published results. In a number of cases this proved to be impossible, which meant that considerable amounts of time were spent trying to locate the causes for any discrepancies. With the assistance of the relevant authors, a number of mistakes were actually found in the published results. These have now been corrected, and the codes have been successfully validated. Having performed these checks, the resulting dynamo codes are powerful tools in the study of solar and stellar dynamos.

4.1 The dynamo model

4.1.1 The $\alpha\omega$ equations

Ignoring meridional motions, the mean velocity field, $\mathbf{u}$, can be expressed in the following form:

$$\mathbf{u} = \Omega(r,\theta) r \sin\theta \mathbf{e}_\phi, \tag{4.1}$$

where, $\Omega(r,\theta)$ is the imposed differential rotation profile. It is assumed that the form of $\Omega(r,\theta)$ is maintained by the non-magnetic forces acting on the fluid (e.g. gravity, turbulent stresses etc). As this model is axisymmetric, it is convenient to use the standard poloidal-toroidal decomposition (equation 2.15) for the magnetic field – substituting this into the mean-field dynamo equation (equation 2.40) yields evolution equations for the scalars A and B, which (in the $\alpha\omega$ approximation) are given by:

$$\begin{aligned}\frac{\partial A}{\partial t} &= \frac{\alpha(r,\theta)B}{1+(B/B_o)^2} + \frac{\eta(r)}{r^2}\frac{\partial}{\partial r}\left[r^2\frac{\partial A}{\partial r}\right] + \frac{\eta(r)}{r^2\sin\theta}\frac{\partial}{\partial\theta}\left[\sin\theta\frac{\partial A}{\partial\theta}\right] \\ &\quad - \frac{\eta(r)A}{r^2\sin^2\theta}\end{aligned} \tag{4.2}$$

$$\begin{aligned}\frac{\partial B}{\partial t} &= \frac{\partial(A\sin\theta)}{\partial\theta}\frac{\partial\Omega}{\partial r} - \frac{\sin\theta}{r}\frac{\partial(Ar)}{\partial r}\frac{\partial\Omega}{\partial\theta} + \frac{1}{r}\frac{\partial}{\partial r}\left[\eta(r)\frac{\partial(Br)}{\partial r}\right] \\ &\quad + \frac{1}{r^2}\frac{\partial}{\partial\theta}\left[\frac{\eta(r)}{\sin\theta}\frac{\partial(B\sin\theta)}{\partial\theta}\right].\end{aligned} \tag{4.3}$$

Various terms in equations (4.2) and (4.3) require further explanation. The function $\alpha(r,\theta)$, which occurs in equation (4.2), represents the spatial distribution of the α-effect. α-quenching has been represented in a simple way by making use of an expression of the form given by equation (2.38), and quenching is taken to be dependent solely upon the (dominant) toroidal field component in this $\alpha\omega$ model. The constant B_o, given in equation (4.2), defines the value of B at which quenching effects becomes significant. The function $\eta(r)$ represents the magnetic diffusivity, which is a quantity that we would expect to be enhanced by turbulence. Since the intensity of the turbulence within a star might be expected to vary in a (roughly) spherically symmetric fashion, it is reasonable to assume that this diffusive coefficient is independent of θ.

These equations can now be non-dimensionalised, using scalings similar to those given in equation (3.7):

$$\begin{aligned}
&r \rightarrow R_*\tilde{r} && && t \rightarrow (R_*^2/\eta_o)\tilde{t} \\
&A \rightarrow (\alpha_o R_*^2 B_o/\eta_o)\tilde{A} && && B \rightarrow B_o\tilde{B} \\
&\alpha \rightarrow \alpha_o\tilde{\alpha}(\tilde{r},\theta) && \eta \rightarrow \eta_o\tilde{\eta}(\tilde{r}) && \Omega \rightarrow \Omega_o\tilde{\Omega}(\tilde{r},\theta).
\end{aligned} \tag{4.4}$$

where, R_* is the stellar radius, and η_o, α_o and Ω_o are characteristic values of the magnetic diffusivity, α-effect and angular velocity respectively. Dropping the tildes, the non-dimensionalised equations are given by:

$$\begin{aligned}
\frac{\partial A}{\partial t} &= \frac{\alpha(r,\theta)B}{1+B^2} + \frac{\eta(r)}{r^2}\frac{\partial}{\partial r}\left[r^2\frac{\partial A}{\partial r}\right] + \frac{\eta(r)}{r^2\sin\theta}\frac{\partial}{\partial\theta}\left[\sin\theta\frac{\partial A}{\partial\theta}\right] \\
&\quad -\frac{\eta(r)A}{r^2\sin^2\theta}
\end{aligned} \tag{4.5}$$

$$\begin{aligned}
\frac{\partial B}{\partial t} &= D\frac{\partial(A\sin\theta)}{\partial\theta}\frac{\partial\Omega}{\partial r} - D\frac{\sin\theta}{r}\frac{\partial(Ar)}{\partial r}\frac{\partial\Omega}{\partial\theta} + \frac{1}{r}\frac{\partial}{\partial r}\left[\eta(r)\frac{\partial(Br)}{\partial r}\right] \\
&\quad +\frac{1}{r^2}\frac{\partial}{\partial\theta}\left[\frac{\eta(r)}{\sin\theta}\frac{\partial(B\sin\theta)}{\partial\theta}\right].
\end{aligned} \tag{4.6}$$

The non-dimensional parameter appearing in these equations is the dynamo number,

$$D = \frac{\alpha_o \Omega_o R_*^3}{\eta_o^2}. \tag{4.7}$$

These are now the $\alpha\omega$ equations in their final form, for this model which takes α-quenching as the sole nonlinearity. However, before these can be integrated numerically, we need to decide how we are going to apply them to solar and stellar dynamos.

4.1.2 Model set-up

As discussed in Chapter 2, the region of interest for dynamos in late-type stars is probably around the base of the convection zone. It therefore makes sense to choose the computational domain so that it contains the convection zone and the overshoot layer. These equations are solved in a region that represents a meridional cut through a spherical shell: $0 \leq \theta \leq \pi$, $r_{in} \leq r \leq r_{out}$, where r_{out} is taken to be the stellar surface and r_{in} depends upon the location of the overshoot layer within the star. For the Sun, the base of the convection zone occurs at around $r = 0.7$, so the choice of $r_{in} = 0.6$ should ensure that the overshoot layer is entirely contained within the computational domain. The computational domain for a solar dynamo calculation is shown in Figure 4.1.

Appropriate boundary conditions must be chosen in order to complete the set-up of the model. On the axis of the domain (i.e. at $\theta = 0$ and $\theta = \pi$), the choice of boundary conditions is determined by the fact that the radial components of the magnetic field and the current must remain finite. These requirements are satisfied by taking

$$A = B = 0 \quad \text{at} \quad \theta = 0 \ \text{ and } \ \theta = \pi. \tag{4.8}$$

The enhancement of the magnetic diffusivity due to the effects of turbulence will be greatest within the convection zone. We would therefore expect the effective magnetic diffusivity to decrease rapidly with depth, below the base of the convection zone, until

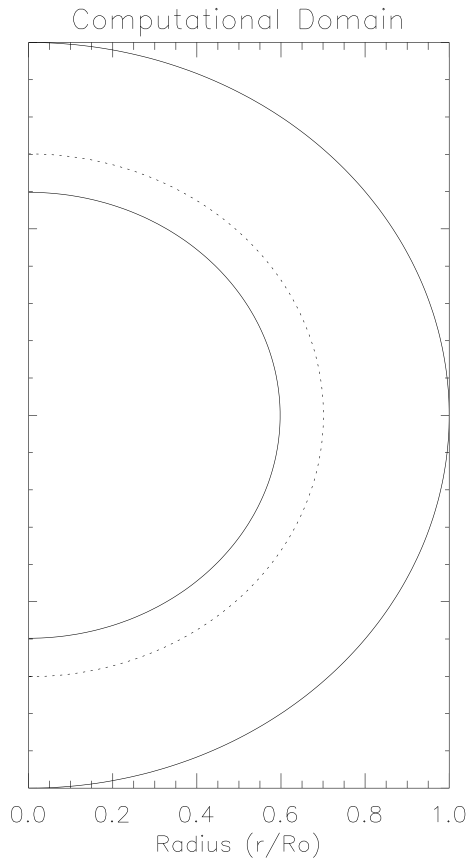

Figure 4.1: The computational domain for a solar dynamo calculation: $0 \leq \theta \leq \pi$, $0.6 \leq r \leq 1.0$. The base of the convection zone ($r = 0.7$) is indicated by a dotted line.

the turbulent enhancement becomes negligible. Since the magnetic diffusivity in the lower part of the overshoot layer is small, magnetic fields that are generated around the base of the convection zone will not readily propagate (diffusively) towards the inner radius of the computational domain. It is therefore reasonable to set:

$$A = B = 0 \quad \text{at} \quad r = r_{in}. \tag{4.9}$$

The outer radius of the domain corresponds to the surface of the star. Since stellar atmospheres are extremely tenuous when compared to the interior of a star, a magnetohydrostatic force balance above the surface of a star will be dominated by magnetic stresses. For equilibrium, we therefore require the magnetic field to be force-free. The simplest example of a force-free field is the case of a potential field, where the current vanishes everywhere. Assuming axisymmetry, any purely poloidal, force-free magnetic fields are also potential fields. Above the solar surface the large-scale magnetic field is observed to be mainly poloidal, which suggests that the (very commonly used) assumption that the current vanishes above the stellar surface is probably a reasonable one in this global axisymmetric dynamo model. In terms of the magnetic field, equations (2.7) and (2.15) mean that this current-free condition can be expressed as

$$\mathbf{j} = \frac{1}{\mu_o}\nabla \times \mathbf{B} = \frac{1}{\mu_o}\nabla \times [B\mathbf{e}_\phi + \nabla \times (A\mathbf{e}_\phi)] = 0 \quad \text{for} \quad r > r_{out}. \tag{4.10}$$

It is easy to see that this condition, coupled with the fact that B must vanish at the poles, implies that

$$B = 0 \quad \text{and} \quad \nabla^2 A - \frac{A}{r^2 \sin^2\theta} = 0 \quad \text{for} \quad r > r_{out}. \tag{4.11}$$

In order that there be no surface currents at $r = r_{out}$, all three components of the magnetic field must be continuous there. Given the conditions at the poles, this means that B, A and $\partial A/\partial r$ must all be continuous at the surface. So, in terms of boundary conditions there we need:

$$B = 0 \quad \text{at} \quad r = r_{out} \tag{4.12}$$

and

$$A \text{ matches smoothly onto a solution of } \nabla^2 A - \frac{A}{r^2 \sin^2\theta} = 0. \tag{4.13}$$

4.2 Numerical scheme

4.2.1 Discretisation of the equations

Having specified the details of the model, we are now in a position to choose a numerical scheme. The numerical scheme employed by Markiel (1999) uses a non-uniform computational grid in order to allow the concentration of grid-points around regions of interest. This is clearly a useful feature to include in a code of this type. For the case where the sole nonlinearity is α-quenching, Markiel's code seems to solve the mean-field equations very efficiently. It is mainly for this reason that I decided to closely follow the numerical method described by Markiel (1999). The other advantage of using such similar numerical schemes is that it makes it easier to compare results from the two codes. Since they are written entirely independently, but based on very similar numerical ideas, it means that if they are giving results that are the same, then the coding is more likely to be correct in both cases.

Using the method described by Markiel, the computational domain is covered by a mesh consisting of lines of constant r and lines of constant θ. The lines of constant θ are evenly spaced, stretching from pole to pole, whilst the lines of constant r are non-uniformly distributed. These lines are labelled by integer indices, with the lines of constant θ being labelled by the integer $j \in [1, J]$ ($j = 1$ corresponding to the North pole, $j = J$ to the South pole), and the lines of constant r being labelled by the integer $i \in [1, I]$ ($i = 1$ corresponds to the inner radius of the computational grid and $i = I$ corresponds to the outermost grid-point). For the ease of the application of the numerical scheme, I is always taken to be an odd integer. In order to simplify the discretisation of the equations, some structure is imposed upon the spacings of the lines of constant r: even numbered lines are constrained to be halfway between the odd numbered ones. A staggered mesh is used, which means that the variables A and B are not stored at every grid-point: A is only stored at grid-points that correspond to odd values of j and even values of i, B is only stored at grid-points with odd values of both i and j. Staggered meshes of this form are often used for flux conservative problems. As discussed by Markiel (1999), where more details can be found, the main benefit of this staggered grid is to improve the accuracy of the representation of the source terms in the mean-field equation. An example of a segment of the computational domain is shown in Figure 4.2.

The use of a non-uniform grid presents certain difficulties in the accurate representation of derivatives – an issue discussed in detail by Markiel (1999). Centred derivatives on a uniform grid can be used in order to achieve 2nd order accuracy in space. Since the lines of constant θ on this grid are uniformly spaced it is easy to illustrate that here. Using the notation $A_{i,j}$ to represent the value of the variable A at the grid-point (i, j), the first partial derivative of A with respect to θ, at the point $(i, j + 1)$ can be approximated by

$$\frac{\partial A}{\partial \theta}_{i,j+1} = \frac{A_{i,j+2} - A_{i,j}}{2\Delta\theta} + \mathrm{O}\left((\Delta\theta)^2\right), \tag{4.14}$$

where $\Delta\theta$ in the (constant) angle between the lines of constant θ. This derivative is exactly centred at grid-points with even values of both i and j. Similarly, the second partial derivative of A with respect to θ, centred at (i, j), is given by

$$\frac{\partial^2 A}{\partial \theta^2}_{i,j} = \frac{A_{i,j+2} - 2A_{i,j} + A_{i,j-2}}{4(\Delta\theta)^2} + \mathrm{O}\left((\Delta\theta)^2\right). \tag{4.15}$$

This derivative is exactly centred at grid-points with even values of i and odd values of j. It is easy to show using Taylor series expansions that these expressions correspond to the appropriate derivatives, with (as indicated) error terms of order $(\Delta\theta)^2$.

Given the non-uniform nature of the radial spacing of the grid, it follows that care needs to be taken concerning the location of the centering of the derivatives. Radial derivatives of B are in fact properly centred at grid-points with even values of i and odd values of j. This follows because the even grid lines of constant radius are constrained

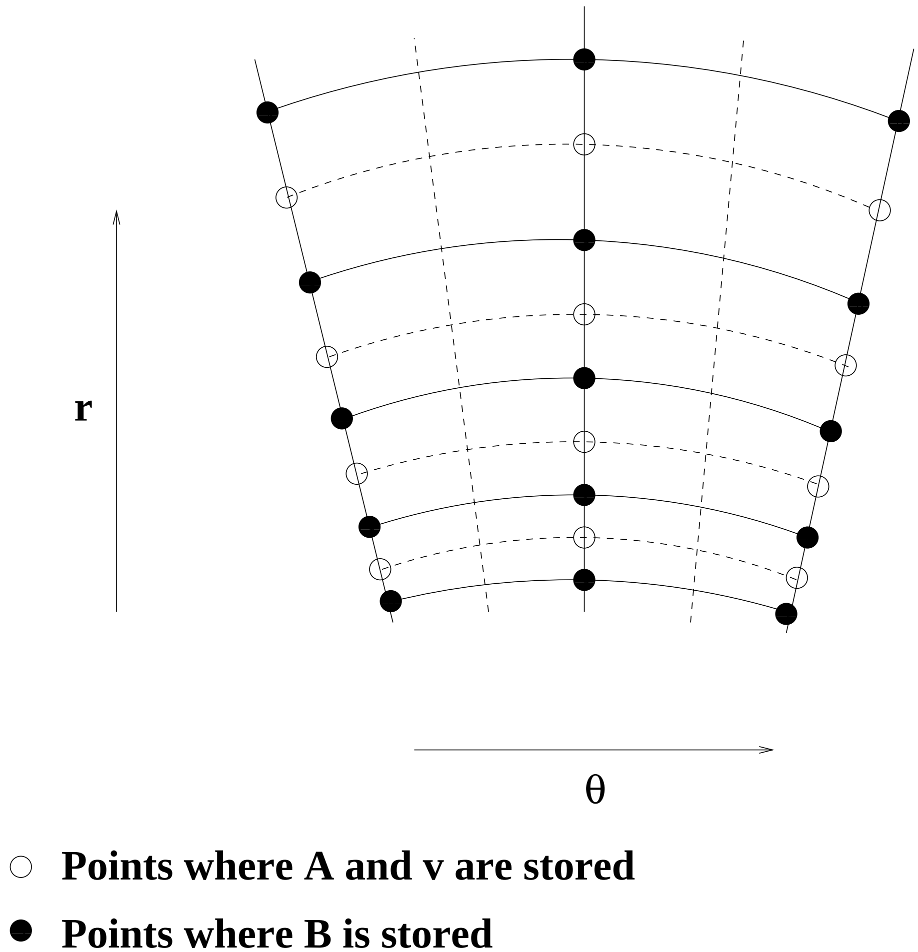

Figure 4.2: A section showing the layout of the mesh grid-points. The solid lines represent odd numbered grid lines in r and θ, whilst the dashed lines represent even lines. A and B are stored only at the points shown. The lines are evenly spaced in θ, non-uniform in r – even radial lines are always halfway between odd ones.

to be midway between the odd lines. However, radial derivatives of A are not centred exactly at grid-points. For example, the derivative

$$\frac{\partial A}{\partial r} = \frac{A_{i+1,j} - A_{i-1,j}}{r_{i+1} - r_{i-1}}, \tag{4.16}$$

(where r_i is the location of the i^{th} line of constant radius) is centred at $(r_{i+1} + r_{i-1})/2$, which probably will not coincide with r_i. A representation of this form only gives the derivative accurate to first order in space. Similar problems exist for higher order radial derivatives of all the variables. The problem is solved by using expressions for these derivatives on either side of the grid-point of interest to perform a linear interpolation. The resulting expressions for these derivatives at this grid-point are now correct to second order. The details of the discretisation of the equations are discussed at length by Markiel (1999), so it will not be discussed further here.

The time-stepping scheme used by Markiel (1999) was a 1st order Euler scheme (see, for example, Press et al., 1986). The time-step that can be used in this explicit scheme is tightly constrained: the scheme will be unstable if the time taken for information to propagate diffusively across a spatial cell is less than the time-step used (Press et al., 1986). So, if we have narrow cells in a region of high diffusivity then we require a small time-step in order to ensure stability. A typical time-step used in Markiel's calculations seemed to be of the order of 10^{-5} diffusion times – application of the time-stepping constraint ensures that the temporal accuracy is comparable to the spatial accuracy. Given that it was computationally inexpensive to use a scheme that was accurate to second order, the time-stepping scheme is used here is a 2nd order Adams-Bashforth scheme (see, for example, Iserles, 1996). This should be more accurate than the first order Euler scheme, although a very brief comparison of the two numerical schemes (as well as a third order Adams-Bashforth scheme) suggested that the precise choice of scheme made very little difference for this problem – all the schemes were stable and they seemed to produce virtually identical results.

4.2.2 Implementation of the boundary conditions

The boundary conditions for this problem were discussed in Section 4.1.2. Although the boundary conditions are essentially the same as those described by Markiel (1999), slightly different methods have been used in order to implement them here. Condition (4.8), which forces the variables to vanish at the poles, is easily satisfied by setting

$$A_{i,1} = B_{i,1} = A_{i,J} = B_{i,J} = 0 \quad \forall \;\; i. \tag{4.17}$$

The fact that the grid is both staggered and non-uniform in radius means that more care needs to be taken with the radial boundary conditions. A convenient way of implementing the boundary conditions at the inner radius (given by equation 4.9) is by placing the innermost ($i = 1$) radial grid-point just below $r = r_{in}$, in such a way as to ensure that first even grid-point ($i = 2$) coincides exactly with $r = r_{in}$. Since even radial grid-points are arranged so that they lie at exactly the mid-point between adjacent odd radial grid-points, the effective value of B at $r = r_{in}$ is easily obtained by interpolation. The boundary conditions at the base of the computational domain, which state that A and B must vanish at $r = r_{in}$, are therefore satisfied by setting

$$A_{2,j} = 0 \quad \text{and} \quad B_{1,j} = -B_{3,j} \quad \forall \;\; j. \tag{4.18}$$

The boundary conditions that need to be applied at the outer radius of the domain are rather more complicated than those described above. The condition that B vanishes at this boundary is accomplished in precisely the same way as for the inner boundary. The outermost (odd) grid-point is placed just outside the surface of the star in such a way as to ensure that the final even point coincides exactly with the surface. The value of B at the surface itself is again found by interpolation, and this results in a condition on B at the outermost grid-point:

$$B_{I,j} = -B_{I-2,j} \quad \forall \;\; j. \tag{4.19}$$

The condition on A at the surface is far more problematic, and much harder to implement. Condition (4.13) states that we need to map A onto a potential field in such a way as to ensure that A and its radial derivative are continuous at the surface. The method used here is an iterative technique described by Dikpati and Choudhuri (1994), details of which are given below. It is also possible to determine the boundary values of A by means of a matrix multiplication (Jepps, 1975). Jepps also used an iterative method in some of his calculations, although it was significantly less efficient than that described by Dikpati and Choudhuri (1994), and so it was found to be less efficient than his matrix method.

In order that there be no sources of magnetic field at infinity, we require

$$A(r,\theta) \rightarrow 0 \;\; \text{as} \;\; r \rightarrow \infty. \tag{4.20}$$

The general solution for the potential field can, therefore, be written in the form

$$A(r,\theta) = \sum_l \psi_l r^{-(l+1)} P_l^1(\cos\theta) \quad \text{for} \;\; r \geq r_{out}. \tag{4.21}$$

where, l is a positive integer, the ψ_l are constant coefficients and $P_l^1(\cos\theta)$ are the associated Legendre functions. The orthogonality relationship for these associated Legendre polynomials is (see, for example, Abramowitz and Stegun, 1968)

$$\int_0^\pi P_l^1(\cos\theta) P_n^1(\cos\theta)\sin\theta \mathrm{d}\theta = \frac{2l(l+1)}{(2l+1)}\delta_{ln}. \tag{4.22}$$

By making use of this relationship, it is possible to derive an expression for ψ_n which makes use of the values of A at the stellar surface (see, for example, Dikpati and Choudhuri, 1994)

$$\psi_n = \left[\frac{2n+1}{2n(n+1)}\right] r_{out}^{n+1} \int_o^\pi A(r_{out},\theta) P_n^1(\cos\theta)\sin\theta \mathrm{d}\theta. \tag{4.23}$$

The boundary condition on A requires the continuity of the radial derivative of A at the solar surface. From equation (4.21), the radial derivative of A must be given by

$$\frac{\partial A}{\partial r} = -\sum_l (l+1)\psi_l r_{out}^{-(l+2)} P_l^1(\cos\theta) \quad \text{at} \;\; r = r_{out}. \tag{4.24}$$

Satisfying equation (4.24) with the ψ_l coefficients given by equation (4.23) gives a smooth transition onto a potential field.

The iterative procedure used to implement this condition is relatively simple. The numerical grid is set up so that the outermost even radial grid location coincides with the stellar surface, so the values of A at the surface are given by $A_{I-1,j}\ \ \forall j$. At each time-step, the values of $A_{I-1,j}$ from the previous time-step are used as an initial guess for the new surface values. As described by Markiel (1999), an extended Simpson's rule (Press et al., 1986) can be used to calculate the coefficients ψ_n in equation (4.23). Using equation (4.24), these coefficients are then used to calculate an approximation to the radial derivative of A at the surface. Linear interpolation, based upon interior values of A, can then be used to provide an alternative expression for the radial derivative of A at the surface:

$$\begin{aligned} \frac{\partial A_{I-1,j}}{\partial r} \quad = \quad & \frac{(r_{I-1}-r_{I-3})^2-(r_{I-1}-r_{I-5})^2}{(r_{I-1}-r_{I-5})(r_{I-1}-r_{I-3})(r_{I-5}-r_{I-3})} A_{I-1,j} \\ & + \frac{(r_{I-1}-r_{I-5})}{(r_{I-1}-r_{I-3})(r_{I-5}-r_{I-3})} A_{I-3,j} \\ & + \frac{(r_{I-3}-r_{I-1})}{(r_{I-1}-r_{I-5})(r_{I-5}-r_{I-3})} A_{I-5,j}. \end{aligned} \tag{4.25}$$

Equating this expression for the derivative with that given by equation (4.24) leads to a new approximation for the values of $A_{I-1,j}$ (since all the other quantities are known). These values can then be fed back into equation (4.23) in order to find the new potential field. This process can be iterated until the correct values of $A_{I-1,j}$ have been found to an acceptable level of accuracy. Given that the explicit time-stepping scheme requires small time-steps, the initial guess in the iteration is fairly close to the true value, and the iteration was found to converge very rapidly – only 3 or 4 iterations were generally required in order to achieve convergence. About 20 associated Legendre modes were found to be sufficient to ensure the convergence of the sum given by equation (4.21) although 40 modes were used in most calculations.

At this stage, it is worth comparing the implementation of these boundary conditions with the methods used by Markiel (1999). All the methods are very similar, with the exception of the condition on A at the outer radius of the domain, which is rather different. Markiel's grid was set up slightly differently, in that he used an even number of grid-points, with the surface corresponding to r_{I-2} rather than r_{I-1}. This means that there is an additional even grid-point outside the surface of the star, and r_{I-2} is treated as an interior point, at which the equations are solved. In the same way as that described above, Markiel used equation (4.23) in order to calculate the coefficients ψ_n. These coefficients were than used in equation (4.21) to calculate the values of A at $r = r_I$. This was then used as the outer boundary condition at the next time-step. In the validation checks carried out by Markiel, this method gave results that were consistent with previously published work. This method certainly ensures that A is mapped continuously onto a potential field, although just after the boundary conditions have been calculated, it would appear to introduce a discontinuity in the radial derivative of A at $r = r_{I-2}$. After the equations have been evolved (just before the next calculation of the boundary conditions), this discontinuity jumps to $r = r_I$. Since the time-step is small, it is reasonable to suppose that these discontinuities are small, and this is in some way converging onto the correct solution (particularly for a model where there is little activity at the surface). The applicability of this alternative technique is investigated in some of the models that are described later on in the chapter.

4.2.3 Initial conditions

In any time-stepping code, such as this one, some initial conditions must be specified. A seed magnetic field must be present in order for dynamo action to occur. Provided that the initial field is small, and not too close to any particular eigensolution of the kinematic problem, it should not have have a significant effect on the final solution. The initial conditions used by Markiel (1999) were chosen so as to satisfy these constraints in such a way as to minimise the time taken for the dynamo to reach a statistically steady state. In the region of the base of the convection zone, B was set equal to a small linear combination of $P_1^1(\cos\theta)$ and $P_2^1(\cos\theta)$, whilst A was set equal to zero. This combination of $P_1^1(\cos\theta)$ and $P_2^1(\cos\theta)$ implies that this initial perturbation is not one of pure parity. Everywhere else, A and B were initially set equal to zero. Similar initial conditions were used in this model. The results seem to be insensitive to the precise form of this initial perturbation from the trivial state.

4.3 Code validation

4.3.1 Linear results

Before any code can be used in an investigation of solar and stellar dynamos, it must be carefully tested. The $\alpha\omega$ (kinematic) dynamo equations have been solved as an eigenvalue problem by Stix (1976). In Stix's "model 4", these equations are solved in a spherical shell with $r_{in} = 0.5R_\odot$ and $r_{out} = R_\odot$. The boundary conditions are as described in Section 4.1.2, apart from the condition on B at the inner radius of the domain: rather than $B = 0$, instead $\partial(rB)/\partial r = 0$ was used. This corresponds to treating the inner core as a perfectly conducting sphere. In this model, the angular velocity of the Sun was assumed to be constant on cylindrical surfaces, so $\Omega(r,\theta) = r^2\sin^2\theta$. A simple form was used for the α-effect, $\alpha(r,\theta) = \cos\theta$, and the magnetic diffusivity was taken to be constant.

Markiel used this model as a means of testing his code – the only alteration that was required was to change the lower boundary condition for B. This means that this was a good test of most aspects of the code. After removing the α-quenching term, the solutions either grow exponentially or decay (depending on the value of D). Interval bisection can be used to establish the critical dynamo numbers to an acceptable level of accuracy. As a further check, the frequencies of oscillation of the resulting dynamo waves can also be compared. Given that this seems to be a useful check of the code, it was decided to perform the same calculations using this new code. The resolution employed by Markiel consisted of a uniform grid with 65 odd grid-points (129 total) in latitude and and 22 odd grid-points (44 total) in radius. Henceforth, the grid size will always be quoted in terms of the number of odd grid-points. Since A and B are only stored at roughly half the total number of grid-points used, this gives a more accurate impression of the fineness of the grid. Markiel (1999) demonstrated that this resolution was sufficient to ensure the convergence of the critical dynamo numbers, D_c – doubling the number of grid-points in either direction changed D_c by only a fraction of a percent. Initial checks carried out with this new code agreed with this finding. However, it was found that increasing the resolution had a more significant effect (of the order of 1.5%) on the frequencies of oscillation. For this reason, the results described here were carried out using a 97x44 grid. Doubling the number of grid-points in either direction now made only a fraction of a percent difference to both the critical dynamo numbers and the frequencies of oscillation. By way of comparison, in the equivalent eigenvalue problem that was considered by Stix (1976), adequately converged solutions were obtained by considering only 10 grid-points in radius and only 9 associated Legendre modes in the expansion of the latitudinal part.

The critical dynamo numbers, D_c (both positive and negative), found by Stix, Markiel and this code are shown in Table 4.1. It should be noted that both Stix and Markiel used a slightly different definition for their dynamo numbers, the magnitude of which corresponds to the square root of the dynamo number defined in equation (4.7) – the magnitudes of my values have been adjusted accordingly in order to allow easier comparison. In all studies it was found that dipolar modes are preferred for negative dynamo numbers, whilst quadrupolar modes are preferred for positive values. For negative dynamo numbers, the dynamo waves migrate equatorwards, with the migration reversed for positive dynamo numbers. Comparing the calculations carried out here with

		Stix	Markiel	My code
Negative D	D_c	–95.74	–94.55 ± 0.05	–93.51 ± 0.03
	Frequency	79.18	75.5 ± 0.3	74.27 ± 0.4
Positive D	D_c	83.00	82.35 ± 0.05	83.99 ± 0.03
	Frequency	81.48	79.6 ± 0.1	82.47 ± 0.5

Table 4.1: A comparison of the critical dynamo numbers and frequencies of oscillation. The level of accuracy of these determined values is also indicated. The grid sizes used are enough to ensure convergence in each case – more details are given in the text.

those of Stix, the critical dynamo numbers differ by 2.3% for negative D and 1.2% for positive D whilst the frequencies differ by 6.2% for positive D and by 1.2% for negative D. Closer agreement on the frequencies is obtained when my code is run at Stix's critical dynamo numbers (2.2% discrepancy for negative D and 0.1% discrepancy for positive D). Given the uncertainties in the different numerical schemes that were used to obtain these results, these values are in acceptable agreement. This test also suggests that the results from Markiel's code are in good agreement with those obtained from my code. The results here were found to be insensitive to the choice of time-step – since the time-step is limited by the stability requirements and the time-stepping scheme is second order, this is unsurprising. The use of double precision arithmetic (as opposed to single precision) also made no discernable difference to the results.

4.3.2 Nonlinear calculations

The linear results described above enabled most aspects of the code to be checked. As a further test, the code was used to try to reproduce results from some solar dynamo calculations from Markiel's thesis. Rather surprisingly, although the results were qualitatively similar for most of the cases tried, there were significant quantitative differences between the results from the two dynamo codes. Also, for an α-effect that was concentrated around the equator, there were actually major qualitative differences: for a certain range of the parameters, Markiel found an oscillatory mode driven by the radial shear, whereas my code produced a steady mode driven by the latitudinal shear. This suggested a problem with the imposed velocity shear profiles, which could only be resolved by a detailed comparison of the two dynamo codes – I am grateful to Andrew Markiel for allowing me to have access to his dynamo code for this purpose.

Analysis of Markiel's code showed that the discrepancy between the two codes lay in the analytic fit to the imposed radial shear. For these particular simulations, there appears to be an erroneous factor of two in the imposed shear in Markiel's code, which artificially increases the effect of the radial shear for these calculations. This explains why Markiel found behaviour dominated by the radial shear rather than the latitudinal shear for an α-effect that was heavily restricted to low latitudes. The analytic fit to the radial shear that was used in my code has been double-checked against a computer-generated shear profile derived from the imposed rotation law, so this would seem to be correct. This probable error only affects the results that appear in the final chapter of Markiel's thesis and does not effect any of the idealised interface calculations described in Markiel and Thomas (1999). The validation check carried out in Section 4.4.2 (see later) provides further evidence that the shear profile that is used in my code is correct. Removing this factor of two from Markiel's code now allows us to perform a detailed comparison of the two codes.

In all cases considered, the results were qualitatively identical. One detailed comparison was carried out in order to verify that the codes are giving results that are in agreement with each other. Having non-dimensionalised Ω in terms of the surface equatorial rotation rate, and η in terms of the convection zone diffusivity, the input profiles for this model are as follows:

$$
\begin{aligned}
\alpha(r,\theta) &= \cos\theta \exp\left[-\left(\frac{r-0.71}{0.025}\right)^2\right] \qquad (4.26)\\
\Omega(r,\theta) &= \Omega_c + \frac{1}{2}\left[1+\Phi\left(\frac{r-0.685}{0.025}\right)\right]\left(P - Q\cos^2\theta - R\cos^4\theta\right)\\
\eta(r) &= \left(\frac{1-\eta_c}{2}\right)\left[1+\Phi\left(\frac{r-0.685}{0.025}\right)\right] + \eta_c,
\end{aligned}
$$

where Φ represents the error function, $\eta_c = 0.01$, $P = 0.0571$, $Q = 0.123$, $R = 0.155$ and $\Omega_c = 0.915$. The spatial dependence of $\Omega(r,\theta)$ is chosen so as to provide an analytic fit to the inferred solar rotation profile, with a narrow transition region (representing the tachocline), at $r = 0.7$, matching the rigidly rotating core to the differentially rotating convection zone. The profile for $\eta(r)$ provides a smooth transition (for the magnetic diffusivity) from the turbulent convection zone, where the diffusivity is assumed to be enhanced, to the highly conducting region below. The α-profile represents a tachocline-based α-effect. Similar input profiles are used for Figure 6.16 of Markiel (1999), although a smaller value of η_c was used in those calculations. It should be noted that the solutions will look slightly different to those given in Markiel's thesis due to the correction that has been applied to the analytic fit to the radial shear profile, and the fact that linear contour spacings are used as opposed to logarithmic ones. As mentioned previously, Markiel uses a slightly different definition of D from that given by equation (4.7): using my definition, $D = -1.0 \times 10^6$. Markiel used a non-uniform grid using 64 radial grid-points and 65 latitudinal ones – the grid used for my code was chosen to be as similar as possible to this one. Virtually identical initial conditions were also used, and the solutions were evolved for the same length of time.

Contours of toroidal field, plotted against latitude and time at $r = 0.68$, from both codes are shown in Figure 4.3. The time-scales on these figures are in terms of the dimensionless units (diffusion times) described in equation (4.4). The peak toroidal fields at $r = 0.68$ for these calculations are 3.20 and 3.14 for Markiel's code and my code respectively (dimensionless units are again used). The periods of oscillation are 0.0097

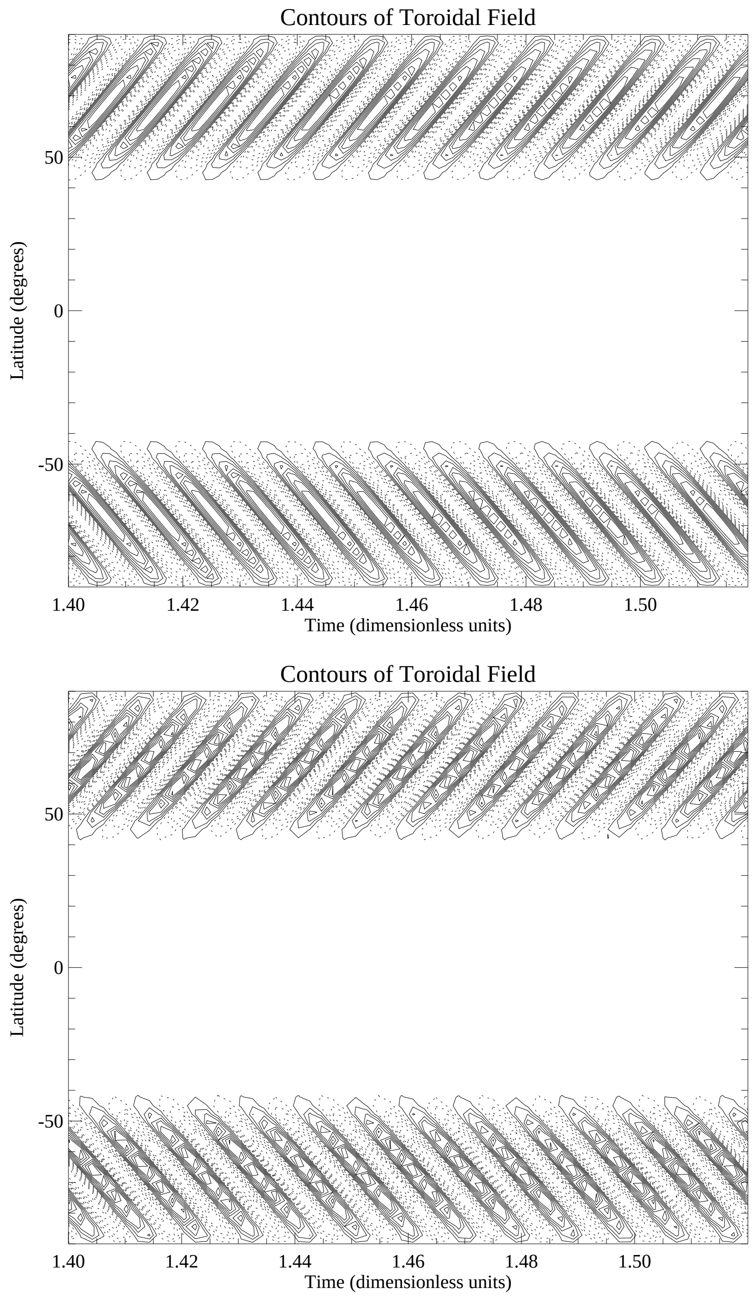

Figure 4.3: Contours of toroidal field, plotted against latitude and time at $r = 0.68$, for my code (top) and Markiel's code (bottom). The contour spacings are the same in each plot, with solid contours corresponding to positive values of B and dashed contours corresponding to negative values.

units, for my code, and 0.0094 units for Markiel's code. The differences between these values for the two codes are of the order of 2-3% – these discrepancies are perfectly acceptable given the differences between the two codes.

It is important to consider to what extent these results are dependent upon the resolution of the grid. Given the uncertainties involved in the placement of the radial grid-points, it is easier to perform resolution checks using a uniform grid – this also means that we can assess the effects of using a non-uniform grid as opposed to one where the spacing is uniform. Initially a 101x65 uniform grid was used and, after evolving the equations for the same length of time, the resulting oscillations were qualitatively the same as those shown in Figure 4.3. The values of the period and the peak toroidal field were 0.0096 and 3.06 respectively. These values are in good agreement with the results from the non-uniform grid despite the very different radial grid-point coverage. This suggests that a radial resolution of 101 grid-points is probably sufficient to give a solution of acceptable accuracy.

Table 4.2 summarises the results from the runs carried out at different grid resolutions. These resolution checks indicate that, although the results are relatively insensitive to an increase in the radial resolution, doubling the number of latitudinal grid-points has a significant effect upon the values of the period and the peak field (a 19% decrease in the period and an 8% decrease in the peak field). Having said that, despite substantial differences in these values, the overall pattern of behaviour of the dynamo oscillations seems to be unaffected by an increase in the number of grid-points in the mesh. In any numerical survey, it is necessary to select a grid resolution in such a way as to achieve a balance between numerical accuracy and computation time. It should also be remembered that even extremely high resolution mean-field simulations are only capable of producing a qualitative picture of the operation of a stellar dynamo. These results suggest that a resolution of 101x65 is probably sufficient for an exploration of parameter space, although a finer mesh is needed for more detailed calculations.

Resolution	Period of oscillation	Peak toroidal field
101x65	0.0096	3.06
151x65	0.0099	3.11
101x97	0.0084	2.90
151x97	0.0085	2.92
101x129	0.0079	2.81
101x161	0.0077	2.76
101x193	0.0076	2.74

Table 4.2: Resolution checks for the uniform grid code. Grid resolution is quoted in terms of number of odd radial grid-points x number of odd latitudinal points. The periods of oscillation are given correct to 2 decimal places, which reflects the accuracy of the measurement.

4.4 Variants to the model

4.4.1 A macrodynamic nonlinearity

In the model that has been discussed throughout this chapter so far, the only nonlinear effect is that of α-quenching. An additional possible nonlinear mechanism is the macrodynamic back-reaction of the Lorentz force upon the mean azimuthal velocity – see Section 2.4.4 for a summary of previous solar dynamo models which incorporate this effect.

In this modified model, the mean velocity field is now given by

$$\mathbf{u} = \Omega(r,\theta) r \sin\theta \mathbf{e}_\phi + v\mathbf{e}_\phi, \tag{4.27}$$

where v represents the azimuthal velocity perturbation (poloidal motions are again neglected). In keeping with previous studies (see also Chapter 3), it is assumed that the evolution of v is governed solely by magnetic and diffusive effects. The evolution equation for v is the spherical analogue of equation (3.3)

$$\begin{aligned}\frac{\partial v}{\partial t} &= \frac{1}{r^2 \sin\theta \mu_o \rho}\left[\frac{\partial (A\sin\theta)}{\partial\theta}\frac{\partial (Br)}{\partial r} - \frac{\partial (B\sin\theta)}{\partial\theta}\frac{\partial (Ar)}{\partial r}\right] \\ &\quad + \frac{r}{\rho}\frac{\partial(\rho\nu)}{\partial r}\frac{\partial}{\partial r}\left[\frac{v}{r}\right] + \frac{\nu(r)}{r^2}\frac{\partial}{\partial r}\left[r^2\frac{\partial v}{\partial r}\right] + \frac{\nu(r)}{r^2\sin\theta}\frac{\partial}{\partial\theta}\left[\sin\theta\frac{\partial v}{\partial\theta}\right] \\ &\quad - \frac{\nu(r) v}{r^2\sin^2\theta},\end{aligned} \tag{4.28}$$

where $\rho(r)$ is the fluid density and $\nu(r)$ is the fluid viscosity. It is assumed throughout that

$$\nu(r) = \tau\eta(r), \tag{4.29}$$

(see, for example, Tobias, 1997a; Weiss and Tobias, 1997; Phillips et al., 2002) where the non-dimensional constant τ is the magnetic Prandtl number. This proportional relationship represents the fact that we would expect both quantities to experience a similar enhancement due to the effects of turbulence. This simple parameterised form for the turbulent viscosity is adequate for this mean-field model. The density is also taken to be a function of radius only, and can be adjusted so as to take into account the effects of stratification within a star. The evolution equations for A and B are identical in this modified model apart from the fact that $\Omega(r,\theta)$ is now replaced by $\Omega(r,\theta) + v/(r\sin\theta)$.

These equations are non-dimensionalised using the scalings given by equation (4.4). Additional scalings are required for the new quantities:

$$v \to R_*\Omega_o\tilde{v} \qquad \rho(r) \to \rho_o\tilde{\rho}(\tilde{r}). \tag{4.30}$$

Dropping the tildes results in the following set of equations

$$\frac{\partial A}{\partial t} = \frac{\alpha(r,\theta)B}{1+B^2} + \frac{\eta(r)}{r^2}\frac{\partial}{\partial r}\left[r^2\frac{\partial A}{\partial r}\right] + \frac{\eta(r)}{r^2\sin\theta}\frac{\partial}{\partial\theta}\left[\sin\theta\frac{\partial A}{\partial\theta}\right] - \frac{\eta(r)A}{r^2\sin^2\theta} \tag{4.31}$$

$$\begin{aligned}\frac{\partial B}{\partial t} &= D\frac{\partial(A\sin\theta)}{\partial\theta}\frac{\partial\Omega}{\partial r} + \frac{D}{\sin\theta}\frac{\partial(A\sin\theta)}{\partial\theta}\frac{\partial}{\partial r}\left[\frac{v}{r}\right] - \frac{D\sin\theta}{r}\frac{\partial(Ar)}{\partial r}\frac{\partial\Omega}{\partial\theta} \\ &\quad - \frac{D\sin\theta}{r^2}\frac{\partial(Ar)}{\partial r}\frac{\partial}{\partial\theta}\left[\frac{v}{\sin\theta}\right] + \frac{1}{r}\frac{\partial}{\partial r}\left[\eta(r)\frac{\partial(Br)}{\partial r}\right] \\ &\quad + \frac{1}{r^2}\frac{\partial}{\partial\theta}\left[\frac{\eta(r)}{\sin\theta}\frac{\partial(B\sin\theta)}{\partial\theta}\right]\end{aligned} \tag{4.32}$$

$$\begin{aligned}\frac{\partial v}{\partial t} &= \frac{\Lambda}{r^2\sin\theta\rho(r)}\left[\frac{\partial(A\sin\theta)}{\partial\theta}\frac{\partial(Br)}{\partial r} - \frac{\partial(B\sin\theta)}{\partial\theta}\frac{\partial(Ar)}{\partial r}\right] \\ &\quad + \frac{\tau r}{\rho(r)}\frac{\partial(\rho\eta)}{\partial r}\frac{\partial}{\partial r}\left[\frac{v}{r}\right] + \frac{\tau\eta(r)}{r^2}\frac{\partial}{\partial r}\left[r^2\frac{\partial v}{\partial r}\right] + \frac{\tau\eta(r)}{r^2\sin\theta}\frac{\partial}{\partial\theta}\left[\sin\theta\frac{\partial v}{\partial\theta}\right] \\ &\quad - \frac{\tau\eta(r)v}{r^2\sin^2\theta}.\end{aligned} \tag{4.33}$$

In these equations, the α-quenching term has been retained – this effect can easily be removed if required. The additional non-dimensional parameter, Λ, is defined by

$$\Lambda = \frac{B_o^2\alpha_o R_*}{\mu_o\rho_o\Omega_o\eta_o^2}. \tag{4.34}$$

In the absence of the α-quenching term, Λ can be eliminated from the equations by a rescaling of A and B ($A \to \Lambda^{-\frac{1}{2}}\tilde{A}$, $B \to \Lambda^{-\frac{1}{2}}\tilde{B}$), as discussed in Chapter 3. If α-quenching is included, it is not possible to remove Λ entirely, and this rescaling results in a modification of the quenching term. The model equations in their final form are given by

$$\frac{\partial A}{\partial t} = \frac{\alpha(r,\theta)B}{1+(B^2/\Lambda)} + \frac{\eta(r)}{r^2}\frac{\partial}{\partial r}\left[r^2\frac{\partial A}{\partial r}\right] + \frac{\eta(r)}{r^2\sin\theta}\frac{\partial}{\partial\theta}\left[\sin\theta\frac{\partial A}{\partial\theta}\right] - \frac{\eta(r)A}{r^2\sin^2\theta} \tag{4.35}$$

$$
\begin{aligned}
\frac{\partial B}{\partial t} \quad = \quad & D\frac{\partial(A\sin\theta)}{\partial\theta}\frac{\partial\Omega}{\partial r} + \frac{D}{\sin\theta}\frac{\partial(A\sin\theta)}{\partial\theta}\frac{\partial}{\partial r}\left[\frac{v}{r}\right] - \frac{D\sin\theta}{r}\frac{\partial(Ar)}{\partial r}\frac{\partial\Omega}{\partial\theta} \\
& -\frac{D\sin\theta}{r^2}\frac{\partial(Ar)}{\partial r}\frac{\partial}{\partial\theta}\left[\frac{v}{\sin\theta}\right] + \frac{1}{r}\frac{\partial}{\partial r}\left[\eta(r)\frac{\partial(Br)}{\partial r}\right] \\
& +\frac{1}{r^2}\frac{\partial}{\partial\theta}\left[\frac{\eta(r)}{\sin\theta}\frac{\partial(B\sin\theta)}{\partial\theta}\right]
\end{aligned} \tag{4.36}
$$

$$
\begin{aligned}
\frac{\partial v}{\partial t} \quad = \quad & \frac{\mathrm{sign}(D)}{r^2\sin\theta\rho(r)}\left[\frac{\partial(A\sin\theta)}{\partial\theta}\frac{\partial(Br)}{\partial r} - \frac{\partial(B\sin\theta)}{\partial\theta}\frac{\partial(Ar)}{\partial r}\right] \\
& +\frac{\tau r}{\rho(r)}\frac{\partial(\rho\eta)}{\partial r}\frac{\partial}{\partial r}\left[\frac{v}{r}\right] + \frac{\tau\eta(r)}{r^2}\frac{\partial}{\partial r}\left[r^2\frac{\partial v}{\partial r}\right] + \frac{\tau\eta(r)}{r^2\sin\theta}\frac{\partial}{\partial\theta}\left[\sin\theta\frac{\partial v}{\partial\theta}\right] \\
& -\frac{\tau\eta(r)v}{r^2\sin^2\theta}.
\end{aligned} \tag{4.37}
$$

Boundary conditions for v are chosen to try to complement the magnetic boundary conditions. In order that the perturbation to the angular velocity should remain finite at the poles

$$
v = 0 \quad \text{at} \quad \theta = 0 \;\text{ and }\; \theta = \pi. \tag{4.38}
$$

The boundary condition for v at the inner radius of the domain is taken to be

$$
v = 0 \quad \text{at} \quad r = r_{in}. \tag{4.39}
$$

This reflects the fact that we would not expect the dynamo and its associated velocity perturbation to penetrate far into the low-diffusivity portion of the domain. The magnetic conditions (given by equation 4.9) also imply that the Lorentz force vanishes at the base of the domain. At the surface, the vacuum boundary conditions for the magnetic field suggest that a stress-free condition is appropriate

$$
\frac{\partial}{\partial r}\left(\frac{v}{r}\right) = 0 \quad \text{at} \quad r = r_{out}. \tag{4.40}
$$

Numerically, the addition of v is implemented in a relatively straightforward way. Like A, v is stored only at grid-points with an even radial index and an odd latitudinal index. The boundary conditions for v at the base of the domain and on the axis are enforced in exactly the same way as for A (see equations 4.17 and 4.18). At the stellar surface, the radial derivative of v/r can be expressed using interior values of v in an exactly analogous way to the radial derivative of A (see equation 4.25). Equating this derivative to zero results in an expression for $v_{I-1,j}$. In terms of initial conditions, v is set equal to zero everywhere at the start of each simulation. The checking of this code is deferred until Chapter 6, where it is compared with results from Chapter 5.

4.4.2 A meridional flow

Another feature that can be incorporated into the model is an imposed meridional flow (see, for example, Dikpati and Charbonneau, 1999; Bonanno et al., 2002; Küker et al., 2002). Although meridional motions are neglected in this thesis, it was decided to include this possibility in the numerical code. This extends the range of problems that it can be used to investigate in the future. Apart from anything else, as described below, it provides an additional means of testing the validity of the other aspects of the code. The mean velocity field is now given by

$$\mathbf{u} = u_r(r,\theta)\mathbf{e_r} + u_\theta(r,\theta)\mathbf{e}_\theta + \Omega(r,\theta) r \sin\theta \mathbf{e}_\phi, \tag{4.41}$$

where u_r and u_θ are specified functions of r and θ. With α-quenching as the sole non-linearity, the evolution equations for A and B are given by

$$\begin{aligned} \frac{\partial A}{\partial t} &= \frac{\alpha(r,\theta)B}{1+(B/B_o)^2} - \frac{u_r}{r}\frac{\partial(Ar)}{\partial r} - \frac{u_\theta}{r\sin\theta}\frac{\partial(A\sin\theta)}{\partial\theta} \\ &\quad + \frac{\eta(r)}{r^2}\frac{\partial}{\partial r}\left[r^2\frac{\partial A}{\partial r}\right] + \frac{\eta(r)}{r^2\sin\theta}\frac{\partial}{\partial\theta}\left[\sin\theta\frac{\partial A}{\partial\theta}\right] - \frac{\eta(r)A}{r^2\sin^2\theta} \end{aligned} \tag{4.42}$$

$$
\begin{aligned}
\frac{\partial B}{\partial t} &= \frac{\partial (A\sin\theta)}{\partial \theta}\frac{\partial \Omega}{\partial r} - \frac{\sin\theta}{r}\frac{\partial (Ar)}{\partial r}\frac{\partial \Omega}{\partial \theta} - \frac{1}{r}\frac{\partial (Bru_r)}{\partial r} \\
&\quad -\frac{1}{r}\frac{\partial (Bu_\theta)}{\partial \theta} + \frac{1}{r}\frac{\partial}{\partial r}\left[\eta(r)\frac{\partial (Br)}{\partial r}\right] + \frac{1}{r^2}\frac{\partial}{\partial \theta}\left[\frac{\eta(r)}{\sin\theta}\frac{\partial (B\sin\theta)}{\partial \theta}\right].
\end{aligned} \tag{4.43}
$$

These equations can be non-dimensionalised in the same way as before, making use of the additional scalings

$$
u_r(r,\theta) \rightarrow U_o\tilde{u}_r(\tilde{r},\theta) \qquad u_\theta(r,\theta) \rightarrow U_o\tilde{u}_\theta(\tilde{r},\theta), \tag{4.44}
$$

where U_o is a representative value of the meridional flow. The equations become

$$
\begin{aligned}
\frac{\partial A}{\partial t} &= \frac{\alpha(r,\theta)B}{1+B^2} - R_u\frac{u_r}{r}\frac{\partial (Ar)}{\partial r} - R_u\frac{u_\theta}{r\sin\theta}\frac{\partial (A\sin\theta)}{\partial \theta} \\
&\quad +\frac{\eta(r)}{r^2}\frac{\partial}{\partial r}\left[r^2\frac{\partial A}{\partial r}\right] + \frac{\eta(r)}{r^2\sin\theta}\frac{\partial}{\partial \theta}\left[\sin\theta\frac{\partial A}{\partial \theta}\right] - \frac{\eta(r)A}{r^2\sin^2\theta}
\end{aligned} \tag{4.45}
$$

$$
\begin{aligned}
\frac{\partial B}{\partial t} &= D\frac{\partial (A\sin\theta)}{\partial \theta}\frac{\partial \Omega}{\partial r} - D\frac{\sin\theta}{r}\frac{\partial (Ar)}{\partial r}\frac{\partial \Omega}{\partial \theta} - R_u\frac{1}{r}\frac{\partial (Bru_r)}{\partial r} \\
&\quad -R_u\frac{1}{r}\frac{\partial (Bu_\theta)}{\partial \theta} + \frac{1}{r}\frac{\partial}{\partial r}\left[\eta(r)\frac{\partial (Br)}{\partial r}\right] + \frac{1}{r^2}\frac{\partial}{\partial \theta}\left[\frac{\eta(r)}{\sin\theta}\frac{\partial (B\sin\theta)}{\partial \theta}\right],
\end{aligned} \tag{4.46}
$$

where

$$
R_u = \frac{U_oR_*}{\eta_o} \tag{4.47}
$$

is a magnetic Reynolds number controlling the relative influence of the meridional flow. The new advective terms in the equations require little by way of new numerical techniques. Linear interpolation is used to find expressions for the fluxes at all the necessary grid-points, and the derivatives are then calculated in the usual way.

Since the model of Dikpati and Charbonneau (1999) is very similar to this one, that provides an obvious means of checking this code. I therefore attempted to reproduce their (so-called) reference solution – for details, see Dikpati and Charbonneau (1999) – using my code. A small modification to the code was required in order to restrict the solutions to dipolar symmetry. The qualitative appearance of the solutions obtained agreed with those of Dikpati and Charbonneau, however there was a significant discrepancy in the period of oscillation (about 10%) and a massive discrepancy (approximately 2 orders of magnitude difference) in the peak toroidal fields at the base of the convection zone. I contacted the authors to try to establish the cause for these problems, and I am grateful to both Mausumi Dikpati and Paul Charbonneau for their assistance. We established that there were several typographical errors in the paper which had a major bearing upon the results. Most importantly, the parameter controlling the strength of the α-quenching is actually 500G rather than 10^5G, which is the value quoted in the paper. This explains (at least in part) the significant discrepancy in the peak toroidal fields.

Given that there were still uncertainties concerning some of the details of the model, we carried out a set of detailed checks involving my code and Paul Charbonneau's code. For these simulations, the meridional circulation was taken to have the same form as that used by Dikpati and Charbonneau (1999) apart from the fact that it is taken to close at the base of the convection zone ($r = 0.7$) rather than at the base of the computational domain. The components of this meridional flow are given by

$$\begin{aligned} u_r(r,\theta) &= \left(\frac{2}{r^2}\right)\left[-\frac{2}{3}\zeta + \frac{c_1}{2}\zeta^{1.5} - \frac{4c_2}{9}\zeta^{1.75}\right]\left(2\cos^2\theta - \sin^2\theta\right) \\ u_\theta(r,\theta) &= \left(\frac{2}{r^3}\right)\left[-1 + c_1\zeta^{0.5} - c_2\zeta^{0.75}\right]\sin\theta\cos\theta, \end{aligned} \tag{4.48}$$

where

$$\zeta(r) = \frac{1}{r} - 1, \tag{4.49}$$

and, defining $\zeta_b = \zeta(0.7)$,

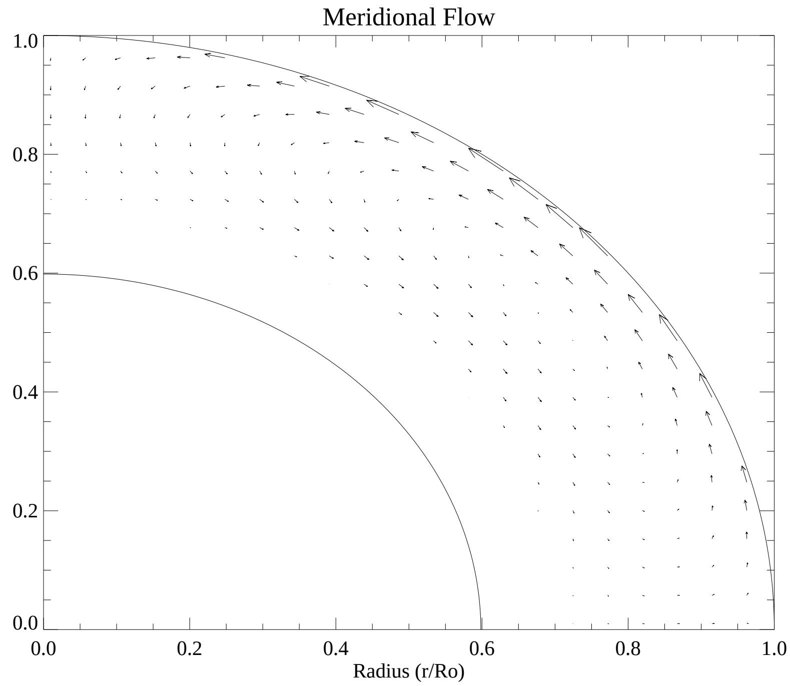

Figure 4.4: Flow vectors for the imposed meridional circulation. The arrows indicate the magnitude and direction of the flow in the northern hemisphere.

$$c_1 = 4\zeta_b^{-0.5} \quad \text{and} \quad c_2 = 3\zeta_b^{-0.75}. \tag{4.50}$$

This corresponds to a meridional flow which consists of a single cell in each hemisphere: the flow is polewards at the surface (normalised so that the maximum flow speed, occurring at $\theta = \pi/4$, is equal to unity) and equatorwards at the base of the convection zone. The details of the meridional flow at the base of the convection zone are unknown, but this prescribed velocity field is certainly plausible. Figure 4.4 shows the meridional flow vectors in the region of computation.

All other input parameters to this model are identical to those described in Dikpati and Charbonneau (1999), but (for completeness) it is worth briefly summarising them here. This Babcock-Leighton model has a modified α-term, which is assumed to be

	Charbonneau's values	Values from this code
Period of oscillation (years)	47.7	47.5
Peak toroidal field at $r = 0.7$ (KG)	45.3	44.4
Peak radial field at $r = 1.0$ (KG)	13.0	13.6

Table 4.3: A comparison between the two codes. These values have been quoted in terms of physical values. The scalings used to convert these values from the non-dimensional quantities are identical to those described by Dikpati and Charbonneau (1999), apart from the α-quenching parameter, which is set at 5.0×10^3G.

due to the decay of active regions. The active regions are surface manifestations of the toroidal field at the base of the convection zone, so this source term is taken to be non-local in B. The term proportional to $\alpha(r, \theta)$, that appears in equation (4.45), is replaced by $S(r, \theta, B)$, which is defined by

$$\begin{aligned} S(r,\theta,B) &= \frac{1}{2}\left[1+\Phi\left(\frac{r-0.95}{0.01}\right)\right]\left[1-\Phi\left(\frac{r-1.0}{0.01}\right)\right]\sin\theta\cos\theta \\ &\quad \times\frac{B(0.7,\theta,t)}{1+B(0.7,\theta,t)^2} \end{aligned} \tag{4.51}$$

where Φ is the standard error function, and $B(0.7, \theta, t)$ corresponds to B at the base of the convection zone. The profiles for the differential rotation and magnetic diffusivity are very similar to those given by equation (4.26), with η_c taken to be 0.02 and the base of the convection zone taken to be at $r = 0.7$.

The results from a high resolution (128 odd radial grid-points and 96 odd latitudinal points in the hemispherical domain) comparison are shown in Figure 4.5. This suggests that these codes are giving very similar results. A comparison of some global quantities is given in Table 4.3. All the values match up to within a few percent. This is a convincing validation of all aspects of the code, including the radial shear term that caused the

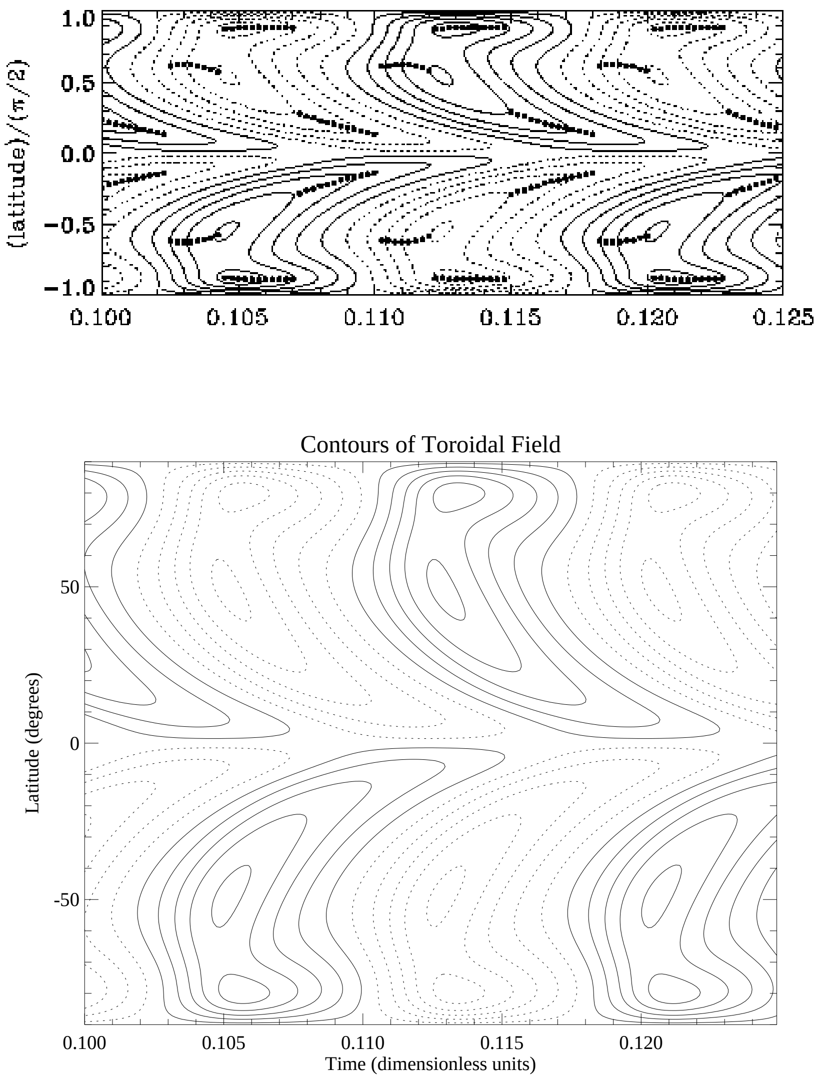

Figure 4.5: Contours of toroidal field at $r = 0.7$, plotted against latitude and time. The top plot shows results from Paul Charbonneau's code, the lower plot is produced by my code. The solid dots on the top plot indicate the location of the peak field. Contour spacings are the same in each plot, with solid contours corresponding to positive values of B and dashed contours corresponding to negative values.

discrepancy with Markiel's code. Given that the source of the poloidal field is near the surface in this Babcock-Leighton model, we might expect the radial field there to be particularly sensitive to the boundary conditions used. Another simulation was carried out using a Markiel-like implementation of the potential field condition, and this produced a marked increase (of about 11%) in the peak surface radial field. This discrepancy is presumably due to the fact that Markiel's method does not completely ensure that the radial derivative of A is continuous at the surface. So, whilst this method seems to be perfectly adequate for interface dynamos, it will lead to inaccuracies in a model of this type.

In principle, it is possible to combine a meridional flow with the macrodynamic non-linearity that was described in the previous section. Equations (4.35) and (4.36) must be modified, as described above, to include the advection terms. Additional advection terms are also required in the equation governing the velocity perturbation. Equation (4.37) therefore becomes

$$\begin{aligned}\frac{\partial v}{\partial t} = {} & \frac{\mathrm{sign}(D)}{r^2\sin\theta\rho(r)}\left[\frac{\partial(A\sin\theta)}{\partial\theta}\frac{\partial(Br)}{\partial r}-\frac{\partial(B\sin\theta)}{\partial\theta}\frac{\partial(Ar)}{\partial r}\right] \\ & -R_u\frac{u_r}{r}\frac{\partial(vr)}{\partial r}-R_u\frac{u_\theta}{r\sin\theta}\frac{\partial(v\sin\theta)}{\partial\theta}+\frac{\tau r}{\rho(r)}\frac{\partial(\rho\eta)}{\partial r}\frac{\partial}{\partial r}\left[\frac{v}{r}\right] \\ & +\frac{\tau\eta(r)}{r^2}\frac{\partial}{\partial r}\left[r^2\frac{\partial v}{\partial r}\right]+\frac{\tau\eta(r)}{r^2\sin\theta}\frac{\partial}{\partial\theta}\left[\sin\theta\frac{\partial v}{\partial\theta}\right]-\frac{\tau\eta(r)v}{r^2\sin^2\theta}.\end{aligned} \tag{4.52}$$

This combined model takes no account of any back-reaction of the magnetic field on the meridional flow. Whilst this could be regarded as being inconsistent, the precise nature of the returning flow around the base of the convection zone in the Sun is very poorly understood. The effects of compressibility should lead to the returning flow being weaker at the base of the convection zone than it is at the surface, but there are no reliable observations to support this idea (see Section 1.3.3). It therefore seems unnecessary to further complicate the model by allowing feedback on an already poorly determined meridional flow.

4.4.3 $\alpha^2\omega$ dynamo models

So far, all the dynamo models in this chapter have been of $\alpha\omega$ type. In the case of the Sun, the presence of strong differential rotation makes this a natural approximation to use. Other stars may have weaker differential rotation, and may therefore require the solution of the full $\alpha^2\omega$ equations. The evolution equations for a system of this type are given by

$$\begin{aligned}\frac{\partial A}{\partial t} &= \frac{\alpha(r,\theta)B}{1+(|\mathbf{B}|/B_o)^2} + \frac{\eta(r)}{r^2}\frac{\partial}{\partial r}\left[r^2\frac{\partial A}{\partial r}\right] + \frac{\eta(r)}{r^2\sin\theta}\frac{\partial}{\partial\theta}\left[\sin\theta\frac{\partial A}{\partial\theta}\right] \\ &\quad -\frac{\eta(r)A}{r^2\sin^2\theta}\end{aligned} \tag{4.53}$$

$$\begin{aligned}\frac{\partial B}{\partial t} &= \frac{\partial(A\sin\theta)}{\partial\theta}\frac{\partial\Omega}{\partial r} - \frac{\sin\theta}{r}\frac{\partial(Ar)}{\partial r}\frac{\partial\Omega}{\partial\theta} - \frac{1}{r}\frac{\partial}{\partial r}\left[\frac{\alpha(r,\theta)}{1+[|\mathbf{B}|/B_o]^2}\frac{\partial(Ar)}{\partial r}\right] \\ &\quad -\frac{1}{r^2}\frac{\partial}{\partial\theta}\left[\frac{\alpha(r,\theta)}{\sin\theta(1+[|\mathbf{B}|/B_o]^2)}\frac{\partial(A\sin\theta)}{\partial\theta}\right] + \frac{1}{r}\frac{\partial}{\partial r}\left[\eta(r)\frac{\partial(Br)}{\partial r}\right] \\ &\quad +\frac{1}{r^2}\frac{\partial}{\partial\theta}\left[\frac{\eta(r)}{\sin\theta}\frac{\partial(B\sin\theta)}{\partial\theta}\right].\end{aligned} \tag{4.54}$$

Two modifications have been made to equations (4.5) and (4.6). The main modification is the inclusion of the α-terms in the B equation, but also the α-quenching terms have been changed so that quenching is now dependent upon $|\mathbf{B}|$ (the magnitude of the total magnetic field, as a function of r and θ) rather than B. In an $\alpha^2\omega$ model, the poloidal components of the magnetic field are likely to be comparable in magnitude to the toroidal component, so the α-quenching must be adjusted to reflect this.

These equations can be non-dimensionalised using scalings that are virtually identical to those given by equation (4.4), apart from the scaling used for A, which is given by

$$A \rightarrow B_o R_* \tilde{A}. \tag{4.55}$$

The equations now become

$$\frac{\partial A}{\partial t} = R_\alpha \frac{\alpha(r,\theta)B}{1+|\mathbf{B}|^2} + \frac{\eta(r)}{r^2}\frac{\partial}{\partial r}\left[r^2\frac{\partial A}{\partial r}\right] + \frac{\eta(r)}{r^2\sin\theta}\frac{\partial}{\partial\theta}\left[\sin\theta\frac{\partial A}{\partial\theta}\right] - \frac{\eta(r)A}{r^2\sin^2\theta} \tag{4.56}$$

$$\begin{aligned}\frac{\partial B}{\partial t} = {} & R_\omega \frac{\partial(A\sin\theta)}{\partial\theta}\frac{\partial\Omega}{\partial r} - R_\omega\frac{\sin\theta}{r}\frac{\partial(Ar)}{\partial r}\frac{\partial\Omega}{\partial\theta} \\ & -R_\alpha\frac{1}{r}\frac{\partial}{\partial r}\left[\frac{\alpha(r,\theta)}{1+|\mathbf{B}|^2}\frac{\partial(Ar)}{\partial r}\right] - R_\alpha\frac{1}{r^2}\frac{\partial}{\partial\theta}\left[\frac{\alpha(r,\theta)}{\sin\theta(1+|\mathbf{B}|^2)}\frac{\partial(A\sin\theta)}{\partial\theta}\right] \\ & +\frac{1}{r}\frac{\partial}{\partial r}\left[\eta(r)\frac{\partial(Br)}{\partial r}\right] + \frac{1}{r^2}\frac{\partial}{\partial\theta}\left[\frac{\eta(r)}{\sin\theta}\frac{\partial(B\sin\theta)}{\partial\theta}\right].\end{aligned} \tag{4.57}$$

The non-dimensional parameters here are given by

$$R_\alpha = \frac{\alpha_o R_*}{\eta_o} \quad \text{and} \quad R_\omega = \frac{\Omega_o R_*^2}{\eta_o}. \tag{4.58}$$

In the $\alpha\omega$ problem, it was possible to write $D = R_\alpha R_\omega$ to eliminate one of these parameters via a rescaling of A, however that is not possible here. This model required a slight extension to the code that was used for the original model.

This is the final dynamo model that has been derived as an extension of the basic model. Having described these models and the techniques used in their numerical simulation, we are now in a position to apply them to solar and stellar dynamos.

Chapter 5

The Solar Dynamo

The previous chapter described, in general terms, the way in which mean-field dynamo theory can be used to model stellar dynamos numerically. This chapter is concerned with the application of these ideas to the solar dynamo. As discussed in Chapter 2, the solar dynamo has already been the subject of several studies, most of which select specific input profiles for $\alpha(r,\theta)$, $\Omega(r,\theta)$ and $\eta(r)$ and then vary the dynamo number. Helioseismological observations provide us with information regarding the solar differential rotation profile (see Section 1.3.1), so the spatial dependence of $\Omega(r,\theta)$ is relatively well-determined. There is rather more uncertainty surrounding the spatial dependence of $\alpha(r,\theta)$ and $\eta(r)$. The aim of this chapter is to carry out a survey of the solar dynamo, with particular reference to its dependence upon the functional forms of $\alpha(r,\theta)$ and $\eta(r)$. It is found that the most solar-like solutions are obtained for an α-effect that is confined to the base of the convection zone and is also suitably truncated at the poles. For negative values of the dynamo number it is possible to find solutions that are of approximately dipolar symmetry, the dominant feature of which is a low-latitude oscillatory band of magnetic activity, which migrates equatorwards as the cycle progresses. This survey forms an important foundation for the more ambitious models which are described in the next chapter.

5.1 The solar model

The computational domain for a solar dynamo calculation is shown, in the previous chapter, in Figure 4.1. The domain stretches from pole to pole ($0 \leq \theta \leq \pi$), so the dynamo is free to select its own parity. The inner radius of the computational domain (r_{in}) is taken to be at $r = 0.6$, so the radial extent of the domain is given by $0.6 \leq r \leq 1.0$. In the Sun, we know that the base of the convection zone occurs at around $r = 0.7$ – this will need to be taken into account when formulating input profiles for $\Omega(r, \theta)$, $\alpha(r, \theta)$ and $\eta(r)$. This computational domain will be used for all the solar dynamo calculations that are described in this thesis.

The functional form for the analytic fit to the solar rotation profile is virtually the same as that used by Markiel (1999) – almost identical profiles have also been used in several other solar dynamo studies (see, for example, Charbonneau and MacGregor, 1997; Dikpati and Charbonneau, 1999; Ossendrijver, 2000). The characteristic angular velocity, used for the non-dimensionalisation, is taken to be the surface angular velocity at the equator. So, the non-dimensional profile for $\Omega(r, \theta)$ is given by

$$\Omega(r, \theta) = \Omega_c + \frac{1}{2}\left[1 + \Phi\left(\frac{r - 0.7}{0.025}\right)\right]\left(P - Q\cos^2\theta - R\cos^4\theta\right), \tag{5.1}$$

where Φ represents the standard error function, $P = 0.0571$, $Q = 0.123$, $R = 0.155$ and $\Omega_c = 0.943$. These parameters are chosen in such a way as to accurately reflect the surface differential rotation on the Sun, with the polar regions rotating slower than the equatorial regions. The core is assumed to rotating rigidly at some intermediate rate, ie. faster than the poles, but slower than the equator. This functional form for $\Omega(r, \theta)$ leads to a "tachocline"-like region at the base of the convection zone. This region is the site of a layer of strong radial shear, which is negative at high latitudes and positive at low latitudes. Contours of constant angular velocity are shown in Figure 5.1. A comparison of this analytic function with the profile shown in Figure 1.4 indicates good agreement

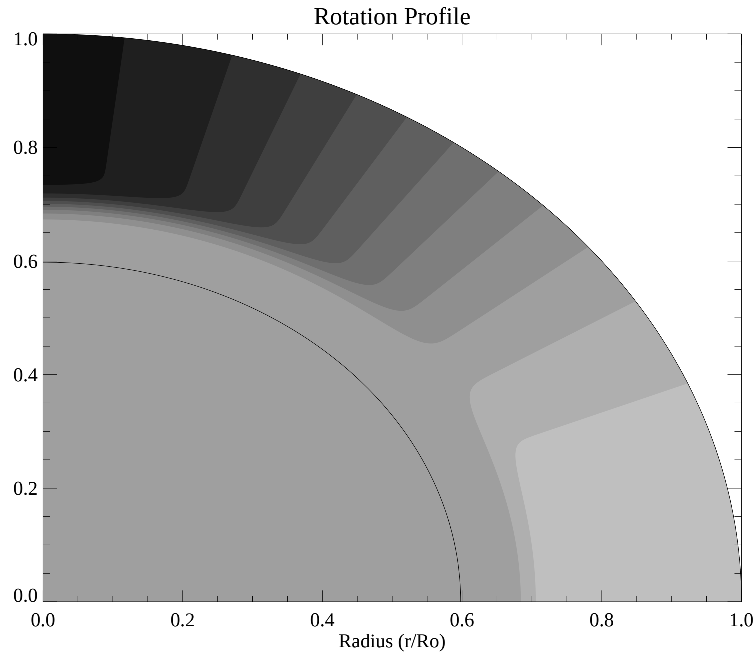

Figure 5.1: An analytic fit to the solar rotation profile. This plot shows evenly spaced contours of constant angular velocity, where darker shades of grey correspond to slower rotation rates. Only the northern hemisphere is shown here – this profile is symmetric about the equator.

with the helioseismological inversion.

Whilst the differential rotation profile is fairly well determined, we know far less about the spatial dependence of the magnetic diffusivity. For $0.7 \leq r \leq 1.0$, the effects of turbulence within the convection zone should lead to an enhancement of the magnetic diffusivity in that region. We would expect lower values of the magnetic diffusivity below the turbulent region, with some transition region at the base of the convection zone. Markiel (1999) investigated two cases: one where the transition region was very thin (20% of the width of the tachocline), and one which had a thicker transition region (of a similar width to the tachocline). Markiel found that the thin transition region seemed to favour steady modes for negative values of the dynamo number (or, alternatively, negative values of the α-effect in the northern hemisphere), whilst oscillatory interface modes were found, for a certain range of the parameters, for the thicker transition region. Markiel and Thomas (1999) demonstrated, using numerical techniques, that it is the latitudinal shear that is responsible for the generation of these steady modes and the radial shear that is responsible for the interface modes.

Markiel and Thomas also explain this behaviour using a simple physical argument based upon loops of poloidal magnetic field diffusing radially inwards through the base of the convection zone. A sharp decrease in the magnetic diffusivity implies that the base of the loop very rapidly enters a region of low magnetic diffusivity. The base of this loop will, therefore, not readily penetrate far below the interface. This leads to the build-up of poloidal magnetic field, with a strong latitudinal component, just below the base of the convection zone. The action of the radial shear, on the radial components of the loop, will lead to the production of toroidal field of opposite signs at opposite ends of the loop. As this toroidal field diffuses back into the convection zone, the α-effect then produces poloidal magnetic field of opposite senses at each end of the loop. This leads to flux cancelling with the original poloidal field, at one end of the loop, and poloidal field reinforcement at the other. This causes migration of the magnetic field, and explains how oscillatory activity arises in an interface dynamo. By contrast, the latitudinal shear, acting upon the strong latitudinal component of the poloidal field, produces toroidal field of only one sign (since only the lower portion of the loop penetrates below the base of the convection zone). When this diffuses back into the convection zone, the α-effect will produce poloidal field of only one sense and this will either cancel with the existing field (leading to overall decay) or reinforce it (leading to a steady mode). This solar rotation profile, coupled with a negative value of the α-effect in the northern hemisphere, provides the correct conditions for reinforcement, which leads to a steady mode (Markiel and Thomas, 1999). These steady modes are unlikely to be suppressed by the correction of the (probably) erroneous factor of 2 in Markiel's model (see Section 4.3.2): correcting this would only enhance the effects of the latitudinal shear. Because a thicker transition region represents a more gradual transition, the latitudinal component of the poloidal field will be less intense around the base of the convection zone. This will reduce the influence of the latitudinal shear, thus reducing the possibility of a steady mode swamping the oscillatory interface modes. It is mainly for this reason that a thicker transition region for the magnetic diffusivity is adopted in the simulations that are described below.

The magnetic diffusivity profile is given by

$$\eta(r) = \left(\frac{1-\eta_c}{2}\right)\left[1+\Phi\left(\frac{r-0.7}{0.025}\right)\right]+\eta_c, \tag{5.2}$$

where η_c is the ratio of the magnetic diffusivity at the inner radius of the domain to the magnetic diffusivity within the convection zone. A similar functional form for $\eta(r)$ has been used in numerous existing dynamo models (see, for example, Dikpati and Charbonneau, 1999; Ossendrijver, 2000; Küker et al., 2002). It actually differs slightly from that of Markiel – in his profile there is a small discontinuity in the radial derivative of $\eta(r)$, although the effects of such a discontinuity are negligible in the finite differencing approximation. Typically in these calculations, $\eta_c = 0.01$. The smaller the value of η_c, the harder it will be for magnetic flux to diffuse radially inwards below the base of the convection zone. This will enhance the latitudinal component of the poloidal field, below the interface, which (as discussed above) may lead to steady modes. It is therefore important to vary the value of η_c in these simulations in order to determine the sensitivity of the dynamo model to the precise value used. The magnetic diffusivity profile is shown in Figure 5.2.

The functional form for $\alpha(r,\theta)$ is even less certain, and part of the aim of this chapter is to assess the influence that different forms for $\alpha(r,\theta)$ have upon the dynamo. Standard mean-field dynamo theory would suggest that an α-effect that is driven by turbulent convection should be distributed throughout the convection zone. A suitable profile for this form of the α-effect is

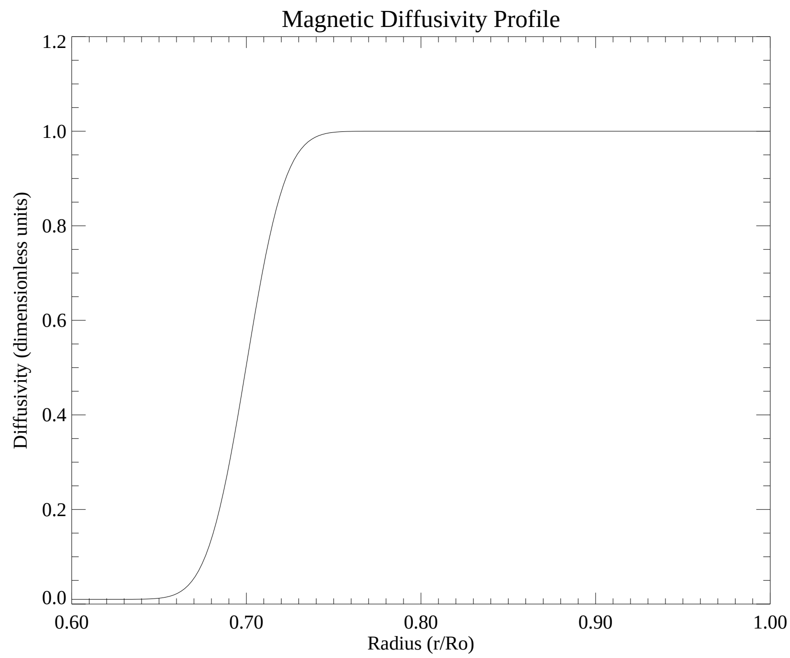

Figure 5.2: The dependence of the magnetic diffusivity upon radius.

$$\alpha(r,\theta) = \frac{1}{2}\left[1 + \Phi\left(\frac{r-0.7}{0.025}\right)\right]\cos\theta. \tag{5.3}$$

The $\cos\theta$ dependence reflects that fact that the twisting motion that occurs as a consequence of the Coriolis force should be antisymmetric about the equator, and it is also expected to be strongest at the poles. This α-profile is shown in Figure 5.3. As discussed in Section 2.4.3, there is evidence to suggest that an α-effect that is driven by turbulent convection may change sign within the convection zone. This may have an important effect upon the operation of the dynamo, however only the simple case that is shown in Figure 5.3 is considered here.

Other possible mechanisms for an α-effect were discussed in Section 2.4.3. One possibility is an α-effect that is concentrated at the solar surface. Mason et al. (2002) showed that, in the absence of a meridional flow, an α-effect that is operating at the surface is

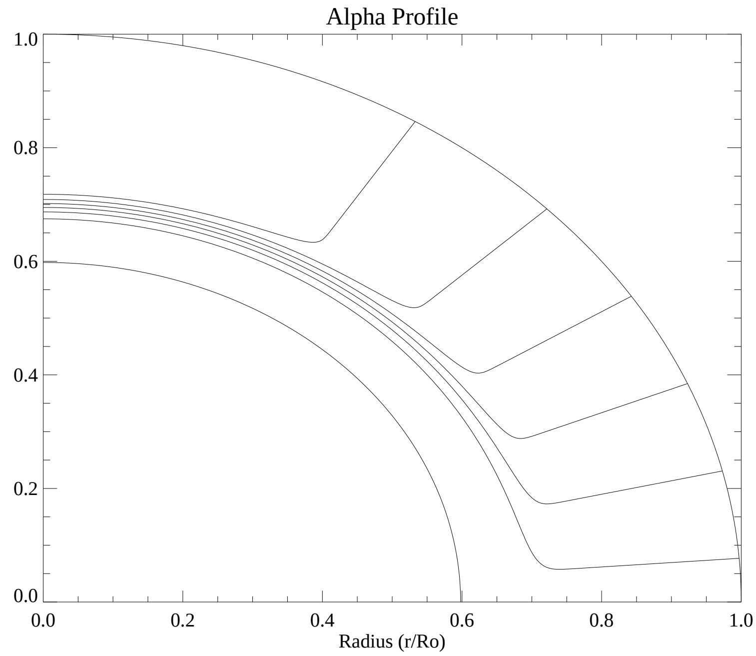

Figure 5.3: Contours of constant $\alpha(r,\theta)$ for an α-effect that is operating throughout the convection zone. Only the northern hemisphere is shown here – α is antisymmetric about the equator.

rendered insignificant if another form of the α-effect is operating within deeper regions of the convection zone, even if the deeper-lying α-effect is much smaller than that operating at the surface. The possibility of a surface α-effect is therefore ignored here. The only other (obvious) possible location for an α-effect is the region around the tachocline. Section 2.4.3 discussed how a mechanism such as magnetic buoyancy could lead to an α-effect concentrated around this region. An appropriate functional form for an α-effect of this type is

$$\alpha(r,\theta) = f(\theta)\exp\left[-\left(\frac{r-r_\alpha}{0.025}\right)^2\right], \tag{5.4}$$

where $r_\alpha \in [0.7, 0.75]$ is a parameter that can be varied in order to adjust the overlap between the α layer and the shear layer. The width of this α layer is taken to be the same as that of the tachocline. Three different functional forms have been adopted for $f(\theta)$, all of which preserve the antisymmetry of $\alpha(r,\theta)$ about the equator:

$$f(\theta) = \cos\theta\,, \quad \cos\theta\sin^2\theta \quad \text{or} \quad \cos\theta\sin^4\theta. \tag{5.5}$$

Similar functional dependencies upon θ have been used by, for example, Rüdiger and Brandenburg (1995), Moss and Brooke (2000) and Covas et al. (2001b). Markiel (1999) adopted a similar radial distribution for $\alpha(r,\theta)$, to that given in equation (5.4), although he restricted attention purely to situations where the α-effect was either strongest at the poles, with $f(\theta) = \cos\theta$, or was very heavily restricted to low latitudes. His low-latitude α-effect was confined to low latitudes by a gaussian function of latitude, which represented a more severe high-latitude "cut off" than any of profiles that are given in equation (5.5). The latitudinal dependence of an α-effect that is driven by (for example) magnetic buoyancy is very difficult to establish. As discussed in Section 2.4.3, it is possible that the strong shear in the tachocline (particularly at high latitudes) may suppress the non-axisymmetric buoyancy instability. This implies that this form of the α-effect may well be reduced at high latitudes rather than being strongest at the poles. An example of an α-effect of this form is shown in Figure 5.4.

In this survey, the dynamo model that is used is the basic $\alpha\omega$ model that was described in Section 4.1. There is therefore no meridional flow, and the sole nonlinearity is taken to be due to α-quenching. How an α-effect will react to a strong field will depend upon the physical mechanism that is responsible for driving it. A strong field will suppress an α-effect that is driven by convective turbulence, whilst a buoyantly-driven α-effect actually requires a strong field in order to operate (although if the field is too strong, the flux will presumably buoyantly rise out of the dynamo region before it can twist and contribute towards an α-effect). For simplicity, it is assumed here that regardless of the physical mechanisms that are involved, there exists some magnetic field

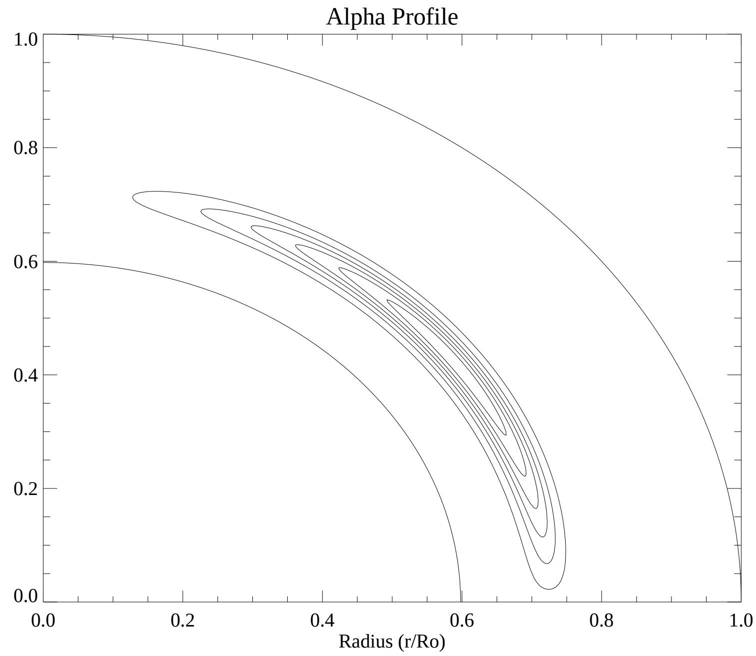

Figure 5.4: Contours of constant $\alpha(r,\theta)$ for an α-effect that is restricted to the base of the convection zone, $f(\theta) = \cos\theta \sin^2\theta$. Only the northern hemisphere is shown here – α is antisymmetric about the equator.

strength which will lead to the suppression of the α-effect. As discussed in Section 2.3.3, there is still a certain amount of controversy surrounding the issue of whether or not a turbulent α-effect is suppressed by a substantially sub-equipartition-strength magnetic field. This problem has been addressed by Charbonneau and MacGregor (1996), who showed that a strongly quenched α-effect is capable of producing equipartition-strength magnetic fields in an idealised-interface model. The simple parameterisation that has been used should be regarded as a convenient means of limiting the growth of the dynamo in the nonlinear regime. For ease of reference, the equations (which were described in the previous chapter) are reproduced here:

$$\frac{\partial A}{\partial t} = \frac{\alpha(r,\theta)B}{1+B^2} + \frac{\eta(r)}{r^2}\frac{\partial}{\partial r}\left[r^2\frac{\partial A}{\partial r}\right] + \frac{\eta(r)}{r^2\sin\theta}\frac{\partial}{\partial\theta}\left[\sin\theta\frac{\partial A}{\partial\theta}\right] - \frac{\eta(r)A}{r^2\sin^2\theta} \tag{5.6}$$

$$\frac{\partial B}{\partial t} = D\frac{\partial(A\sin\theta)}{\partial\theta}\frac{\partial\Omega}{\partial r} - D\frac{\sin\theta}{r}\frac{\partial(Ar)}{\partial r}\frac{\partial\Omega}{\partial\theta} + \frac{1}{r}\frac{\partial}{\partial r}\left[\eta(r)\frac{\partial(Br)}{\partial r}\right] + \frac{1}{r^2}\frac{\partial}{\partial\theta}\left[\frac{\eta(r)}{\sin\theta}\frac{\partial(B\sin\theta)}{\partial\theta}\right]. \tag{5.7}$$

The boundary conditions for this model are described in Chapter 4: $A = B = 0$ at $r = 0.6$, $\theta = 0$ and $\theta = \pi$; at $r = 1.0$, $B = 0$ and A matches smoothly onto a potential field.

At this stage, it is worth considering how this dynamo model fits in with those studied previously. With the exception of Markiel (1999), previous investigations using a dynamo model of this form either impose dipolar symmetry upon the model (see, for example, Prautzsch, 1993; Rüdiger and Brandenburg, 1995; Ossendrijver, 2000) or treat the base of the convection zone as an idealised interface between regions of high and low magnetic diffusivity (Charbonneau and MacGregor, 1996, 1997; Markiel and Thomas, 1999). In the simulations that are described below, no restriction is placed upon the parity of the dynamo and there are no discontinuities in the magnetic diffusivity profile. As the only existing model of a similar type, many of the details of this model are closely related to that of Markiel (1999). In terms of the equations, the only significant difference is in the α-quenching parameterisation: most of Markiel's calculations used a more severe $\exp(-B^2)$ dependence on B, rather than $1/(1+B^2)$. The similarities and differences between the two models for the input profiles for $\Omega(r,\theta)$, $\eta(r)$ and $\alpha(r,\theta)$ have been discussed above. In terms of the α-profile, it is only in Section 5.2.2 that there is significant qualitative overlap between this survey and that of Markiel (1999), although there are other important quantitative differences between the two models.

This slight overlap was intentional given that the calculations that were carried out by Markiel are affected by a possible error in the analytic fit to the radial shear profile, as discussed in Section 4.3.2. Since this erroneous factor of 2 affects the radial shear but not the latitudinal shear terms, it cannot be scaled out of the equations, so it may alter both the quantitative and the qualitative behaviour of the dynamo. It therefore seems worthwhile to revisit an α-effect of this form in order to investigate the influence that this problem may have had upon the behaviour of the dynamo. All other forms for the α-effect are different, in either their latitudinal or radial distribution, to those considered by Markiel.

In the next section, this model is used to carry out a detailed survey of the solar dynamo. Various aspects of the model are varied in order to identify all the key patterns of behaviour. Bearing in mind the results of the resolution checks (given in Table 4.2), preliminary simulations were carried out using a resolution of 101 (uniformly distributed) radial and 97 latitudinal grid-points (101x97) in order to survey a wide range of parameter space. Higher resolution (101x193) simulations were then carried out for the regions of interest. The code is designed so as to periodically produce snapshots of the spatial distribution of the magnetic field, as well as plots showing the time evolution of the toroidal field at constant radius or latitude. The level of magnetic activity in the system can be monitored by evaluating

$$E = \int \left(B^2 + \frac{1}{r^2} \left[\frac{\partial (Ar)}{\partial r} \right]^2 + \frac{1}{r^2 \sin^2\theta} \left[\frac{\partial (A \sin\theta)}{\partial \theta} \right]^2 \right) \mathrm{d}V, \tag{5.8}$$

where the integral is taken over the whole computational domain. Finally, some measure of the asymmetry in the model can be obtained by monitoring the parity, P, which is defined by

$$P = \frac{E_q - E_d}{E_q + E_d}, \tag{5.9}$$

where E_d and E_q are the magnetic energies associated with (respectively) the dipolar

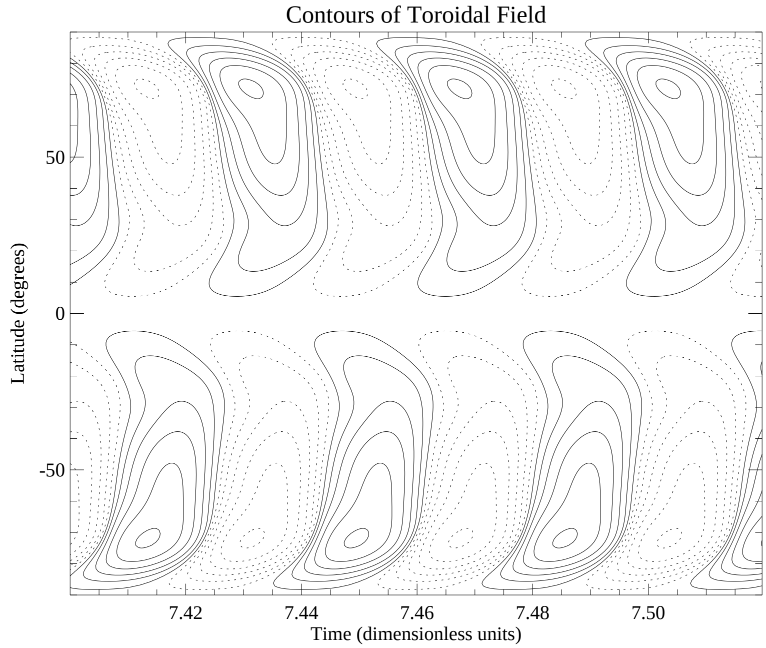

Figure 5.5: Contours of constant toroidal field, plotted against latitude and time, at the base of the convection zone ($r = 0.7$), for the distributed α-effect. Contours are equally spaced, solid lines correspond to positive values of B, dashed lines correspond to negative values. $D = 4.0 \times 10^5$.

and quadrupolar components of the magnetic field. With this definition, a purely dipolar field has $P = -1$ and a purely quadrupolar field has $P = 1$. Although the time-evolution of E and P is not discussed in any detail in this chapter, the analysis of these quantities provides the simplest means of determining whether or not the solution has properly converged.

5.2 A survey of the solar dynamo

5.2.1 A distributed α-effect

The initial set of simulations were carried out using an α-effect that is distributed throughout the convection zone, ie. $\alpha(r, \theta)$ is given by equation (5.3). The ratio of magnetic diffusivities, η_c, is set equal to 0.01. For positive values of the dynamo number, oscillatory behaviour is found for $D \gtrsim 1.0 \times 10^5$. For a survey of this form, it is not necessary to accurately determine the values of the critical dynamo numbers, however it is important (for comparative purposes) to know approximately what these values are. Figure 5.5 shows contours of constant toroidal field for $D = 4.0 \times 10^5$, plotted against latitude and time, at the base of the convection zone ($r = 0.7$). The bulk of the magnetic activity is at high latitudes, and the symmetry of this solution is dipolar. Driven by the radial shear at the base of the convection zone, the toroidal field at the base of the convection zone propagates equatorwards at high latitudes and polewards at low latitudes.

Figure 5.6 shows the distribution of toroidal magnetic field as a function of radius and time. This plot clearly shows that the toroidal field does not penetrate far into the region of low magnetic diffusivity, below the base of the convection zone. It also demonstrates that the bulk of the convection zone is occupied by toroidal field, and that it appears to be propagating radially outwards. Radial propagation of this form is driven by the strong latitudinal shear within the convection zone – the radial propagation follows lines of constant angular velocity. This process is analogous to the latitudinal propagation driven by the radial shear in an oscillatory interface mode. For all negative values of D, steady modes are found. As described in the previous section, such modes are driven by the latitudinal shear. The symmetry of these modes is dependent upon the precise choice of D, however dipolar symmetry seems to be (on the whole) preferred. The solution shown in Figure 5.7 is the negative D analogue to Figure 5.5.

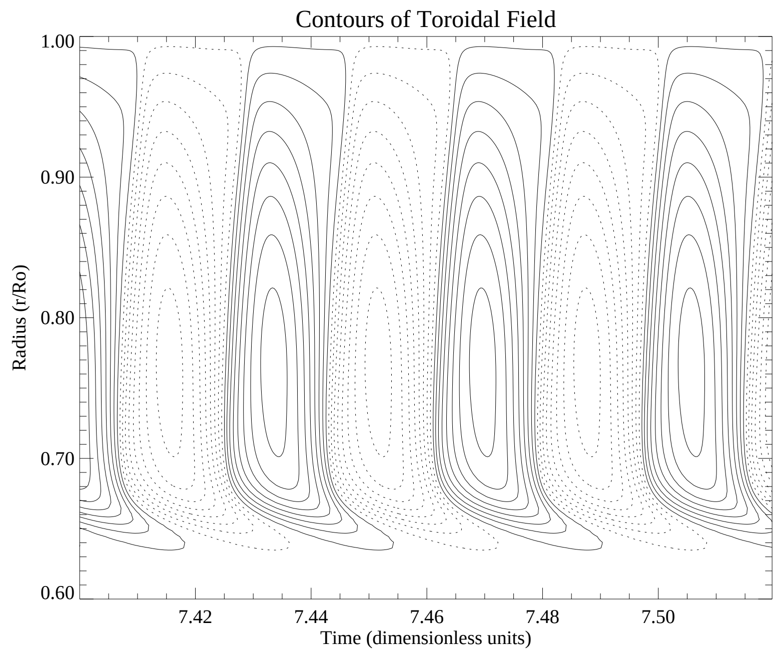

Figure 5.6: Contours of constant toroidal field, plotted against radius and time, at 60° latitude, for the distributed α-effect. Contours are equally spaced, solid lines correspond to positive values of B, dashed lines correspond to negative values. $D = 4.0 \times 10^5$.

In order to verify that these results are robust to small changes in the model parameters, several other simulations were carried out. Firstly, η_c was varied away from 0.01 (values of 0.1 and 1.0×10^{-4} were used), and it was found that the solutions are qualitatively insensitive to these variations. Also, the centre of the α-effect transition region was moved from $r = 0.7$ (which was the value given in equation 5.3) to $r = 0.75$. Although this resulted in slightly larger critical dynamo numbers, the qualitative forms of the solutions were unaltered. Although few details were supplied, Prautzsch (1993) seemed to find similar patterns of behaviour in his model. These results strongly suggest that a model with a distributed α-effect is incapable of producing solutions that match up to the observed properties of the solar magnetic cycle. For negative values of the dynamo number, no oscillatory solutions are found. For positive values, oscillatory solu-

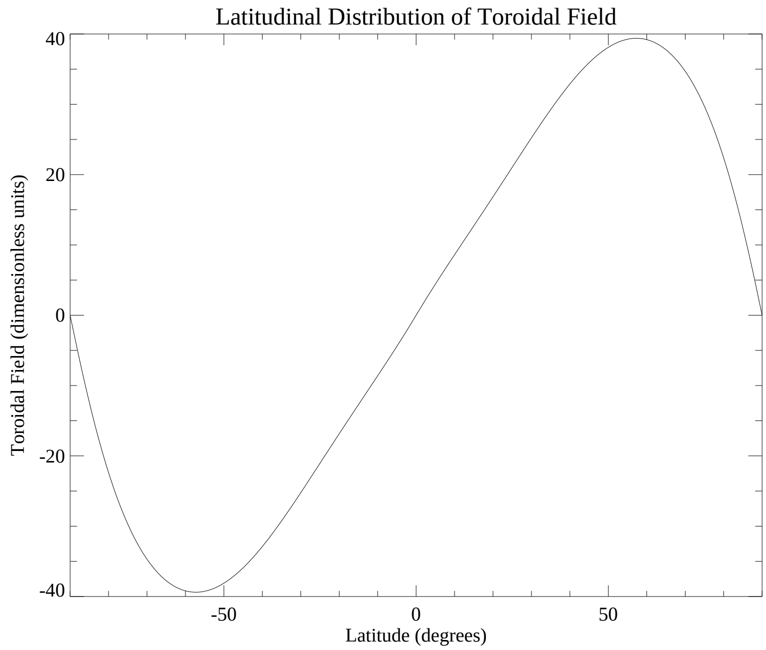

Figure 5.7: A dipolar steady mode. This shows the variation of toroidal field with latitude, at the base of the convection zone ($r = 0.7$), for a distributed α-effect. $D = -4.0 \times 10^5$.

tions are found, however they are dominated by high-latitude features, and the direction of propagation of any low-latitude features is polewards rather than equatorwards. This is totally inconsistent with the magnetic activity that is observed on the Sun.

5.2.2 An α-effect confined to the base of the convection zone

The results described above would appear to rule out the possibility of a distributed α-effect. It is therefore important to establish whether or not an α-effect that is confined to the base of the convection zone is capable of producing solutions that more closely resemble the solar magnetic cycle. In the simulations that are described below, the α-effect is represented by the expression given by equation (5.4). By varying the parameter

r_α, and the function $f(\theta)$, it is possible to carry out a wide-ranging survey of dynamo models of this type.

Initially, attention is restricted to the case where $f(\theta) = \cos\theta$. Markiel (1999) investigated a similar functional form for α, so this should be a useful comparison. Given the probable error in the form of Markiel's analytic radial shear profile, and the fact that there are several differences in the details of the model, we would expect there to be quantitative differences in the results, however there ought to be some qualitative similarities in the solutions that are obtained. The parameter r_α is first set equal to 0.725 – this represents a 50% overlap between the α layer and the tachocline region. The value of the magnetic diffusivity ratio, η_c, is initially taken to be 0.01. All of Markiel's calculations used an very small value for η_c (1.0×10^{-4}) so, for the purposes of comparison, it will be necessary to investigate the sensitivity of the solutions to variations in this ratio of diffusivities. Markiel's definition of the dynamo number differs from that used here, although (effectively) similar ranges of values are investigated in the two surveys.

For negative values of D, for this initial set of parameters, the critical dynamo number is approximately -4.0×10^5. This critical value is significantly larger than that found for the case where the α-effect is distributed throughout the convection zone. Given that $\alpha(r, \theta)$ is now restricted to a smaller portion of the computational region, this result is not surprising. For moderately supercritical (negative) values of the dynamo number, the solution is found to be oscillatory. Figure 5.8 shows contours of toroidal field at the base of the convection zone for $D = -7.5 \times 10^5$. The main feature of this solution is that the oscillating magnetic fields are confined to high latitudes rather than low latitudes. This is to be expected given that the radial shear and the α-effect are both strongest at high latitudes. During each cycle, the toroidal field propagates polewards along contours of constant angular velocity at the base of the convection zone. Figure 5.9 shows the spatial distribution of the toroidal field at the end of this simulation: it is clear that the bulk of the magnetic activity is confined to the region around the base of the convection

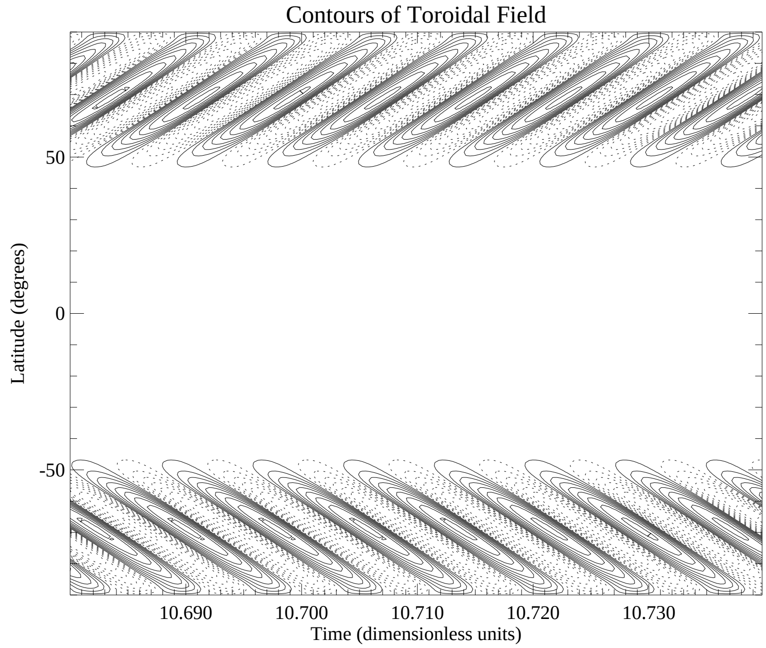

Figure 5.8: Contours of constant toroidal field, plotted against latitude and time, at the base of the convection zone ($r = 0.7$). Contours are equally spaced, solid lines correspond to positive values of B, dashed lines correspond to negative values. $f(\theta) = \cos\theta$, $\eta_c = 0.01$, $r_\alpha = 0.725$ and $D = -7.5 \times 10^5$. Magnetic oscillations are confined to high latitudes and migrate polewards.

zone. The poloidal field lines are similarly distributed. Another aspect of this solution that should be mentioned is that the characteristic latitudinal length-scale of the field variation is rather short when compared to the solar observations – this is most clearly seen in Figure 5.9. This may be a consequence of the idealised nature of some aspects of the model and so may not be of major importance, however it is important to bear this issue in mind when analysing these results.

Larger (more negative) values of D lead to a qualitative change in the behaviour of the dynamo. As the solution is evolved in time, initial oscillations (driven by the radial shear) are soon swamped by a steady mode. As described above, this steady

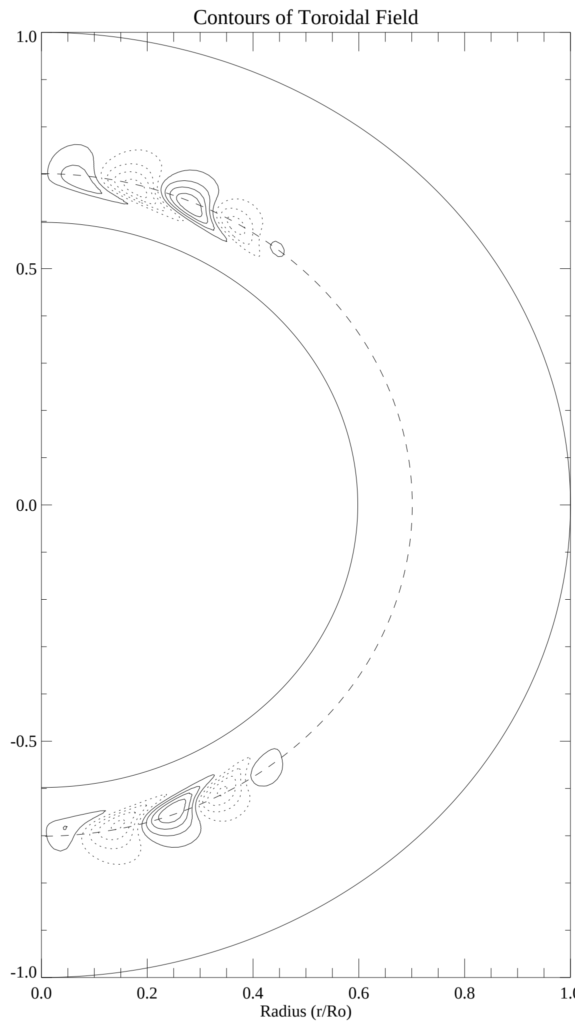

Figure 5.9: The spatial distribution of the toroidal field within the computational domain at an instant in time. The contours of constant B are equally spaced, solid lines correspond to positive values of the toroidal field, dashed lines correspond to negative values. $f(\theta) = \cos\theta$, $\eta_c = 0.01$, $r_\alpha = 0.725$ and $D = -7.5 \times 10^5$. Magnetic activity is confined to the area around the base of the convection zone.

mode is driven by the latitudinal shear. The threshold value of D, at which this change of behaviour occurs is approximately $D = -1.0 \times 10^6$. A solution of this form (for

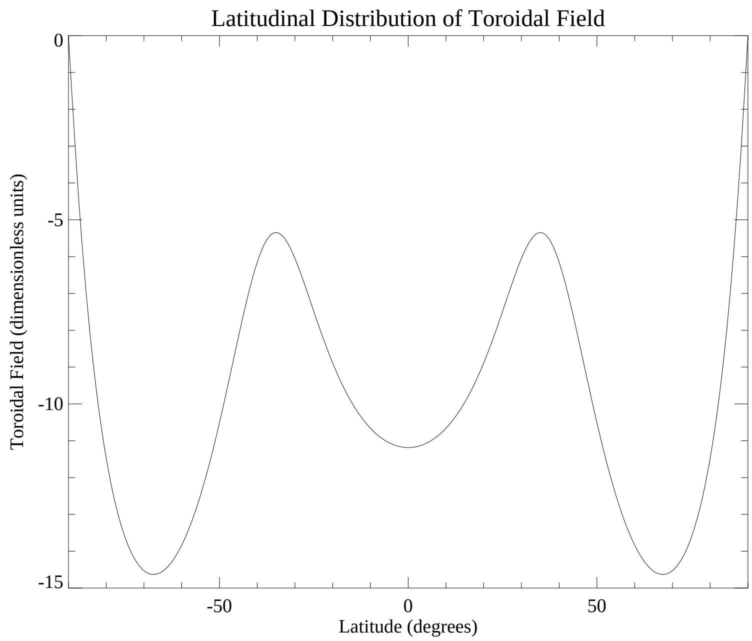

Figure 5.10: A quadrupolar steady mode. This plot shows the variation of toroidal field with latitude, at the base of the convection zone ($r = 0.7$). $f(\theta) = \cos\theta$, $\eta_c = 0.01$, $r_\alpha = 0.725$ and $D = -1.5 \times 10^6$.

$D = -1.5 \times 10^6$) is shown in Figure 5.10. Further increases in the magnitude of D do not lead to any more qualitative changes. These results are qualitatively similar to those of Markiel (1999), who also found oscillatory modes for moderately supercritical dynamo numbers and steady modes for more supercritical values, albeit in a different region of parameter space. This model fails to reproduce any of the major features of the solar dynamo: the dynamo is steady for a wide range of values of the dynamo number, and any oscillations that do occur are confined to high latitudes.

For this particular model, with $f(\theta) = \cos\theta$ and $r_\alpha = 0.725$, negative values of the dynamo number have failed to produce solar-like behaviour. The difficulty with positive values of D is that, if low-latitude oscillatory features do occur, the direction of the propagation of magnetic activity there should be polewards rather than equatorwards

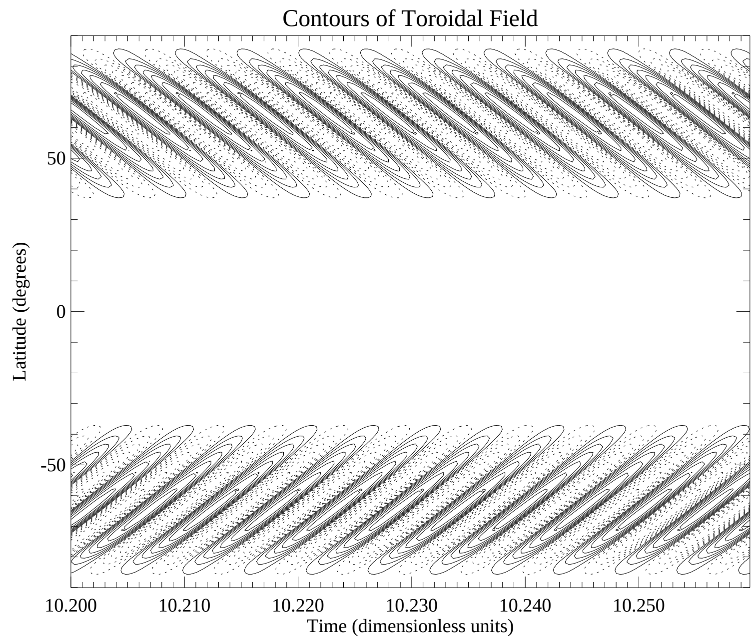

Figure 5.11: As Figure 5.8, but here $f(\theta) = \cos\theta$, $\eta_c = 0.01$, $r_\alpha = 0.725$ and $D = 1.5 \times 10^6$. Note that the direction of propagation is now equatorwards rather than polewards.

(Parker, 1955b). This is clearly not desirable in a solar dynamo model, but this should be verified before positive values of the dynamo number can be ignored. The critical dynamo number for positive values of D is approximately $D = 4.0 \times 10^5$. As we would expect, moderately supercritical values of the dynamo number (again) produce oscillatory magnetic fields at high latitudes, which are confined to the region around the base of the convection zone. The only way in which this solution differs from the solution shown in Figures 5.8 and 5.9 is that the waves now propagate equatorwards as the cycle progresses rather than polewards. This is a direct consequence of the reversal of the sign of the dynamo number. However, as D is increased, these oscillatory modes persist and are not suppressed by the appearance of a steady mode. Figures 5.11 and 5.12 show contours of toroidal field at the base of the convection zone for $D = 1.5 \times 10^6$ and

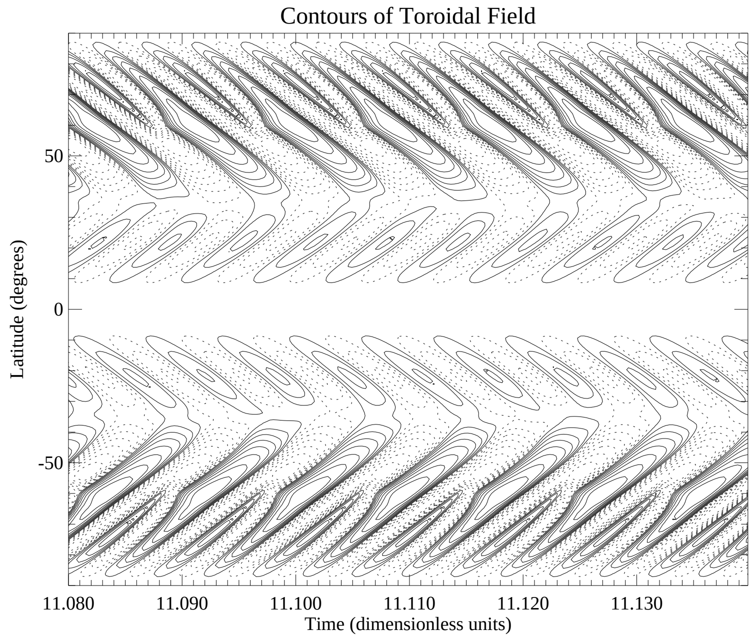

Figure 5.12: As Figure 5.8, but now $f(\theta) = \cos\theta$, $\eta_c = 0.01$, $r_\alpha = 0.725$ and $D = 3.5\times10^6$. The polewards propagation of activity at low latitudes is not solar-like.

$D = 3.5 \times 10^6$ respectively. For $D = 1.5 \times 10^6$, the dynamo action is still confined to high latitudes at the base of the convection zone. As D is increased (beyond approximately $D = 2.5 \times 10^6$), the strong high-latitude features are joined by weak low-latitude (polewards propagating) features. Figure 5.12 shows that, for $D = 3.5 \times 10^6$, the high-latitude branch of the dynamo appears to fragment – there are now two clear frequencies of oscillation in the high-latitude branch of the dynamo. As for the results for negative values of D, these results are similar to those of Markiel. Although this behaviour is very interesting, it does not reflect what is observed on the Sun. In particular, the incorrect (polewards) propagation of magnetic fields at low latitudes suggests that positive values of the dynamo number are not going to produce solar-like behaviour. Attention therefore needs to be focused upon varying the other details of the model, so that negative values of D can produce stronger oscillations at low latitudes.

One of the most obvious parameters to try varying is the ratio of magnetic diffusivities, η_c. As mentioned above, all of the similar calculations carried out by Markiel used $\eta_c = 1.0 \times 10^{-4}$, which represents a very large difference (four orders of magnitude) between the values of the magnetic diffusivity in the overshoot region and the convection zone. Putting $\eta_c = 1.0 \times 10^{-4}$ in my model initially leads to oscillations, but these are always eventually swamped by a steady mode (for all negative dynamo numbers). Given the relatively sharp gradient in the magnetic diffusivity, the mechanism for the production of this steady mode is presumably similar to that of Markiel's "thin" transition region (described in Section 5.1), with the latitudinal shear again playing a key role. The fact that Markiel managed to find oscillatory solutions for this very small value of η_c is probably a consequence of the error in the imposed shear, which increases the relative influence of the radial shear compared to the latitudinal shear. This suggests that attention should be focused upon larger values of η_c than those investigated by Markiel. For $\eta_c = 0.1$, oscillatory solutions are again found. Taking $D = -7.5 \times 10^5$ produces a solution which is virtually identical to that shown in Figure 5.8. A quantitative comparison of the two solutions also suggests very close agreement. With $\eta_c = 0.01$, the peak toroidal field at $r = 0.7$ is 2.2054 dimensionless units, and the period of oscillation is 0.00786 dimensionless units – increasing η_c by a factor of 10 leads to a 7% decrease in the peak field and a 5% decrease in the period. Overall, there is clearly a fairly close agreement between the solutions for $D = -7.5 \times 10^5$. This agreement is totally lost for larger values of the dynamo number: rather than reverting to a steady mode, the solution remains oscillatory. Figure 5.13 shows contours of toroidal field at the base of the convection zone for $D = -3.5 \times 10^6$. The key new feature seen here is a weak low-latitude oscillatory band which migrates equatorwards as the cycle progresses. Although the toroidal field at low latitudes is much weaker than that at high latitudes, this is the first solution to be found that has low-latitude oscillations with the correct direction of propagation, and that is of dipolar symmetry. The message from these particular sim-

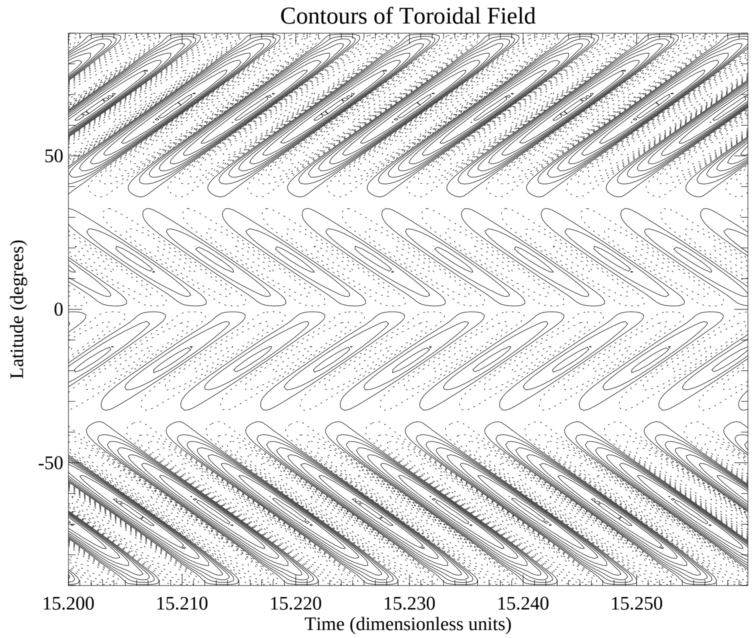

Figure 5.13: As Figure 5.8, but here $f(\theta) = \cos\theta$, $\eta_c = 0.1$, $r_\alpha = 0.725$ and $D = -3.5 \times 10^6$. This is an oscillatory dipolar mode with the correct direction of propagation at low latitudes.

ulations seems to be that lower values of η_c favour steady modes, whilst higher values favour oscillatory ones. Before any conclusions are reached concerning the "best" value of η_c, it is worth investigating variations of the other main parameter in the problem.

Varying the value of the parameter r_α should have a significant effect upon the behaviour of the dynamo. Smaller values of r_α give a larger overlap between the radial shear layer and the α layer. In quantitative terms, increasing this overlap should lead to smaller critical dynamo numbers – if the α layer and the radial shear layer are nearly coincident, then the diffusive coupling of the two layers becomes less important from the point of view of the operation of the dynamo. It should also be pointed out that the tachocline region will be the location of the strongest toroidal field, and therefore it will also be the region where α-quenching is strongest. For a "conventional" α-effect that is

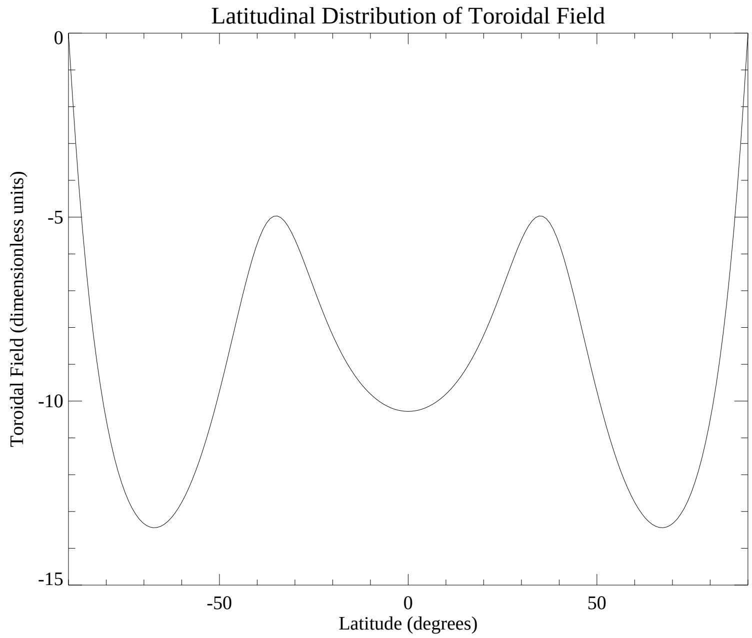

Figure 5.14: A quadrupolar steady mode. As Figure 5.10, but now $f(\theta) = \cos\theta$, $\eta_c = 0.01$, $r_\alpha = 0.75$ and $D = -1.5 \times 10^6$.

driven by convective turbulence, it is difficult to see how this situation, where there is a large overlap between the shear layer and the α layer, could lead to the generation of super-equipartition magnetic fields. However, for an α-effect that is driven by (for example) magnetic buoyancy, this is not a problem since equipartition fields actually enhance the instability (although it is assumed that this effect is quenched at some larger magnetic field strength). Increasing the parameter r_α reduces the overlap between the shear layer and the α-layer – the diffusive transport of magnetic fields now becomes a more important factor in the operation of the dynamo. We would also expect a smaller overlap to lead to a larger critical dynamo number.

Increasing r_α to 0.75 leads to a slight increase (about 10%) in the magnitude of the critical dynamo number. It is found that, for all negative values of the dynamo number, early oscillations are quickly suppressed by a steady mode. Figure 5.14 shows

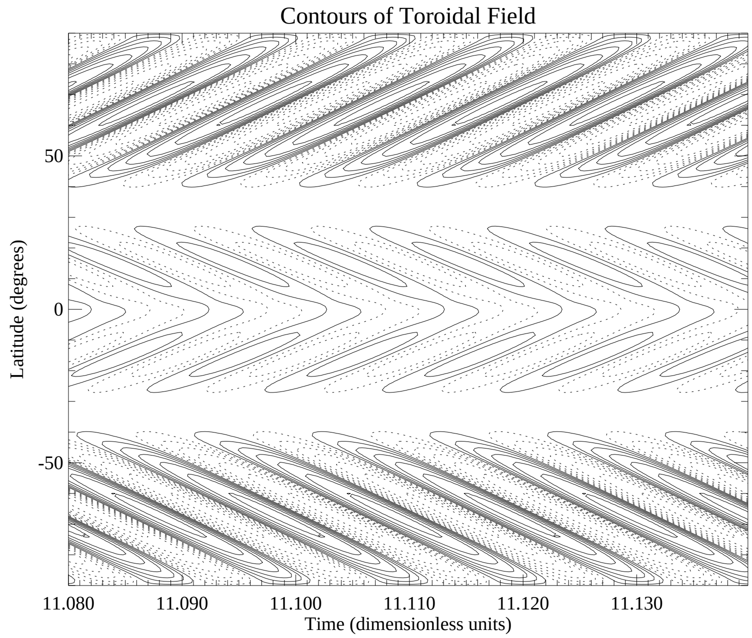

Figure 5.15: As Figure 5.8, but here $f(\theta) = \cos\theta$, $\eta_c = 0.01$, $r_\alpha = 0.7$ and $D = -7.5\times10^5$.

the toroidal field at the base of the convection zone for $D = -1.5 \times 10^6$. This steady mode is typical of the kind of solutions that are found for this larger value of r_α. Again, it is the latitudinal shear that is responsible for the generation of these steady modes. Since there is now no overlap between the shear layer and the α layer, poloidal magnetic field that is produced within the convection zone must diffuse into the low-diffusivity region below, before the radial shear can act upon it. This decrease in the magnetic diffusivity leads to poloidal field, with a strong latitudinal component, accumulating just below the convection zone. As discussed previously, this (when coupled with the latitudinal shear) will tend to lead towards a steady mode.

Setting $r_\alpha = 0.7$ corresponds to 100% overlap between the tachocline and the α-effect. This should promote the effects of the radial shear, thus leading to oscillatory modes – this is exactly what is found. The critical dynamo number for this set of parameters is much smaller than that found previously (approximately -1.0×10^5). For moderately

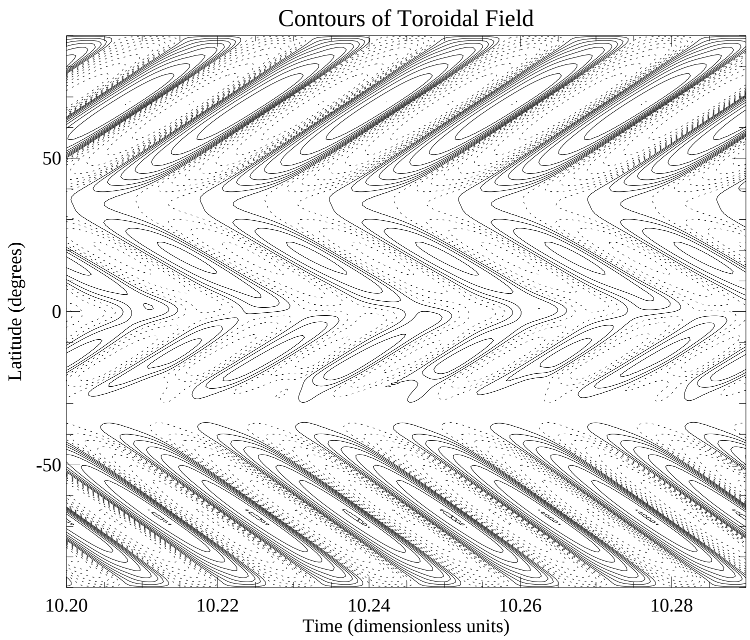

Figure 5.16: As Figure 5.8, but here $f(\theta) = \cos\theta$, $\eta_c = 0.01$, $r_\alpha = 0.7$ and $D = -1.5\times10^6$. Note the parity fluctuations in this oscillatory solution.

supercritical values of the dynamo number, the magnetic activity is again confined to high latitudes. Weak low-latitude oscillations are found for $D \lesssim -5.0 \times 10^5$ – these magnetic fields at low latitudes propagate equatorwards during each cycle. Figure 5.15 shows contours of toroidal field, at the base of the convection zone, for $D = -7.5 \times 10^5$. The key features to note here are that the low-latitude oscillations are (again) much weaker than those at high latitudes, and the dominant parity is quadrupolar. As the magnitude of D is increased, the dynamo remains oscillatory. Figure 5.16 shows the equivalent plot for $D = -1.5 \times 10^6$. The only qualitative change exhibited by this solution is that the parity is now time dependent.

At this stage, it is useful to summarise the main findings, so far, for an α-effect that is confined to the base of the convection zone. For $f(\theta) = \cos\theta$, both steady and oscillatory solutions have been found. The general trends seem to be fairly clear: oscillatory modes favour larger values of η_c and smaller values of r_α, steady modes favour smaller values of η_c and larger values of r_α. Unfortunately, the oscillatory solutions that have been found are not particularly solar-like. Although low-latitude oscillations have been found, which propagate equatorwards (for negative values of D), the parity is not always dipolar and, more importantly, the magnetic fields at high latitudes are always much stronger. These properties are both unsatisfactory from the point of view of matching up to observations of the large-scale solar magnetic field. One way of promoting low-latitude features over high-latitude ones would be to "truncate" the α-effect at the poles – ie. take $f(\theta)$ to be $\cos\theta\sin^2\theta$ or $\cos\theta\sin^4\theta$. Some physical justification for adopting profiles of these forms was given in Section 5.1, and it seems that this is the only obvious way of suppressing the activity at high latitudes.

5.2.3 A "truncated" α-effect

Having carried out a survey of the relevant portions of parameter space for $f(\theta) = \cos\theta$, it has become clear that α-profiles that are more restricted at the poles are more likely to produce solar-like solutions. In the simulations that follow, η_c is fixed at 0.01, but r_α is varied. This value of η_c seems physically reasonable and it has been shown that it is possible to produce oscillatory solutions, with $\eta_c = 0.01$, for certain values of r_α. This restricts the parameter space down to a more manageable level and allows more scope to experiment with different values of r_α.

Initially we take $f(\theta) = \cos\theta\sin^2\theta$ and $r_\alpha = 0.7$. For $D \lesssim -5.0\times10^5$, oscillatory solutions are again found – the critical dynamo number here is approximately five times larger than that found for the equivalent case with $f(\theta) = \cos\theta$. We expect a larger value for the critical dynamo number for this "truncated" α-effect since $\alpha(r,\theta)$ is restricted to a smaller portion of the domain. For slightly supercritical values of D, the dynamo oscillations are restricted to high latitudes and the solution is similar in form to that shown in Figure 5.8. However, only a modest increase in the magnitude of D is

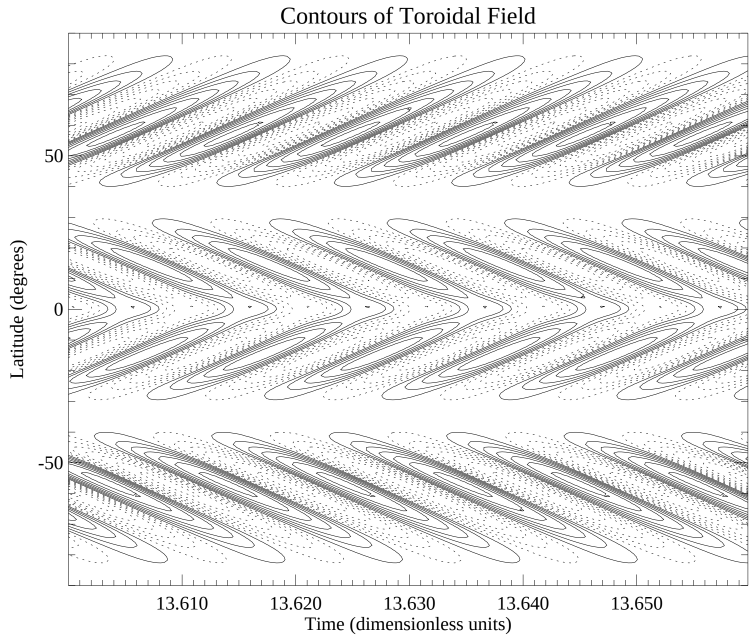

Figure 5.17: As Figure 5.8, but now $f(\theta) = \cos\theta\sin^2\theta$, $\eta_c = 0.01$, $r_\alpha = 0.7$ and $D = -1.0 \times 10^6$. The toroidal field in the low-latitude branch is now of a comparable magnitude to the high-latitude field.

required before low-latitude oscillations are excited. Figures 5.17 and 5.18 show contours of toroidal field at the base of the convection zone for $D = -1.0\times10^6$ and $D = -2.0\times10^6$ respectively. The main feature of these two solutions is that, particularly in the solution corresponding to the larger value of the dynamo number, the magnetic fields at high and low latitudes are of comparable magnitudes. Although the high-latitude fields are still (comparatively) too large, this solution is a step in the right direction towards solar-like behaviour.

Increasing r_α to 0.725 results in a marked increase (by about a factor of 3) in the magnitude of the critical dynamo number. However, for all values of D that were investigated, early oscillations (which are confined to high latitudes) are eventually suppressed by a steady mode. Figure 5.19 shows a steady mode for $D = -2.0 \times 10^6$. As before,

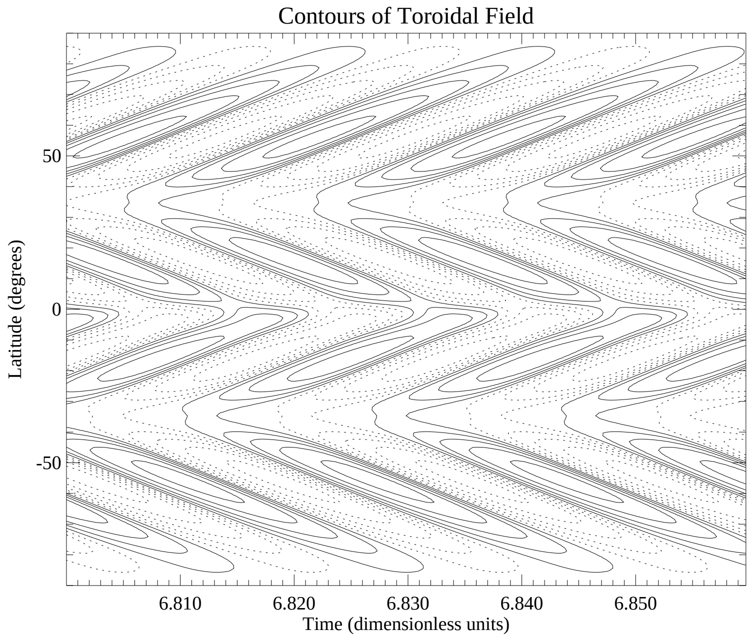

Figure 5.18: As Figure 5.8, but now $f(\theta) = \cos\theta\sin^2\theta$, $\eta_c = 0.01$, $r_\alpha = 0.7$ and $D = -2.0 \times 10^6$.

setting $r_\alpha = 0.75$ also results in steady modes for all negative values of the dynamo number.

Finally, a set of simulations were carried out for $f(\theta) = \cos\theta\sin^4\theta$: this gives an α-effect that is more concentrated around low latitudes. As before, sets of simulations were carried out for $r_\alpha = 0.7, 0.725$ and 0.75 – in addition, in order to perform a more thorough survey of the dependence of the dynamo upon r_α, simulations were also carried out for $r_\alpha = 0.71$ and $r_\alpha = 0.72$. In general terms, for any given value of r_α, we would expect larger critical dynamo numbers in these simulations than in those described previously. This is (again) a consequence of the fact that $\alpha(r,\theta)$ is non-zero over a smaller portion of the computational domain.

The results from these simulations fall into two broad categories. For $r_\alpha = 0.72, 0.725$ and 0.75, the overlap between the tachocline and the α layer is relatively small. As found

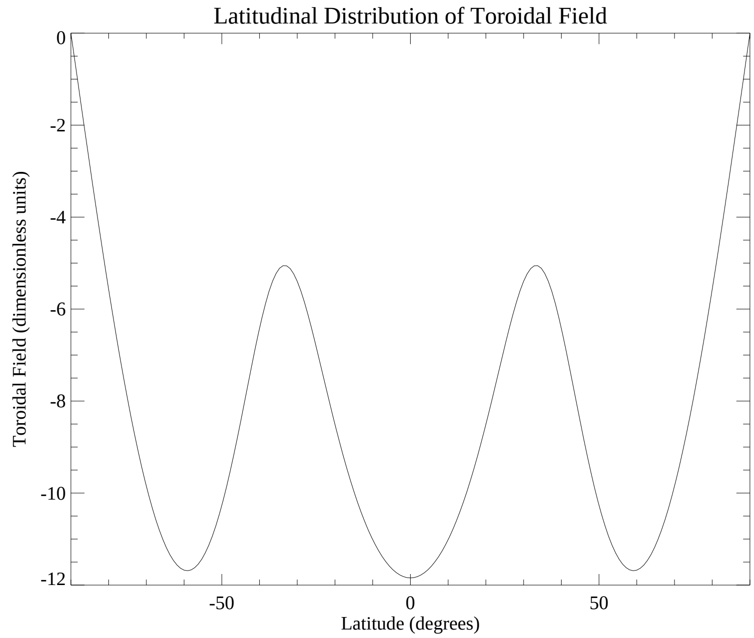

Figure 5.19: A quadrupolar steady mode. As Figure 5.10, but here $f(\theta) = \cos\theta \sin^2\theta$, $\eta_c = 0.01$, $r_\alpha = 0.725$ and $D = -2.0 \times 10^6$.

in previous simulations, these larger values for r_α again lead to steady modes, which are similar in form to that shown in Figure 5.19. Increasing the overlap between the shear layer and the α layer leads to a qualitative change in the behaviour of the dynamo. For $r_\alpha = 0.7$ and 0.71, oscillatory solutions were found. Although there are quantitative differences, such as a smaller critical dynamo number ($D = -7.5 \times 10^5$) for the $r_\alpha = 0.7$ case, these two cases are qualitatively very similar. The fact that there is a range of values, for r_α, over which the qualitative behaviour is similar, is important from the point of view of the robustness of the results that are obtained. Since the results for $r_\alpha = 0.7$ and 0.71 are so similar, rather than discussing both cases, I will concentrate upon describing one of them in detail. Out of the two cases, $r_\alpha = 0.71$ is possibly the most physically realistic: the magnetic buoyancy instability (and therefore any α-effect that it drives) requires a negative radial gradient in B – this condition is more likely to

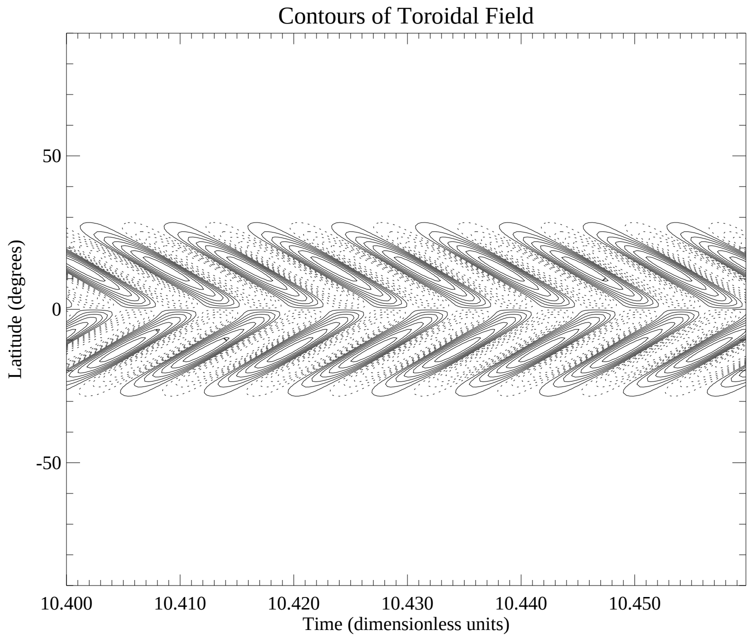

Figure 5.20: As Figure 5.8, but here $f(\theta) = \cos\theta\sin^4\theta$, $\eta_c = 0.01$, $r_\alpha = 0.71$ and $D = -2.0 \times 10^6$. This oscillatory solution is confined to low latitudes, is of dipolar symmetry, and has the correct direction of propagation.

be satisfied in the outer regions of the tachocline.

For $r_\alpha = 0.71$, dynamo oscillations are found for $D \lesssim -1.5 \times 10^6$. Figure 5.20 shows contours of toroidal magnetic field at the base of the convection zone for $D = -2.0 \times 10^6$. For all moderately supercritical dynamo numbers, the solution is qualitatively identical to that shown here. It can clearly be seen that the oscillatory magnetic field is not only confined to low latitudes, but is also dipolar with the correct direction of propagation. This is the first solution to be found that possesses all these "solar-like" features. The strongest toroidal magnetic fields, in this solution, occur just below the base of the convection zone, with the bulk of the magnetic activity also confined to this region.

Further increases in the magnitude of the dynamo number lead to the appearance of weaker high-latitude oscillatory features. Figures 5.21 and 5.22 show contours of toroidal

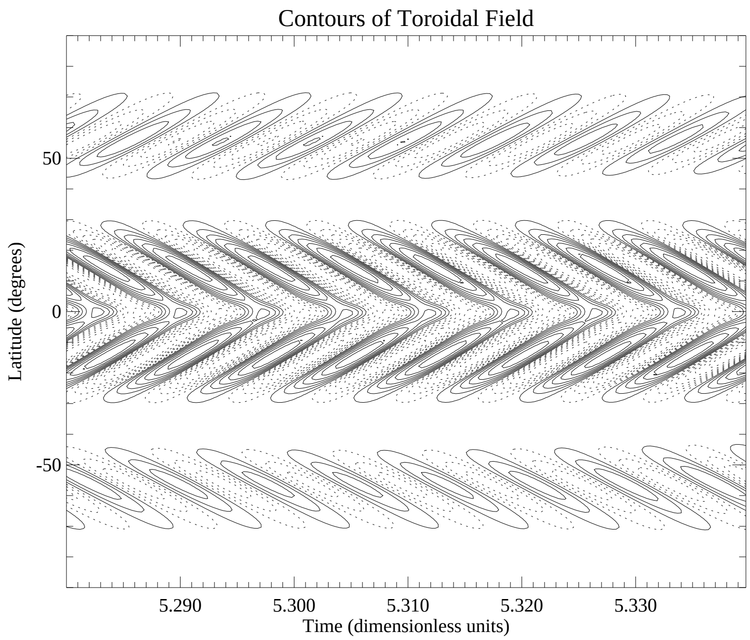

Figure 5.21: As Figure 5.8, but now $f(\theta) = \cos\theta\sin^4\theta$, $\eta_c = 0.01$, $r_\alpha = 0.71$ and $D = -2.5 \times 10^6$. Note that this is now of predominantly quadrupolar parity and there is now a weak high-latitude branch.

field at the base of the convection zone for $D = -2.5 \times 10^6$ and $D = -3.0 \times 10^6$ respectively. Both these solutions have weak high-latitude features, which migrate polewards, and strong low-latitude features, which migrate equatorwards. The other notable feature about both of these solutions is that the overall symmetry is now quadrupolar rather than dipolar.

5.3 Summary

The aim of the survey, described in this chapter, was to assess the impact that different functional forms for $\alpha(r, \theta)$ and (to a lesser extent) $\eta(r)$ have upon the behaviour of this solar dynamo model. Since the internal differential rotation profile of the Sun is

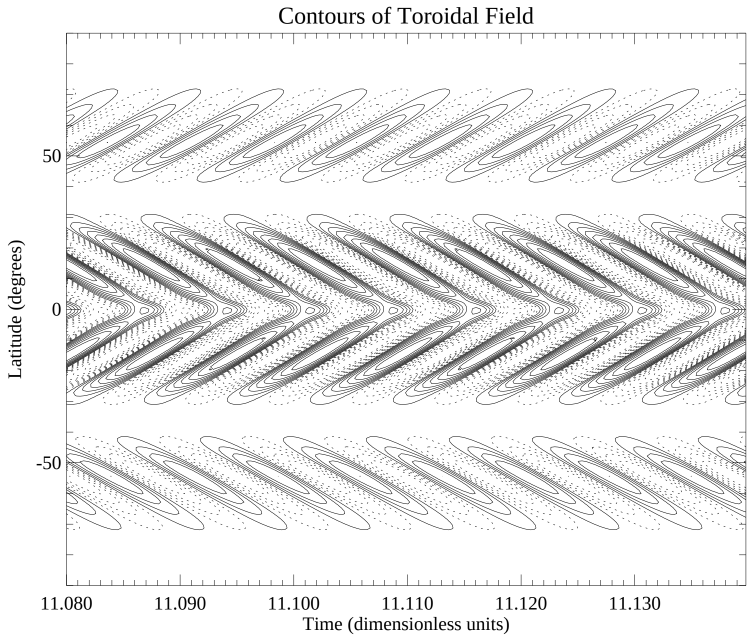

Figure 5.22: As Figure 5.8, but here $f(\theta) = \cos\theta\sin^4\theta$, $\eta_c = 0.01$, $r_\alpha = 0.71$ and $D = -3.0 \times 10^6$.

relatively well known, this was taken to be the same throughout all these simulations, whilst the other parameters were varied. It was established that a distributed α-effect, that operates throughout the convection zone, does not seem to be capable of producing solar-like oscillatory behaviour. For an α-effect that was confined to the base of the convection zone, both steady and oscillatory solutions were found. Oscillatory modes only seem to be preferred for α-profiles that overlap significantly with the tachocline. Variations in the core-envelope magnetic diffusivity ratio also had a qualitative influence on the form of the solution: steady modes arose for smaller values of the parameter η_c (such as that used by Markiel), whilst oscillatory modes occurred for larger values. An α-effect that is strongest at the poles leads to high-latitude oscillatory dynamo action – a "truncated" α-effect is needed in order to produce dynamo action that is concentrated at low latitudes. The most "solar-like" of the solutions was, for moderately supercritical

Type of α-effect	Qualitative behaviour of the dynamo
Distributed α-effect	$D > 0$: Oscillations distributed throughout the convection zone, with most of the activity at mid and high latitudes. $D < 0$: (Mostly dipolar) Steady modes.
α-effect confined to the base of the convection zone	All for $D < 0$: $f(\theta) = \cos\theta$: High-latitude oscillations or steady modes. Steady modes preferred for larger values of r_α ($r_\alpha \gtrsim 0.725$). Oscillatory solutions preferred for low r_α ($r_\alpha \lesssim 0.725$). Low η_c favours steady modes, larger η_c favours oscillations. $f(\theta) = \cos\theta\sin^2\theta$: Oscillations or steady modes ($\eta_c = 0.01$). Steady modes for $r_\alpha \gtrsim 0.72$, oscillations otherwise. Polar oscillations comparable to low-latitude oscillations. $f(\theta) = \cos\theta\sin^4\theta$: Oscillations or steady modes ($\eta_c = 0.01$). Steady modes for $r_\alpha \gtrsim 0.72$, oscillations otherwise. Low-latitude oscillations stronger than high-latitude branch.

Table 5.1: Table summarising the main results of the chapter.

dynamo numbers, of dipolar symmetry and confined to low latitudes. Larger values of the dynamo number produced weak high-latitude features and tended to favour quadrupolar symmetry. For ease of reference, the main results concerning the dependence of the dynamo upon the α-effect are summarised in Table 5.1.

Whilst active regions on the Sun are confined to low latitudes, it is still quite possible that there is a weak high-latitude branch of the dynamo. Besides the evidence from the simulations described above, the high-latitude branch of the torsional oscillations, shown in Figure 1.5, suggests that there may be some magnetic activity at high latitudes. Simulations of magnetic flux tubes, rising through the convection zone (see, for example, Caligari et al., 1998), suggest that any toroidal field at the base of the convection zone, that is responsible for the production of active regions, must be of the order of 10^5G. This is roughly 10 times the equipartition value at the base of the convection zone (Parker, 1993), and so these active regions are the surface manifestation of very strong magnetic fields. Weaker magnetic fields will not be as susceptible to the magnetic buoyancy instability, and any weaker flux that does rise into the convection zone is likely to become disrupted by the turbulent fluid motions around it. The consequence of this is that only the strongest magnetic fields may reach the surface of the Sun. Any weaker magnetic flux within the convection zone is liable to be "pumped" back into the overshoot layer by the action of turbulent convection (Tobias et al., 2001). It is also possible that the strong radial shear at high latitudes may suppress non-axisymmetric (undular) buoyancy instabilities there (Tobias and Hughes, 2004), thus preventing the emergence of bipolar loops, at high latitudes, at the solar surface. Bearing these arguments in mind, it therefore seems quite plausible that there might be a weak high-latitude branch to the solar dynamo that never gives rise to active regions.

The parity of the solutions that have been obtained is an interesting issue. Most previous studies impose dipolar symmetry upon their solutions, so this parity-selection problem does not arise. In the most solar-like model, dipolar solutions are only found for moderately supercritical dynamo numbers. Larger values of D push us further into the nonlinear regime and, with this α-quenching nonlinearity, quadrupolar solutions now appear to be preferred. It should be noted that this parameterised quenching mechanism is clearly an over-simplification of the nonlinear aspects of the solar dynamo, and we would expect that parity selection in the nonlinear regime might be particularly sensitive to the precise nonlinearity used. This issue is one aspect of the solar dynamo that is investigated in the next chapter.

Chapter 6

Torsional Oscillations

The dynamo model that was described in the previous chapter was successful in reproducing many of the features of the solar dynamo. In this chapter, the results from that survey are used as the basis for an investigation into the constraints that are imposed upon the solar dynamo by the (so-called) torsional oscillations. Since it is generally accepted that these perturbations to the solar angular velocity are magnetically driven, it is necessary to modify the basic dynamo model so that it now includes the perturbation to the angular velocity caused by the azimuthal component of the Lorentz force – see Section 4.4.1. As described in Chapter 2, this effect has been incorporated into numerous solar dynamo models, both in Cartesian geometry (Tobias, 1996b, 1997b; Phillips et al., 2002; Brooke et al., 2002) and spherical geometry (Belvedere et al., 1990; Küker et al., 1999; Moss and Brooke, 2000; Covas et al., 2000a,b; Tavakol et al., 2002). It should also be mentioned that torsional oscillations have been generated by considering a model that incorporates the microdynamic back-reaction of the magnetic field upon the turbulent stresses within the solar convection zone (see, for example, Pipin, 1999). Whilst this is certainly one possible mechanism, attention here will focus upon the macrodynamic scenario, which seems to be a more natural candidate for the production of torsional oscillations near the interface region at the base of the convection zone.

The spherical model of Moss and Brooke (which is virtually the same as the model that has subsequently been studied by Covas and collaborators) employs a magnetic diffusivity profile which depends only very weakly upon radius: $\eta(r)$ only varies by a factor of 2 across the domain, with a very wide diffusivity transition region at the base of the convection zone (approximately 10% of the solar radius). As pointed out by Moss and Brooke, this probably underestimates the change in $\eta(r)$ around the base of the convection zone, and the resulting dynamo behaviour is not particularly interface-like. Since a steep radial gradient in the magnetic diffusivity leads to steep radial gradients in the magnetic field, a large number of grid-points are required in order to resolve the resulting magnetic features. Typically, in the simulations of Moss and Brooke (2000), the highest resolution mesh that could readily be used employed 61 radial grid-points and 101 latitudinal grid-points. In the simulations that are described below, a higher resolution mesh allows us to investigate more realistic profiles for the magnetic diffusivity (like the one that was considered in the previous chapter). Although this is relatively expensive in terms of computation time, this is far more satisfactory from the point of view of modelling an interface-like solar dynamo.

In this chapter, this modified model is first compared with the "best" solar-like solution from the previous chapter. A close correspondence is found, which suggests that the numerical scheme has been correctly implemented. It is demonstrated that this model produces a perturbation to the angular velocity which, on subtraction of a suitable time-average, resembles the observed pattern of torsional oscillations within the Sun. In keeping with previous studies, it is found that time-dependent modulation occurs once the magnetic Prandtl number is decreased from unity. Brooke et al. (2002) suggest that solar-like torsional oscillations are incompatible with low values of the magnetic Prandtl number. This suggestion is investigated within the context of this model. Finally, the effects of stratification are put into the model, and the resulting oscillations are compared to the observations described by Vorontsov et al. (2002).

6.1 Model set-up

The only nonlinearity that was incorporated into the dynamo model in the previous chapter was due to α-quenching. As mentioned above, in order to produce torsional oscillations, it is necessary to allow the magnetic field to perturb the angular velocity profile. The relevant equations were described in Section 4.4.1, along with the appropriate numerical details. For ease of reference, it is worth restating those equations here:

$$\begin{aligned}\frac{\partial A}{\partial t} &= \frac{\alpha(r,\theta)B}{1+(B^2/\Lambda)} + \frac{\eta(r)}{r^2}\frac{\partial}{\partial r}\left[r^2\frac{\partial A}{\partial r}\right] + \frac{\eta(r)}{r^2\sin\theta}\frac{\partial}{\partial\theta}\left[\sin\theta\frac{\partial A}{\partial\theta}\right] \\ &\quad -\frac{\eta(r)A}{r^2\sin^2\theta}\end{aligned} \tag{6.1}$$

$$\begin{aligned}\frac{\partial B}{\partial t} &= D\frac{\partial(A\sin\theta)}{\partial\theta}\frac{\partial\Omega}{\partial r} + \frac{D}{\sin\theta}\frac{\partial(A\sin\theta)}{\partial\theta}\frac{\partial}{\partial r}\left[\frac{v}{r}\right] - \frac{D\sin\theta}{r}\frac{\partial(Ar)}{\partial r}\frac{\partial\Omega}{\partial\theta} \\ &\quad -\frac{D\sin\theta}{r^2}\frac{\partial(Ar)}{\partial r}\frac{\partial}{\partial\theta}\left[\frac{v}{\sin\theta}\right] + \frac{1}{r}\frac{\partial}{\partial r}\left[\eta(r)\frac{\partial(Br)}{\partial r}\right] \\ &\quad +\frac{1}{r^2}\frac{\partial}{\partial\theta}\left[\frac{\eta(r)}{\sin\theta}\frac{\partial(B\sin\theta)}{\partial\theta}\right]\end{aligned} \tag{6.2}$$

$$\begin{aligned}\frac{\partial v}{\partial t} &= \frac{\mathrm{sign}(D)}{r^2\sin\theta\rho(r)}\left[\frac{\partial(A\sin\theta)}{\partial\theta}\frac{\partial(Br)}{\partial r} - \frac{\partial(B\sin\theta)}{\partial\theta}\frac{\partial(Ar)}{\partial r}\right] \\ &\quad +\frac{\tau r}{\rho(r)}\frac{\partial(\rho\eta)}{\partial r}\frac{\partial}{\partial r}\left[\frac{v}{r}\right] + \frac{\tau\eta(r)}{r^2}\frac{\partial}{\partial r}\left[r^2\frac{\partial v}{\partial r}\right] + \frac{\tau\eta(r)}{r^2\sin\theta}\frac{\partial}{\partial\theta}\left[\sin\theta\frac{\partial v}{\partial\theta}\right] \\ &\quad -\frac{\tau\eta(r)v}{r^2\sin^2\theta}.\end{aligned} \tag{6.3}$$

All the previously published, two-dimensional, spherical simulations which incorporate this dynamic nonlinearity, are of $\alpha^2\omega$-type – as in the previous chapter, attention here is focused entirely upon the $\alpha\omega$ limit. Unless stated otherwise, $\rho(r)$ is taken to be constant throughout the domain. The boundary conditions are as described in Section 4.4.1: the magnetic conditions are identical to those described in the previous chapter, whilst $v = 0$ on every boundary apart from at $r = 1.0$, where a stress-free condition is applied.

In equation (6.1), the parameter Λ (which is defined by equation 4.34) controls the strength of the α-quenching relative to the other nonlinearity. Only two cases are considered in this chapter: either α-quenching is "switched off" entirely (formally $\Lambda \to \infty$) or Λ is, somewhat arbitrarily, set equal to 100.0. This value of Λ corresponds to the inclusion of weak α-quenching – smaller values of Λ (and therefore stronger quenching) were briefly investigated and found to lead to behaviour similar to that seen in the previous chapter. The parameter Λ depends upon the peak value for α, the peak value for the turbulent magnetic diffusivity and the quenching field strength. All of these values are very poorly-determined, and it is therefore difficult to write down a "realistic" value for Λ. Given the length of time that is required to run each simulation, it is not possible to perform a wide survey of Λ-space, but it is to be hoped that $\Lambda = 100.0$ is in some way representative of the situation where weak α-quenching is operating in tandem with the macrodynamic nonlinearity. One aspect of the dynamo that we might expect to be particularly sensitive to the combination of nonlinearities is that of parity selection in the nonlinear regime. With α-quenching as the sole nonlinearity, for even the most solar-like solution, dipolar symmetry was lost as the dynamo number was made increasingly supercritical. The way in which these nonlinearities affect the relative nonlinear stability of the dipolar and quadrupolar modes is an issue that deserves investigation.

The (unperturbed) differential rotation profile that is used in this model is identical to that given in equation (5.1). So

$$\Omega(r,\theta) = \Omega_c + \frac{1}{2}\left[1 + \Phi\left(\frac{r-0.7}{0.025}\right)\right]\left(P - Q\cos^2\theta - R\cos^4\theta\right), \qquad (6.4)$$

where Φ represents the standard error function, $P = 0.0571$, $Q = 0.123$, $R = 0.155$ and $\Omega_c = 0.943$. The model of Moss and Brooke does not use an analytic fit to the solar rotation profile – instead it uses an interpolation to the SOHO MDI data, taken from Kosovichev et al. (1997). As the analytic fit that is used here is based upon a different set of observations (Schou et al., 1998), there are slight qualitative differences between this profile and that used by Moss and Brooke – most notably, their profile has a wider tachocline region. Subsequent studies by Covas and collaborators employ more recent direct interpolations of the observational data – the inversion taken from Howe et al. (2000), in particular, is much closer to the analytic fit that is used here. In a direct comparison of these different differential rotation profile inversions, Covas et al. (2001a) find that the results are qualitatively insensitive to changes in the rotation profile. This suggests that the use of an analytic fit, as opposed to a direct interpolation of the observational data, should make little difference to the results.

The major difference between this model and all the previous studies, which incorporate this dynamic nonlinearity in spherical geometry, is in the spatial dependence of the magnetic diffusivity. All previous spherical studies involving this nonlinearity (for numerical reasons) impose a magnetic diffusivity profile that has only a very weak dependence upon radius. The resulting dynamo oscillations are therefore not really of "interface-type". As described in the previous chapter, it is possible in this model to investigate, arguably, a more realistic situation: there is a large (positive) radial gradient in $\eta(r)$, at the base of the convection zone, leading to a significant increase in $\eta(r)$ as we pass from the overshoot region into the convection zone. Most "α-quenched" solar dynamo models, which incorporate a realistic rotation law, use a magnetic diffusivity profile of this form (see, for example, Dikpati and Charbonneau, 1999; Ossendrijver, 2000; Küker et al., 2002). So, as before, $\eta(r)$ is given by

$$\eta(r) = \left(\frac{1-\eta_c}{2}\right)\left[1+\Phi\left(\frac{r-0.7}{0.025}\right)\right]+\eta_c. \tag{6.5}$$

Throughout this chapter, as was the case for the majority of the previous chapter, the ratio of magnetic diffusivities, η_c, is taken to be 0.01. In the previous chapter, it was seen that this steep radial gradient in $\eta(r)$ leads to the concentration of strong magnetic fields just below the base of the convection zone. If $\eta(r)$ only depends weakly upon r, as in the simulations of Moss and Brooke, there will be less of a tendency for strong fields to accumulate around the base of the convection zone, and it is reasonable to suppose that the character of the dynamo will be very different. This fact was illustrated in the previous chapter by a simple variation of the value of η_c.

Finally, the α-profile must be specified. For the case where α-quenching is the sole nonlinearity, the most solar-like solutions were obtained for an α-profile that was heavily concentrated around the equator and overlapped significantly with the tachocline region. Therefore, motivated by these findings, the α-profile is taken to be

$$\alpha(r,\theta) = \cos\theta\sin^4\theta\exp\left[-\left(\frac{r-0.71}{0.025}\right)^2\right], \tag{6.6}$$

throughout this set of simulations.

6.2 Preliminary calculations

In keeping with the simulations that were described in the previous chapter, these calculations were carried out using a 101x193 mesh. It is not possible to perform significantly higher resolution calculations using this code, for a range of parameter values, without using an extremely large quantity of computer processor time. A very limited number of simulations, at higher resolution, were carried out in order to demonstrate the adequacy of this level of resolution for this modified version of the code. The easiest way to check the validity of this code is by comparing the results that it produces with those described, in the previous chapter, for the α-quenched simulations. The time evolution of these simulations can be monitored (as before) by analysing the magnetic energy and the parity. Another global quantity that can be monitored here is the perturbation kinetic energy

$$E_k = \int \frac{1}{2}\rho v^2 \mathrm{d}V, \tag{6.7}$$

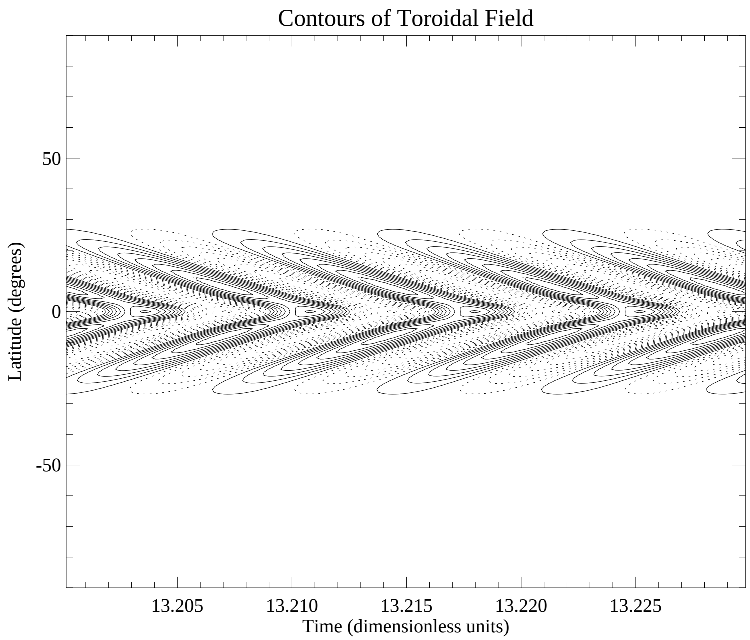

Figure 6.1: Contours of constant toroidal field, plotted against latitude and time, at the base of the convection zone ($r = 0.7$). Contours are equally spaced, solid lines correspond to positive values of B, dashed lines correspond to negative values. Here, there is no α-quenching, and $D = -2.0 \times 10^6$. Note that the parity is quadrupolar rather than dipolar.

where the integral is taken over the whole computational domain. Once all these time-series have converged, we can be sure that the solution has reached a statistically steady state. For all these preliminary calculations, the magnetic Prandtl number, τ, is set equal to unity – smaller values of τ will produce time-dependent behaviour, and this is investigated later on in the chapter.

In the previous chapter, it was found that the critical dynamo number for this model is approximately $D = -1.5 \times 10^6$. The resulting dynamo waves were confined to low latitudes, migrated towards the equator, and the global solution was of dipolar parity. Initially, in this modified model, α-quenching is switched off so that the only nonlinear effect is the macrodynamic back-reaction of the Lorentz force upon the angular velocity. Most of the features of the previous solution are preserved with this change of nonlinearity. Figure 6.1 shows contours of toroidal field at the base of the convection zone for $D = -2.0 \times 10^6$. This demonstrates the low-latitude confinement of magnetic activity, as well as the fact that the magnetic field migrates equatorwards during each cycle. However, it can clearly be seen that the dominant parity is now quadrupolar rather than dipolar. From the point of view of reproducing the pattern of behaviour currently observed in the solar dynamo, this is obviously unsatisfactory, although it is possible that the solar magnetic field has previously gone through phases of quadrupolar symmetry. We would expect that the parity selection might be sensitive to the precise choice of nonlinearity, so the agreement of this solution with all the other aspects of the α-quenching case suggests that this modification to the code has been correctly implemented. As noted in Chapter 5, it is worth mentioning in passing that the latitudinal length-scale of the dynamo-generated magnetic fields is shorter than that observed on the Sun.

Despite not being of dipolar parity, a pure parity mode of this form should still drive torsional oscillations that are symmetric about the equator. In order to observe this oscillatory signal, it is necessary to subtract a time-average from the total velocity perturbation. Since observations of torsional oscillations (see, for example, Vorontsov et al., 2002) are described in terms of perturbations to the angular velocity, once this time-average has been subtracted, the residual for v is divided by $r \sin\theta$ in order to present these perturbations in terms of an angular velocity rather than a linear velocity. This will have the effect of emphasising high-latitude oscillations: a relatively small linear velocity, near the the axis of rotation, will provide a greater perturbation to the angular velocity than an equivalent linear velocity further away from the rotational axis. Perturbations to the angular velocity at the base of the convection zone, for $D = -2.0 \times 10^6$, are shown in Figure 6.2.

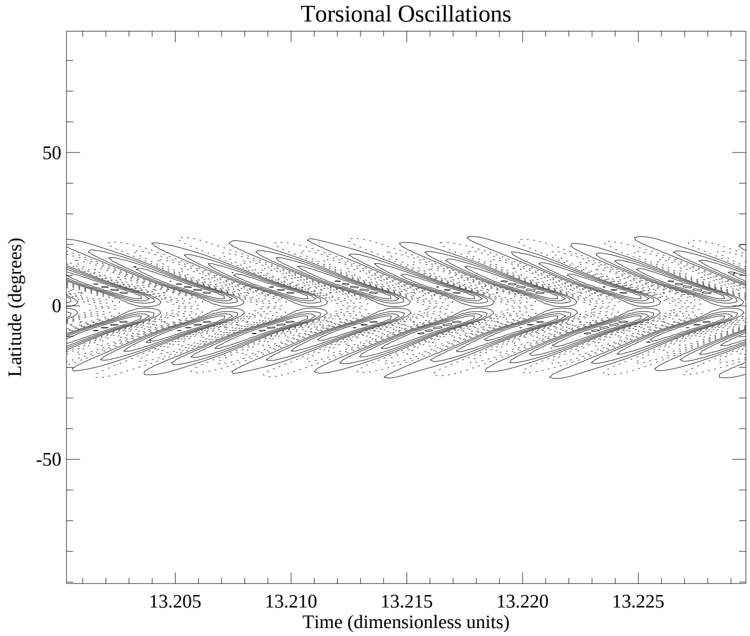

Figure 6.2: As Figure 6.1, but now showing the torsional oscillations at the base of the convection zone ($r = 0.7$). The frequency of oscillation is double that of the magnetic frequency.

The torsional oscillations that are shown in Figure 6.2 are symmetric about the equator and are confined to low latitudes at the base of the convection zone. The spatial distribution of these oscillations coincides with the location of the dynamo-generated magnetic fields. A comparison of the oscillations shown in Figures 6.1 and 6.2 confirms the fact that the frequency of the torsional oscillations is twice that of the basic magnetic cycle – this is a consequence of the fact that the Lorentz force depends quadratically upon the magnetic field. Besides the fact that the parity of this solution is quadrupolar rather than dipolar, the other discrepancy between this solution and solar observations is the absence of a high-latitude branch to the torsional oscillations (Vorontsov et al., 2002).

It was shown in the previous chapter that it is possible to excite magnetic oscillations

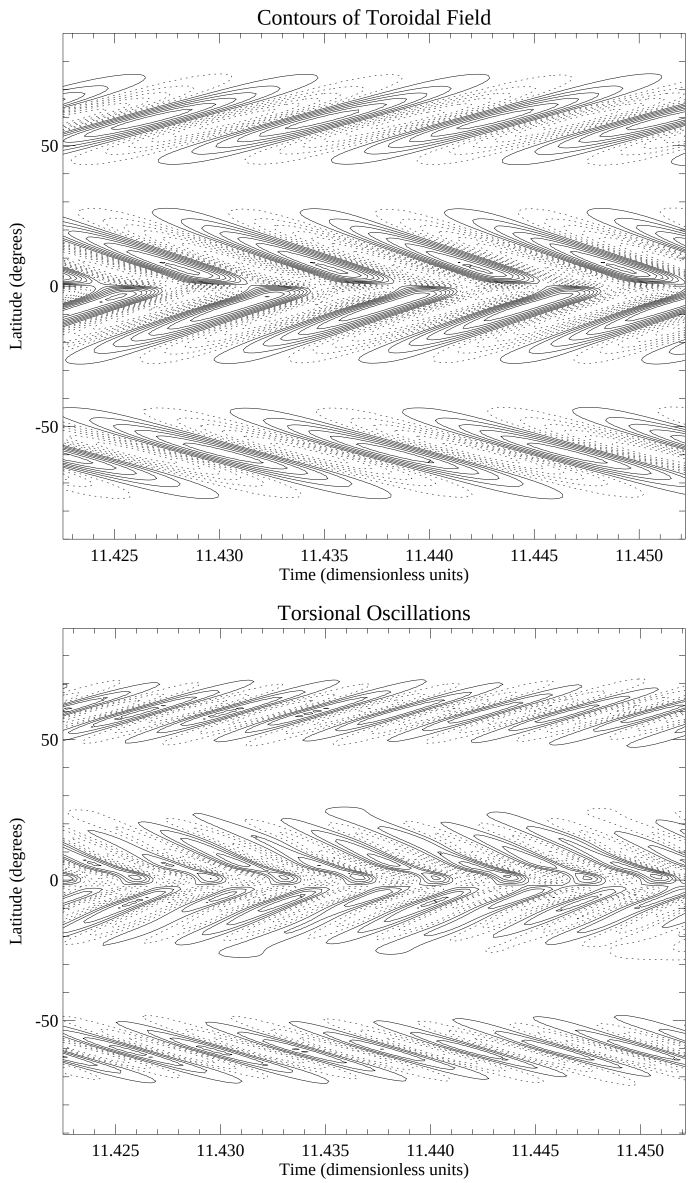

Figure 6.3: Contours of constant toroidal field (top) and the torsional oscillations (bottom), plotted against latitude and time, at the base of the convection zone. Contours are equally spaced, solid lines correspond to positive values, dashed lines correspond to negative values. There is no α-quenching and $D = -2.5 \times 10^6$.

at high latitudes, in this model, by increasing the magnitude of the dynamo number. For values of $D \lesssim -2.25 \times 10^6$, the dynamo possesses a high-latitude branch. As was discussed in Section 5.3, it is possible that there may be activity at high latitudes, at the base of the solar convection zone, that never produces active regions. It appears that this polar branch is necessary from the point of view of the torsional oscillations. Figure 6.3 shows the time evolution of the latitudinal distribution of both the toroidal field and the torsional oscillations, at the base of the convection zone, for $D = -2.5 \times 10^6$. The key new feature is the appearance of a high-latitude branch in the plot showing the torsional oscillations. It should be mentioned that the solution is now weakly modulated, and this is most clearly seen at low latitudes in the torsional oscillations. The parity of the solution is no longer predominantly quadrupolar – in fact it is time dependent, although it varies over a relatively long time-scale (of the order of a diffusion time). Similar behaviour is observed as the magnitude of the dynamo number is increased further. A comparison of this solution with the equivalent plot for the α-quenched case, as shown in Figure 5.21, reveals a slight qualitative difference in the relative strengths of the two branches of the dynamo. The polar branch is still weaker than the equatorial branch, but (with this macrodynamic nonlinearity) there is less of a difference in the peak fields than was seen for the α-quenched case.

Although this model has successfully produced a pattern of oscillations which resembles those observed on the Sun, there is still the problem associated with the parity of the solution. When the sole nonlinearity was due to α-quenching, dipolar solutions were found for moderately supercritical dynamo numbers, whilst predominantly quadrupolar solutions were found for larger values of D. As shown above, if the sole nonlinearity is due to the influence of the Lorentz force upon the differential rotation profile, solutions seem to be either quadrupolar (for moderately supercritical dynamo numbers) or exhibit time-dependent fluctuations in parity (for larger values of the dynamo number). This clearly demonstrates the sensitivity of the parity of the solution to the precise choice

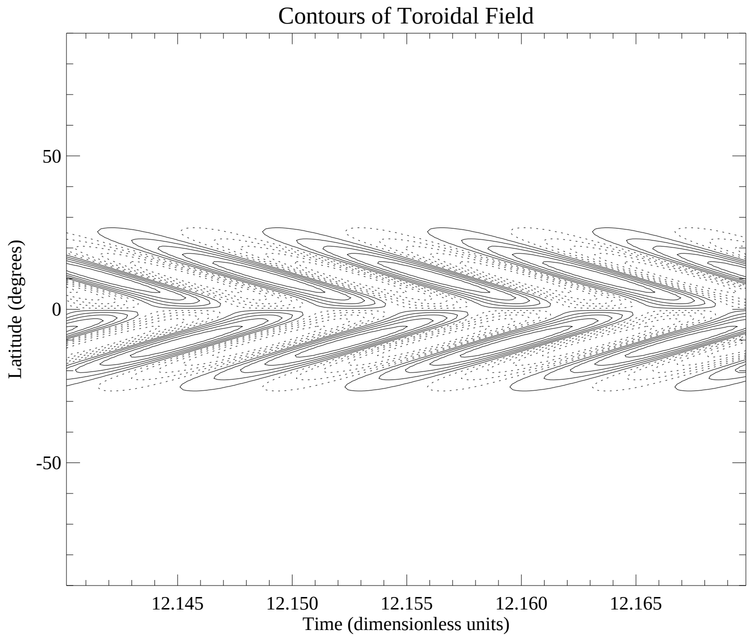

Figure 6.4: As Figure 6.1, but here there is α-quenching. $\Lambda = 100.0$ and $D = -2.0 \times 10^6$.

of nonlinear quenching mechanism. Ideally, we would like to produce a solution that is of predominantly dipolar parity and simultaneously produces a solar-like torsional oscillation pattern.

By setting $\Lambda = 100.0$, it is possible to look at the consequences of having two competing nonlinearities. Contours of toroidal field at the base of the convection zone, for $D = -2.0 \times 10^6$, are shown in Figure 6.4. As found before, for this value of D, magnetic activity is restricted to low latitudes, but the preferred parity is now dipolar. The associated torsional oscillations are identical in form to those shown in Figure 6.2 – a pure parity mode (of either symmetry) will always drive a symmetric velocity perturbation. Increasing the magnitude of D again leads to the appearance of high-latitude magnetic features along with a high-latitude branch to the torsional oscillations. Figure 6.5 shows the time-evolution of the latitudinal distribution of both the toroidal field and the torsional oscillations, at the base of the convection zone, for $D = -2.5 \times 10^6$. In contrast to

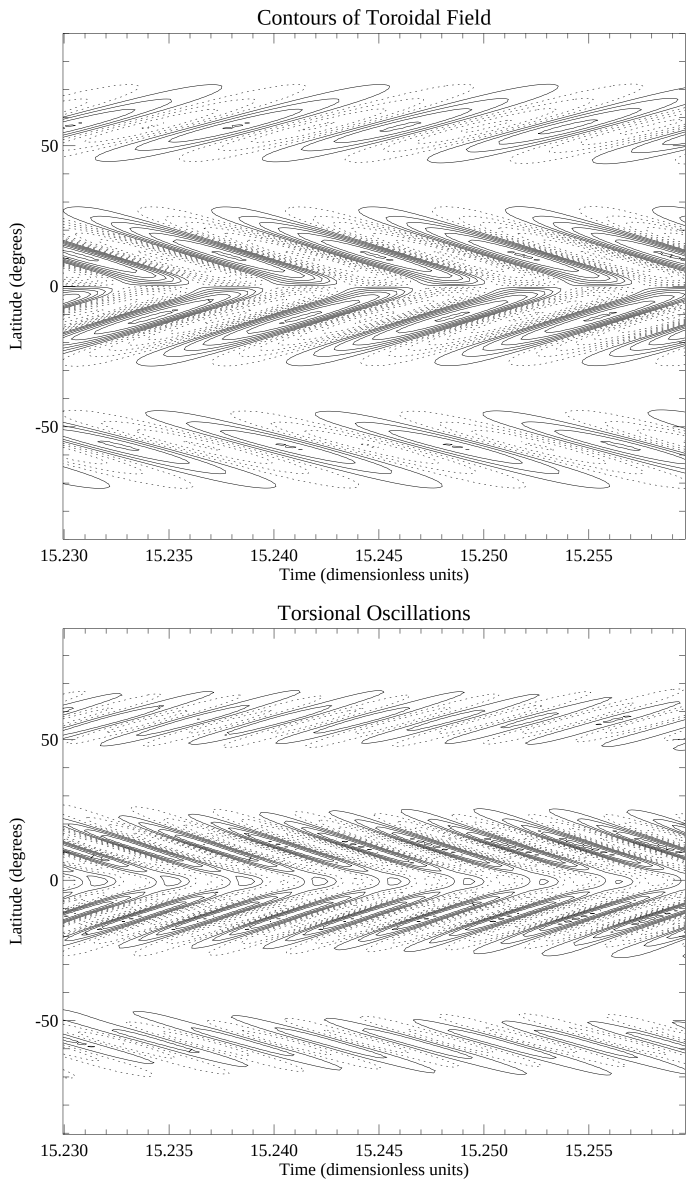

Figure 6.5: As Figure 6.3, with contours of constant toroidal field (top) and torsional oscillations (bottom). Here, there is α-quenching, with $\Lambda = 100.0$, and $D = -2.5 \times 10^6$. This is a dipolar solution with a weak high-latitude branch.

previous simulations, the dynamo now has a polar branch and is still of predominantly dipolar parity. It is possible to see a weak modulation in the amplitude of the torsional oscillations, but there is no significant time-dependent behaviour in the parity of the solution. This has clearly been suppressed by the addition of α quenching to the system. Further (modest) increases in the magnitude of the dynamo number seem to lead to no qualitative changes to the overall form of the solution.

The solution shown in Figure 6.5 represents the most solar-like solution that has been found (for $\tau = 1.0$) with this model. Prior to carrying out these simulations, it was not possible to predict which combination of nonlinearities would lead to dipolar parity persisting well into the nonlinear regime. Clearly the parameterised nature of the α-quenching process is an idealised version of what is actually likely to be happening within the Sun, so it is difficult to come to any firm conclusions regarding the relative importance of different nonlinearities in the solar dynamo. Having said that, these calculations have demonstrated that it is possible to tune the nonlinearities in this (interface-like) mean-field model in order to produce many of the main observational features of the solar magnetic activity and torsional oscillations.

6.3 Time-dependent solutions

6.3.1 Motivation

Recurrent grand minimum phases are known to occur in the solar magnetic activity, with a mean separation of about 200 years (see Section 1.2.2). It is well-known that by taking a value of the magnetic Prandtl number, τ, that is substantially less than unity, it is possible to produce magnetic cycles that are modulated on a longer time-scale (see, for example, Tobias, 1996b, 1997b; Küker et al., 1999; Moss and Brooke, 2000; Brooke et al., 2002). The modulational time-scale is determined by the value of τ, which determines the separation in scales between the magnetic relaxation time and the viscous relaxation time of the fluid. Small values of τ imply that any velocity perturbation will decay away on a much longer time-scale than the associated magnetic fields. If this velocity perturbation is large enough to suppress dynamo action, this may then lead to prolonged periods of reduced activity. The most detailed study of time-dependent behaviour, in a spherical model, has been carried out by Moss and Brooke (2000). They focused primarily upon low values of the magnetic Prandtl number (typically, $\tau = 0.01$) and, even for mildly supercritical solutions, intermittent behaviour was found for these simulations. Having said that, slightly larger values of τ seemed to favour doubly periodic solutions, which may be more closely related to the observed solar magnetic activity, although the "grand minima" of these solutions are not very deep. In the calculations that are described in this section, the effects of reducing the value of τ are investigated for the model that was described in the previous section. As discussed above, this model is more interface-like than that of Moss and Brooke (2000), so should perhaps be viewed more as a spherical analogue (with a realistic rotation law) of the calculations described by Tobias (1997b) and Brooke et al. (2002).

Brooke et al. (2002) claim that solar-like torsional oscillations are incompatible with low values of the magnetic Prandtl number – they refer to this problem as the "Prandtl number dilemma". This rather surprising result is based upon simulations that were carried out for their Cartesian model, and one of the primary aims of the simulations that are described below was to investigate this issue. Certainly we would expect an oscillatory magnetic field to drive an oscillatory component to the angular velocity perturbation, regardless of the value of τ, and it is difficult to see how such a dynamo could saturate in the nonlinear regime without these torsional oscillations. It is possible that the problem centres around the need to subtract a time-average from the total velocity perturbation in order to reveal the oscillatory signal. Since the torsional oscillations are relatively weak, it is virtually impossible to pick out any oscillations without the subtraction of this time-average. For strongly modulated solutions, this time-average will be

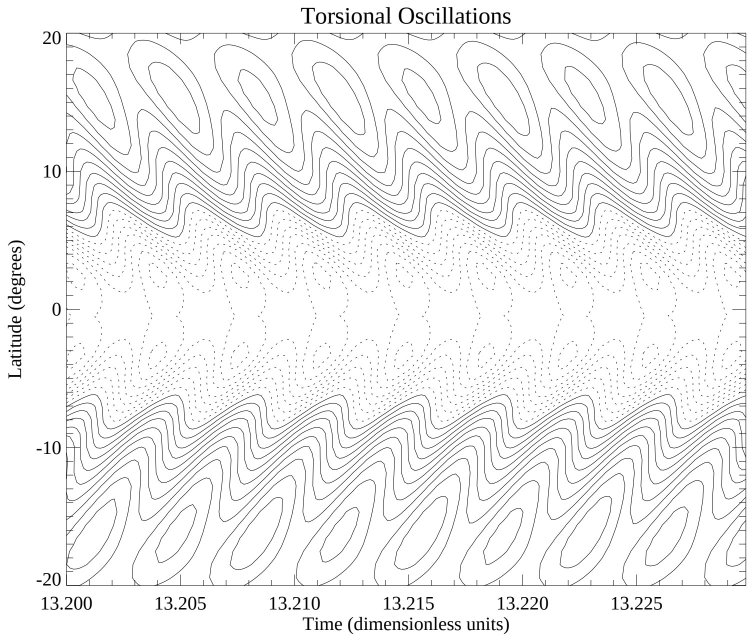

Figure 6.6: Contours showing the perturbation to the total angular velocity after the subtraction of a time-averaged quantity, plotted against latitude and time, at the base of the convection zone ($r = 0.7$). Here, attention is restricted to low latitudes, and the time-average that has been subtracted is independent of latitude. Contours are equally spaced, solid lines correspond to positive perturbations to the angular velocity, dashed lines correspond to negative perturbations. Here, there is no α-quenching, and $D = -2.0 \times 10^6$.

a function of time and therefore it may not be possible to take an average over a short enough time period to reveal the higher frequency oscillations – they may be swamped by the large-scale (lower frequency) modulation. Having said that, Brooke et al. (2002) seem to fail to find torsional oscillations even for solutions that are only very weakly modulated, so this is presumably not the only problem.

The solution to this problem may be in the way in which the time-average is actually calculated. Although their model is Cartesian rather than spherical, Brooke et al. (2002)

effectively pick some value of the radius and then look at the total velocity perturbation at that radius (as a function of latitude). They then pick some latitude and calculate the average velocity perturbation at this single point in space. They then subtract this single time-averaged quantity from the total velocity perturbation at **all** latitudes at the fixed radius. This averaging procedure therefore takes no account of the fact that the time-average may vary with latitude. Whilst this method should reveal the presence of any oscillations at the latitude at which this average is taken, the fact that the time-averaged perturbation is clearly not latitude-independent implies that we may not see oscillations at other latitudes. Figure 6.2 shows a pattern of torsional oscillations that plausibly averages to zero at all latitudes – none of the plots that are shown in Brooke et al. (2002) satisfy this property. This may have lead to spurious conclusions regarding the spatial distribution of torsional oscillations. To illustrate this, Figure 6.6 shows the solution from Figure 6.2, after a similar latitude-independent time-average has been applied. The average has been taken at a latitude of about 7 degrees, where the oscillations are strongest in Figure 6.2. Although an oscillatory signal (of the same period) is visible, it is not possible to identify the torsional oscillation pattern that was shown in Figure 6.2, even for $\tau = 1.0$. Varying the latitude at which the time-average is taken did not enhance this oscillatory signal. The apparent absence of torsional oscillations is probably a consequence of the fact that the solution described here varies much more dramatically with latitude than those found in the simplified model that was described by Brooke et al. (2002) – the subtraction of a latitude-independent time-average is therefore inadequate. This confirms the need to allow the time-average to be a function of latitude, and the conclusions of Brooke et al. (2002) should therefore be treated with caution.

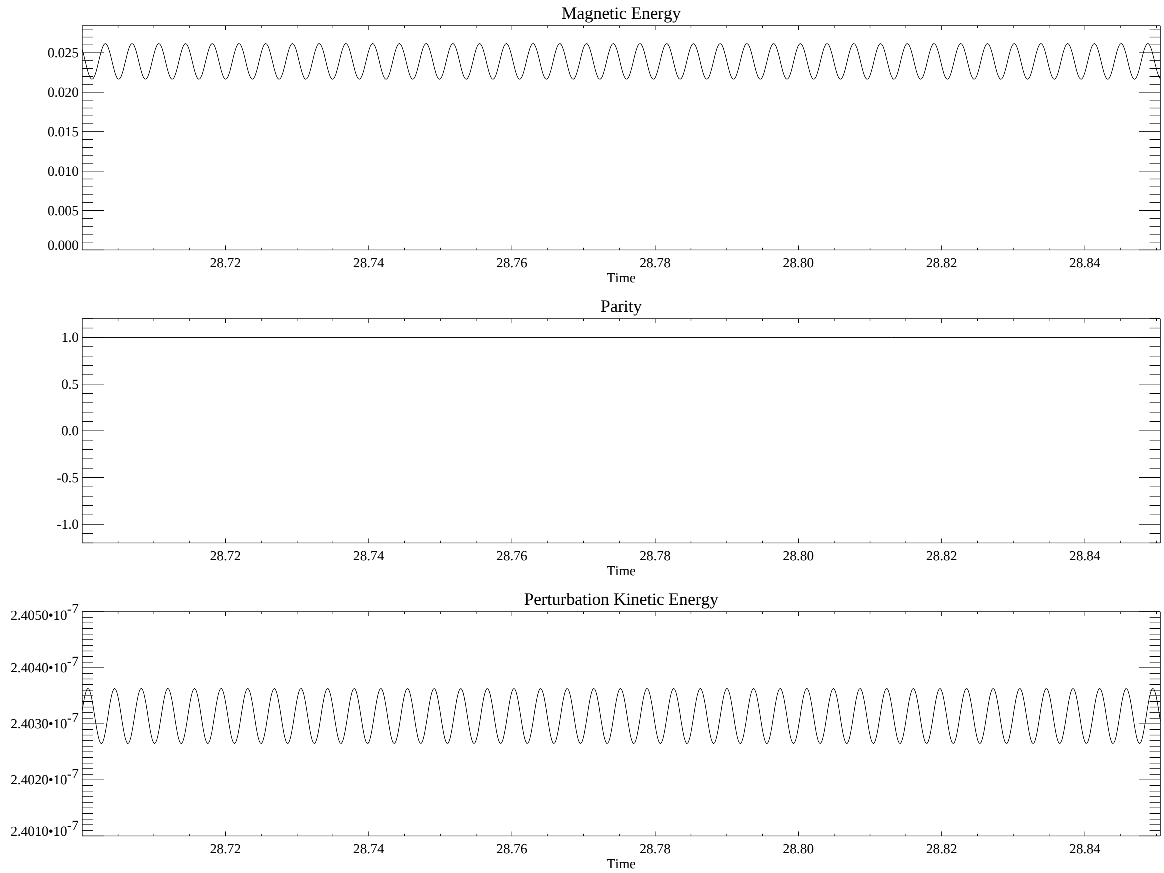

Figure 6.7: Time series for the magnetic energy (top), parity (middle) and the perturbation kinetic energy (bottom). As before, time is measured in dimensionless units. For all of these plots $\tau = 0.05$, there is no α-quenching, and $D = -1.5 \times 10^6$.

6.3.2 Results for $\tau = 0.05$

As an initial investigation, the magnetic Prandtl number is fixed at $\tau = 0.05$. This value is selected somewhat arbitrarily, but it should be small enough to produce time-dependent behaviour for sufficiently large values of the dynamo number. For these simulations, α-quenching is initially removed, but the effects of including this additional nonlinearity are briefly investigated later on. Although torsional oscillations form an important part of this study, and are described in detail later on in the chapter, it is

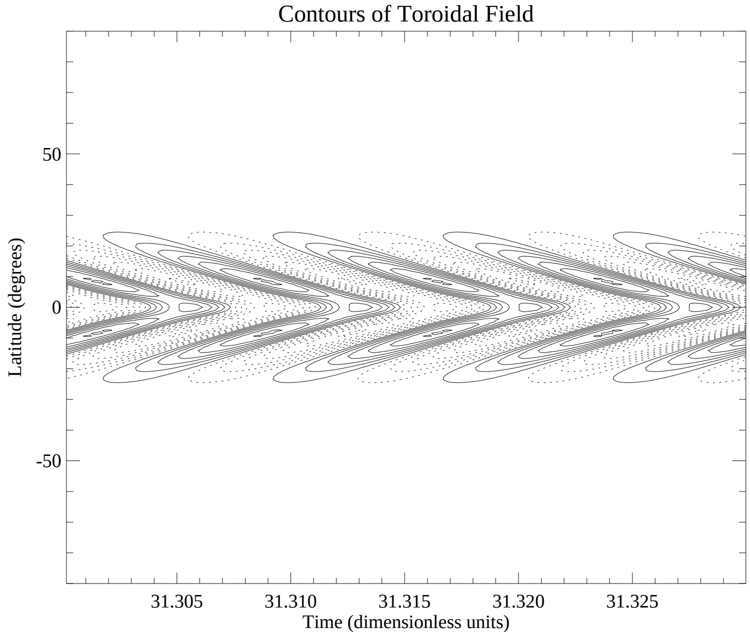

Figure 6.8: As Figure 6.1, but here $\tau = 0.05$, there is no α-quenching, and $D = -1.5 \times 10^6$.

also of interest to establish (in more general terms) the influence that low magnetic Prandtl numbers have upon the time-dependent behaviour of the dynamo.

Mildly supercritical solutions are produced by taking $D = -1.5 \times 10^6$. Figure 6.7 shows how various quantities – the total magnetic energy, the parity and the perturbation kinetic energy – evolve with time, for this set of parameters. These oscillations are singly periodic, with no modulation observed in any of these time-series. Figure 6.8 shows contours of constant toroidal field, at the base of the convection zone, plotted against latitude and time. As would be expected, the magnetic activity is confined to low latitudes and migrates equatorwards during each magnetic cycle.

A qualitative change in behaviour is observed when the magnitude of the dynamo number is increased. For $D = -2.0 \times 10^6$, the solution is now multiply-periodic – at least 2 frequencies can be picked out from the time-series that are shown in Figure 6.9. This solution differs from that found for $D = -1.5 \times 10^6$ in several ways. The most notable

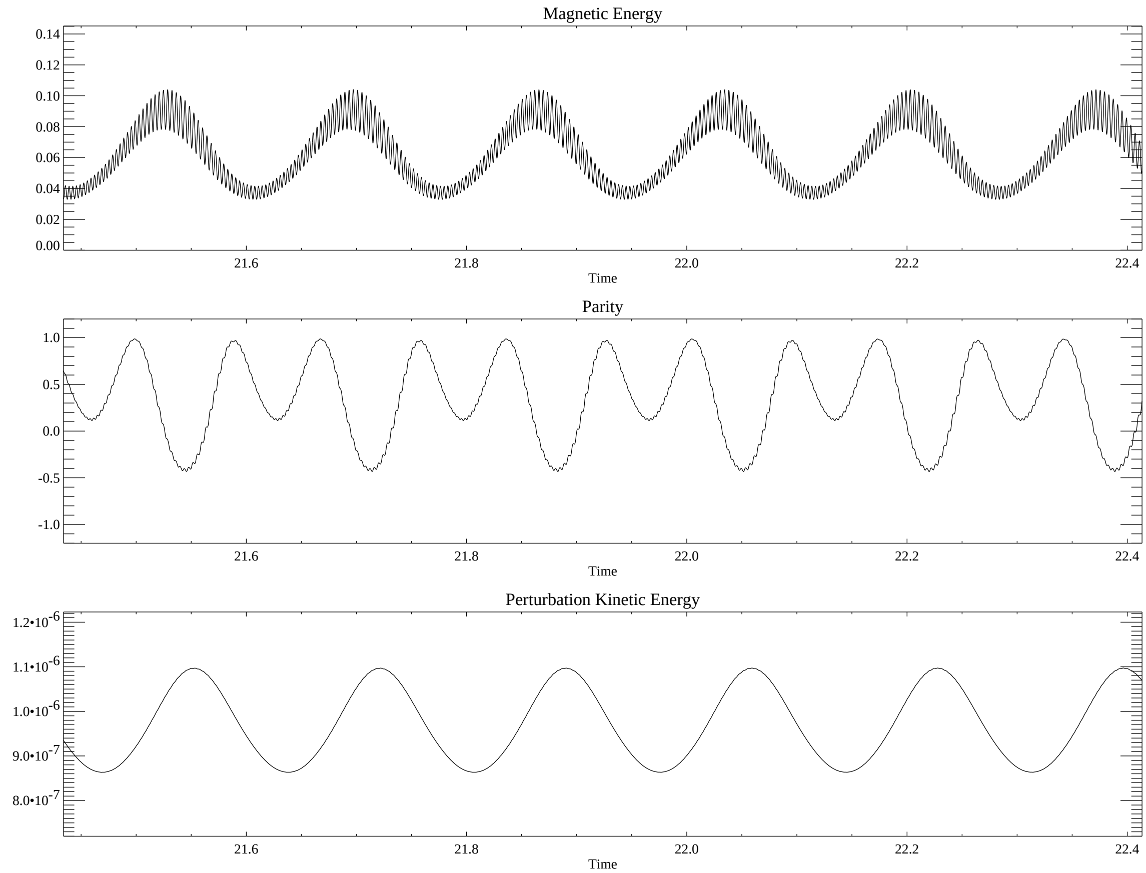

Figure 6.9: Time series for the magnetic energy (top), parity (middle) and the perturbation kinetic energy (bottom). As before, time is measured in dimensionless units. For all of these plots $\tau = 0.05$, there is no α-quenching, and $D = -2.0 \times 10^6$.

difference is the fact that the total magnetic energy shows significant periodic changes, varying by almost a factor of 3 as the dynamo oscillates between active phases and "grand minima". A frequency analysis indicates that the ratio of the magnetic cycle frequency to the main modulational frequency is approximately 45 : 1. By way of comparison, the observed ratio of the magnetic cycle frequency to the frequency of occurrence of grand minima is approximately 10 : 1 for the Sun. Other notable features of Figure 6.9 include the fluctuations in the parity of the solution and the fact that the modulation

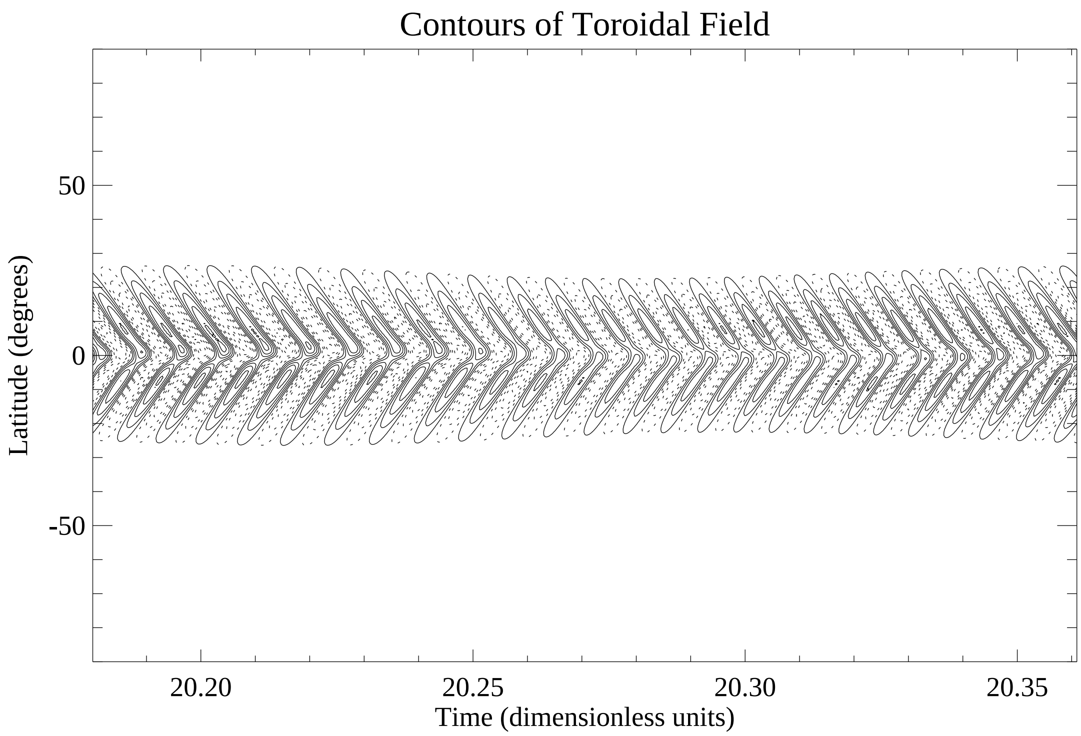

Figure 6.10: As Figure 6.1, but here $\tau = 0.05$, there is no α-quenching, and $D = -2.0 \times 10^6$. Note the modulation in the amplitude and parity of the oscillations.

of the perturbation kinetic energy seems to completely mask the fluctuations due to the torsional oscillations. This last fact is of particular importance when considering the impact that high levels of modulation may have upon the torsional oscillations, as will be seen later. Figure 6.10 shows contours of toroidal field, at the base of the convection zone, for $D = -2.0 \times 10^6$. Although this solution is clearly modulated, this plot illustrates the fact that the grand minima phases for $\tau = 0.05$ are not particularly deep.

For the solutions for $\tau = 1.0$, that were described in Section 6.2, it was found that taking $D = -2.5 \times 10^6$ resulted in the excitation of weak magnetic oscillations (and associated torsional oscillations) at high latitudes in addition to the strong low-latitude

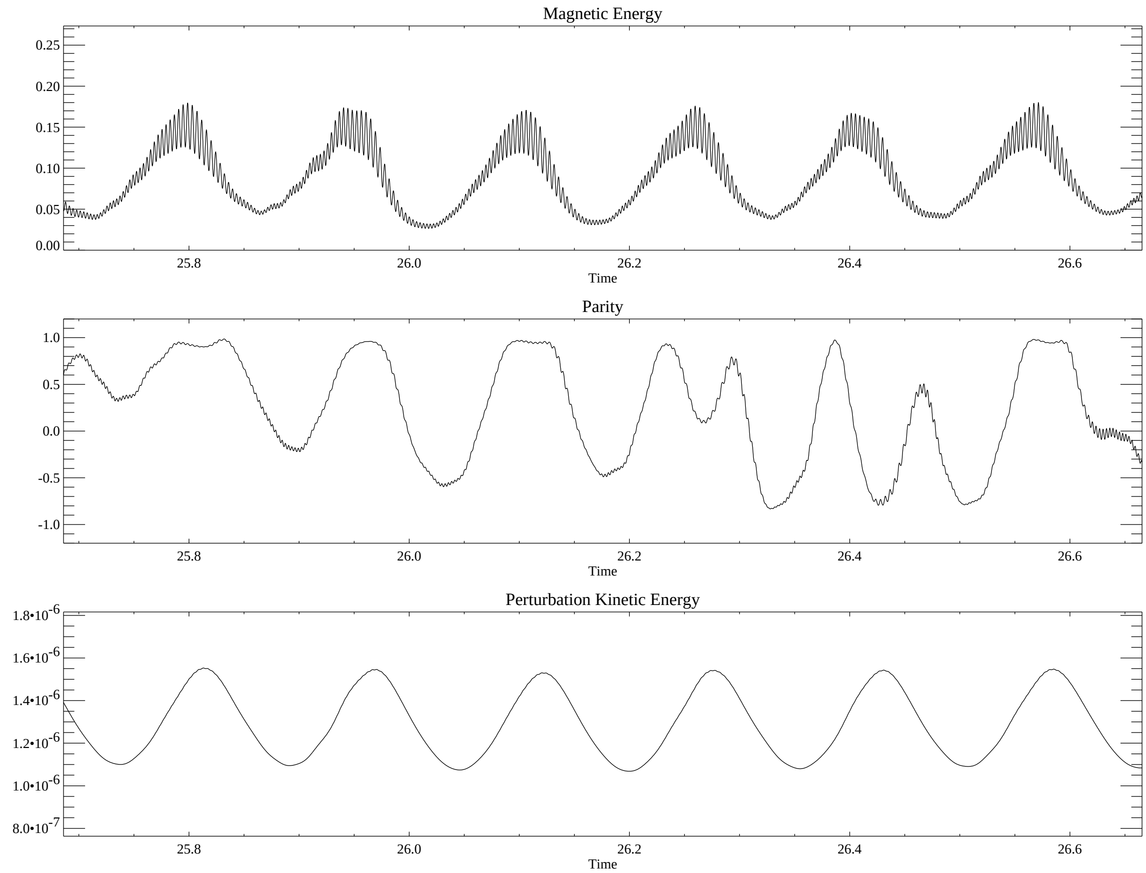

Figure 6.11: Time series for the magnetic energy (top), parity (middle) and the perturbation kinetic energy (bottom). As before, time is measured in dimensionless units. For all of these plots $\tau = 0.05$, there is no α-quenching, and $D = -2.5 \times 10^6$.

features. The time-series for $D = -2.5 \times 10^6$ are shown in Figure 6.11. As before, appreciable modulation is observed in the magnetic energy. This modulation now appears to be chaotic, although there is still a dominant frequency component associated with the main modulational time-scale. Certainly the parity fluctuations are now chaotic. Interestingly it appears that, for this set of parameters, significant modulation in the magnetic energy always seems to be associated with modulation in the parity of the solution. Figure 6.12 shows contours of constant toroidal field, at the base of the con-

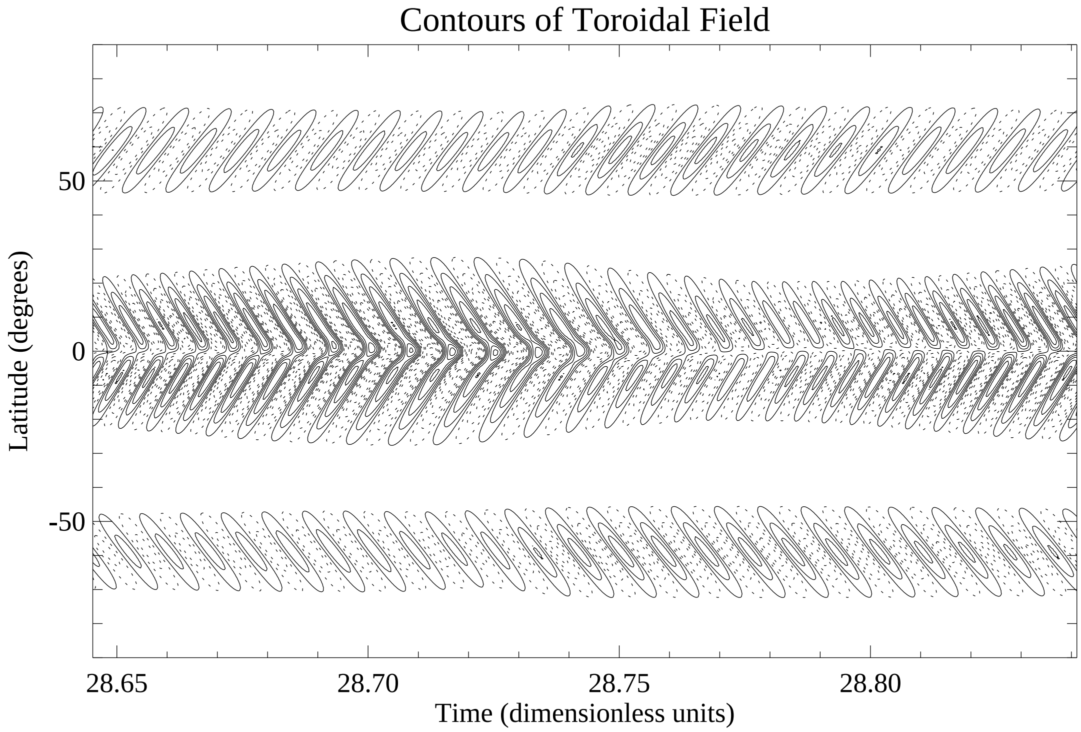

Figure 6.12: As Figure 6.1, but here $\tau = 0.05$, there is no α-quenching, and $D = -2.5 \times 10^6$.

vection zone, for $D = -2.5 \times 10^6$. Significant modulation is observed here, although the high-latitude branch seems to be out of phase with the the low-latitude branch. This "decoupling" between the modulation of the magnetic activity at high and low latitudes appears to be a recurrent feature of this model. Similarly time-dependent behaviour is observed as the magnitude of the dynamo number is increased further and, as shown in Figure 6.13, the modulation becomes increasingly chaotic.

Adding α-quenching back into the model, by setting $\Lambda = 100.0$, should make a qualitative difference to the results. This instantaneous quenching mechanism places a significant restriction upon the peak magnetic field strength and therefore also the peak magnitude of the Lorentz force. This may reduce the velocity perturbation and therefore

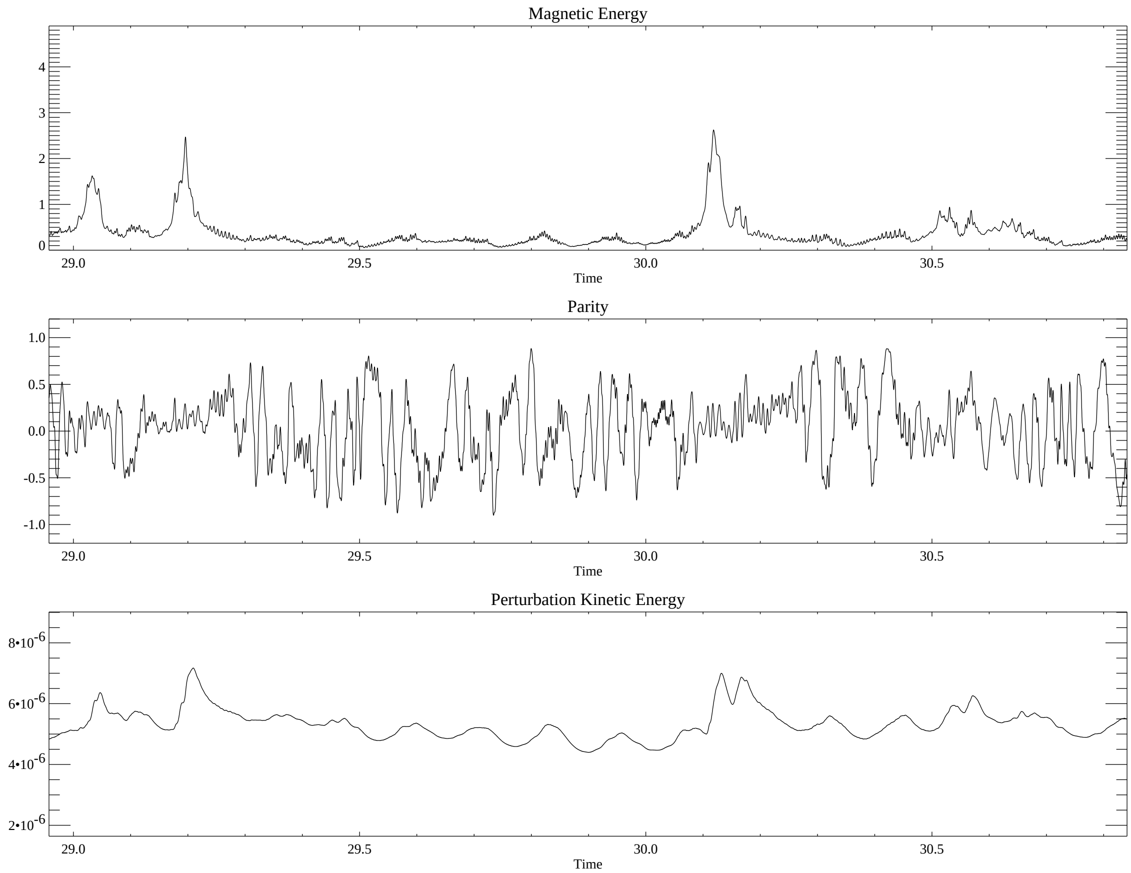

Figure 6.13: Time series for the magnetic energy (top), parity (middle) and the perturbation kinetic energy (bottom). As before, time is measured in dimensionless units. For all of these plots $\tau = 0.05$, there is no α-quenching, and $D = -3.0 \times 10^6$.

may limit the modulational effects. What is actually observed is that this additional quenching delays the onset of modulation – the solution is still singly periodic and dipolar for $D = -2.0 \times 10^6$. However, a further increase in the magnitude of D rapidly leads to the onset of significant chaotic modulation, both in terms of the magnetic energy and the parity of the solution. This is illustrated in Figure 6.14, which shows time-series for $D = -2.5 \times 10^6$. A comparison of Figures 6.11 and 6.14 suggests that the extent of modulation, for this value of the dynamo number, is similar for the quenched and the

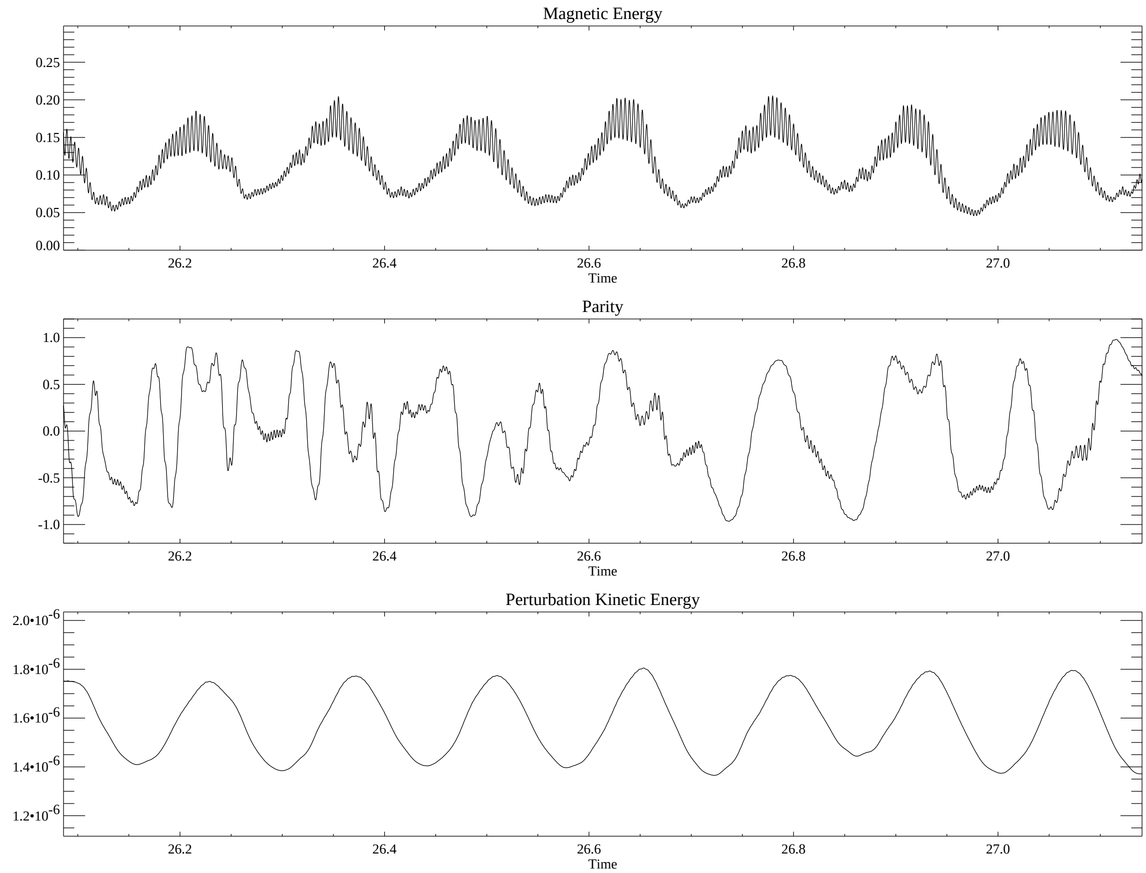

Figure 6.14: Time series for the magnetic energy (top), parity (middle) and the perturbation kinetic energy (bottom). As before, time is measured in dimensionless units. For all of these plots $\tau = 0.05$, $D = -2.5 \times 10^6$ and $\Lambda = 100.0$.

unquenched cases. For this value of the magnetic Prandtl number, the only effect that adding α-quenching seems to have is to delay the onset of time-dependent behaviour.

6.3.3 Varying the value of τ

Having established the existence of highly modulated solutions for a fixed value of the magnetic Prandtl number, it is now important to test the sensitivity of these solutions to variations in the value of τ. For $\tau = 0.05$ it was found that the more the magnitude

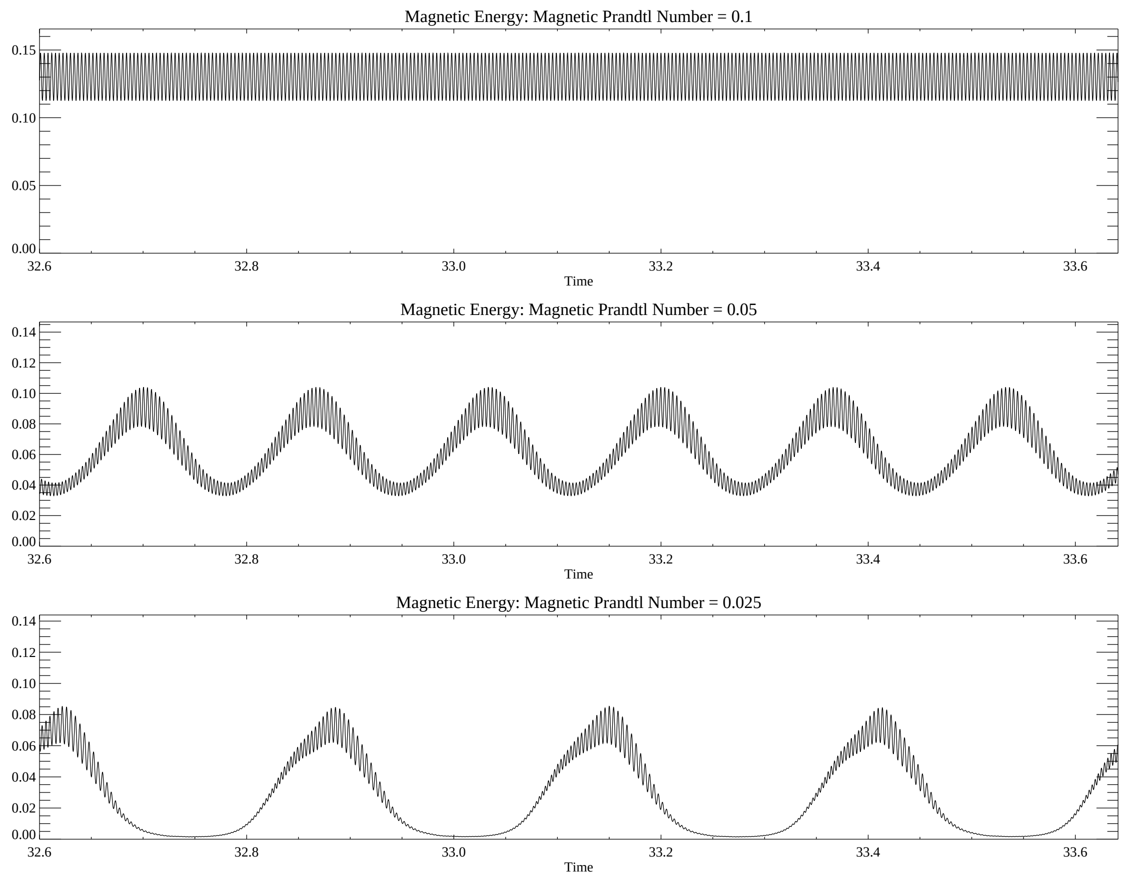

Figure 6.15: A comparison of the time series for the magnetic energy for $\tau = 0.1$ (top), $\tau = 0.05$ middle (middle) and $\tau = 0.025$ (bottom). As before, time is measured in dimensionless units. For all of these plots $D = -2.0 \times 10^6$ and there is no α-quenching.

of the dynamo number is increased, the more time-dependent the dynamo becomes. Figures 6.15 and 6.16 demonstrate the influence that different values of τ have upon the modulation of the magnetic energy time series, for $D = -2.0 \times 10^6$ and $D = -2.5 \times 10^6$ respectively. There is no α-quenching in any of the solutions that are described in this section. The general trend is clear: modulation becomes more dramatic, with longer periods of modulation, for lower values of the magnetic Prandtl number.

The only singly periodic solution that is shown here is for $D = -2.0 \times 10^6$ and $\tau = 0.1$.

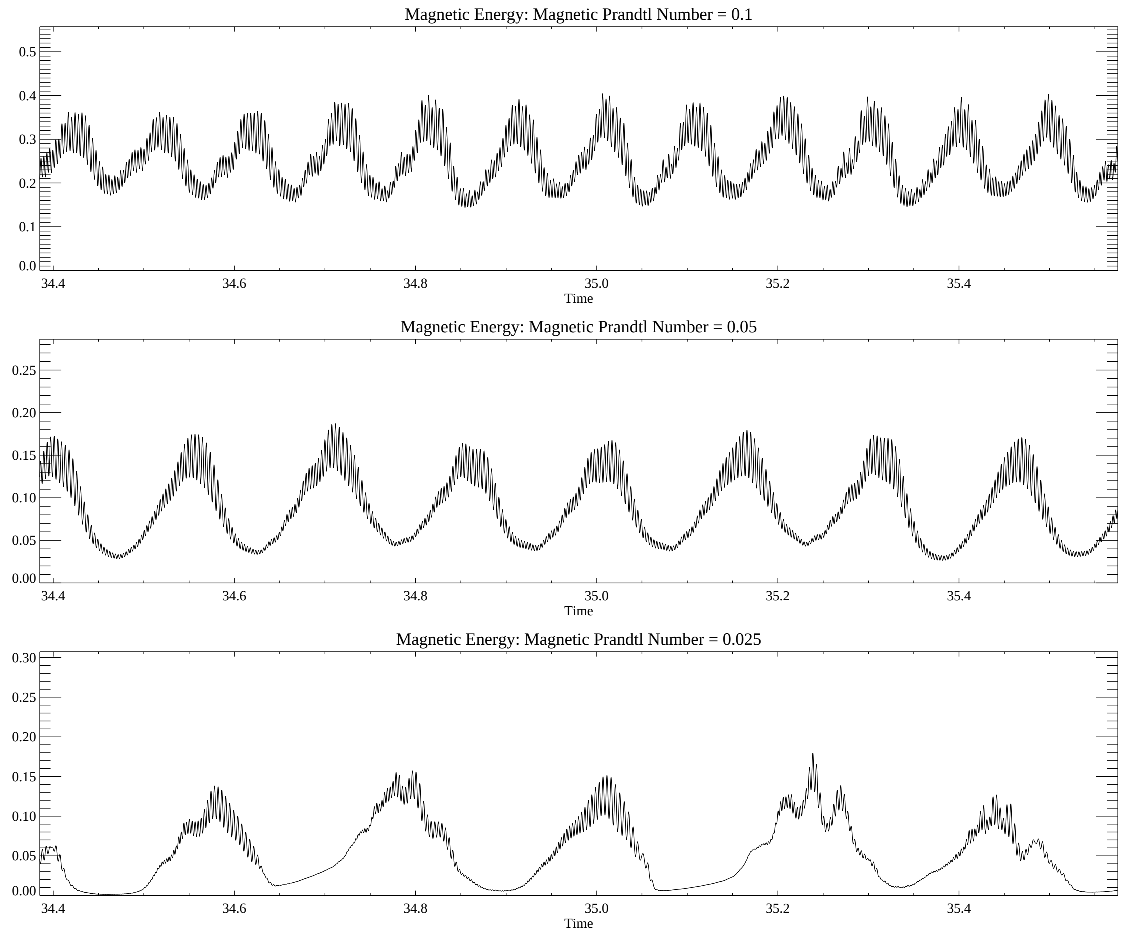

Figure 6.16: A comparison of the time series for the magnetic energy for $\tau = 0.1$ (top), $\tau = 0.05$ middle (middle) and $\tau = 0.025$ (bottom). As before, time is measured in dimensionless units. For all of these plots $D = -2.5 \times 10^6$ and there is no α-quenching.

Figure 6.17 shows contours of constant toroidal field at the base of the convection zone for $D = -2.0 \times 10^6$ and $\tau = 0.1$. The parity of this solution is steady and quadrupolar and, as before, activity is confined to low latitudes at the base of the convection zone.

As was seen in the previous section, $\tau = 0.05$ gives a modulated solution, for this value of the dynamo number, with a well-defined dominant frequency of modulation. This remains the case when τ is reduced to 0.025. Figure 6.18 shows contours of toroidal

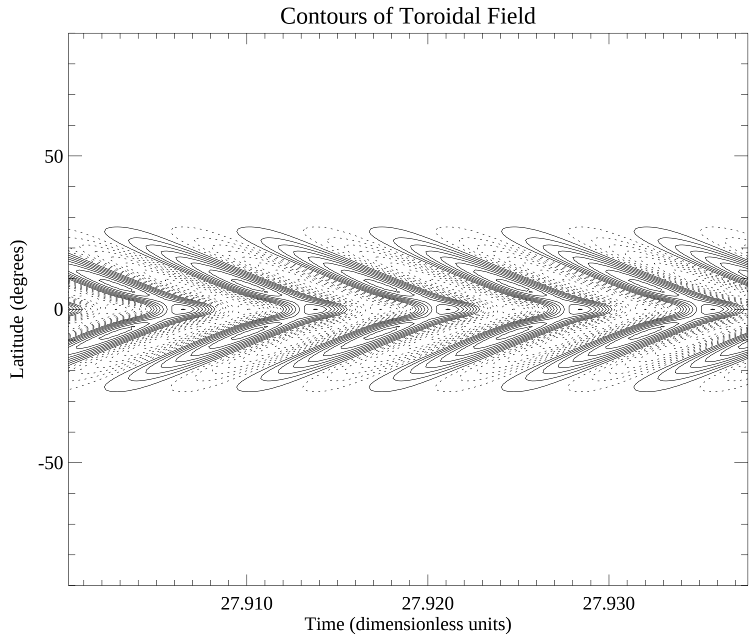

Figure 6.17: As Figure 6.1, but here $\tau = 0.1$, there is no α-quenching, and $D = -2.0\times10^6$.

field at the base of the convection zone for $D = -2.0 \times 10^6$ and $\tau = 0.025$. The temporal range for this plot has been chosen so as to include a grand minimum phase – as the dynamo enters and leaves this period of reduced activity, it possesses the kind of asymmetry that was observed at the very end of the Maunder minimum. One problem with this solution is that the periods of reduced activity are too long. As can be seen in Figure 6.15, the dynamo actually spends more time in grand minima phases than it does in active phases. What is more, significant oscillations in the magnetic energy, on the magnetic cycle time-scale, are only observed for a relatively small fraction of each modulational cycle. This behaviour is therefore no longer solar-like.

A more extreme example of this kind of behaviour is found for $D = -2.0 \times 10^6$ and $\tau = 0.01$ – the relevant time-series for this solution are shown in Figure 6.19. This solution is characterised by prolonged grand minima, which are periodically interrupted by brief phases of activity. It appears that low values of the magnetic Prandtl number

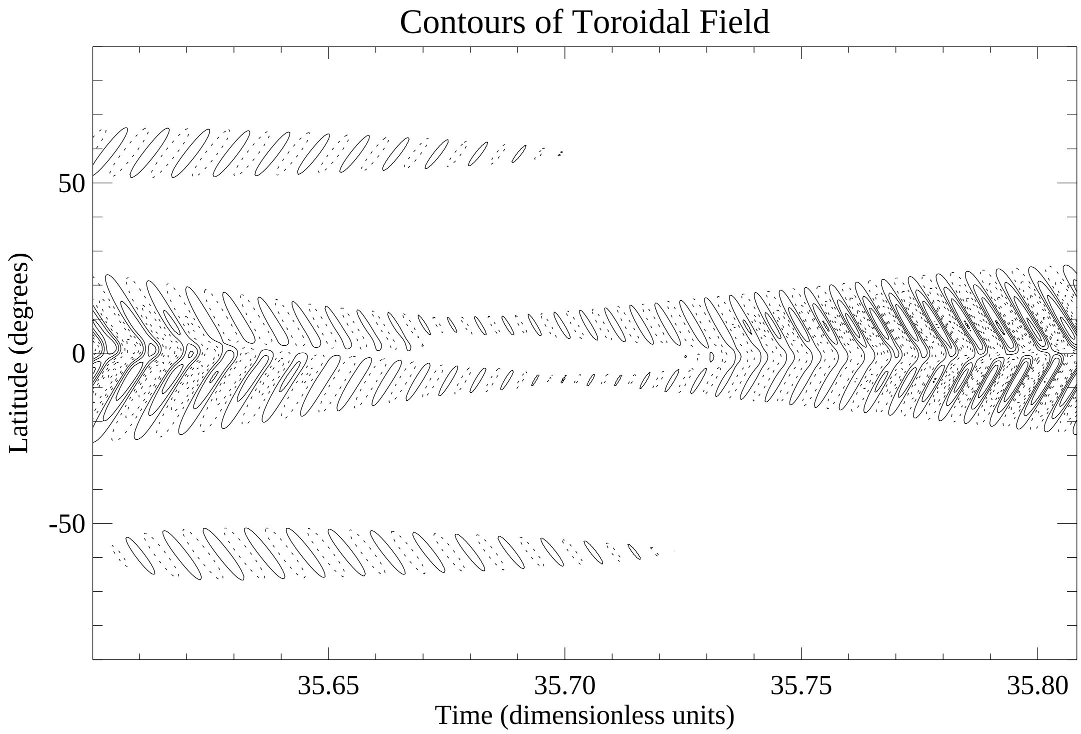

Figure 6.18: As Figure 6.1, but here $\tau = 0.025$, there is no α-quenching, and $D = -2.0 \times 10^6$. This shows a prolonged grand minimum phase.

tend to prolong the inactive phases of the dynamo, whilst leaving virtually unaltered the time spent during active phases. This is unsurprising given that low value of τ imply that large velocity perturbations, which are responsible for the suppression of dynamo action, take longer to decay. In the Sun, we appear to observe this scenario in reverse: prolonged active phases with short grand minima. Similar behaviour was found by Brooke et al. (2002), for moderately supercritical values of the dynamo number and low values of τ, in their Cartesian model. The time-dependent nature of the parity is also rather non-solar like – the parity is roughly constant during grand minima phases, with significant fluctuations tending to occur only during active phases. Moss and Brooke (2000) found similar behaviour in the low-τ regime in their spherical model. So, although this solution

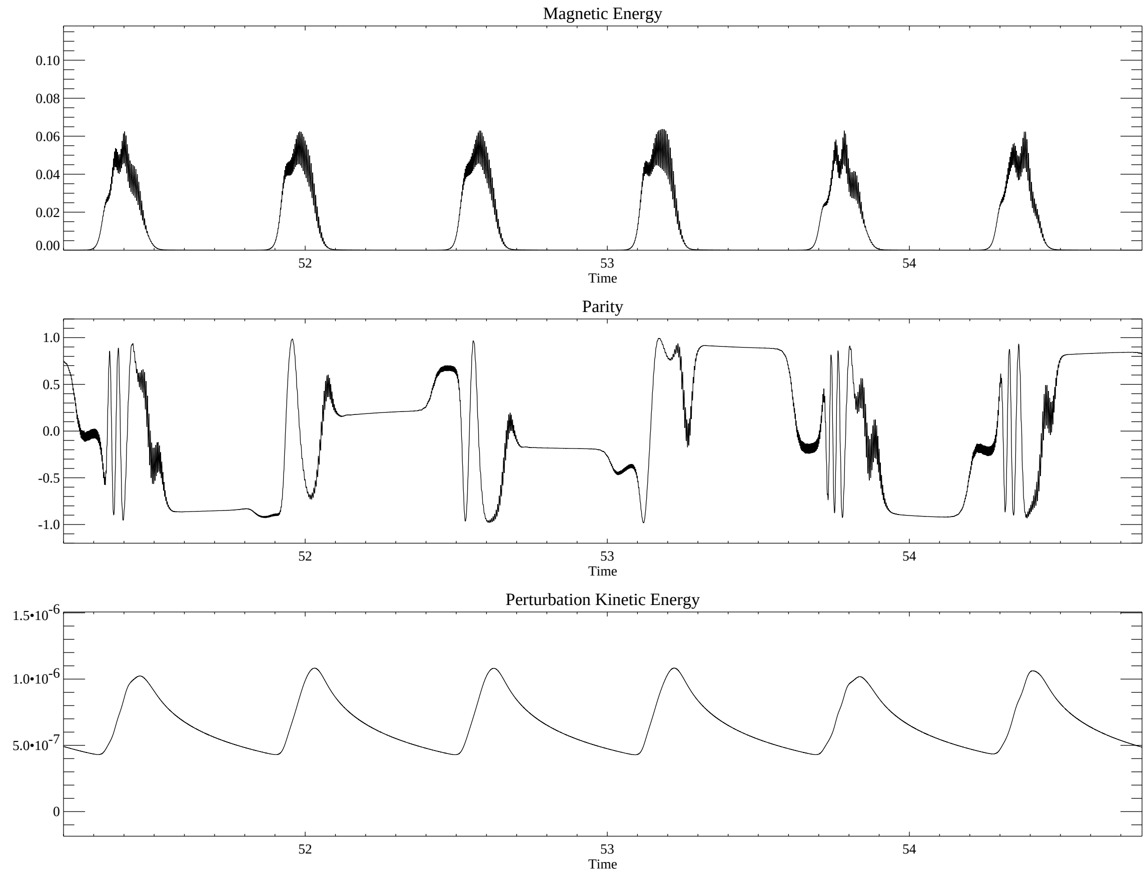

Figure 6.19: Time series for the magnetic energy (top), parity (middle) and the perturbation kinetic energy (bottom). As before, time is measured in dimensionless units. For all of these plots $\tau = 0.01$, there is no α-quenching, and $D = -2.0 \times 10^6$.

is mathematically interesting, its applicability to the solar dynamo is probably only limited.

For $D = -2.5 \times 10^6$ the solution is rather more modulated, although it is still possible to pick out a dominant frequency of modulation. As before, the general trend is for lower values of the magnetic Prandtl number to lead to longer, and deeper, periods of reduced activity. Again, it should be noted that the grand minima phases for $\tau = 0.025$ are comparable in duration to the active phases. This again suggests that lower values of

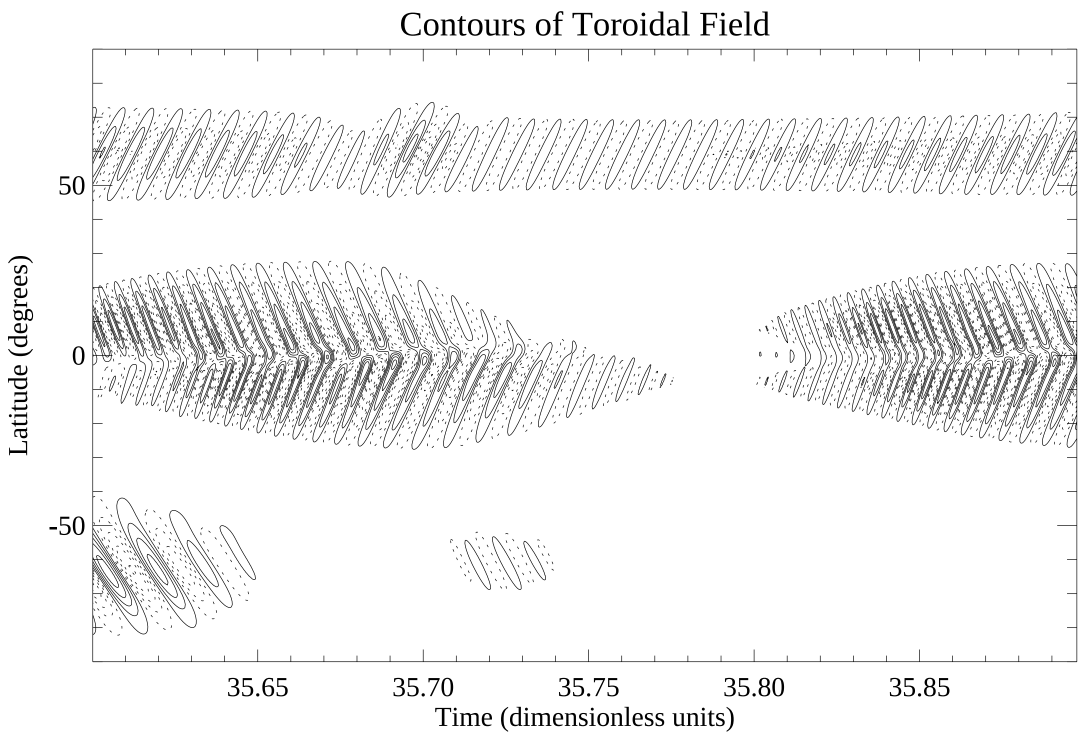

Figure 6.20: As Figure 6.1, but here $\tau = 0.025$, there is no α-quenching, and $D = -2.5 \times 10^6$.

τ will result in non-solar like behaviour. The strong modulation that is observed for $\tau = 0.025$ is shown in Figure 6.20. The high-latitude branch of the dynamo seems to be modulated independently and, although generally weaker, this will complicate the overall modulation of the time-series for the magnetic energy.

In their Cartesian models, Tobias (1997b) and Brooke et al. (2002) managed to quantify the way in which the modulational time-period scales with the magnetic Prandtl number. They found that the mean period between grand maxima is approximately proportional to τ^{-n}, for some value of n – Tobias found n to be 0.5, whilst Brooke et al. found that $n = 0.67$ gave a better approximation to the scaling law. Given that different dynamo numbers were used, as well as different ranges for τ, it is not surprising that

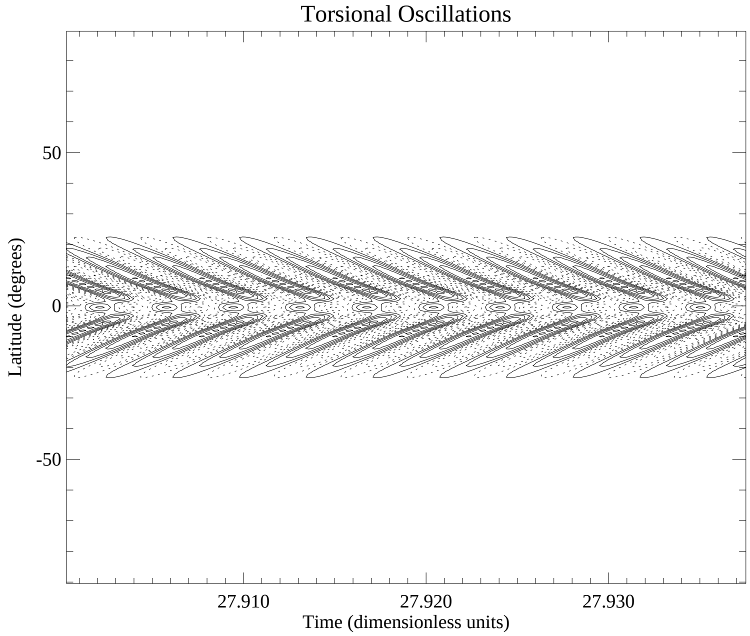

Figure 6.21: As Figure 6.1, but here showing torsional oscillations at the base of the convection zone ($r = 0.7$). Here, $\tau = 0.1$, there is no α-quenching, and $D = -2.0 \times 10^6$.

slightly different values were obtained. The results from this spherical model are largely consistent with this general scaling: $n = 0.6$ was found to give the best fit to the results for $D = -2.5 \times 10^6$, and the results for $D = -2.0 \times 10^6$ seem to be largely consistent with this. It proved rather more difficult to pick out a scaling law for the peak value of the magnetic energy, but it is clear that lower values of τ lead to lower peak values of the magnetic energy. This is easily explained by noting that a reduction in the value of τ implies less viscous diffusion and therefore larger velocity perturbations can arise. These larger velocity perturbations will more efficiently suppress the generation of magnetic fields.

6.3.4 Torsional oscillations in the low-τ regime

Having identified the main patterns of modulation that arise in the low-τ regime, it is now time to focus upon the effects that such modulation has upon the torsional oscillations. Brooke et al. (2002) assert that torsional oscillations are incompatible with small values of the magnetic Prandtl number. Their claim is illustrated, for $\tau = 0.1$, using a seemingly un-modulated solution that occurs for a moderately supercritical value of the dynamo number (as shown in Figure 5 of their paper). Using the results described above, taking $\tau = 0.1$ and $D = -2.0 \times 10^6$ probably corresponds to an equivalent solution in this spherical model. Figure 6.21 shows torsional oscillations at the base of the convection zone, for these parameter values, after the subtraction of a latitude-dependent time-average. It can clearly be seen that it is possible to produce solar-like torsional oscillations, with a clear pattern of alternating bands of faster and slower than average flow, which migrate towards the equator as the cycle progresses. A comparison of Figure 6.21 and Figure 6.17 confirms that the period of oscillation for these torsional oscillations is half that of the magnetic cycle. This seems to confirm the suggestion, made in Section 6.3.1, that the failure of Brooke et al. to find torsional oscillations for low values of τ may be a consequence of an inadequate, latitude-independent, time-averaging procedure. Small values of τ may lead to more latitude-dependence in the velocity perturbation because there is less viscous diffusion to smooth it out.

A far more interesting problem is posed by the modulated solutions that are found, for $\tau = 0.1$, for larger values of D. In order to produce a polar branch to the torsional oscillations (as observed by, for example, Vorontsov et al., 2002), larger values of the dynamo number must be investigated. Torsional oscillations at the base of the convection zone, for $D = -2.5 \times 10^6$, are shown in Figure 6.22. Because of the fact that significant modulation is now present, it is necessary to take the time-average over a much shorter time-period in order to reveal the correct pattern of torsional oscillations. Although there are clearly well-defined bands of oscillations (at both low and high latitudes) in

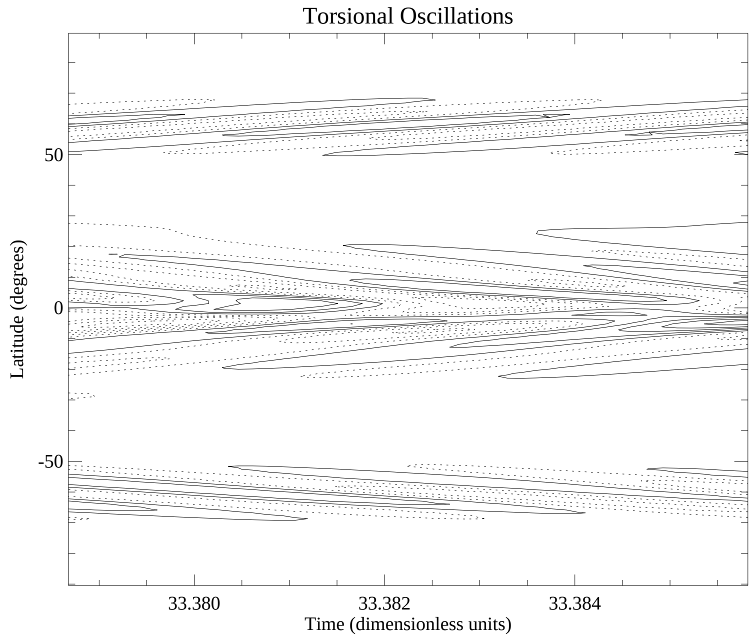

Figure 6.22: As Figure 6.21, but here, $\tau = 0.1$, there is no α-quenching, and $D = -2.5 \times 10^6$. The time-average has been taken over (roughly) two magnetic cycles.

Figure 6.22, there is evidence of the overall modulation, particularly at low latitudes. If the time-average is taken over a longer period of time, upon the subtraction of this average from the total angular velocity perturbation, oscillations of this frequency will be masked by the lower frequency large-scale modulation to the perturbation kinetic energy. So modulation does not rule out the possibility of torsional oscillations, but the time-average needs to be done carefully, and over a relatively short time-period, in order to identify the appropriate oscillatory signal.

For a given value of the dynamo number, it has been shown that smaller values of τ tend to produce more extreme modulation. Having said that, for $D = -1.5 \times 10^6$ and $\tau = 0.05$, the magnetic energy is still a singly periodic function of time. As would be expected, torsional oscillations are again found – like those shown in Figure 6.21, these are confined to low latitudes at the base of the convection zone. The lack of modulation implies that the appearance of these torsional oscillations is relatively insensitive to the time-averaging procedure. The same can not be said for larger values of D, where (as has already been demonstrated) the solution becomes significantly modulated and this means that a relatively short time-average is needed. For $\tau = 0.05$, Figure 6.23 shows torsional oscillations at the base of the convection zone for $D = -2.0 \times 10^6$ and $D = -2.5 \times 10^6$. As would be expected, these oscillations are confined to low latitudes for $D = -2.0 \times 10^6$ and there is a two-banded structure for $D = -2.5 \times 10^6$. Despite the modulation, and therefore the need to take a relatively short time-averaging period, this shows that it is still possible to get solar-like torsional oscillations despite the fact that we are in the highly modulated low-τ regime.

For the highly modulated solutions found for $\tau = 0.025$ it becomes much harder to find torsional oscillations. This is mainly due to the fact that there are now prolonged periods of time where there is very little magnetic activity. As commented on in the previous section, the modulation found for this value of τ is more extreme than that found on the Sun, but it is of interest to establish the "limits" of solar-like torsional oscillations. For $D = -2.0 \times 10^6$ it is clear that, even during active phases, significant oscillations in the magnetic energy at the magnetic cycle frequency are confined to a relatively brief time interval. This will almost certainly restrict the production of torsional oscillations. In fact it is found that, with this increased modulation, it is necessary to take the time-average over an even shorter time-period in order to see the torsional oscillations. Figure 6.24 shows torsional oscillations at the base of the convection zone for $D = -2.0 \times 10^6$ and $\tau = 0.025$. It is still possible (at low latitudes) to pick out the familiar oscillatory pattern, despite the need for a very short period for the time-average.

To summarise, it has been shown that solar-like torsional oscillations are compatible with the low-τ regime. For moderately supercritical (un-modulated) solutions, low-latitude oscillations can be found regardless of the time-period that is used for the averaging procedure. This explicitly contradicts the findings of Brooke et al. (2002). For

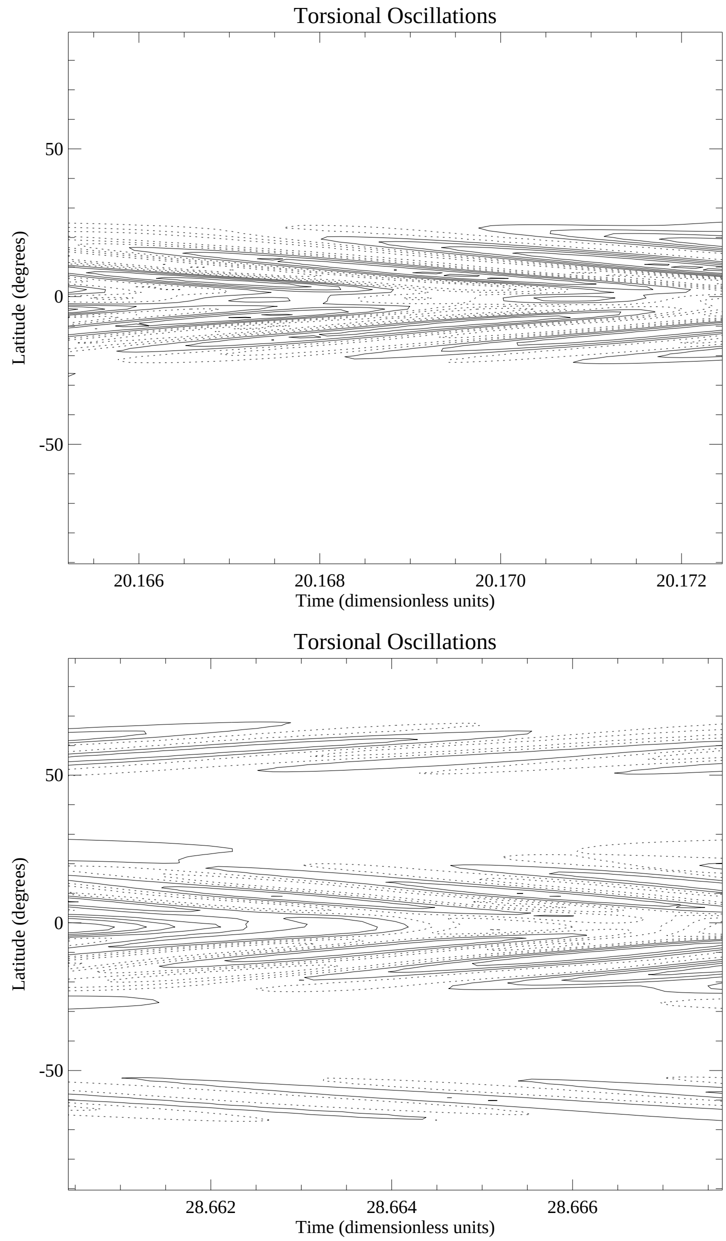

Figure 6.23: As Figure 6.21, but here $\tau = 0.05$, $D = -2.0\times10^6$ (top) and $D = -2.5\times10^6$ (bottom). The time-average has been taken over approximately two magnetic cycles.

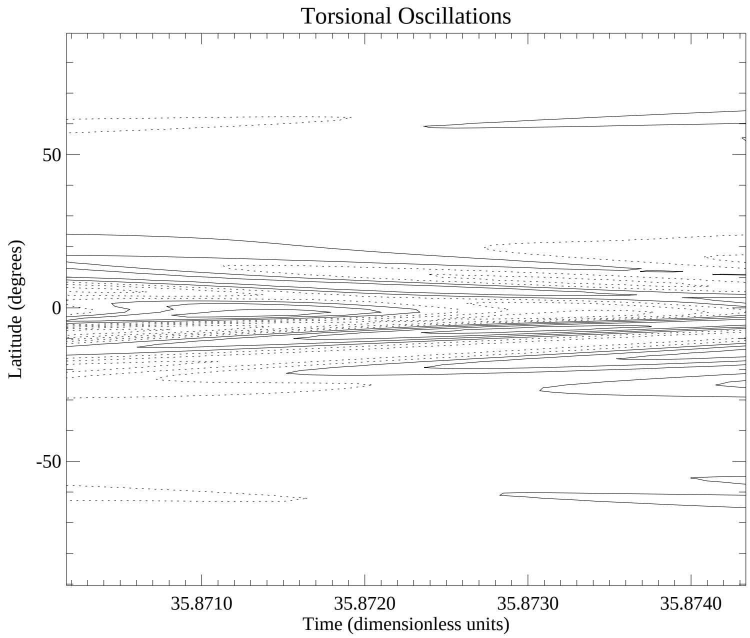

Figure 6.24: As Figure 6.21, but here $\tau = 0.025$, there is no α-quenching, and $D = -2.0 \times 10^6$. For this highly modulated solution, the time-average has been taken over about one magnetic cycle.

larger values of D, the only limiting factor appears to be the extent of the modulation. Some sort of oscillatory signal, with a frequency that is twice that of the magnetic cycle, is always present. In order to observe this signal it is necessary to subtract a time-average from the total angular velocity perturbation. The fact that the time-average is itself a function of time means that it must be taken over a short time-period in order to reveal this weak, high-frequency, oscillatory signal. The more modulated the solution, the shorter this time-period must be.

6.4 The effects of stratification

The latitudinal distribution of any torsional oscillations that have been found so far in this chapter compares very favourably with the solar observations (Vorontsov et al., 2002). However, all the simulated torsional oscillations have been confined to the base of the convection zone – this is not what is inferred from helioseismology. The results of Vorontsov et al. (2002) suggest that the torsional oscillations on the Sun, particularly at low latitudes, are actually strongest at the surface. At high latitudes, Vorontsov et al. (2002) find that strong oscillations at the surface extend downwards almost to the base of the convection zone, although it should be pointed out that this region corresponds to the area of greatest observational uncertainty. Whether or not this is the case, it does seems certain that strong torsional oscillations are observed at the surface, and the dynamo model must be capable of explaining this.

The most plausible explanation for this discrepancy in the spatial distribution of torsional oscillations centres around the density profile. For all the simulations that have been carried out so far in this chapter, density has been taken to be constant. In the Sun, it is known that the density of the fluid at the photosphere is several orders of magnitude smaller than the density at the base of the convection zone (see, for example, Stix, 2002). Most of this density variation occurs near the surface, with the density scale-height increasing with increasing depth. It is this low density at the surface that may explain the presence of strong torsional oscillations there, because even a small perturbation to the local angular momentum could then lead to a large perturbation to the angular velocity. In this section, the effects of a non-constant density profile are investigated, in an attempt to reproduce the spatial distribution of the observed torsional oscillations in the Sun.

One possible approach to this problem would be to take a density profile that has been computed from a realistic model of the solar convection zone (see, for example, Christensen-Dalsgaard et al., 1996). Since this mean-field model already represents a somewhat idealised version of the Sun, it makes more sense to use some physically plausible analytic form for the density profile which can be varied in some simple way so as to adjust the level of stratification. The functional form that is used here is one that has been previously used, in a different context, by van Ballegooijen and Choudhuri (1988) and Dikpati and Charbonneau (1999):

$$\rho(r) = \left(\frac{1}{r} - 1\right)^m, \tag{6.8}$$

for some positive value of m. By varying m, it is possible to investigate the response of the torsional oscillations to different levels of stratification – larger values of m correspond to a more stratified fluid. With this functional form, both the density and the density scale-height within the convection zone decrease with increasing radius. The reason that a simple power law is not used is because that would imply that the density scale height would increase with increasing radius. The only significant unphysical aspect of this functional form is that it implies that the density is identically equal to zero at the surface. Since $r = 1.0$ is on the boundary of the domain, the equations are never solved at this point, which means that this vanishing density does not present a significant numerical problem. This minor problem is outweighed by the simplicity of this functional form, which otherwise possesses the main observed qualitative properties of the solar density profile. Given that an idealised density profile has been used, these calculations should be viewed as being illustrative in nature.

For the simulations that are described in this section, two different values of the dynamo number are used. It has previously been found that $D = -2.0 \times 10^6$ gives torsional oscillations that are confined to low latitudes, whilst there is an additional polar branch for $D = -2.5 \times 10^6$. For the vast majority of the simulations that have been carried out, there is no α-quenching, but a few additional calculations were carried out in order to check the robustness of the conclusions to the addition of this extra nonlinearity. Since we have already established that it is still possible to generate torsional oscillations in the low-τ regime, τ is set equal to unity throughout these simulations.

Figure 6.25 shows the spatial distribution of the torsional oscillations, for $D = -2.0 \times 10^6$, for four different values of m. As before, for all values of m, activity is confined to low latitudes for this dynamo number. However, whilst the magnetic activity remains confined to the base of the convection zone for all values of m, the radial distribution of torsional oscillations seems to be particularly sensitive to the level of density stratification. For the two smaller values of m ($m = 0.5$ and $m = 2.0$) torsional oscillations remain confined to the base of the convection zone. For $m = 5.0$, weak features are observed at the surface, although the strongest oscillations still occur at the base of the convection zone. A modest increase in the stratification, achieved by taking $m = 6.0$, leads the surface features becoming much stronger than those at the base of the convection zone. Figure 6.26 shows the torsional oscillations at $r = 0.975$, plotted against latitude and time, for $m = 6.0$. A striking feature of Figure 6.26 is the relative lack of latitudinal migration in these oscillations. This is presumably a consequence of the fact that these perturbations at the surface are being driven by magnetic oscillations at the base of the convection zone. Angular momentum is transported to the surface via the action of viscous stresses. In addition to the radial transport, angular momentum will also spread out diffusively in the latitudinal direction. This may be the reason for the relative lack of latitudinal migration that is observed at the surface in Figure 6.26. So, whilst the radial distribution of the torsional oscillations bears a closer resemblance to the solar observations, the latitudinal distribution shows less agreement.

Another interesting effect that is caused by the addition of this stratification relates to the parity of the solution. For small values of m, and therefore relatively unstratified density profiles, the parity is (as before) predominantly quadrupolar for this set of parameters. This non-solar-like preference towards quadrupolar symmetry was a problem that was solved, in Section 6.2, by the addition of α-quenching to the system. Interestingly, for highly stratified density profiles, the preferred symmetry is now dipolar. This

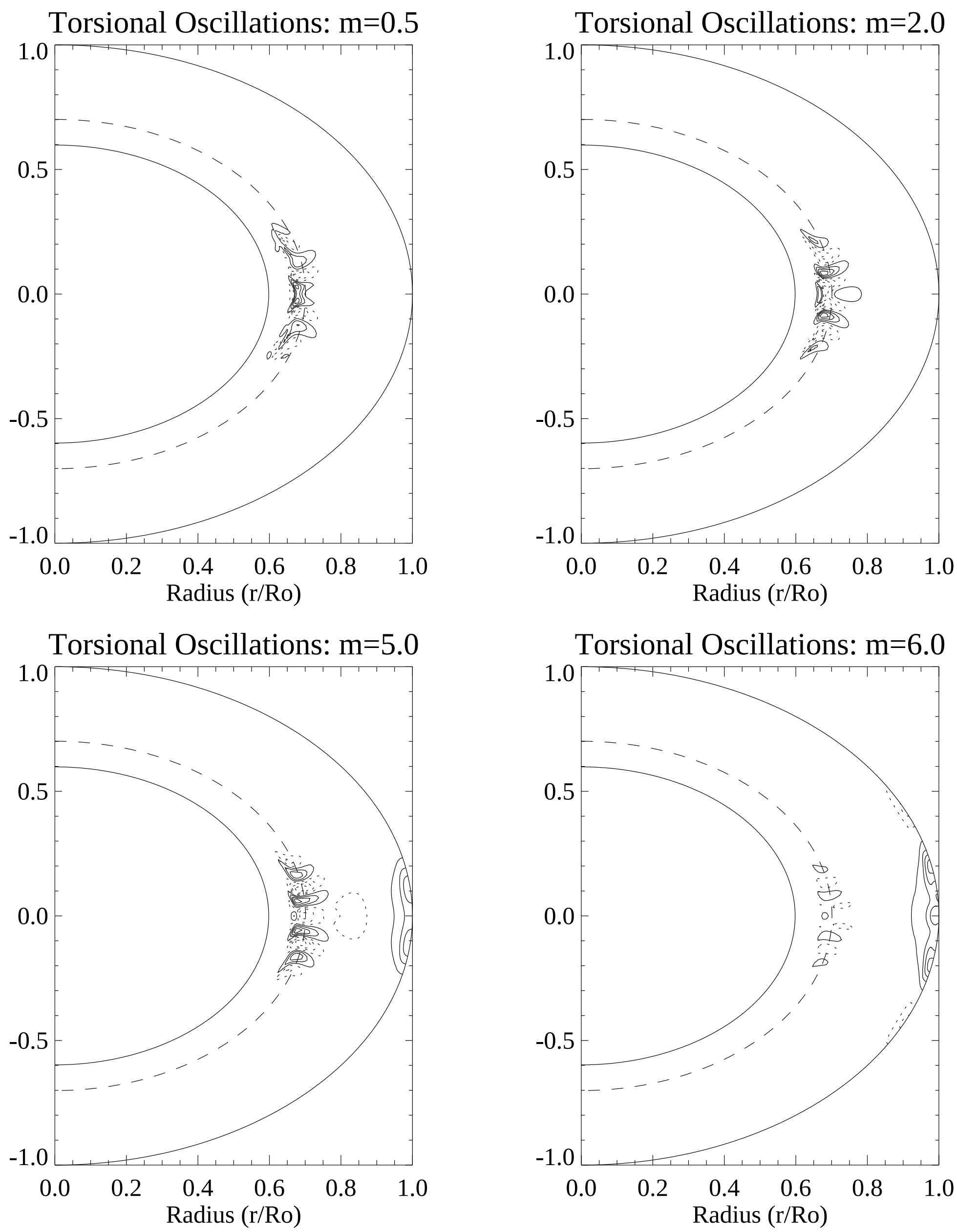

Figure 6.25: The spatial distribution of torsional oscillations for $m = 0.5$ (top left), $m = 2.0$ (top right), $m = 5.0$ (bottom left) and $m = 6.0$ (bottom right). Contours are equally spaced, solid lines correspond to positive perturbations to the angular velocity, dashed lines correspond to negative perturbations. $\tau = 1.0$ and $D = -2.0 \times 10^6$.

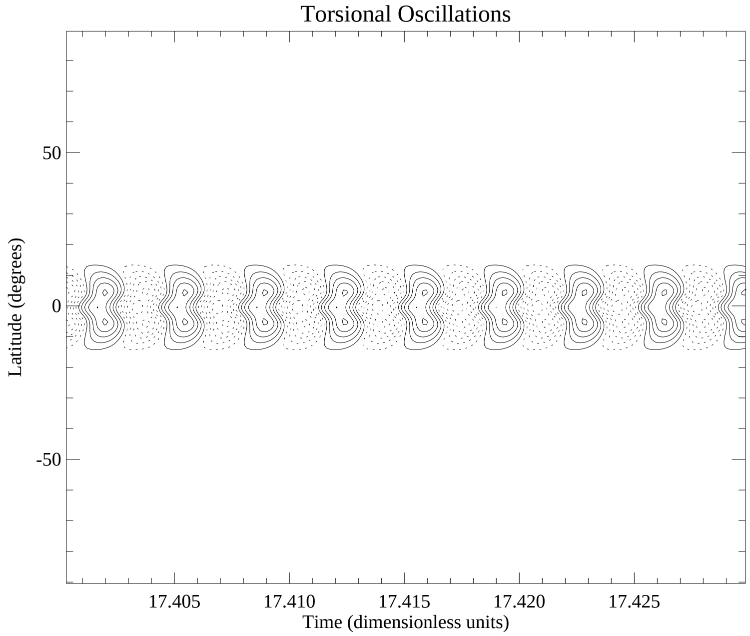

Figure 6.26: Torsional oscillations, plotted against latitude and time, at a fixed radius just below the surface ($r = 0.975$). Contours are equally spaced, solid lines correspond to positive perturbations to the angular velocity, dashed lines correspond to negative perturbations. Here, there is no α-quenching, $\tau = 1.0$, $m = 6.0$ and $D = -2.0 \times 10^6$.

is illustrated in Figure 6.27, which shows contours of the toroidal field at the base of the convection zone for $m = 6.0$. One consequence of this density profile is that the density at the base of the convection zone is decreasing rapidly with increasing radius. The influence of the Lorentz force is increased in regions of low density in equation (6.3), which results in the appearance of larger velocity perturbations. This will cause the dynamo to saturate at a lower peak field. In some sense, a similar situation arises when α-quenching is added to the system, so it is perhaps unsurprising that dipolar symmetry should again be preferred. Certainly these results suggest that the addition of density stratification could provide a novel solution to the problem of parity selection in solar dynamo models.

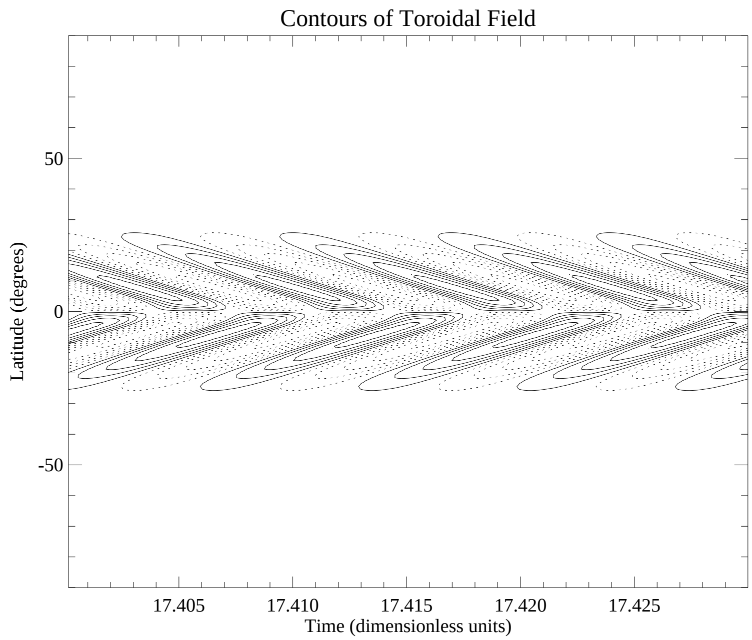

Figure 6.27: As Figure 6.1, but here $\tau = 1.0$, $m = 6.0$, there is no α-quenching, and $D = -2.0 \times 10^6$. Note the dipolar symmetry.

Spatial plots showing the torsional oscillations for the same four values of m, for $D = -2.5 \times 10^6$, are shown in Figure 6.28. A polar branch to the torsional oscillations is seen in all cases. As before, larger values of m promote the appearance of oscillatory features at the surface. Weak surface oscillations are found for $m = 5.0$, but for $m = 6.0$ these oscillations become so strong that the deeper lying oscillations are no longer visible on this plot. The radial distribution of the torsional oscillations, for this highly stratified case, is similar to that observed by Vorontsov et al. (2002), in that there are strong oscillations at the surface at both high and low latitudes. One major difference is that the oscillations at high latitudes are very much confined to the surface layers, rather than extending deep down into the convection zone. This could be a consequence of the idealised nature of the model, but it may also be the case that this feature is a consequence of inaccuracies in the observations at high latitudes within the convection

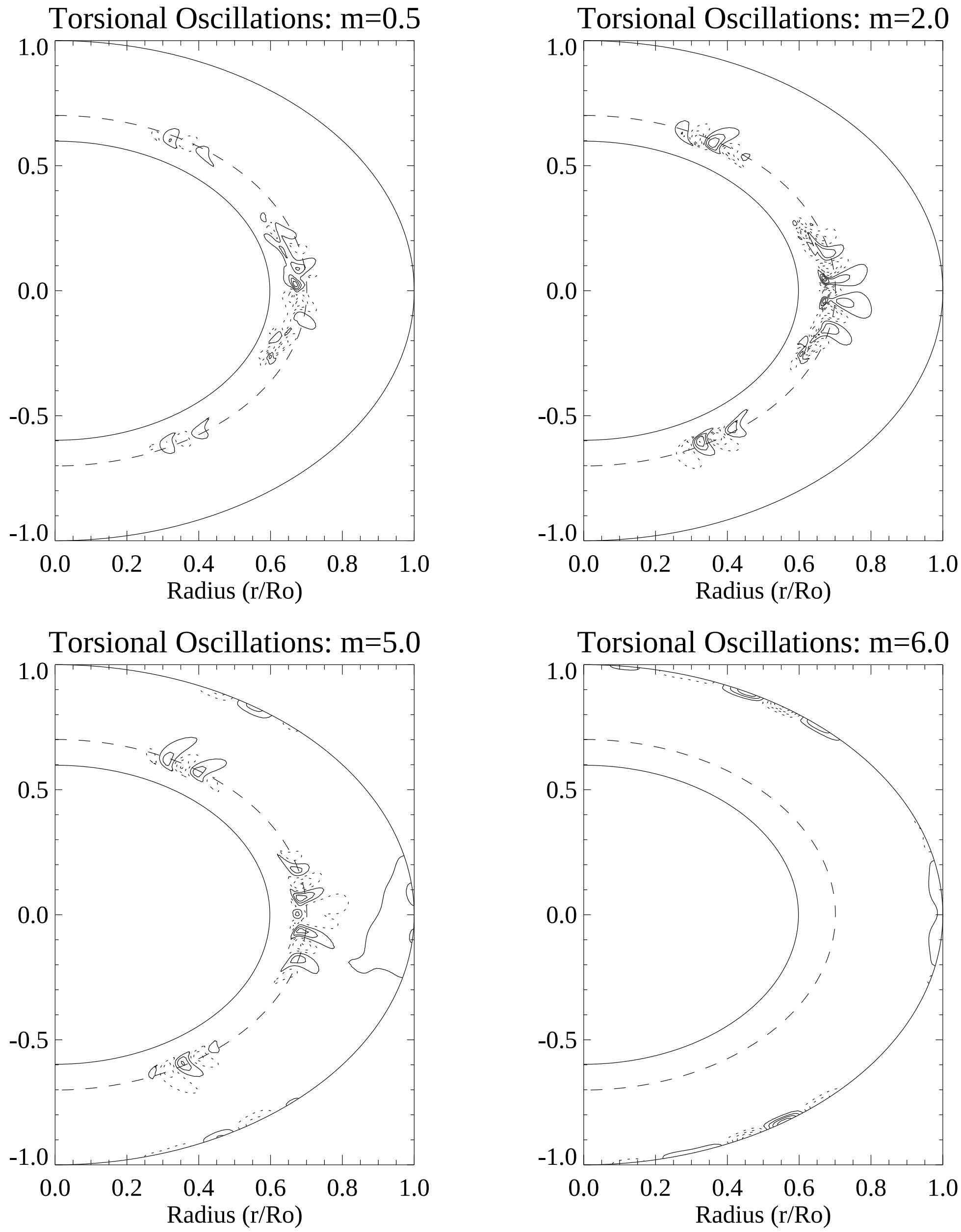

Figure 6.28: The spatial distribution of torsional oscillations for $m = 0.5$ (top left), $m = 2.0$ (top right), $m = 5.0$ (bottom left) and $m = 6.0$ (bottom right). Contours are equally spaced, solid lines correspond to positive perturbations to the angular velocity, dashed lines correspond to negative perturbations. $\tau = 1.0$ and $D = -2.5 \times 10^6$.

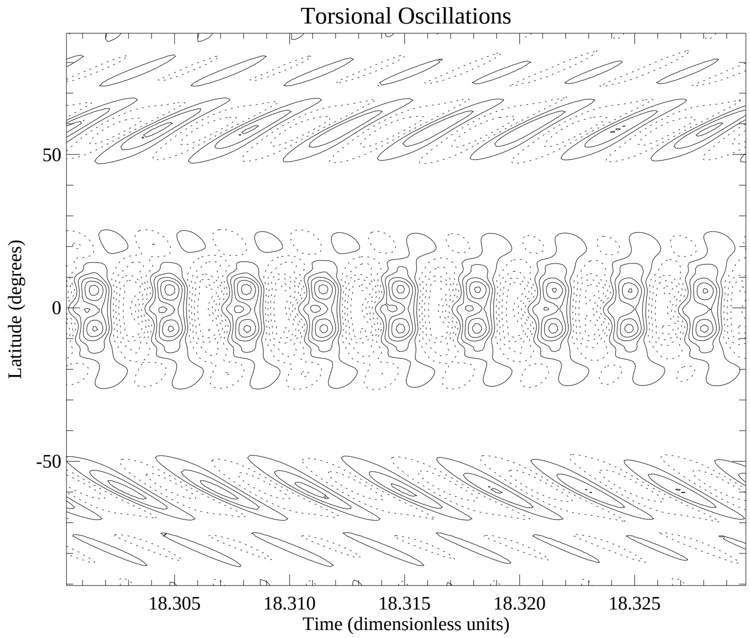

Figure 6.29: As Figure 6.26, but here $\tau = 1.0$, $m = 6.0$, there is no α-quenching, and $D = -2.5 \times 10^6$.

zone. Figure 6.29 shows a plot of the torsional oscillations at $r = 0.975$, for $m = 6.0$, as a function of latitude and time. Whilst there is still very little variation with latitude near the equator, clear bands of migratory torsional oscillations can be seen at high latitudes, where there is no interference from bands of activity that are propagating in the other direction. Figure 6.30 shows contours of toroidal field at the base of the convection zone, for $m = 6.0$. For the unstratified case, the parity of the solution was time-dependent, for $D = -2.5 \times 10^6$. For $m = 0.5$, the solution is of mixed parity, but for $m \gtrsim 2.0$ the parity is steady and predominantly dipolar, although a weak quadrupolar component is also present.

Although these calculations are probably very idealised they strongly suggest that, for a sufficiently stratified convection zone, torsional oscillations at the surface can be driven by a dynamo that is operating around the base of the convection zone. The

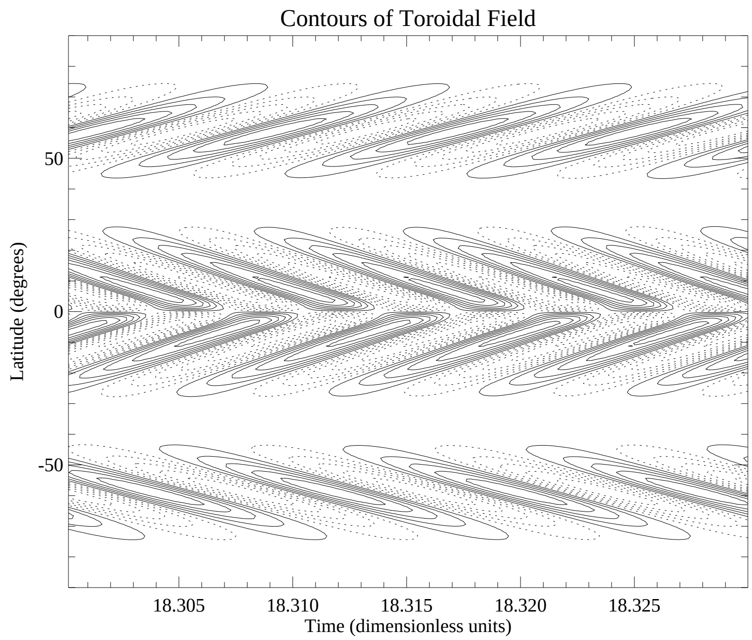

Figure 6.30: As Figure 6.1 but here $\tau = 1.0$, $m = 6.0$, there is no α-quenching, and $D = -2.5 \times 10^6$.

robustness of these conclusions was tested by running a set of calculations that incorporated α-quenching, and it was found that much the same results were obtained. The lack of latitudinal migration at low latitudes is a slight concern. More realistic models are probably needed in order to establish whether or not this behaviour is due to the simplified nature of this mean-field model. An encouraging feature of these calculations is the fact that these models seem to favour dipolar parity.

6.5 Summary and discussion

One of the primary aims of this chapter was to demonstrate that it is possible to reproduce many of the observed features of the solar torsional oscillations by modifying the original dynamo model so that it incorporates the macrodynamic back-reaction of the Lorentz force upon the angular velocity profile. The observed polar branch of the torsional oscillations is reproduced in the simulations only when there is an associated high-latitude branch to the dynamo. For such solutions, the latitudinal distribution of the dynamo-generated torsional oscillations is in excellent agreement with the results from the helioseismological inversions (Vorontsov et al., 2002), with oscillatory branches at both low and high latitudes. In many respects, the torsional oscillations actually place a stronger constraint upon solar dynamo models that the observed butterfly diagram, because they provide information at all latitudes. Another finding of Vorontsov et al. (2002) is that the torsional oscillations are strongest at the surface of the Sun – this is rather harder to reconcile with this interface-like dynamo model as this model naturally produces torsional oscillations around the base of the convection zone. A solution to this problem is obtained by considering models which include the effects of density stratification. Using a somewhat illustrative density profile, it has been shown that it is possible for a dynamo that is concentrated around the base of the convection zone to excite strong oscillations at the surface of the computational domain. Whilst this model represents a rather simplified version of the solar convection zone, these results do suggest that stratification may provide the key to resolving the potential problem that is posed by the fact that the radial location of the dynamo and the radial location of the strongest torsional oscillations seem to be very different. Whilst writing this chapter, I found a preprint of a very recently submitted paper, in which the authors also investigate the effects of stratification upon the solar torsional oscillations (Covas et al., 2003). Although the details of the model are rather different from that described here, they reach similar conclusions regarding the effects of a non-constant density profile upon the torsional oscillations.

Another important issue that was addressed in this chapter concerned the compatibility of solar-like torsional oscillations with the low-τ regime. Brooke et al. (2002) have claimed that it is not possible to have solar-like torsional oscillations for small values of the magnetic Prandtl number, even for very weakly modulated solutions. As, arguably, the most plausible theory for the long-term modulation of the solar cycle relies upon a small value for the magnetic Prandtl number, this claim (if true) would have some serious consequences. In this model, it is found that reducing the value of τ leads to strong modulation, with prolonged grand minima for small enough values of the magnetic Prandtl number. Contrary to the suggestion of Brooke et al. (2002), torsional oscillations are in fact found in this model for low values of τ. Even for strongly modulated solutions, torsional oscillations can be found provided that the required time-average (which needs to be subtracted from the total velocity perturbation in order to reveal the torsional oscillations) is taken over a short enough time-period. The so-called "Prandtl number dilemma" of Brooke et al. (2002) seems to have been caused by the fact that they used a latitude-independent method of time-averaging – one thing that this chapter highlights is the need to make this time-average latitude-dependent. By taking this time-average in the correct way, it has been shown that torsional oscillations and the modulated low-τ regime are not incompatible.

An interesting possibility is that torsional oscillations may also be capable of making more fundamental distinctions between different formulations for the solar dynamo. Babcock-Leighton models (see, for example, Dikpati and Charbonneau, 1999) rely upon a meridional circulation which is directed polewards at the surface and equatorwards at the base of the convection zone. In order to produce a solar-like butterfly diagram, these models require the flow at the base of the convection zone to be strong enough to advect the toroidal magnetic field equatorwards – with their meridional flow, Dikpati and Charbonneau (1999) find that the required Reynolds number for the flow is of the order of 10^3 (see equation 4.47). In their model, the polewards flow at the surface is an order of magnitude larger than the equatorwards flow at the base of the convection zone. The effects of compressibility suggest that this must be the case for any physically reasonable flow. Therefore, if this flow is strong enough to advect the magnetic field equatorwards at the base of the convection zone, it is reasonable to suppose that this will have a similarly significant effect on the torsional oscillations at the surface. In particular, it is difficult to imagine how the surface torsional oscillations, at low latitudes, could continue to migrate equatorwards, against this strong flow. The only logical conclusion is that the Reynolds number of this flow is not large enough to cause significant changes to the torsional oscillation pattern. By corollary, it is then unlikely that the subsurface flow would be strong enough to cause equatorward propagation of the deep-lying toroidal field. If any form of circulation-dominated dynamo is to be believed, it must get round this constraint that is imposed by the torsional oscillations.

Chapter 7

Dynamos in Rapidly Rotating Late-type Stars

As discussed in Chapter 1, the Sun is a relatively slowly rotating late-type star. Many investigations have focused upon the solar dynamo, but with a few exceptions (see, for example, Kitchatinov et al., 2000), the issue of magnetic field generation in more rapidly rotating late-type stars has largely been ignored by dynamo theorists. Given that these stars seem to behave in a rather "non-solar" fashion, with no well-defined magnetic cycles and large high-latitude starspots (see Section 1.2.3), there must be a different kind of dynamo mechanism in operation (a possibility first suggested by Knobloch et al., 1981). The most widely studied rapidly rotating late-type star is the K0 dwarf AB Doradus, which can reasonably be assumed to be a typical example of a star of this type. This is a young main sequence star that is rotating approximately 50 times more rapidly than the Sun. Doppler maps of its surface reveal strong high-latitude magnetic features and weak low-latitude features. In this chapter, particular emphasis is placed upon the effects that an increased rotation rate might have upon the internal differential rotation profile for a star like AB Doradus. A mixture of observational evidence and theoretical arguments is used to produce a plausible differential rotation profile for stars of this type. This rotation profile is then built into the mean-field dynamo models that were described in Chapter 4, in an attempt to reproduce some of the known key features of these rapid rotators. The first part of this chapter contains work that was the subject of a recent paper (Bushby, 2003a).

7.1 Stellar differential rotation

Compared to what we know about the Sun, relatively little is known about the internal differential rotation of other stars. As discussed in Section 1.3.2, a variety of techniques have been employed to investigate trends in stellar surface differential rotation. The key fact that such studies have found is that the time taken for the equator to "lap" the poles is nearly independent of the rotation rate of the star. For a star like AB Doradus, this lap-time corresponds to many more rotational periods (approximately 220) than it does for the Sun (more like 4 or 5 rotational periods). The convection zone in a rapidly rotating late-type star will therefore appear to be rotating virtually as a solid body. Given the lack of any other observational information regarding these stars, it is worth reviewing some observational and theoretical aspects of differential rotation within the Sun before thinking about more rapidly rotating late-type stars.

Before helioseismology revealed the internal differential rotation profile of the Sun, dynamo theorists generally made the assumption that the angular velocity distribution within the Sun is constant along cylindrical surfaces that are aligned with the rotation axis (see, for example, Stix, 1976). The basis for this assumption was the Taylor-Proudman theorem: if rotation is sufficiently rapid, then the Coriolis force dominates the dynamics, which leads to a velocity field that does not vary in the direction parallel to the rotation axis. Estimates of the Taylor number (which represents the ratio of the Coriolis force to the viscous force) within the solar convection zone, suggest that differential rotation there should be strongly influenced by the Coriolis force. Clearly, if dynamics in the solar convection zone are dominated by rotational effects, the same would undoubtedly be true for AB Doradus. Simulations of compressible convection in a rotating spherical shell (see, for example, Glatzmaier and Gilman, 1982; Gilman and Miller, 1986) strongly support the idea that rapid rotation does tend to enforce cylindrical angular velocity contours. Further evidence of this kind of behaviour comes from an experiment carried out in a zero-gravity environment (Hart et al., 1986). This experiment studied thermal convection in a rotating spherical shell, with a simulated radial "gravity" (provided by imposing a strong electric field across the shell). Rapid rotation leads to convection rolls which are nearly parallel to the rotation axis at lower latitudes, and bend towards to poles at higher latitudes. This (so-called) banana cell pattern is a direct consequence of the dominating influence of the Coriolis force, and we would expect convection of this type to drive a cylindrical differential rotation pattern.

The key observational facts concerning the solar internal differential rotation, as inferred from helioseismology, were discussed in Section 1.3.1. The fact that the angular velocity, within the bulk of the convection zone, is not constant along cylindrical surfaces – instead it is (approximately) constant along lines of constant latitude – was one of the major surprises of the initial helioseismological findings. The most plausible explanation for this behaviour is that the transport of angular momentum by Reynolds stresses is sufficiently efficient that it is possible to overcome the Taylor-Proudman constraint. The effects of these Reynolds stresses are very difficult to model numerically, since fluctuations over small spatial scales must be properly represented at the same time as the large-scale variations within the convection zone. This separation in spatial scales covers several orders of magnitude. Having said that, more recent simulations are capable of entering the turbulent regime and they are beginning to produce differential rotation profiles that bear a closer resemblance to the Sun than the earlier simulations described above (see, for example, Miesch et al., 2000; Brun and Toomre, 2002).

Theoretical attempts to model the solar differential rotation often rely on the (so-called) Λ-effect, which is a parameterisation of the non-diffusive part of the Reynolds stress tensor in a rotating fluid (Rüdiger, 1989). In a model which ignored meridional motions, Küker et al. (1993) found that it was possible to tune the parameters involved with the Λ-effect in such a way as to produce a solar-like differential rotation profile. A problem with this model arises when meridional flows are included, since the non-conservative part of the centrifugal force drives a meridional flow. For a rapidly rotating system, this meridional flow will tend to redistribute the angular momentum in such a way as to produce a Taylor-Proudman-like state. Kitchatinov and Rüdiger (1995) manage to get round this problem by allowing the turbulent heat transport to be anisotropic (due to the effects of rotation upon convective turbulence). Such anisotropic conditions can drive a baroclinic flow which, under the correct circumstances, could counteract the centrifugally driven meridional flow. In their model, Kitchatinov and Rüdiger (1995) find that a relatively small heat transport anisotropy, which results in a pole that is a few degrees warmer than the equator, is sufficient to maintain a solar-like differential rotation profile. A similar study, carried for a star with a substantially higher angular velocity, suggests that the angular velocity within the convection zone of a rapidly rotating late-type star should be approximately constant on cylinders whose axes are aligned with the rotation axis (Rüdiger et al., 1998). One thing that should be stressed is that the derivation of these models relies upon linearising the evolution equations for the small-scale fluctuations. This procedure can be justified for small values of the Reynolds number, but given that the the Reynolds number is large within stellar convection zones, this approach is certainly open to criticism. Having said that, it is a self-consistent theory that reproduces many aspects of the solar rotation law.

Although highlighting several important physical ideas, these solar models do not provide a definitive solution to the problem of stellar differential rotation. It therefore seems sensible not to rely too heavily upon them for information regarding differential rotation in rapidly rotating late-type stars. Whilst these models suggest that baroclinic effects may be sufficient to counteract the influence of the Coriolis force in the Sun, it seems unlikely that this situation would persist for much more rapidly rotating stars. Therefore, it will be assumed that the Taylor-Proudman constraint is satisfied within the convection zones of stars like AB Doradus, leading to cylindrical angular velocity contours. The helioseismological data indicate that the solar core is rotating rigidly – presumably due to the presence of a magnetic field within the core which will eliminate any differential rotation. Cores in rapidly rotating stars should also be rotating rigidly for the same reason. In order that there be no net torque upon the core it must be rotating at some intermediate rate, i.e. more rapidly than the polar regions but slower than the equator, as observed in the Sun. A shear layer is therefore required at the base of the convection zone in order to ensure that the angular velocity profile is smooth. This is directly analogous to the solar tachocline, although the spatial distribution of the shear is rather different. A shear layer of this form is absent from any of the rapidly rotating simulations that are described above, which mostly impose stress-free conditions at the inner and outer radii of the convection zone. This tachocline-like layer is the key new feature of this model.

In order to apply these ideas to a dynamo model, it is necessary to produce a functional form for $\Omega(r, \theta)$ that provides a smooth transition from a rigidly rotating core to a Taylor-Proudman state within the convection zone. After non-dimensionalising with respect to the core angular velocity, the following non-dimensional angular velocity profile was used:

$$\Omega(r, \theta) = 1.0 + \frac{1}{2}\left[1 + \Phi\left(\frac{r - 0.7}{0.025}\right)\right](0.0046s - c), \tag{7.1}$$

where Φ represents the standard error function, $s = r\sin\theta$ represents the distance from the rotation axis, and the parameter c controls the difference between the core angular velocity and the polar angular velocity at the base of the convection zone. The number 0.0046 controls the magnitude of the surface differential rotation – this particular value was chosen to mirror the observed lap-time on AB Doradus of about 220 days (Donati and Collier Cameron, 1997). The base of the convection zone is taken to be at $r = 0.7$. The depth of the convection zone in late-type stars is closely related to spectral type, with "later" late-type stars possessing deeper convective envelopes. This is something that can be investigated later on, but initially taking $r = 0.7$ allows easier comparison with the Sun. The width of the shear layer is controlled by the denominator in the argument of the error function – the value of 0.025 was chosen so as to match the width of the shear layer in the analytic profile used for the Sun (equation 5.1). Finally, the parameter c is initially fixed to be 0.003, which means that the part of the convection zone that rotates at the same rate as the core, is at mid-latitudes, as observed on the Sun. As mentioned previously, it is important that there be no net torque upon the core. In a purely laminar flow it would be possible to calculate the required value of c, but the presence of Reynolds stresses here removes this possibility, so we have to rely (principally) upon physical intuition.

A comparison between the proposed rotation profile for a rapid rotator (as given by equation 7.1) and the analytic fit to the solar rotation profile (as given by equation 5.1) is shown in Figure 7.1. One of the main things to notice here is the large difference between the contour spacings in each plot – the differential rotation in the rapid rotator is relatively small, although the high rotation rate of such stars will compensate for this effect. Other than the angular velocity distribution within the convection zone, the other major difference centres around the tachocline region. Although the structure at high latitudes is similar, for the two profiles, the low-latitude shear is (comparatively) much weaker in the rapid rotator. This will clearly have a major influence upon the behaviour of the dynamo, which we would reasonably expect to naturally produce magnetic activity at high latitudes. This is clearly desirable from the point of view of the production of polar starspots in rapidly rotating late-type stars.

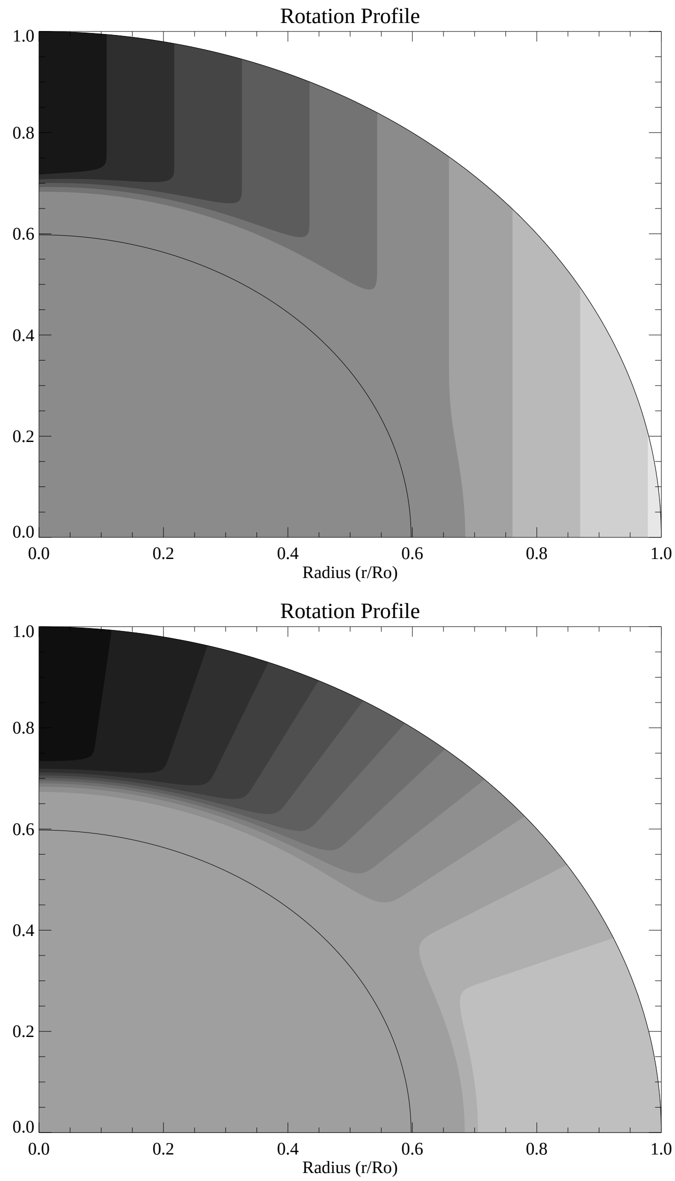

Figure 7.1: Contours of constant Ω for a rapid rotator (top) and an analytic fit to the solar rotation profile (bottom). Within each plot, contours are equally spaced, with separation 0.0005 for the rapid rotator and 0.025 for the Sun. Darker greys correspond to slower rotation rates.

7.2 The dynamo model

Initially, attention is restricted to the $\alpha\omega$ case where the sole nonlinearity is due to α-quenching. Given that the justification of the use of the $\alpha\omega$ limit requires strong differential rotation relative to the α-effect, it could be argued (in this rapidly rotating case where the imposed differential rotation is, at least in solar terms, relatively weak) that the full $\alpha^2\omega$ equations should be studied. This case shall be examined later on in the chapter, but it is first useful to have an understanding of the $\alpha\omega$ limit before extending parameter space to look at the $\alpha^2\omega$ case. So, the usual non-dimensionalised equations can be used:

$$\begin{aligned}\frac{\partial A}{\partial t} &= \frac{\alpha(r,\theta)B}{1+B^2} + \frac{\eta(r)}{r^2}\frac{\partial}{\partial r}\left[r^2\frac{\partial A}{\partial r}\right] + \frac{\eta(r)}{r^2\sin\theta}\frac{\partial}{\partial\theta}\left[\sin\theta\frac{\partial A}{\partial\theta}\right] \\ &\quad -\frac{\eta(r)A}{r^2\sin^2\theta}\end{aligned} \tag{7.2}$$

$$\begin{aligned}\frac{\partial B}{\partial t} &= D\frac{\partial(A\sin\theta)}{\partial\theta}\frac{\partial\Omega}{\partial r} - D\frac{\sin\theta}{r}\frac{\partial(Ar)}{\partial r}\frac{\partial\Omega}{\partial\theta} + \frac{1}{r}\frac{\partial}{\partial r}\left[\eta(r)\frac{\partial(Br)}{\partial r}\right] \\ &\quad +\frac{1}{r^2}\frac{\partial}{\partial\theta}\left[\frac{\eta(r)}{\sin\theta}\frac{\partial(B\sin\theta)}{\partial\theta}\right].\end{aligned} \tag{7.3}$$

As before, these equations are solved numerically for $0 \leq \theta \leq \pi$ and $0.6 \leq r \leq 1.0$, and the base of the convection zone is taken to be at $r = 0.7$. Calculations later on in the chapter will look at deeper convection zones, which will also obviously require larger computational domains, but most of the simulations are carried out for this solar-like domain. The standard boundary conditions are used throughout (see Chapter 4): $A = B = 0$ at $r = 0.6$, $\theta = 0$ and $\theta = \pi$; at $r = 1.0$, $B = 0$ and A matches smoothly onto a potential field.

To complete the specification of the model, input profiles are required for $\eta(r)$ and $\alpha(r,\theta)$. As for the case of the solar dynamo, it is reasonable to suppose that the magnetic diffusivity within the convection zone of a rapidly rotating star should be enhanced by the effects of turbulence. So, the magnetic diffusivity profile that is used here is identical to that used for the solar dynamo (equation 5.2):

$$\eta(r) = \left(\frac{1-\eta_c}{2}\right)\left[1+\Phi\left(\frac{r-0.7}{0.025}\right)\right]+\eta_c, \tag{7.4}$$

where Φ is the error function, and η_c is the ratio of magnetic diffusivities. As for the solar dynamo, η_c is initially set equal to 0.01 for these simulations, although the sensitivity of the dynamo to different values of η_c must (again) be investigated. For $\alpha(r,\theta)$, as in Chapter 5, two different cases are investigated: an α-effect that is distributed throughout the convection zone, and an α-effect that is confined to the base of the convection zone (driven by, for example, the magnetic buoyancy instability). For the distributed case:

$$\alpha(r,\theta) = \frac{1}{2}\left[1+\Phi\left(\frac{r-0.7}{0.025}\right)\right]\cos\theta, \tag{7.5}$$

and for the case where α is confined to the base of the convection zone:

$$\alpha(r,\theta) = f(\theta)\exp\left[-\left(\frac{r-r_\alpha}{0.025}\right)^2\right], \tag{7.6}$$

for some value of $r_\alpha \in [0.7, 0.75]$. It was shown in Chapter 5 that the spatial dependence of the α-effect plays a major role in determining the spatial distribution of the magnetic fields that are generated by the dynamo. The latitudinal distribution is controlled by the function $f(\theta)$. In this model, it is natural to assume that $f(\theta) = \cos\theta$ is an appropriate choice for this function. Given the results from the solar dynamo calculations, it is important to test the sensitivity of the dynamo to changes in $f(\theta)$ and, although most of the calculations that are described in this chapter are carried out for $f(\theta) = \cos\theta$, a few simulations are carried out for an α-effect that is suppressed at high latitudes.

7.3 Numerical results

7.3.1 A distributed α-effect

Given the comparatively weak shear layer, relatively high critical dynamo numbers are to be expected in these simulations. Taking $\eta_c = 0.01$ and a distributed α-effect (given by equation 7.5), the critical dynamo numbers are approximately 4.5×10^6 and -5.5×10^6, for positive and negative values of D respectively. These critical values are approximately 50 times larger than those found for the equivalent calculations carried out for the Sun (see Section 5.2.1). An examination of the two differential rotation profiles, as shown in Figure 7.1, explains this quantitative difference – the contour spacing on these two plots, which determines the magnitude of the differential rotation, differs by a factor of 50.

For positive values of the dynamo number, oscillatory behaviour is found. Figure 7.2 shows contours of toroidal field, at the base of the convection zone, for $D = 1.6 \times 10^7$. This solution is very similar to that found for the equivalent case for the solar dynamo (Figure 5.5), with strong fields at high latitudes at the base of the convection zone. This situation was unacceptable from the point of view of modelling the observed magnetic activity within the Sun, but it could be more applicable to more rapidly rotating stars. The activity at the base of the convection zone is dominated by the region of negative radial shear at high latitudes. Further information regarding the spatial distribution of the magnetic fields is given in Figure 7.3, which shows a snapshot of the toroidal field distribution at the end of a computational run. One of the most important features in this plot is the presence of significant magnetic activity well within the convection zone itself, at lower latitudes. The peak toroidal field within the convection zone is actually comparable to the peak field that is found within the overshoot layer. These "distributed" low-latitude oscillations are driven by the weak radial shear within the convection zone itself. Increasing the value of D does not affect the behaviour of the

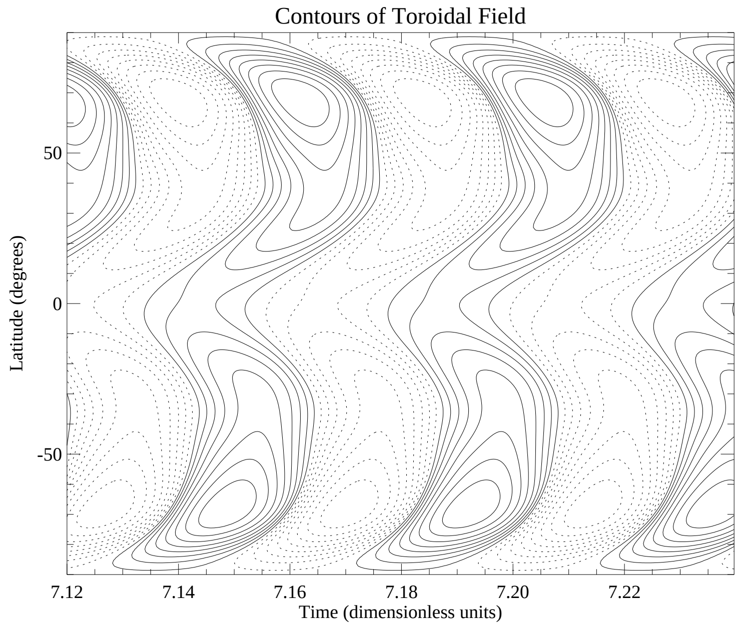

Figure 7.2: Contours of constant toroidal field, plotted against latitude and time, at the base of the convection zone ($r = 0.7$), for the distributed α-effect. Contours are equally spaced, solid lines correspond to positive values of B, dashed lines correspond to negative values. The α-effect is distributed throughout the convection zone and $D = 1.6 \times 10^7$.

dynamo – oscillatory solutions are found for all values that were investigated. If a dynamo of this sort were operating within a rapidly rotating star, it is reasonable to suppose that we would observe surface magnetic features at all latitudes. The strong toroidal fields that accumulate within the stably stratified overshoot layer, at high latitudes, will be susceptible to the magnetic buoyancy instability (assuming that it is not suppressed by the radial shear), which will lead to high-latitude magnetic features at the surface. The distributed portion of the dynamo, by the combined action of convection and magnetic buoyancy, will presumably lead to low-latitude features.

For all negative values of the dynamo number, the strong latitudinal shear within the convection zone of the solar model produced a steady mode. The latitudinal shear

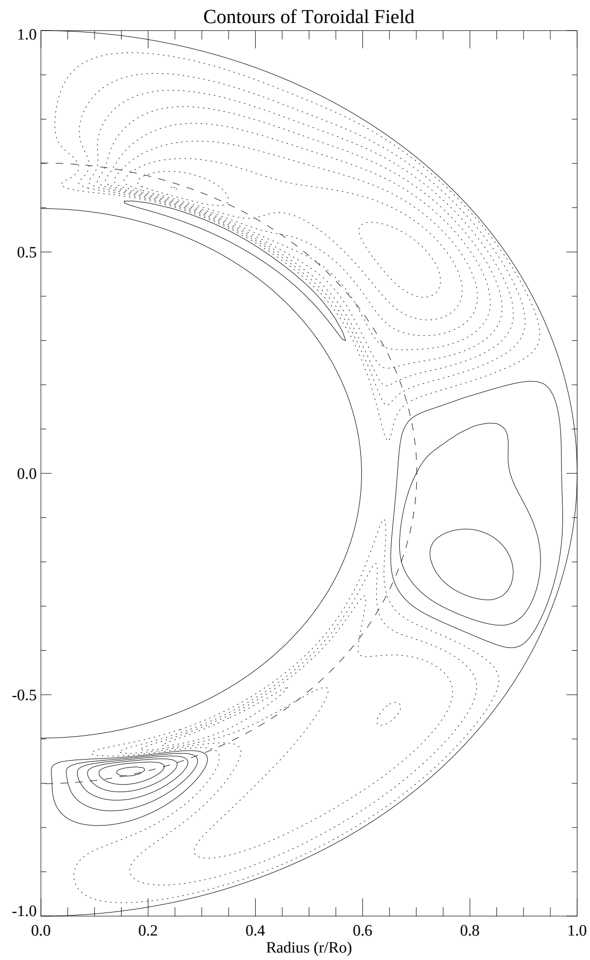

Figure 7.3: The spatial distribution of toroidal field at the end of a computational run, for the distributed α-effect. Contours are equally spaced, solid lines correspond to positive values of B, dashed lines correspond to negative values. The α-effect is distributed throughout the convection zone and $D = 1.6 \times 10^7$.

resulting from this new differential rotation profile is less intense than that seen in the solar rotation profile, so it may not play such a dominant role. In fact, for moderately supercritical values of D, oscillatory solutions are found. Figure 7.4 shows the behaviour of the toroidal field at the base of the convection zone, for $D = -1.6 \times 10^7$ and

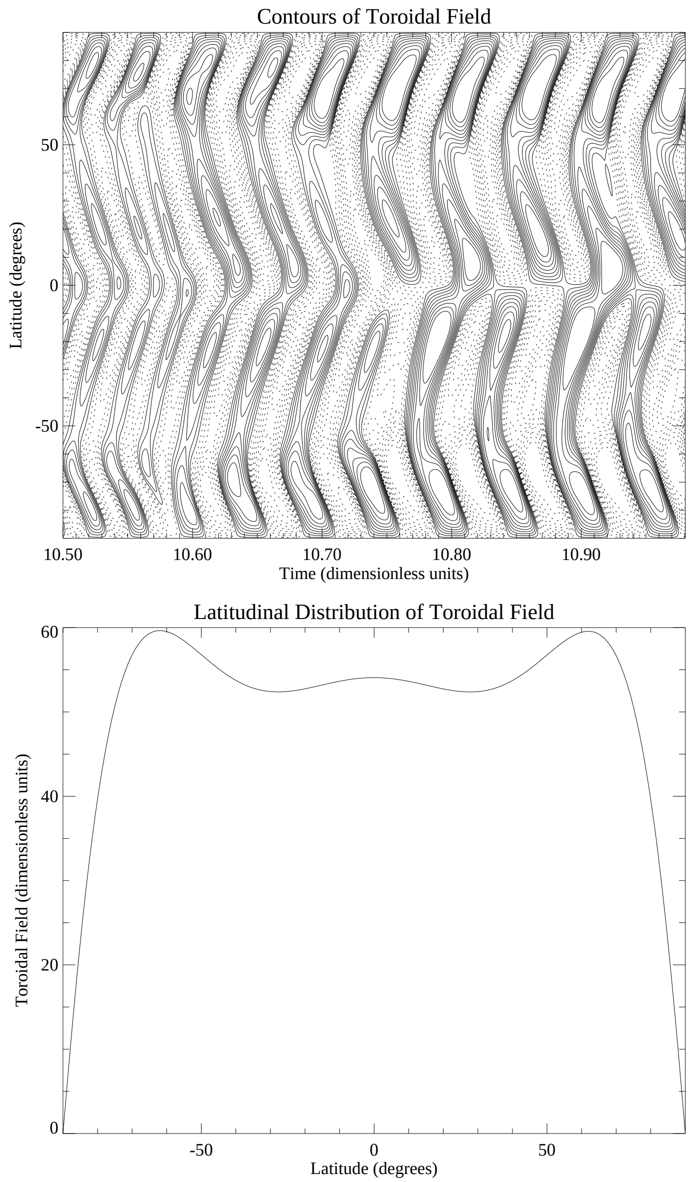

Figure 7.4: The top plot is as Figure 7.2, but for $D = -1.6 \times 10^7$. The bottom plot is for a quadrupolar steady mode with $D = -1.0 \times 10^8$, and shows the dependence of the toroidal field at the base of the convection zone ($r = 0.7$) upon latitude.

$D = -1.0 \times 10^8$. Again, for moderately supercritical values of the dynamo number we see oscillatory solutions with strong features at high latitudes, and distributed activity at lower latitudes. The solution is also rather time-dependent – this is presumably a consequence of the convection zone modes interacting with the interface modes which are driven by the shear in the tachocline at the base of the convection zone. For larger values of D ($D \lesssim -6.4 \times 10^7$), the latitudinal shear is able to drive a steady mode. Neither of these solutions are confined to a small range of latitudes, so would presumably (again) lead to the appearance of magnetic features at all latitudes on the surface of a rapidly rotating late-type star.

Looking at these results, it is difficult to see how any of the solutions that are found for this distributed α-effect could produce polar features that were significantly stronger than those at low latitudes. Another criticism that can be applied to a distributed α-effect concerns the issue of quenching. As described in Section 2.3.3, it is possible that an α-effect that is driven by turbulent convection may be suppressed by substantially sub-equipartition magnetic fields. This would imply that it would be very difficult, for a distributed α-effect, to produce equipartition magnetic fields anywhere within the convection zone of a rapidly rotating star. This would obviously restrict the magnitude of the peak magnetic fields that emerge at the surface. Finally it should also be noted that the distributed part of the dynamo may be particularly sensitive to the use of the $\alpha\omega$ approximation. Oscillations within the convection zone are driven by the very weak differential rotation – if the α-effect is strong, it is reasonable to suppose that differential rotation within the convection zone may not be the dominant regenerative mechanism for the toroidal field. These considerations suggest that a distributed α-effect is unlikely to be the dominant form for the α-effect within rapidly rotating late-type stars.

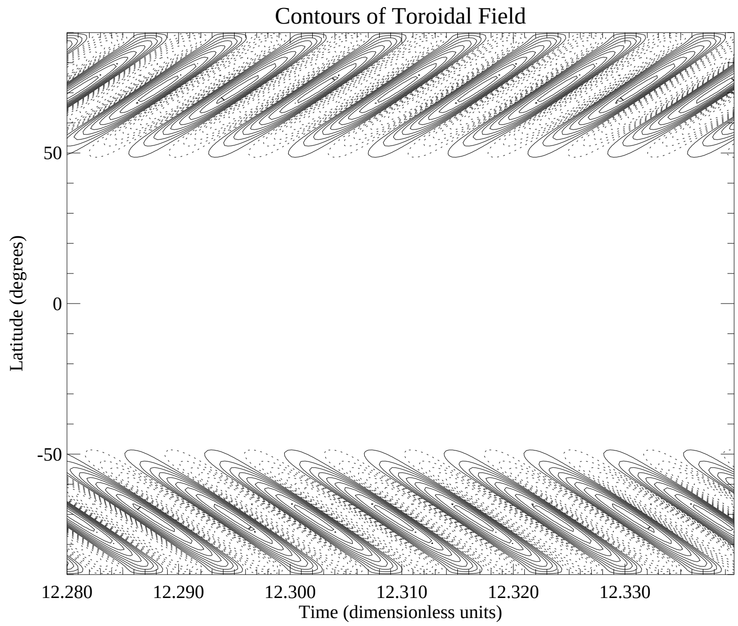

Figure 7.5: Contours of constant toroidal field, plotted against latitude and time, at the base of the convection zone ($r = 0.7$). Contours are equally spaced, solid lines correspond to positive values of B, dashed lines correspond to negative values. $f(\theta) = \cos\theta$, $\eta_c = 0.01$, $r_\alpha = 0.725$ and $D = -6.4 \times 10^7$.

7.3.2 An α-effect confined to the base of the convection zone

The other obvious possible location for an α-effect is around the base of the convection zone. In these simulations $\alpha(r, \theta)$ is given by equation (7.6), and r_α and $f(\theta)$ are initially taken to be 0.725 and $\cos\theta$ respectively. As for the distributed case, η_c is set equal to 0.01. For negative values of D, dynamo action sets in at about $D = -3.4 \times 10^7$. The resulting dynamo oscillations are confined to high latitudes and, driven by the radial shear at the base of the convection zone, they migrate polewards. This behaviour is illustrated by Figure 7.5, which shows contours of toroidal field, at the base of the convection zone, for $D = -6.4 \times 10^7$. As would be expected, the dynamo is confined to the region around the base of the convection zone. This spatial distribution is shown in Figure 7.6.

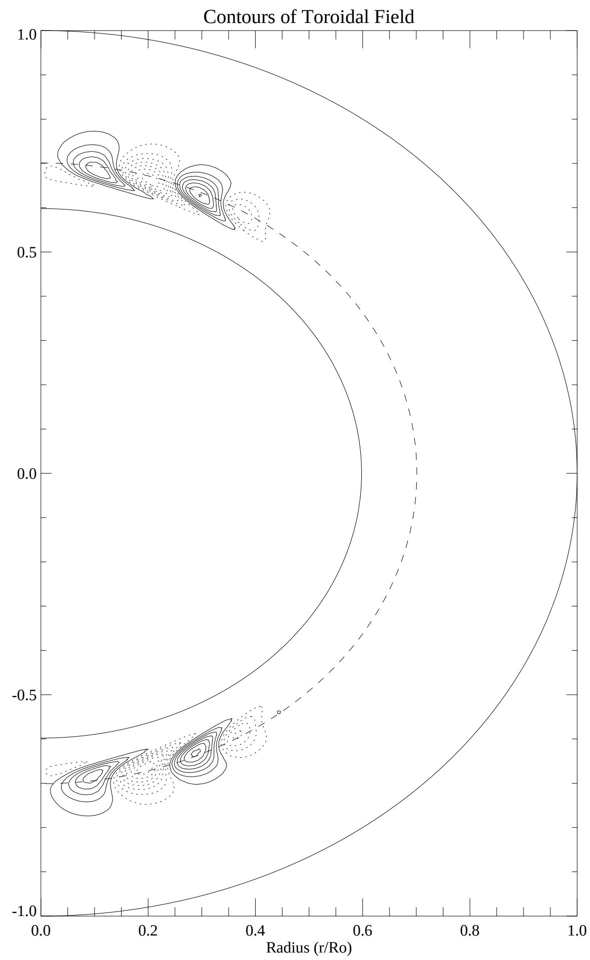

Figure 7.6: The spatial distribution of toroidal field at the end of a computational run. Contours are equally spaced, solid lines correspond to positive values of B, dashed lines correspond to negative values. $f(\theta) = \cos\theta$, $\eta_c = 0.01$, $r_\alpha = 0.725$ and $D = -6.4 \times 10^7$.

Solutions of this form were found for the solar dynamo, for these values of the parameters, for moderately supercritical dynamo numbers. However, a modest increase in the magnitude of the dynamo number led to the suppression of these oscillations by a steady mode. No steady modes are observed here, which is presumably a consequence of the fact that the latitudinal shear plays a less dominant role in the dynamo model,

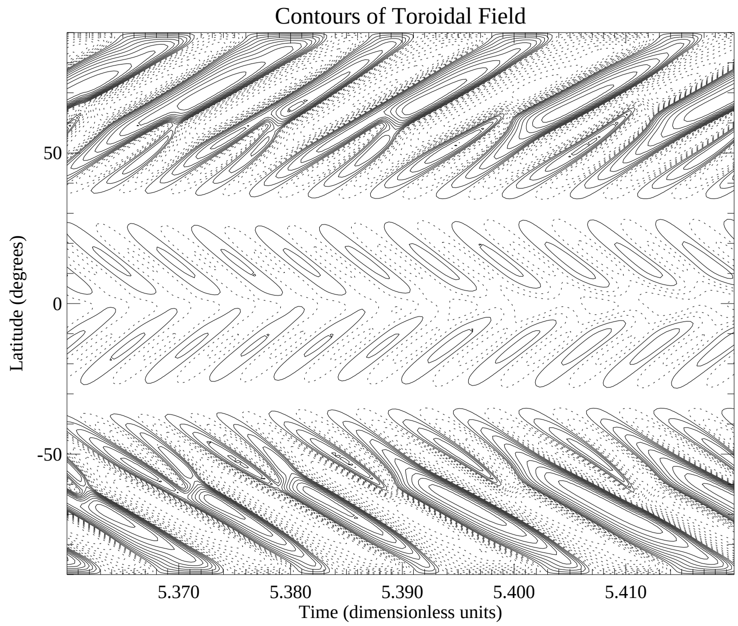

Figure 7.7: As Figure 7.5, but here $f(\theta) = \cos\theta$, $\eta_c = 0.01$, $r_\alpha = 0.725$ and $D = -4.0 \times 10^8$. Note the strong high-latitude branch and the appearance of only very weak low-latitude oscillations.

with this modified differential rotation profile. For the "rapid rotator" model that is described here, the behaviour that is shown in Figures 7.5 and 7.6 seems to be remarkably insensitive to changes in the magnitude of the dynamo number. Magnetic activity is confined entirely to high latitudes, at the base of the convection zone, until D is made more negative than about -4.0×10^8. Figure 7.7 shows contours of constant toroidal field at the base of the convection zone, for $D = -4.0 \times 10^8$. There is now a weak low-latitude oscillatory branch to the dynamo, in addition to the strong high-latitude features. The fact that this low-latitude branch only occurs for highly supercritical values of the dynamo number is due to the fact that the low-latitude shear in the differential rotation profile is extremely weak. There is now also evidence of (slight) modulation in the total magnetic energy along with some fragmentation in the high-latitude oscillatory

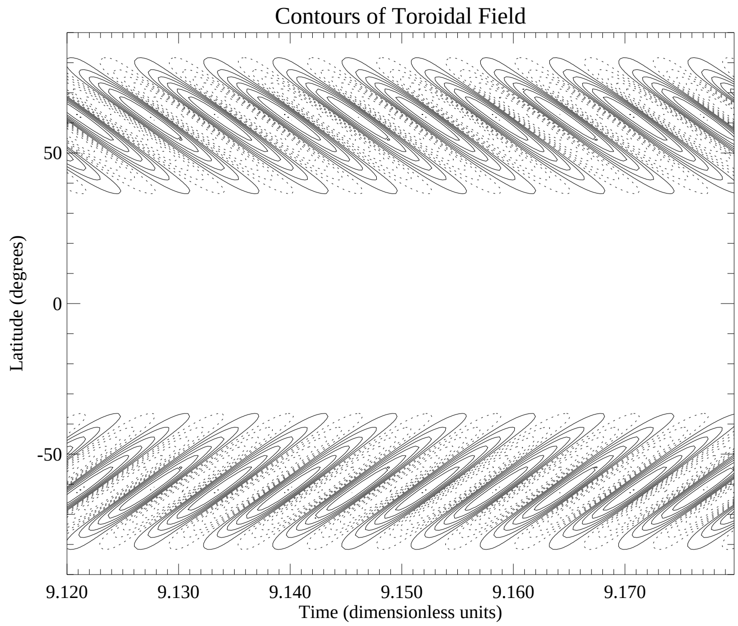

Figure 7.8: As Figure 7.5 but with $f(\theta) = \cos\theta$, $\eta_c = 0.01$, $r_\alpha = 0.725$ and $D = 6.4 \times 10^7$. This solution is characterised by high-latitude oscillations which migrate equatorwards.

branch. Despite these additional features this does not change the fact that, for all negative values of D, there are strong magnetic fields at high latitudes.

Very similar results are obtained for positive values of the dynamo number. The critical dynamo number is slightly larger (approximately 3.7×10^7), but moderately supercritical dynamo numbers, as shown in Figure 7.8, still produce high latitude oscillations that are confined to the base of the convection zone. The only qualitative difference is due to the change of sign of the dynamo number: the oscillations now propagate equatorwards rather than polewards. As for negative values of the dynamo number, a large increase in the magnitude of the dynamo number is required in order to excite low-latitude oscillations. Figure 7.9 shows contours of toroidal field at the base of the convection zone for $D = 4.0 \times 10^8$. This is virtually identical to the solution shown in Figure 7.7, apart from the reversal in the direction of propagation of the magnetic

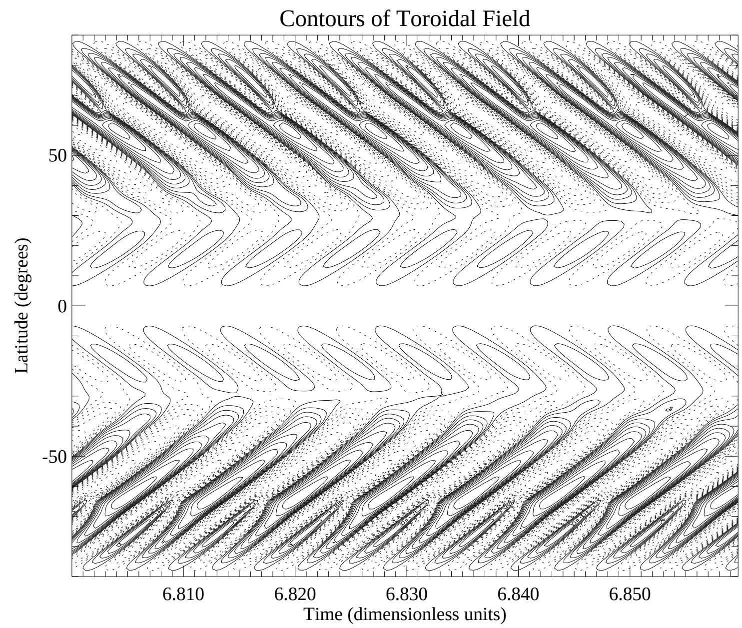

Figure 7.9: As Figure 7.5, but here $f(\theta) = \cos\theta$, $\eta_c = 0.01$, $r_\alpha = 0.725$ and $D = 4.0\times10^8$.

fields.

The key fact to note about these simulations is that strong high latitude oscillatory magnetic activity occurs over a wide range of both positive and negative values of the dynamo number. It is possible to excite low-latitude oscillations, but only for highly supercritical values of the dynamo number. This tendency to produce polar magnetic fields is a direct consequence of the fact that the tachocline is concentrated at high latitudes. The results from this model clearly highlight a possible cause for the existence of high-latitude starspots on rapidly rotating stars.

7.3.3 Robustness of results

In a model of this form, it is important to determine the sensitivity of the results to small changes in the parameters, particularly given that there are several aspects of the model that are (observationally) poorly constrained. Given the fact that solutions corresponding to negative values of D seem to be more sensitive to these small changes, the discussion here will concentrate upon negative values of the dynamo number. Positive values of D always seem to produce oscillatory modes, which are similar in form to those described above.

Variations in the value of η_c

For the solar dynamo calculations that were described in Chapter 5, it was found that the qualitative form of the solution was relatively sensitive to the magnitude of the ratio of magnetic diffusivities, η_c. For negative values of the dynamo number, larger values of η_c tended to favour interface modes, driven by the radial shear, whilst smaller values tended to produce steady modes that are driven by the latitudinal shear. Additional simulations were carried out for the model described in Section 7.3.2, for $\eta_c = 1.0 \times 10^{-4}$ and $\eta_c = 0.1$. It was found that the results are qualitatively insensitive to these variations, with oscillatory interface modes occurring for all the values of the dynamo number that were investigated. These solutions are virtually indistinguishable in form from those that were described in Section 7.3.2. As discussed in Chapter 5, the smaller the value of η_c, the more the diffusive transport of magnetic fields is suppressed within the overshoot layer. This leads to an increased build-up of poloidal field, with a strong latitudinal component, just below the interface. In the solar case, the interaction of this latitudinal component of the magnetic field with the latitudinal shear resulted in the production of a steady mode, for negative values of the dynamo number. In this rapid rotator model, the latitudinal shear clearly plays a less dominant role and the preferred solution remains oscillatory, with strong high-latitude features.

Variations in the value of r_α

Another parameter that can be varied is r_α – this controls the overlap between the tachocline and the α layer, with larger values of r_α corresponding to a smaller overlap.

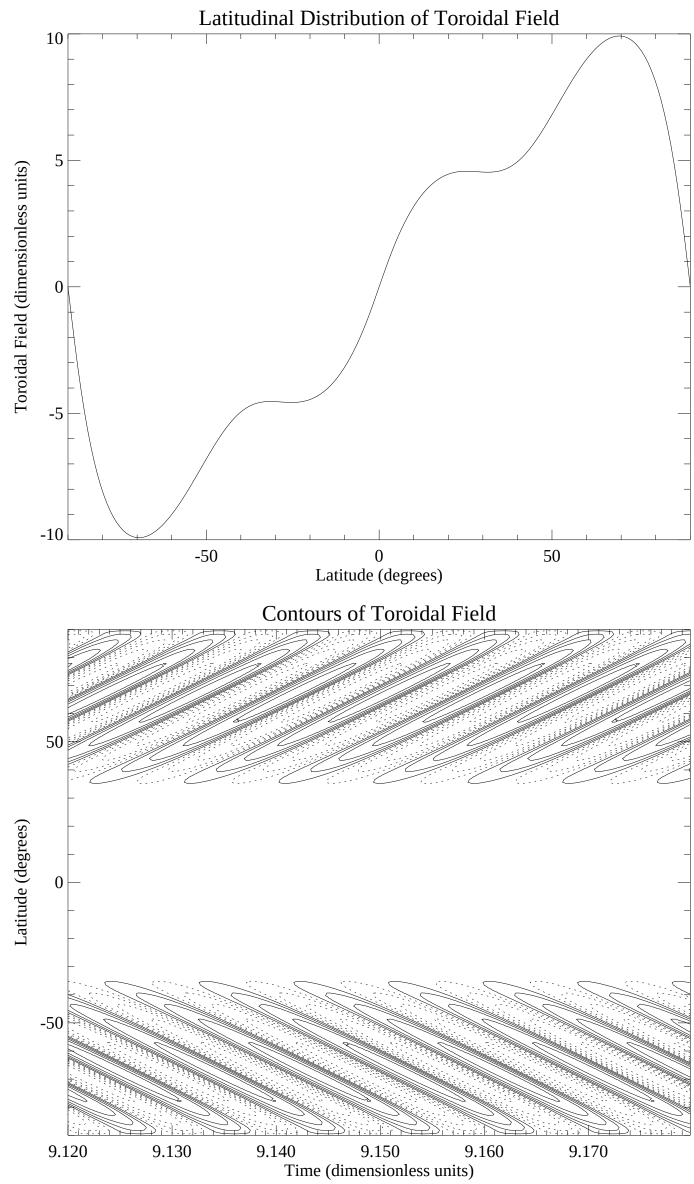

Figure 7.10: The top plot is a dipolar steady mode with $D = -6.4 \times 10^7$ and $r_\alpha = 0.75$. It shows the dependence upon latitude of the toroidal field at the base of the convection zone ($r = 0.7$) upon latitude. The bottom plot is as Figure 7.5, but here $D = -6.4 \times 10^7$ and $r_\alpha = 0.7$.

In the solar calculations, negative values of the dynamo number were found to produce steady modes for larger values of r_α and oscillatory modes for smaller values. The value $r_\alpha = 0.725$ represented a borderline case, with mildly supercritical values of D producing oscillatory magnetic fields and larger values producing steady modes. It has already been shown in this rapid rotator model that $r_\alpha = 0.725$ seems to favour only oscillatory modes. This is again evidence of the reduced influence of the latitudinal shear, which appears to be the driving force behind the production of steady modes. A series of simulations were carried out for $r_\alpha = 0.7$ and $r_\alpha = 0.75$. Figure 7.10 shows the behaviour of the toroidal field, at the base of the convection zone, for $D = -6.4 \times 10^7$ for both of these cases. The main difference that is caused by taking the smaller value of r_α is, as would be expected, a marked reduction in the magnitude of the critical dynamo number. For supercritical values of D, the oscillatory pattern is very similar to that found previously. For $r_\alpha = 0.75$, steady modes seem to be preferred for negative values of the dynamo number. As shown in Figure 7.10, the resulting toroidal magnetic field is distributed over all latitudes, showing no particular preference for high or low latitudes. Despite the appearance of this steady mode for larger values of r_α, there does seem to be a relatively large range of values of r_α which favour dynamos which are dominated by oscillatory high-latitude magnetic activity.

Variations in the rotation profile

Although it is based upon plausible physical arguments, the functional form for $\Omega(r, \theta)$ represents one of the most uncertain aspects of the model. It has been shown that a tachocline that is concentrated at high latitudes naturally gives rise to polar magnetic fields. Clearly, the latitudinal distribution of the magnetic fields will depend closely upon the nature of this tachocline. The constant c, that is given in equation (7.1), is the key parameter in the determination of the spatial form of the tachocline – so far c has been set equal to 0.003. As mentioned previously, although it is not possible to calculate the correct value of c, it is important that it should imply that there is no net torque upon the core. In the case of the Sun, as shown in Figure 7.1, it appears that a weak shear at low latitudes (at the base of the convection zone) can balance a much stronger shear at high latitudes. This is possible due to the fact that the distance from the rotation axis, at the base of the convection zone, is greatest at low latitudes. Because of this, a relatively weak shearing motion at low latitudes can still lead to a large torque – a much larger shear is required at high latitudes in order to provide a torque of equal magnitude. A comparison of the solar rotation profile (as shown in Figure 7.1) with that postulated for the rapid rotator, highlights several important points. In both rotation profiles, the core rotates at a rate that is comparable with fluid at mid-latitudes within the convection zone. As we go to higher latitudes (at the base of the convection zone) within the Sun, there is a rapid transition to a region of strong negative radial shear. This transition is much more gradual for the rapid rotator, which means that we need to go to higher latitudes to find a strong negative radial shear. Applying the ideas that were discussed above, this will lead to a reduction in the torque due to the negative radial shear in the rapid rotator when compared to the equivalent negative radial shear within the Sun. It therefore seems plausible that only a very weak radial shear at low latitudes should be sufficient to ensure that there is no net torque on the core of this rapid rotator.

Additional sets of simulations were carried out for two different core rotation rates: this corresponded to perturbing the parameter c to $c = 0.0025$ and $c = 0.0035$. The resulting rotation profiles are shown in Figure 7.11. For $c = 0.0025$, we have a core that is rotating slightly less rapidly with respect to the convection zone – this results in a weaker shear at high latitudes and a stronger shear layer at low latitudes at the base of the convection zone. Taking $c = 0.0035$ results in a more rapidly rotating core with a virtually non-existent radial shear at low latitudes. It is possible that neither of these modified profiles represents a rotation profile for which the net torque will vanish on the

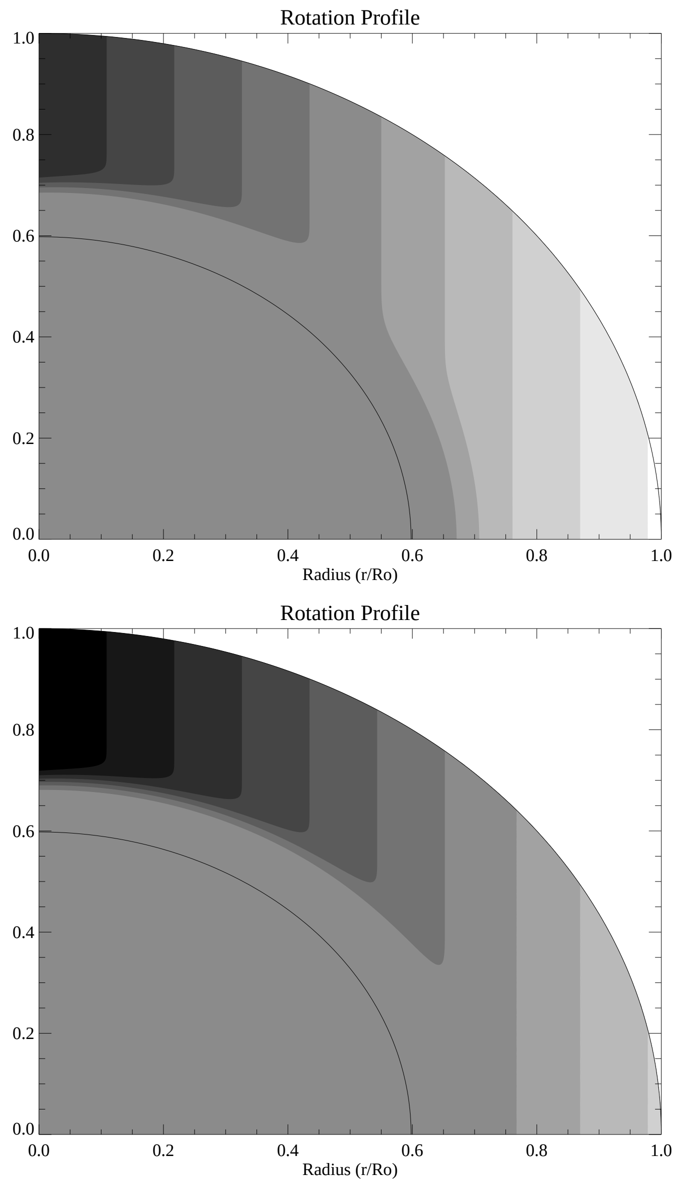

Figure 7.11: Contours of constant Ω for a rapid rotator with $c = 0.0025$ (top) and $c = 0.0035$ (bottom). Within each plot, contours are equally spaced, with separation 0.0005. Darker greys correspond to slower rotation rates.

core. In the $c = 0.0025$ case it seems unlikely that the weaker shear at high latitudes could balance the torque due to the stronger shear at lower latitudes, whilst the absence of any significant positive shear at the base of the convection zone for $c = 0.0035$ will cause a similar problem. Given that these probably represent "borderline" cases it is worth briefly investigating their properties – if strong high-latitude features are still found, we can be confident that this is a robust feature of the model. Unsurprisingly, the strong shear at high latitudes for $c = 0.0035$ leads to polar features – these are similar in form to those described previously, so will not be discussed further here. For $c = 0.0025$, mildly supercritical dynamo numbers lead to oscillations that are concentrated into high latitudes at the base of the convection zone, as shown in Figure 7.12. More supercritical values of the dynamo number lead to the appearance of low-latitude oscillations in addition to these high-latitude features. The key result here is that, whether or not there is activity at low latitudes, these modified profiles still result in dynamo action, the dominant feature of which is activity at high latitudes.

Variations in the function $f(\theta)$

So far it has been shown that, provided the overlap between the α layer and the tachocline is sufficiently large, an α-effect that is confined to the base of the convection zone leads naturally to high-latitude oscillatory magnetic fields. All the results so far have been obtained for an α-effect that is strongest at the poles, with $f(\theta) = \cos\theta$ (see equation 7.6). For the solar dynamo calculations, it was found that the most solar-like solutions were found for an α-effect that is restricted to lower latitudes. In those calculations, it was argued that the strong radial shear at mid to high latitudes may suppress the non-axisymmetric magnetic buoyancy modes necessary for the operation of an α-effect. This led to the concentration of a magnetic buoyancy-driven α-effect into low latitudes, where the shear is weaker. There is no compelling reason for adopting a "truncated" α-profile of this form for these simulations for rapidly rotating stars. Given

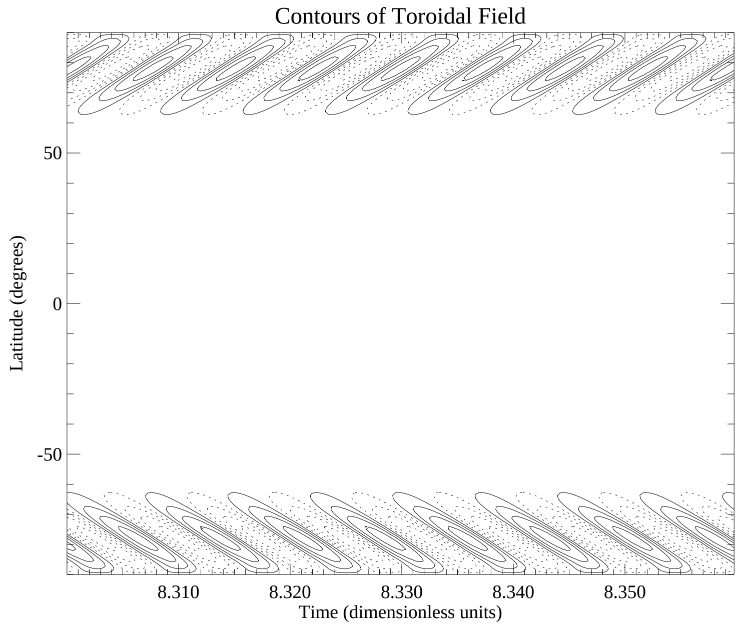

Figure 7.12: As Figure 7.5, but for a modified differential rotation profile. $f(\theta) = \cos\theta$, $\eta_c = 0.01$, $r_\alpha = 0.725$, $c = 0.0025$ and $D = -6.4 \times 10^7$. Oscillations are confined to high latitudes and have a small latitudinal range.

the uncertainties involved with the postulated differential rotation profile, it is impossible to decide whether or not the radial shear at high latitudes is strong enough to suppress the magnetic buoyancy instability there. Also, it has been assumed that the Coriolis force is highly influential in these rapidly rotating stars, and we might expect the twisting effect of loops of magnetic flux to be greatest at the poles. Having said that, it is worth briefly investigating the effects of having a truncated α-profile in a model of this form.

A few simulations have been carried out using truncated α-effects. Taking $f(\theta) = \cos\theta \sin^2\theta$ corresponds to an α-effect that is truncated at the poles, but is not particularly concentrated into low latitudes. The critical dynamo number is now very large (approximately -1.7×10^8) and moderately supercritical dynamo numbers again pro-

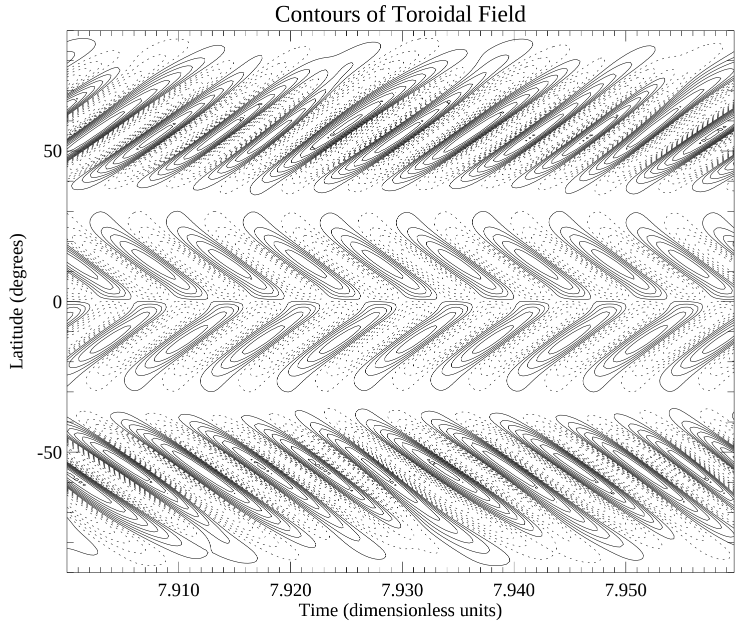

Figure 7.13: As Figure 7.5, but here $f(\theta) = \cos\theta \sin^2\theta$, $\eta_c = 0.01$, $r_\alpha = 0.725$, $D = -4.0 \times 10^8$. Note that the polar branch of the dynamo is still stronger than the low-latitude branch.

duce oscillations that are confined to high latitudes – the toroidal field distribution is similar to that shown in Figures 7.5 and 7.6. Increasing the magnitude of D results in the excitation of oscillations at low latitudes. Figure 7.13 shows contours of toroidal field at the base of the convection zone for $D = -4.0 \times 10^8$. Even for this truncated α-effect, it is clear that the polar branch is still stronger than the low-latitude branch. It is interesting to compare this solution with the equivalent solution from the solar dynamo calculations – for the solar dynamo it was found that this form for the α-effect produced branches at high and low latitudes of a similar strength. The fact that polar features are still dominant for this rapid rotator model is a reflection of the fact that the tachocline is mainly confined to high latitudes. Setting $f(\theta) = \cos\theta \sin^4\theta$ gives an α-effect that is concentrated at low latitudes and results in an even higher value for the critical dynamo

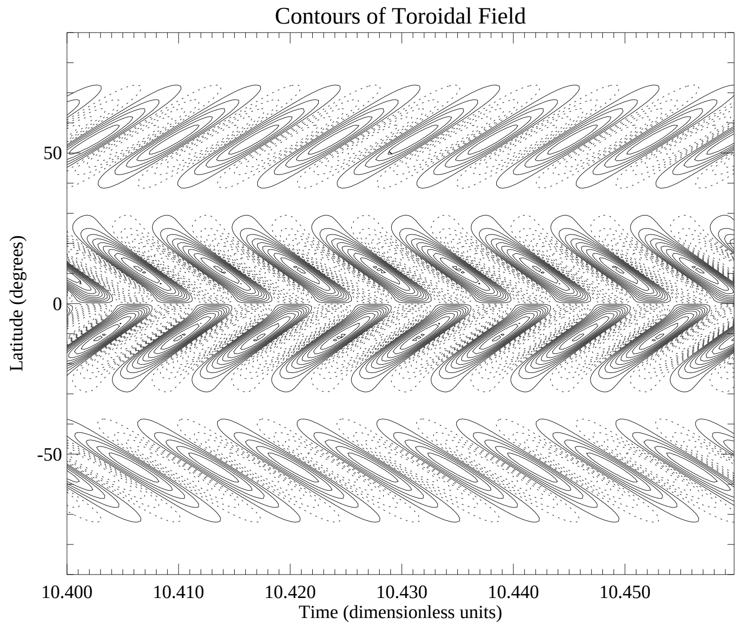

Figure 7.14: As Figure 7.5, but here $f(\theta) = \cos\theta \sin^4\theta$, $\eta_c = 0.01$, $r_\alpha = 0.725$, $D = -4.0 \times 10^8$.

number (approximately -3.0×10^8). For this heavily truncated α-effect, the polar branch is never lost entirely, but the low-latitude branch is now definitely stronger, as shown in Figure 7.14. One thing that should be noted here is that the critical dynamo numbers have become very large – it is quite possible that, despite their very high rotation rates, such large values for D are unattainable in these stars.

These results emphasise the fact that it is not enough simply to have a tachocline that is confined to high latitudes: the distribution of the α-effect is also very important in terms of the spatial distribution of the magnetic fields. If the α-effect is restricted to low latitudes, polar features cease to dominate the resulting dynamo. As stated above, other than what has been seen in the solar dynamo calculations, there seems to be no obvious reason for choosing such a truncated α-effect, particularly given that we know that strong polar features are observed upon the surfaces of these rapidly rotating late-

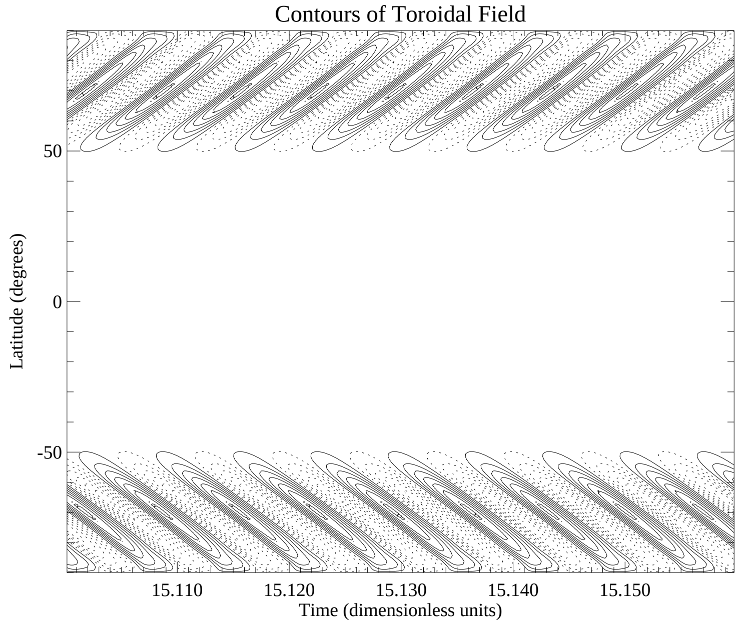

Figure 7.15: As Figure 7.5, but for a simulation involving the macrodynamic nonlinearity. $f(\theta) = \cos\theta$, $\eta_c = 0.01$, $r_\alpha = 0.725$ and $D = -6.4 \times 10^7$.

type stars. This issue highlights our lack of a detailed understanding of the nature of the α-effect – rather than being able to theoretically predict, in advance, the spatial distribution of $\alpha(r, \theta)$, we have to rely upon observations to constrain the α-effect. This problem will be discussed at greater length in the final chapter. For the rest of this chapter, it will simply be assumed that $f(\theta)$ is always given by $\cos\theta$, so that the α-effect is indeed strongest at the poles.

A macrodynamic nonlinearity

Recent observations of AB Doradus suggest that its equatorial rotation rate may be time-dependent, with maximal starspot coverage apparently coinciding with the smallest surface differential rotation (Collier Cameron and Donati, 2002). The most natural explanation for this behaviour is that these variations in differential rotation are a consequence of the dynamical back-reaction of the Lorentz force upon the differential rotation. By adapting the model that was used in Chapter 6, it is possible to investigate how this rapid rotator model is effected by the inclusion of this macrodynamic nonlinearity. Given that only azimuthal velocity perturbations are considered, it is not possible to include Coriolis effects in this model. Since the justification for the unperturbed differential rotation profile relies heavily upon the influence of the Coriolis force, this is not wholly satisfactory. Whilst noting this problem, it still seems worthwhile to briefly test the sensitivity of the model to this change in nonlinearity, at least up to moderately supercritical values of the dynamo number. It is found that the results seem to be highly insensitive to the choice of nonlinearity. For an α-effect that is distributed throughout the convection zone, dynamo action is found at all latitudes with substantial magnetic activity occurring within the convection zone itself. Confining the α-effect to the base of the convection zone, with $f(\theta) = \cos\theta$, leads to strong oscillations at high latitudes at the base of the convection zone. This is illustrated by Figure 7.15, which shows contours of toroidal field at the base of the convection zone for $D = -6.4 \times 10^7$. So, despite this change of nonlinearity, high latitude features are still preferred for this form of the α-effect.

7.4 The $\alpha^2\omega$ model

When relating these results to rapidly rotating late-type stars, it is important to bear in mind that such stars rarely display smooth cyclic behaviour, as discussed in Section 1.2.1. Whilst the model that has been presented here does produce solutions that are dominated by activity at high latitudes, such solutions are oscillatory in nature. Therefore this model clearly does not tell the whole story. One possibility that should be considered is that dynamos in rapidly rotating stars may be of $\alpha^2\omega$-type rather than operating in the $\alpha\omega$ regime. On the basis of an asymptotic study of dynamos in late-type stars, this idea has already been suggested by Paternò et al. (2002). Certainly, this proposal is supported by the fact that a larger Coriolis force should enhance the α-effect in such stars. In order to fully assess possible aspects of dynamo action within these stars, this idea should be investigated.

Assuming that the sole nonlinearity is due to α-quenching, the $\alpha^2\omega$ equations are given by (see Section 4.4.3):

$$\begin{aligned}\frac{\partial A}{\partial t} &= R_\alpha \frac{\alpha(r,\theta)B}{1+|\mathbf{B}|^2} + \frac{\eta(r)}{r^2}\frac{\partial}{\partial r}\left[r^2\frac{\partial A}{\partial r}\right] + \frac{\eta(r)}{r^2\sin\theta}\frac{\partial}{\partial\theta}\left[\sin\theta\frac{\partial A}{\partial\theta}\right] \\ &\quad -\frac{\eta(r)A}{r^2\sin^2\theta}\end{aligned} \tag{7.7}$$

$$\begin{aligned}\frac{\partial B}{\partial t} &= R_\omega \frac{\partial(A\sin\theta)}{\partial\theta}\frac{\partial\Omega}{\partial r} - R_\omega\frac{\sin\theta}{r}\frac{\partial(Ar)}{\partial r}\frac{\partial\Omega}{\partial\theta} \\ &\quad -R_\alpha\frac{1}{r}\frac{\partial}{\partial r}\left[\frac{\alpha(r,\theta)}{1+|\mathbf{B}|^2}\frac{\partial(Ar)}{\partial r}\right] - R_\alpha\frac{1}{r^2}\frac{\partial}{\partial\theta}\left[\frac{\alpha(r,\theta)}{\sin\theta(1+|\mathbf{B}|^2)}\frac{\partial(A\sin\theta)}{\partial\theta}\right] \\ &\quad +\frac{1}{r}\frac{\partial}{\partial r}\left[\eta(r)\frac{\partial(Br)}{\partial r}\right] + \frac{1}{r^2}\frac{\partial}{\partial\theta}\left[\frac{\eta(r)}{\sin\theta}\frac{\partial(B\sin\theta)}{\partial\theta}\right].\end{aligned} \tag{7.8}$$

As described in Section 4.4.3, the fact that the toroidal component of the magnetic field might no longer be significantly larger than the poloidal component means that α-quenching should now be taken to depend upon $|\mathbf{B}|$ rather than B. There are now two non-dimensional parameters: $R_\alpha = \alpha_o R_*/\eta_t$ and $R_\omega = \Omega_o R_*^2/\eta_t$, where α_o is a representative value of the α-effect, R_* is the radius of the star, Ω_o is the core angular velocity and η_t is the peak (turbulent) magnetic diffusivity. The approach that is followed here is to fix R_ω and then to vary R_α. Picking a "reasonable" value for R_ω clearly depends closely upon the value of η_t, since Ω_o and R_* are relatively well-determined for a star like AB Doradus. Throughout these simulations we take $R_\omega = 7.0\times10^5$. For a star of the same size as the Sun, but rotating 50 times more rapidly, this corresponds to taking $\eta_t \simeq 1.0\times10^{12}\mathrm{cm}^2\mathrm{s}^{-1}$. Although somewhat arbitrary, this kind of value for the turbulent magnetic diffusivity has been utilised in solar mean-field dynamo models (see, for example Markiel and Thomas, 1999), and it probably results in a value for R_ω that is physically realistic.

For an α-effect that is distributed throughout the convection zone, the results for positive values of R_α are qualitatively very similar to those found for the $\alpha\omega$ case. Oscillatory solutions are found for $R_\alpha \gtrsim 7.0$, and these persist as R_α is increased. Like the solutions that were described in Section 7.3.1, these oscillations are characterised by strong magnetic fields at high latitudes (at the base of the convection zone) and a significant distributed part of the dynamo at mid to low latitudes within the convection zone. For negative values of R_α, oscillatory solutions are found for $R_\alpha \lesssim -8.0$. As R_α is decreased, these oscillations persist until $R_\alpha \lesssim -20.0$ when the preferred solution becomes a dipolar steady mode. Again, this is qualitatively very similar to the results described in Section 7.3.1 so not much more needs to be said here. Having said that, it is worth noting that this steady mode appears for a value of R_α that is only 2 or 3 times larger than its critical value – for the $\alpha\omega$ case, the onset of the steady mode occurred for rather more supercritical values of the dynamo number. The $\alpha^2\omega$ approximation therefore seems to promote the appearance of the steady mode for negative values of R_α when compared to the equivalent $\alpha\omega$ case.

For the $\alpha\omega$ case, more promising results were obtained for an α-effect that is confined to the base of the convection zone – for these $\alpha^2\omega$ simulations, we again take $f(\theta) = \cos\theta$ and $r_\alpha = 0.725$. As for the distributed case, results for positive values of R_α seem to be qualitatively similar to those found for positive values of the dynamo number for the $\alpha\omega$ case. For $R_\alpha \gtrsim 33.0$, dynamo action is confined to the base of the convection zone and high latitudes. As would be expected for a positive value of $R_\alpha R_\omega$ (which is equal to the dynamo number), the magnetic field migrates equatorwards as the cycle progresses. Low-latitude features are observed once R_α is increased beyond about 100.0. For negative values of R_α, a new solution is found. The critical value of R_α is approximately -30.0, and mildly supercritical values of R_α produce oscillatory solutions which, like the $\alpha\omega$ case, are restricted to high latitudes at the base of the convection zone. However, once $R_\alpha \lesssim -75.0$, these oscillations are suppressed by a new type of steady mode. Figure 7.16 shows the spatial distribution of the toroidal magnetic field at the end of a computational run, for $R_\alpha = -100.0$. This clearly shows that the toroidal field distribution, for this steady mode is concentrated at the base of the convection zone, at high latitudes. The action of magnetic buoyancy on this toroidal field would give rise to magnetic flux appearing at the surface at high latitudes. This solution therefore presents the possibility of a polar spot without the dynamo being oscillatory in nature.

7.5 A deeper convection zone

All the calculations that have been described in this chapter (so far) have been carried out for a solar-like computational domain. The inner radius of the computational domain is taken to be at $r = 0.6$, and the input profiles are chosen so as to imply that the base of the convection zone occurs at $r = 0.7$. The reason for this choice of domain was simply to allow easier comparison with the results that were found in the solar dynamo calculations. With this solar-like convection zone, the main fact that has emerged from these simulations is that the negative radial shear at high latitudes plays a key role in the behaviour of the dynamo. It is thought that cooler main-sequence stars have a deeper convective envelope than the Sun and it is therefore important to establish what effect this may have upon dynamo action in rapidly rotating late-type stars.

It is reasonably straightforward to adapt this model in order to investigate a star with a deeper convection zone. Two cases have been examined: one where the base of the convection zone occurs at $r = 0.5$, in the other it occurs at $r = 0.3$. The inner radius of the computational domain is adjusted accordingly so that the inner radius occurs 0.1 of a stellar radius below the base of the convection zone. Given the increased size of the

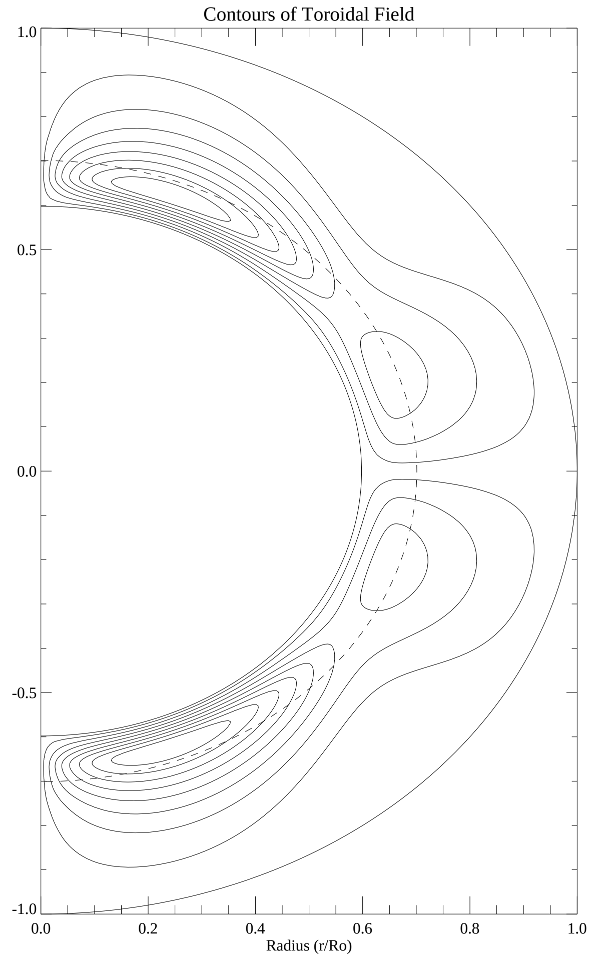

Figure 7.16: The spatial distribution of toroidal field at the end of a computational run, for the $\alpha^2\omega$ case. Contours are equally spaced, solid lines correspond to positive values of B, dashed lines correspond to negative values. $f(\theta) = \cos\theta$, $\eta_c = 0.01$, $r_\alpha = 0.725$ and $R_\alpha = -100.0$.

computational domain, higher numbers of radial grid-points are required to achieve the same level of resolution – this was adjusted appropriately for each set of simulations. In order to reflect the fact that the location of the base of the convection zone has changed, equations (7.4) and (7.5) also need to be modified so that the transition from

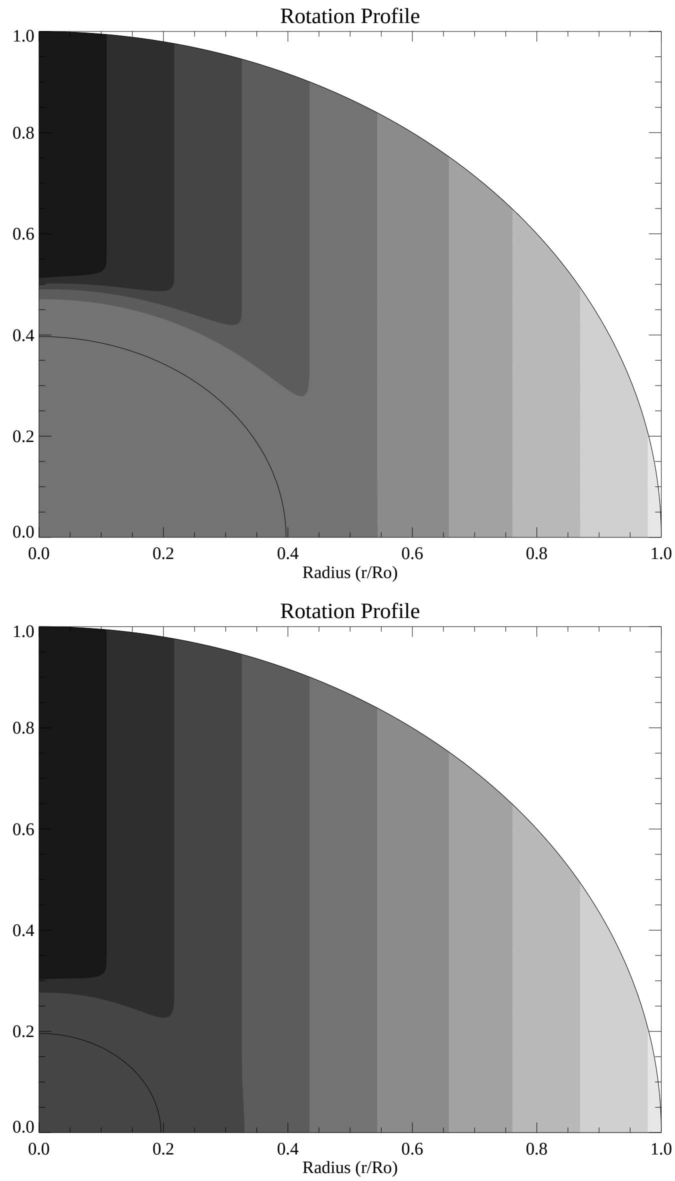

Figure 7.17: Contours of constant Ω for a rapid rotator. In the top plot, the base of the convection zone occurs at $r = 0.5$, in the bottom plot, it occurs at $r = 0.3$. Within each plot, contours are equally spaced, with separation 0.0005. Darker greys correspond to slower rotation rates.

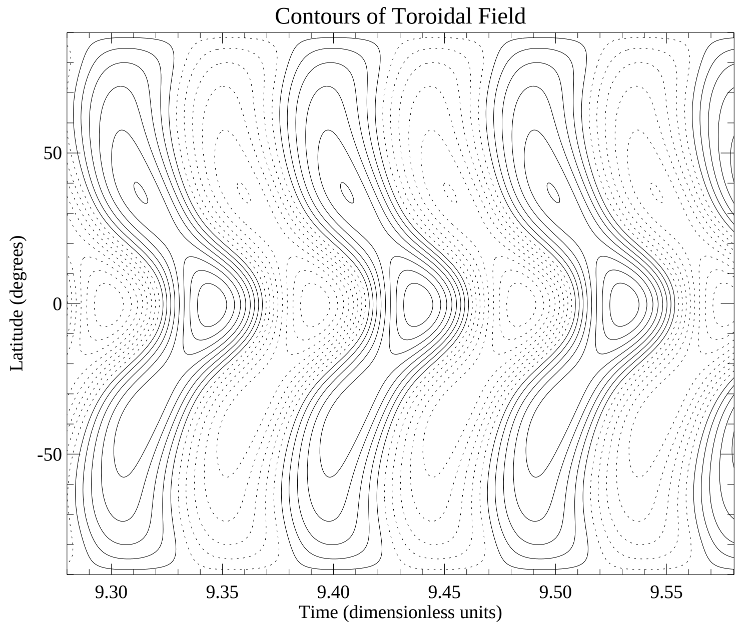

Figure 7.18: Contours of constant toroidal field, plotted against latitude and time, at the base of a deeper convection zone ($r = 0.5$). Contours are equally spaced, solid lines correspond to positive values of B, dashed lines correspond to negative values. The α-effect is distributed throughout the convection zone, $\eta_c = 0.01$ and $D = -4.0 \times 10^6$.

the overshoot layer to the turbulent convection zone occurs at the correct place (0.7 becomes 0.5 or 0.3 accordingly). Finally, the differential rotation profile needs to be altered. This requires not only a change in the location of the transition region, but also the parameter c (given in equation 7.1) needs to be altered in order to preserve the fact that the net torque upon the core should be zero. The following profiles are used:

$$\Omega(r, \theta) = 1.0 + \frac{1}{2}\left[1 + \Phi\left(\frac{r - 0.5}{0.025}\right)\right](0.0046s - 0.0021), \tag{7.9}$$

and

$$\Omega(r, \theta) = 1.0 + \frac{1}{2}\left[1 + \Phi\left(\frac{r - 0.3}{0.025}\right)\right](0.0046s - 0.0011), \tag{7.10}$$

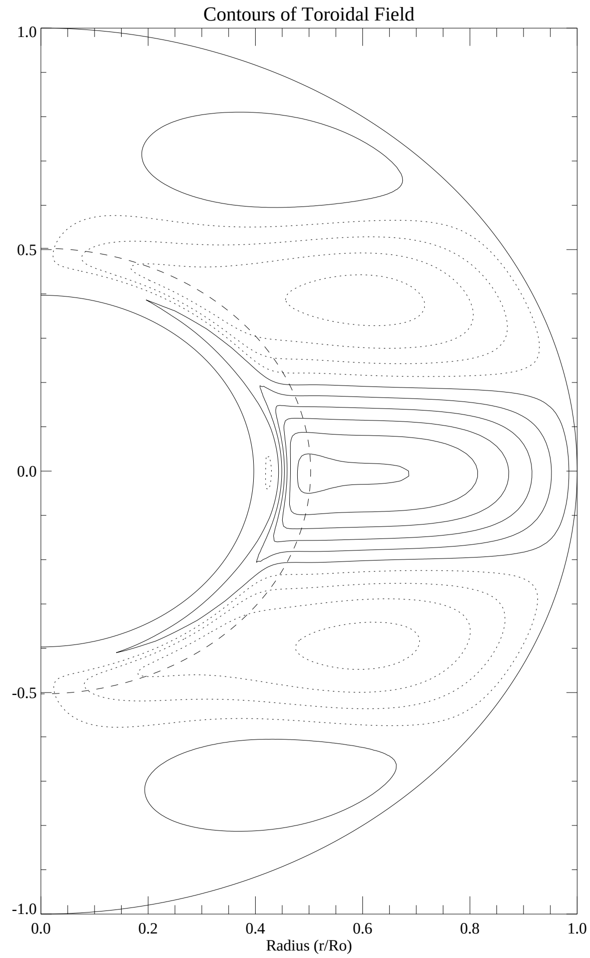

Figure 7.19: The spatial distribution of toroidal field at the end of a computational run. Contours are equally spaced, solid lines correspond to positive values of B, dashed lines correspond to negative values. The parameters are identical to those given in Figure 7.18.

where Φ and s are defined as before. These two rotation profiles are shown in Figure 7.17. It is immediately apparent that a deeper convection zone implies a smaller region of radial shear at high latitudes, both in terms of magnitude and in terms of spatial extent. It seems highly probable that this will have a dramatic effect upon the behaviour of the dynamo.

For the model where the base of the convection zone occurs at $r = 0.5$, the results are not dissimilar to those found previously, although there are obviously quantitative changes. For an α-effect that is distributed throughout the convection zone, this deeper convection zone results in a smaller critical dynamo number (approximately -1.0×10^6). Figure 7.18 shows contours of constant toroidal field at the base of the convection zone, for $D = -4.0 \times 10^6$. Given the absence of a strong high-latitude branch, it is clear that the tachocline region plays only a minor role in the generation of these oscillations. A plot showing the spatial distribution of this solution is shown in Figure 7.19. These oscillations are driven primarily by the weak differential rotation within the convection zone, with the peak fields of this distributed dynamo occurring at low latitudes. For an α-effect that is confined to the base of the convection zone (with $f(\theta) = \cos\theta$ and $r_\alpha = 0.525$), the critical dynamo number is much larger than for the equivalent simulations with the shallower convection zone. This is a reflection of the fact that the shear layer at high latitudes is weaker. Although the critical value has not been determined accurately, $D = -1.0 \times 10^8$ represents a mildly supercritical value of the dynamo number. This value for D leads to oscillatory magnetic fields that are confined to high latitudes at the base of the convection zone. As the magnitude of D is increased, it is possible to excite low-latitude oscillatory features, as shown in Figure 7.20, although this low-latitude branch is always much weaker than the high-latitude branch. Other than the significant changes in the values of the critical dynamo numbers, these results are similar to those described in Section 7.3.2, for the shallower convection zone.

Increasing the depth of the convection zone still further, so that the base of the convection zone occurs at $r = 0.3$, leads to a more pronounced change in the qualitative behaviour of the dynamo. For a distributed α-effect, the solutions seem to be virtually identical to those found for the previous case. Given that the tachocline did not play a major role there, it is unsurprising that these solutions should be largely unaffected by a reduction in the strength of this shear layer. For an α-effect that is confined to the base

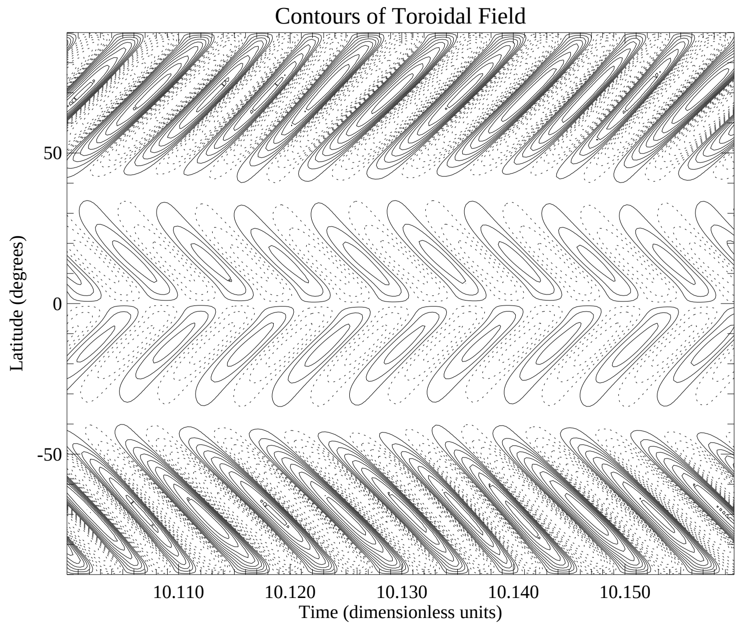

Figure 7.20: Contours of constant toroidal field, plotted against latitude and time, at the base of a deeper convection zone ($r = 0.5$). Contours are equally spaced, solid lines correspond to positive values of B, dashed lines correspond to negative values. The α-effect is confined to the base of the convection zone, $f(\theta) = \cos\theta$, $r_\alpha = 0.525$, $\eta_c = 0.01$ and $D = -4.0 \times 10^8$.

of the convection zone, the critical dynamo number is now very large (approximately -4.0×10^8). Even for mildly supercritical dynamo numbers, the low-latitude oscillatory branch of the dynamo is similar in strength to the high-latitude branch. This is due to the fact that the dynamo number is extremely large – strong enough to excite oscillations at low latitudes, where the radial shear is weak – and the shear at high latitudes is weaker than in previous models. Figure 7.21 shows contours of toroidal field, at the base of the convection zone, for $D = -9.0 \times 10^8$. As can clearly be seen in this diagram, one result of this very deep convection zone is that the dynamo is no longer dominated by high latitude features, with activity evenly distributed over all latitudes. We would therefore

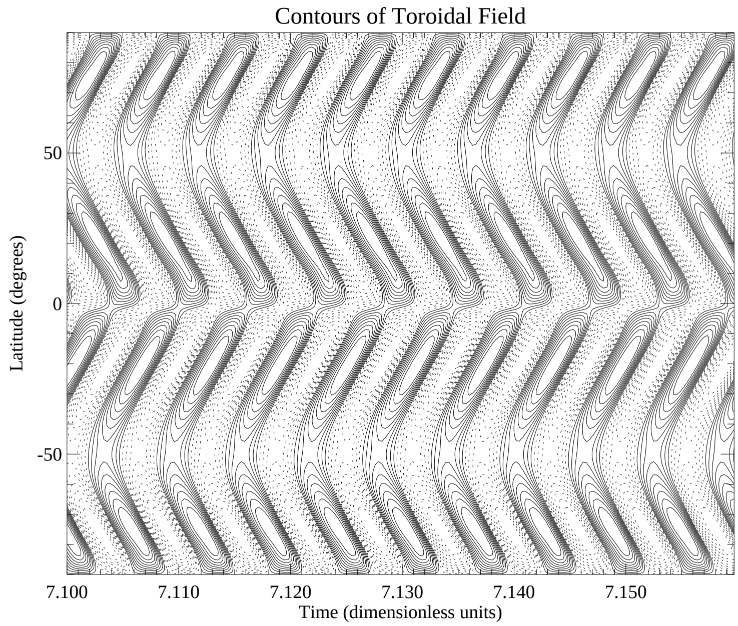

Figure 7.21: Contours of constant toroidal field, plotted against latitude and time, at the base of a deeper convection zone ($r = 0.3$). Contours are equally spaced, solid lines correspond to positive values of B, dashed lines correspond to negative values. The α-effect is confined to the base of the convection zone, $f(\theta) = \cos\theta$, $r_\alpha = 0.325$, $\eta_c = 0.01$ and $D = -9.0 \times 10^8$.

expect late-type stars with very deep convection zones to have surface magnetic features distributed over all latitudes.

There are several important points that are raised by the results from these simulations. One of the most important of these concerns the influence of the core. As seen above, the assumption that there must be no net torque upon the core leads to the radial shear at high latitudes having less of an effect within stars that have deeper convection zones. For a very deep convection zone, it appears that the magnitude of this high-latitude shear may be sufficiently reduced that magnetic field generation is no longer predominantly confined to the poles. It should also be noted that the critical dynamo numbers for these interface modes become very large as the magnitude of this shear decreases. Stars that have very deep convective envelopes may then favour dynamo action that is distributed throughout the convection zone, rather than being confined to its base.

Another way of looking at this is by considering the so-called “tangent cylinder”, which is the cylindrical surface which has the same radius as the core and shares its axis with the rotation axis. Within this tangent cylinder, there is a shear layer at the base of the convection zone which drives an oscillatory interface mode at high latitudes. Outside the tangent cylinder, at low latitudes, the radial shear is much weaker and a much higher dynamo number is required in order to excite oscillatory behaviour. By reducing the size of the core, we are reducing the size (and importance) of the tangent cylinder. The tangent cylinder is also thought to play a key role in the geodynamo, the behaviour of which is also strongly influenced by rapid rotation (for recent reviews see, for example, Fearn, 1998; Jones, 2000).

7.6 Summary and discussion

Observations of rapidly rotating late-type stars suggest that the surface differential rotation on such stars is relatively small when compared to that seen on the Sun. Given the strong dependence of mean-field dynamo models upon differential rotation, we would expect the dynamo regime in a star like AB Doradus to be very different from that operating within the Sun. The differential rotation profile that is used here is based upon several assumptions, most notably that the Taylor-Proudman constraint enforces cylindrical angular velocity contours within the convection zone. If the core is taken to be rotating rigidly, as observed in the Sun, a tachocline-like region is required at the base of the convection zone in order to ensure that the angular velocity profile is smooth. The form of this tachocline region is rather different from that seen at the base of the solar convection zone, in that it is concentrated primarily at high latitudes. In an $\alpha\omega$ dynamo model, a region of strong radial shear at high latitudes is likely to favour magnetic activity there. For an α-effect that is confined to the base of the convection zone, this is precisely what is observed. The resulting oscillations remain confined to high latitudes, around the base of the convection zone, over a very large range of values of the dynamo number – highly supercritical values of D are required to excite even weak oscillations at low latitudes. This definite preference towards activity at high latitudes provides an extremely attractive explanation for the appearance of polar starspots on rapidly rotating late-type stars. An α-effect that is operating throughout the convection zone leads to a distributed dynamo, with magnetic fields at all latitudes. A likely scenario is that a distributed dynamo may be operating in parallel with a dynamo at the base of the convection zone. This may explain the simultaneous occurrence of large high-latitude starspots and weaker low-latitude features on stars like AB Doradus.

Whilst these results were found to be robust to most changes in the model parameters, it was found that restricting the α-effect to low latitudes (unsurprisingly) suppressed the appearance of magnetic fields at high latitudes. This highlights the fact that although the tachocline plays a key role in the dynamo, it is not the only important physical ingredient: the α-effect must be strong enough at the poles to regenerate the poloidal field there. It was found in the solar dynamo calculations that an α-effect that is confined to low latitudes is required in order to reproduce the observed properties of the solar magnetic cycle. This apparent difference highlights one of the main problems that is associated with stellar mean-field dynamo theory, namely that the nature and spatial distribution of the α-effect is still poorly understood. In both the solar calculations and in this chapter, the α-effect has been fixed primarily by observational constraints rather than by theoretical considerations.

Although this $\alpha\omega$ model clearly suggests that the latitudinal distribution of the tachocline may be a key factor in determining the spatial distribution of magnetic fields, it has the drawback that the solutions tend to be oscillatory. Magnetic fields on rapid rotators may vary aperiodically, but these stars do not show smooth cyclic magnetic activity, unlike slower rotating late-type stars. By looking at the $\alpha^2\omega$ case, it was found that it is possible to select the input parameters in such a way as to produce steady modes that are confined to high latitudes, at the base of the convection zone. A steady mode is probably more consistent with the observed magnetic activity, which suggests that the dynamo in these stars may be of $\alpha^2\omega$ type. Whether or not this is the case, both the $\alpha\omega$ and the $\alpha^2\omega$ models rely upon the fact that the tachocline is strongest at high latitudes in order to favour the production of magnetic fields near the poles.

In this chapter, attention has been focused upon a dynamo explanation for polar spots. It has previously been proposed that these high-latitude features might arise simply due to the effect of the Coriolis force on rising loops of buoyant magnetic flux (Granzer et al., 2000). It is certainly true that this will readily produce higher latitude features, but it is far easier to produce such features if the flux is emerging from high latitudes at the base of the convection zone. The results from the dynamo model described here are clearly compatible with this idea. Another possible explanation for high latitude features is that they are the result of a meridional flow sweeping surface flux up towards the poles. Although it is theoretically possible to insert a meridional flow into this dynamo model, using the code described in Section 4.4.2, this has not been investigated here. Since this mean-field code does not attempt to include the effects of flux buoyantly rising to the surface, the advection of these surface magnetic fields is not reproducible here. It is also worth mentioning that, although a rapidly rotating star may possess a strong meridional circulation within its convection zone, it is very difficult to theoretically predict the spatial distribution of such a circulation.

Finally, it is worth considering how dynamos in fully convective stars may be operating. In Section 7.5, it was demonstrated that the influence of the tachocline probably decreases as the depth of the convection zone increases. The radius of the (so-called) tangent cylinder decreases as the radius of the core decreases, and the no-torque condition implies that the strength of the shear layer similarly decreases. So, for stars with a very deep convection zone, we might expect that a distributed dynamo may be favoured over one that is confined to the base of the convection zone. Late M-type main sequence stars are thought to be fully convective – the absence of any tachocline would appear to confirm the idea that a dynamo in these stars must be distributed throughout the star. Since the luminosity of these M-type stars is very small, it is difficult to obtain the strong rotationally broadened spectral lines that are required for Doppler imaging. Having said that, a few Doppler imaging studies have been carried out for these late M-type stars (see, for example Barnes et al., 2002). From these preliminary investigations, it appears that these stars show no particular preference for activity at high latitudes, with starspots found at all latitudes. Although very few of these fully convective stars have been studied using Doppler imaging, these results do seem to support the view that a distributed dynamo is operating in such stars.

Chapter 8

Conclusions and Future Work

Mean-field dynamo theory is capable of reproducing many of the observed features of solar and stellar magnetic activity. As our closest star, much of the observational motivation for dynamos in late-type stars comes from the Sun, but it is reasonable to suppose that the resulting dynamo models may be equally applicable to stars of a similar age and spectral type. Sunspot observations from the latter stages of the Maunder minimum suggest that the large-scale solar magnetic field was, at the time, highly asymmetric about the equator. This behaviour is very unlike the relatively symmetric magnetic activity that has been observed on the Sun in recent years. In Chapter 3, an illustrative Cartesian model was derived from the mean-field equations in order to investigate the occurrence of such asymmetry. Although highly idealised from the point of view of a stellar dynamo, this model demonstrated that it is possible for dipolar and quadrupolar modes to interact, in the nonlinear regime, in such a way as to produce solutions that are characterised by magnetic activity that is confined almost entirely to one hemisphere. These hemispherical solutions were found to be remarkably robust. Although this model is very simple, it clearly supports the idea that dipolar and quadrupolar interactions may be capable of explaining the occurrence of strong equatorial asymmetry in stellar magnetic fields.

More realistic mean-field stellar dynamo models were discussed in Chapter 4. The numerical code that was described in this chapter, having been extensively tested, provides a useful means of studying axisymmetric mean-field models in spherical geometry. This code has not only been widely used in this thesis, but its versatility means that it could be applied to a wide range of different problems in the future. In Chapter 5 the code was applied to the solar dynamo. Taking α-quenching to be the sole nonlinearity, it was found that a distributed α-effect tended to lead to magnetic activity that was dominated by the strong latitudinal shear within the convection zone – for negative values of D, this corresponded to a steady mode. Oscillatory solutions, driven by the radial shear, were found for an α-effect that was confined to the base of the convection zone. In order to prevent the dynamo being dominated by magnetic activity at high latitudes, the α-effect also had to be restricted to low latitudes. It was then found that it was possible to produce solutions that were dominated by low-latitude magnetic fields which migrated equatorwards during each magnetic cycle. An additional (weak) high-latitude branch to the dynamo was found for larger values of the dynamo number.

In Chapter 6, the nonlinear part of the model was modified, so that it included the effects of the macrodynamic back-reaction of the Lorentz force upon the differential rotation. By subtracting a latitude-dependent time-average from the total velocity perturbation, it was shown that it is possible to generate an oscillatory pattern, of migrating bands of flow, that is consistent with many of the observed features of the (so-called) torsional oscillations on the Sun. In order to produce the observed polar branch, it is necessary to take a large enough value of D so that there is a weak polar branch to the dynamo. This presents an apparent paradox: it appears that a high-latitude branch to the dynamo is required in order to reproduce the observed pattern of torsional oscillations, but polar active regions are never observed on the Sun. A possible solution to this problem lies in the fact that the strong radial shear at high latitudes may suppress the undular magnetic buoyancy instability there (Tobias and Hughes, 2004). This means that there may be a polar branch to the dynamo that never produces surface active regions at high latitudes. Having found these torsional oscillations, it was demonstrated that they are compatible with low values of the magnetic Prandtl number. Even for strongly modulated solutions, it was possible to identify the correct pattern of oscillations provided that the time-average was taken over a short enough time-period. Finally, it was shown that by including the effects of density stratification, it is possible to excite strong torsional oscillations at the surface of the domain, despite the fact that the magnetic activity is confined to the base of the convection zone.

Moving away from the solar dynamo, Chapter 7 focused upon more rapidly rotating late-type stars. The proposed rotation profile for such stars was rather different from that of the Sun – a consequence of the fact that the Coriolis force is now assumed to play a dominant role in the dynamics of the convection zone. The most important new feature is that the tachocline region is now confined to high latitudes. This was found to favour magnetic activity near the poles, for an α-effect that was confined to the base of the convection zone. This provides an attractive explanation for the existence of polar starspots on these rapid rotators.

An important aspect of mean-field theory is its ability to highlight the crucial physical processes that are in operation in stellar dynamos. Having said that, it is only able to provide qualitative results for stellar dynamos and its successes have been in reproducing observations rather than possessing any great predictive power. Given that the differential rotation profile within the Sun is relatively well-constrained by observations, the main uncertainties in solar mean-field dynamo models centre around the α-effect. Justifying, in physical terms, the need to have an α-effect that is confined to low latitudes at the base of the convection zone, is not straightforward. If magnetic buoyancy is the dominant physical mechanism that is involved, it is logical that the the site of the α-effect should be around the base of the convection zone. However the low-latitudinal confinement is much harder to understand. If non-axisymmetric magnetic buoyancy instabilities are suppressed by a strong radial shear (Tobias and Hughes, 2004), then this may explain the apparent reduction in the α-effect at high latitudes within the Sun. This suggests that a study into the influence of strong differential rotation (both radial and latitudinal) upon a buoyantly-driven α-effect would be a productive area of future research.

The tachocline itself is another key factor in solar mean-field dynamo models. As the site of strong differential rotation and large-scale magnetic fields, its formation and subsequent stability has already been the subject of a considerable number of studies (as reviewed by, for example, Tobias, 2004). An interesting avenue of research would be to investigate the way in which the magnetic fields that are produced by the dynamo could affect the stability of different regions of the tachocline. In more general terms, there are still unanswered questions regarding the transport of angular momentum within the tachocline. A related issue concerns differential rotation within the solar convection zone. If other stars are assumed to have a rigidly rotating core, it was shown in Chapter 7 that the "no-torque" condition implies that the differential rotation within the convection zone determines the spatial distribution of the tachocline, As discussed in Section 7.1, numerical models are still not capable of reproducing a satisfactory solar-like differential rotation profile, and theoretical models rely upon the (unjustifiable) first order smoothing approximation. Although plausible theoretical arguments were used to produce a differential rotation profile for the rapidly rotating model, a better understanding of the solar differential rotation would enable us to predict the behaviour of other stars with more confidence.

It could be argued that, in its current state, there is not much more that mean-field dynamo theory can tell us about solar and stellar dynamos. This implies that it may be time to investigate alternative approaches to the problem. There are really only two obvious alternatives. Firstly, illustrative models are clearly capable of providing useful insights into specific aspects of solar and stellar dynamos. Complicated dynamical behaviour can often be related to a simple low-order model, which is much easier to analyse than the full dynamo equations. If this low-order model is related to a normal form, the observable patterns of behaviour are robust and shared by a wide range of similar dynamical systems. At the other extreme, we have large-scale simulations. Given the failure of purely hydrodynamical models to reproduce a solar-like differential rotation profile (and the fact that much of the physics is still not well understood) a large-scale simulation of the solar dynamo is rather over-ambitious at this stage. Having said that, although it is unfeasible to attempt to simulate global dynamo models, it is possible to look at more local simulations. An example of this is in the simulation of the small-scale dynamo action by turbulent convection in the solar photosphere (see, for example, Cattaneo et al., 2003). Although such simulations present a serious numerical challenge, there are many aspects of small-scale dynamo action that have yet to be explored.

Bibliography

Abramowitz, M. and Stegun, I. A. (1968). *Handbook of Mathematical Functions*. Dover publications, New York.

Babcock, H. W. (1961). The topology of the Sun's magnetic field and the 22-year cycle. *Astrophys. J.*, 133:572.

Baliunas, S. and Jastrow, R. (1990). Evidence for long-term brightness changes of solar-type stars. *Nature*, 348:520.

Baliunas, S. L. et al. (1995). Chromospheric variations in main-sequence stars. *Astrophys. J.*, 438:269.

Barnes, J. R., James, D. J., and Cameron, A. C. (2002). The boundaries of Doppler imaging: starspot patterns on M dwarfs. *Astron. Nachr.*, 323:333.

Beer, J., Raisbeck, G. M., and Yiou, F. (1991). Time variations of ^{10}Be and solar activity. In Sonett, C. P., Giampapa, M. S., and Matthews, M. S., editors, *The Sun in Time*, page 343. University of Arizon Press.

Beer, J., Tobias, S., and Weiss, N. (1998). An active Sun throughout the Maunder minimum. *Solar Physics*, 181:237.

Belvedere, G., Pidatella, R. M., and Proctor, M. R. E. (1990). Nonlinear dynamics of a stellar dynamo in a spherical shell. *Geophys. Astrophys. Fluid Dynamics*, 51:263.

Bennett, M., Schatz, M. F., Rockwood, H., and Wiesenfeld, K. (2002). Huygen's clocks. *Proc. R. Soc. Lond. A*, 458:563.

Blackman, E. G. and Field, G. B. (2000). Constraints on the magnitude of α in dynamo theory. *Astrophys. J.*, 534:984.

Bonanno, A., Elstner, D., Rüdiger, G., and Belvedere, G. (2002). Parity properties of an advection-dominated solar $\alpha^2\Omega$-dynamo. *Astron. Astrophys.*, 390:673.

Braginsky, S. I. (1964). Self excitation of a magnetic field during the motion of a highly conducting fluid. *Sov. Phys. JETP*, 20:726.

Brandenburg, A. (1994). Solar Dynamos: Computational Background. In Proctor, M. R. E. and Gilbert, A. D., editors, *Lectures on Solar and Planetary Dynamos*, chapter 4. Cambridge University Press.

Brandenburg, A., Krause, F., Meinel, R., Moss, D., and Tuominen, I. (1989). The stability of nonlinear dynamos and the limited role of kinematic growth rates. *Astron. Astrophys.*, 213:411.

Braun, D. C. and Fan, Y. (1998). Helioseismic measurements of the subsurface meridional flow. *Astrophys. J.*, 508:L105.

Brooke, J., Moss, D., and Phillips, A. (2002). Deep minima in stellar dynamos. *Astron. Astrophys.*, 395:1013.

Brooke, J. M., Pelt, J., Pulkkinen, P., and Tuominen, I. (2002). The importance of spatial information in sunspot records. *Highlights in Astronomy*, 12:334.

Bruls, J. H. M. J., Solanki, S. K., and Schüssler, M. (1998). Doppler imaging: the polar spot controversy. *Astron. Astrophys.*, 336:231.

Brun, A. S. and Toomre, J. (2002). Turbulent convection under the influence of rotation: Sustaining a strong differential rotation. *Astrophys. J.*, 570:865.

Bullard, E. C. and Gellman, H. (1954). Homogeneous dynamos and terrestrial magnetism. *Phil. Trans. R. Soc. Lond. A*, 247:213.

Bushby, P. J. (2003a). Modelling dynamos in rapidly rotating late-type stars. *Mon. Not. R. Astron. Soc.*, 342:L15.

Bushby, P. J. (2003b). Strong asymmetry in stellar dynamos. *Mon. Not. R. Astron. Soc.*, 338:655.

Busse, F. H. (2000). Homogeneous dynamos in planetary cores and in the laboratory. *Ann. Rev. Fluid Mech.*, 32:383.

Byrne, P. B. (1992). Starspots. In Thomas, J. H. and Weiss, N. O., editors, *NATO ASIC Proc. 375: Sunspots. Theory and Observations*, page 63.

Caligari, P., Moreno-Insertis, F., and Schüssler, M. (1995). Emerging flux tubes in the solar convection zone. I. Asymmetry, tilt, and emergence latitude. *Astrophys. J.*, 441:886.

Caligari, P., Schüssler, M., and Moreno-Insertis, F. (1998). Emerging flux tubes in the solar convection zone. II. The influence of initial conditions. *Astrophys. J.*, 502:481.

Cattaneo, F., Emonet, T., and Weiss, N. (2003). On the Interaction between Convection and Magnetic Fields. *Astrophys. J.*, 588:1183.

Cattaneo, F. and Hughes, D. W. (1996). Nonlinear saturation of the turbulent alpha effect. *Phys. Rev. E.*, 54:4532.

Charbonneau, P. and MacGregor, K. B. (1996). On the generation of equipartition-strength magnetic fields by turbulent hydromagnetic dynamos. *Astrophys. J.*, 473:L59.

Charbonneau, P. and MacGregor, K. B. (1997). Solar interface dynamos. II. Linear, kinematic models in spherical geometry. *Astrophys. J.*, 486:502.

Chitre, S. and Antia, H. (2003). Seismic sun. In Dwivedi, B., editor, *Dynamic Sun*, chapter 3, page 36. Cambridge University Press.

Choudhuri, A. R. (1998). *The Physics of Fluids and Plasmas*. Cambridge University Press.

Choudhuri, A. R., Schüssler, M., and Dikpati, M. (1995). The solar dynamo with meridional circulation. *Astron. Astrophys.*, 303:L29.

Christensen-Dalsgaard, J. et al. (1996). The Current State of Solar Modeling. *Science*, 272:1286.

Collier Cameron, A. (2002). Starspots as tracers of surface differential rotation. *Astron. Nachr.*, 323:336.

Collier Cameron, A. and Donati, J.-F. (2002). Doin' the twist: secular changes in the surface differential rotation of AB Doradus. *Mon. Not. R. Astron. Soc.*, 329:L23.

Collier Cameron, A. and Unruh, Y. C. (1994). Doppler images of AB Doradus in 1992 January. *Mon. Not. R. Astron. Soc.*, 269:814.

Covas, E., Tavakol, R., and Moss, D. (2000a). Spatiotemporal fragmentation as a mechanism for different dynamical modes of behaviour in the solar convection zone. *Astron. Astrophys.*, 363:L13.

Covas, E., Tavakol, R., and Moss, D. (2001a). Dynamical variations of the differential rotation in the solar convection zone. *Astron. Astrophys.*, 371:718.

Covas, E., Tavakol, R., and Moss, D. (2003). The influence of density stratification and multiple nonlinearities on solar torsional oscillations. *Astron. Astrophys.* Submitted.

Covas, E., Tavakol, R., Moss, D., and Tworkowski, A. (2000b). Torsional oscillations in the solar convection zone. *Astron. Astrophys.*, 360:L21.

Covas, E., Tavakol, R., Tworkowski, A., and Brandenburg, A. (1998). Axisymmetric mean field dynamos with dynamic and algebraic α-quenchings. *Astron. Astrophys.*, 329:350.

Covas, E., Tavakol, R., Vorontsov, S., and Moss, D. (2001b). Spatiotemporal fragmentation and the uncertainties in the solar rotation law. *Astron. Astrophys.*, 375:260.

Cowling, T. G. (1934). The magnetic field of sunspots. *Mon. Not. R. Astron. Soc.*, 94:39.

Cowling, T. G. (1976). *Magnetohydrodynamics*. Monographs on Astronomical Subjects, Bristol: Adam Hilger.

Cowling, T. G. (1981). The present status of dynamo theory. *Ann. Rev. Astron. Astrophys.*, 19:115.

Deluca, E. E. and Gilman, P. A. (1986). Dynamo theory for the interface between the convection zone and the radiative interior of a star. I. Model equations and exact solutions. *Geophys. Astrophys. Fluid Dynamics*, 37:86.

Dikpati, M. and Charbonneau, P. (1999). A Babcock-Leighton flux transport dynamo model with solar-like differential rotation. *Astrophys. J.*, 518:508.

Dikpati, M. and Choudhuri, A. R. (1994). The evolution of the Sun's poloidal field. *Astron. Astrophys.*, 291:975.

Dikpati, M. and Gilman, P. (2001a). Analysis of Hydrodynamic Stability of Solar Tachocline Latitudinal Differential Rotation using a Shallow-Water Model. *Astrophys. J.*, 551:536.

Dikpati, M. and Gilman, P. (2001b). Flux-transport dynamos with α-effect from the global instability of tachocline differential rotation: A solution for magnetic parity selection in the Sun. *Astrophys. J.*, 559:428.

Donahue, R. A., Saar, S. H., and Baliunas, S. L. (1996). A relationship between mean rotation period in lower main-sequence stars and its oberved range. *Astrophys. J.*, 466:384.

Donati, J.-F. and Collier Cameron, A. (1997). Differential rotation and magnetic polarity patterns on AB Doradus. *Mon. Not. R. Astron. Soc.*, 291:1.

Eddy, J. A. (1976). The Maunder Minimum. *Science*, 192:1189.

Fearn, D. (1998). Hydromagnetic flow in planetary cores. *Rep. Prog. Phys.*, 61:175.

Ferriz-Mas, A., Schmitt, D., and Schüssler, M. (1994). A dynamo effect due to instability of magnetic flux tubes. *Astron. Astrophys.*, 289:949.

Galloway, D. J. and Weiss, N. O. (1981). Convection and magnetic fields in stars. *Astrophys. J.*, 243:945.

Gilbert, A. D., Otani, N. F., and Childress, S. (1993). Simple dynamical fast dynamos. In Proctor, M. R. E., Matthews, P. C., and Rucklidge, A. M., editors, *Solar and Planetary Dynamos*, page 129. Cambridge University Press.

Giles, P. M., Duvall, T. L., Scherrer, P. H., and Bogart, R. S. (1997). A subsurface flow of material from the Sun's equator to its poles. *Nature*, 390:52.

Gilman, P. A. (1974). Solar rotation. *Ann. Rev. Astron. Astrophys.*, 12:47.

Gilman, P. A. (1983). Dynamically consistent nonlinear dynamos driven by convection in a rotating spherical shell. II. Dynamos with cycles and strong feedbacks. *Astrophys. J. Supp.*, 53:243.

Gilman, P. A. and Miller, J. (1981). Dynamically consistent nonlinear dynamos driven by convection in a rotating spherical shell. *Astrophys. J. Supp.*, 46:211.

Gilman, P. A. and Miller, J. (1986). Nonlinear convection of a compressible fluid in a rotating spherical shell. *Astrophys. J. Supp.*, 61:585.

Glatzmaier, G. A. (1985). Numerical simulations of stellar convective dynamos. II. Field propagation in the convection zone. *Astrophys. J.*, 291:300.

Glatzmaier, G. A. and Gilman, P. A. (1982). Compressible convection in a rotating spherical shell. V. Induced differential rotation and meridional circulation. *Astrophys. J.*, 256:316.

Glatzmaier, G. A. and Roberts, P. H. (1995). A three-dimensional self-consistent computer simulation of a geomagnetic field reversal. *Nature*, 377:203.

Granzer, T., Scüssler, M., Caligari, P., and Strassmeier, K. G. (2000). Distribution of starspots on cool stars. II. Pre-main-sequence and ZAMS stars between 0.4 $M_\odot$ and 1.7 $M_\odot$. *Astron. Astrophys.*, 355:1087.

Guckenheimer, J. and Holmes, P. (1986). *Nonlinear Oscillations, Dynamical Systems and Bifurcations of Vector Fields. 2nd Printing.* Springer, New York.

Hale, G. E. (1908). On the probable existence of a magnetic field in sun-spots. *Astrophys. J.*, 28:315.

Hale, G. E., Ellerman, F., Nicholson, S. B., and Joy, A. H. (1919). The magnetic polarity of sun-spots. *Astrophys. J.*, 49:153.

Hall, D. S. (1991). Learning about stellar dynamos from longterm photometry of starspots. In Tuominen, I., Moss, D., and Rüdiger, G., editors, *The Sun and Cool Stars: Activity, Magnetism, Dynamos, I.A.U. Colloq. No. 130*, page 353. Berlin: Springer-Verlag.

Hart, J. E., Glatzmaier, G. A., and Toomre, J. (1986). Space-laboratory and numerical simulations of thermal convection in a rotating spherical shell with radial gravity. *Journal of Fluid Mechanics*, 173:519.

Hathaway, D., Gilman, P., Harvey, J. W., Hill, F., Howard, R. B., Jones, H. P., Kasher, J., Leibacher, J. B., Pintar, J., and Simon, G. W. (1996). GONG Observations of Solar Surface Flows. *Science*, 272:1306.

Hathaway, D. H. (1996). Doppler measurements of the Sun's meridional flow. *Astrophys. J.*, 460:1027.

Hide, R. and Palmer, T. N. (1982). Generalization of cowling's theorem. *Geophys. Astrophys. Fluid Dynamics*, 19:301.

Howard, R. and LaBonte, B. J. (1980). The Sun is observed to be a torsional oscillator with a period of 11 years. *Astrophys. J.*, 239:L33.

Howe, R., Christensen-Dalsgaard, J., Hill, F., Komm, R. W., Larsen, R. M., Schou, J., Thompson, M. J., and Toomre, J. (2000). Dynamic variations at the base of the solar convection zone. *Science*, 287:2456.

Hughes, D. W. (1992). The formation of flux tubes at the base of the convection zone. In Thomas, J. H. and Weiss, N. O., editors, *NATO ASIC Proc. 375: Sunspots. Theory and Observations*, page 371.

Iserles, A. (1996). *A First Course in the Numerical Analysis of Differential Equations.* Cambridge University Press.

Jennings, R., Brandenburg, A., Moss, D., and Tuominen, I. (1990). Can stellar dynamos be modelled in less that three dimensions? *Astron. Astrophys.*, 230:463.

Jennings, R. L. (1991). Symmetry breaking in a non-linear $\alpha\omega$-dynamo. *Geophys. Astrophys. Fluid Dynamics*, 57:147.

Jennings, R. L. and Weiss, N. O. (1991). Symmetry breaking in stellar dynamos. *Mon. Not. R. Astron. Soc.*, 252:249.

Jensen, E. (1955). On tubes of magnetic forces embedded in stellar material. *Annales d'Astrophysique*, 18:127.

Jepps, S. A. (1975). Numerical models of hydromagnetic dynamos. *Journal of Fluid Mechanics*, 67:625.

Jones, C. A. (2000). Convection-driven geodynamo models. *Phil. Trans. R. Soc. Lond. A*, 358:873.

Kemp, J. C., Swedlund, J. B., Landstreet, J. D., and Angel, J. R. P. (1970). Discovery of circularly polarized light from a white dwarf. *Astrophys. J.*, 161:L77.

Kippenhahn, R. and Weigert, A. (1990). *Stellar Structure and Evolution.* Springer-Verlag.

Kitchatinov, L. L., Jardine, M., and Donati, J.-F. (2000). Magnetic cycle of LQ Hydrae: observational indications and dynamo model. *Mon. Not. R. Astron. Soc.*, 318:1171.

Kitchatinov, L. L., Pipin, V. V., Makarov, V. I., and Tlatov, A. G. (1999). Solar torsional oscillations and the grand activity cycle. *Solar Physics*, 189:227.

Kitchatinov, L. L. and Rüdiger, G. (1995). Differential rotation in solar-type stars: revisiting the Taylor number puzzle. *Astron. Astrophys.*, 299:446.

Kitchatinov, L. L., Ruediger, G., and Kueker, M. (1994). Lambda-quenching as the nonlinearity in stellar-turbulence dynamos. *Astron. Astrophys.*, 292:125.

Knobloch, E. and Landsberg, A. S. (1996). A new model of the solar cycle. *Mon. Not. R. Astron. Soc.*, 278:294.

Knobloch, E., Rosner, R., and Weiss, N. (1981). Magnetic fields in late-type stars. *Mon. Not. R. Astron. Soc.*, 197:45P.

Knobloch, E., Tobias, S. M., and Weiss, N. O. (1998). Modulation and symmetry changes in stellar dynamos. *Mon. Not. R. Astron. Soc.*, 297:1123.

Köhler, H. (1973). The solar dynamo and estimates of magnetic diffusivity and the α-effect. *Astron. Astrophys.*, 25:467.

Kosovichev, A. G. et al. (1997). Structure and rotation of the solar interior: Initial results from the MDI Medium-L program. *Solar Physics*, 170:43.

Krause, F. and Rädler, K.-H. (1980). *Mean-Field Magnetohydrodynamics and Dynamo Theory.* Oxford: Pergamon.

Küker, M., Arlt, R., and Rüdiger, G. (1999). The Maunder minimum as due to magnetic Λ-quenching. *Astron. Astrophys.*, 343:977.

Küker, M., Rüdiger, G., and Kitchatinov, L. L. (1993). An $\alpha\Omega$-model of the solar differential rotation. *Astron. Astrophys.*, 279:L1.

Küker, M., Rüdiger, G., and Pipin, V. V. (1996). Solar torsional oscillations due to the magnetic quenching of the reynolds stress. *Astron. Astrophys.*, 312:615.

Küker, M., Rüdiger, G., and Schultz, M. (2002). Circulation-dominated solar shell dynamo models with positive alpha-effect. *Astron. Astrophys.*, 374:301.

Larmor, J. (1919). How could a rotating body such as the Sun become a magnet. *Rep. Brit. Assoc. Adv. Sci.*, page 159.

Leighton, R. B. (1969). A magneto-kinematic model of the solar cycle. *Astrophys. J.*, 156:1.

Malkus, W. V. R. and Proctor, M. R. E. (1975). The macrodynamics of alpha-effect dynamos in rotating fluids. *Journal of Fluid Mechanics*, 67:417.

Markiel, J. A. (1999). *Solar and Stellar Dynamo Models*. PhD thesis, University of Rochester.

Markiel, J. A. and Thomas, J. H. (1999). Solar interface dynamo models with a realistic rotation profile. *Astrophys. J.*, 523:827.

Mason, J., Hughes, D. W., and Tobias, S. M. (2002). The competition in the solar dynamo between surface and deep-seated α-effects. *Astrophys. J.*, 580:L89.

Matthews, P. C., Hughes, D. W., and Proctor, M. R. E. (1995). Magnetic buoyancy, vorticity, and three-dimensional flux-tube formation. *Astrophys. J.*, 448:938.

Maunder, E. W. (1904). Note on the distribution of sun-spots in heliographic latitude, 1874-1902. *Mon. Not. R. Astron. Soc.*, 64:747.

Mestel, L. (1968). Magnetic braking by a stellar wind-I. *Mon. Not. R. Astron. Soc.*, 138:359.

Mestel, L. (1999). *Stellar Magnetism*. Oxford University Press.

Miesch, M. S., Elliott, J. R., Toomre, J., Clune, T. L., Glatzmaier, G. A., and Gilman, P. A. (2000). Three-dimensional Spherical Simulations of Solar Convection. I. Differential Rotation and Pattern Evolution Achieved with Laminar and Turbulent States. *Astrophys. J.*, 532:593.

Moffatt, H. K. (1978). *Magnetic Field Generation in Electrically Conducting Fluids*. Cambridge University Press.

Moffatt, H. K. (2002). Reflections on magnetohydrodynamics. In Batchelor, G. K., Moffatt, H. K., and Worster, M. G., editors, *Perspectives in Fluid Dynamics*, chapter 7. Cambridge University Press.

Moss, D. and Brooke, J. (2000). Towards a model for the solar dynamo. *Mon. Not. R. Astron. Soc.*, 315:521.

Noyes, R. W., Hartmann, L. W., Baliunas, S. L., Duncan, D. K., and Vaughan, A. H. (1984). Rotation, convection, and magnetic activity in lower main sequence stars. *Astrophys. J.*, 279:763.

Oláh, K. and Strassmeier, K. G. (2002). Starspot cycles from long-term photometry. *Astron. Nachr.*, 323:361.

Ossendrijver, M. (2003). The solar dynamo. *Astron. Astrophys. Rev.*, 11:287.

Ossendrijver, M., Stix, M., and Brandenburg, A. (2001). Magnetoconcevtion and dynamo coefficients: Dependence of the α effect on rotation and magnetic field. *Astron. Astrophys.*, 376:713.

Ossendrijver, M. A. J. H. (2000). Grand-minima in a buoyancy-driven solar dynamo. *Astron. Astrophys.*, 359:364.

Parker, E. N. (1955a). The formation of sunspots from the solar toroidal field. *Astrophys. J.*, 121:491.

Parker, E. N. (1955b). Hydromagnetic dynamo models. *Astrophys. J.*, 122:293.

Parker, E. N. (1979). *Cosmical Magnetic Fields: their origin and their activity.* Clarendon Press, Oxford.

Parker, E. N. (1993). A solar dynamo surface wave at the interface between convection and nonuniform rotation. *Astrophys. J.*, 408:707.

Paternò, L., Belvedere, G., Kuzanyan, K. M., and Lanza, A. F. (2002). Asymptotic dynamos in late-type stars. *Mon. Not. R. Astron. Soc.*, 336:291.

Phillips, A., Brooke, J., and Moss, D. (2002). The importance of physical structure in solar dynamo models. *Astron. Astrophys.*, 392:713.

Pipin, V. V. (1999). The Gleissberg cycle by a nonlinear $\alpha\Lambda$ dynamo. *Astron. Astrophys.*, 346:295.

Prautzsch, T. (1993). The dynamo mechanism in the deep convection zone of the Sun. In Proctor, M. R. E., Matthews, P. C., and Rucklidge, A. M., editors, *Solar and Planetary Dynamos*, page 249. Cambridge University Press.

Press, W. H., Flannery, B. P., Teukolsky, S. A., and Vetterling, W. T. (1986). *Numerical Recipes*. Cambridge University Press.

Priest, E. R. (1982). *Solar Magnetohydrodynamics*. Reidel, Dordrecht.

Proudman, J. (1916). On the motion of solids in a liquid possessing vorticity. *Proc. R. Soc. Lond. A*, 92:408.

Ribes, J. C. and Nesme-Ribes, E. (1993). The solar sunspot cycle in the Maunder minimum AD1645 to AD1715. *Astron. Astrophys.*, 276:549.

Rice, J. B. (1996). Doppler imaging of stellar surfaces (review). In Strassmeier, K. G. and Linsky, J. L., editors, *IAU Symp. 176: Stellar Surface Structure*, page 19. Kluwer, Dordrecht.

Rice, J. B. (2002). Doppler imaging of stellar surfaces – techniques and issues. *Astron. Nachr.*, 323:220.

Roberts, P. H. (1967). *An Introduction to Magnetohydrodynamics*. Longmans.

Roberts, P. H. (1994). Fundamentals of dynamo theory. In Proctor, M. R. E. and Gilbert, A. D., editors, *Lectures on Solar and Planetary Dynamos*, chapter 1, page 1. Cambridge University Press.

Roberts, P. H. and Soward, A. M. (1975). A unified approach to mean field electrodynamics. *Astron. Nachr.*, 296:49.

Roberts, P. H. and Stix, M. (1972). α-effect dynamos by the Bullard-Gellman formalism. *Astron. Astrophys.*, 18:453.

Rüdiger, G. (1989). *Differential Rotation and Stellar Convection*. Gordon and Breach.

Rüdiger, G. and Brandenburg, A. (1995). A solar dynamo in the overshoot layer: cycle period and butterfly diagram. *Astron. Astrophys.*, 296:557.

Rüdiger, G. and Kichatinov, L. L. (1993). Alpha-effect and alpha-quenching. *Astron. Astrophys.*, 269:581.

Rüdiger, G., Von Rekowski, B., Donahue, R. A., and Baliunas, S. L. (1998). Differential rotation and meridional flow for fast-rotating solar-type stars. *Astrophys. J.*, 494:691.

Saar, S. H. (1996). Recent Measurements of Stellar Magnetic Fields. In Uchida, Y., Kosugi, T., and Hudson, H. S., editors, *IAU Colloq. 153: Magnetodynamic Phenomena in the Solar Atmosphere - Prototypes of Stellar Magnetic Activity*, page 367. Kluwer, Dordrecht.

Schmitt, D. (1987). An $\alpha\omega$-dynamo with an α-effect due to magnetostrophic waves. *Astron. Astrophys.*, 174:281.

Schmitt, D., Schüssler, M., and Ferriz-Mas, A. (1996). Intermittent solar activity by an on-off dynamo. *Astron. Astrophys.*, 311:L1.

Schou, J. et al. (1998). Helioseismic studies of differential rotation in the solar envelope by the Solar Oscillations Investigation using the Michelson Doppler Imager. *Astrophys. J.*, 505:390.

Schrijver, C. J. and Title, A. M. (2001). On the formation of polar spots in sun-like stars. *Astrophys. J.*, 551:1099.

Schrijver, C. J. and Zwaan, C. (1999). *Solar and Stellar Magnetic Activity.* Cambridge University Press.

Schüssler, M., Schmitt, D., and Ferriz-Mas, A. (1997). Long-term variation of solar activity by a dynamo based on magnetic flux tubes. In Schmieder, B., del Toro Iniesta, J. C., and Vazquez, M., editors, *Advances in the Physics of Sunspots*, volume 118 of *A.S.P. Conf. Series*, page 39.

Skumanich, A. (1972). Timescales for CaII emission decay, rotational braking, and lithium depletion. *Astrophys. J.*, 171:565.

Sokoloff, D. and Nesme-Ribes, E. (1994). The Maunder minimum: A mixed-parity dynamo mode? *Astron. Astrophys.*, 288:293.

Spiegel, E. A. and Weiss, N. O. (1980). Magnetic activity and variations in solar luminosity. *Nature*, 287:616.

Spiegel, E. A. and Zahn, R.-P. (1992). The solar tachocline. *Astron. Astrophys.*, 265:106.

Steenbeck, M. and Krause, F. (1969). On the Dynamo Theory of Stellar and Planetary Magnetic Fields. I. AC Dynamos of Solar Type. *Astronomische Nachrichten*, 291:49.

Steenbeck, M., Krause, F., and Rädler, K.-H. (1966). A calculation of the mean electromotive force of an electrically conducting fluid in turbulent motion under the influence of Coriolis forces. *Z. Naturforsch.*, 21a:369.

Stix, M. (1972). Non-linear dynamo waves. *Astron. Astrophys.*, 20:9.

Stix, M. (1976). Differential rotation and the solar dynamo. *Astron. Astrophys*, 47:243.

Stix, M. (2002). *The Sun.* Springer, Berlin.

Strassmeier, K. G. (2002). Doppler images of starspots. *Astron. Nachr.*, 323:309.

Tau, L., Cattaneo, F., and Vainshtein, S. I. (1993). Evidence for the suppression of the alpha-effect by weak magnetic fields. In Proctor, M. R. E., Matthews, P. C., and Rucklidge, A. M., editors, *Solar and Planetary Dynamos*, page 303. Cambridge University Press.

Tavakol, R., Covas, E., Moss, D., and Tworkowski, A. (2002). Effects of boundary conditions on the dynamics of the solar convection zone. *Astron. Astrophys.*, 387:1100.

Tayler, R. J. (1997). *The Sun as a Star.* Cambridge University Press.

Taylor, G. I. (1921). Experiments with rotating fluids. *Proc. R. Soc. Lond. A*, 100:114.

Thelen, J.-C. (2000a). A mean electromotive force induced by magnetic buoyancy instabilities. *Mon. Not. R. Astron. Soc.*, 315:155.

Thelen, J.-C. (2000b). Non-linear $\alpha\omega$-dynamos driven by magnetic buoyancy. *Mon. Not. R. Astron. Soc.*, 315:165.

Tobias, S. M. (1996a). Diffusivity Quenching as a Mechanism for Parker's Surface Dynamo. *Astrophys. J.*, 467:870.

Tobias, S. M. (1996b). Grand minima in nonlinear dynamos. *Astron. Astrophys.*, 307:L21.

Tobias, S. M. (1996c). *Nonlinear solar and stellar dynamos.* PhD thesis, University of Cambridge.

Tobias, S. M. (1997a). Properties of nonlinear dynamo waves. *Geophys. Astrophys. Fluid Dynamics*, 86:287.

Tobias, S. M. (1997b). The solar cycle: parity interactions and amplitude modulation. *Astron. Astrophys.*, 322:1007.

Tobias, S. M. (2002a). Modulation of solar and stellar dynamos. *Astron. Nachr.*, 323:417.

Tobias, S. M. (2002b). The solar dynamo. *Phil. Trans. R. Soc. Lond. A*, 360:2741.

Tobias, S. M. (2004). The Solar Tachocline: formation, stability and its role in the solar dynamo. In preparation.

Tobias, S. M., Brummell, N. H., Clune, T. L., and Toomre, J. (2001). Transport and Storage of Magnetic Field by Overshooting Turbulent Compressible Convection. *Astrophys. J.*, 549:1183.

Tobias, S. M. and Hughes, D. W. (2004). The influence of velocity shear on magnetic buoyancy instability in the solar tachocline. *Astrophys. J.* in press.

Tobias, S. M., Proctor, M. R. E., and Knobloch, E. (1997). The role of absolute instability in the solar dynamo. *Astron. Astrophys.*, 318:L55.

Tobias, S. M., Weiss, N. O., and Kirk, V. (1995). Chaotically modulated stellar dynamos. *Mon. Not. R. Astron. Soc.*, 273:1150.

Ulrich, R. K., Boyden, J. E., Webster, L., Padilla, S. P., and Snodgrass, H. B. (1988). Solar rotation measurements at Mount Wilson. V - Reanalysis of 21 years of data. *Solar Physics*, 117:291.

Vainshtein, S. I. and Cattaneo, F. (1992). Nonlinear restrictions on dynamo action. *Astrophys. J.*, 393:165.

van Ballegooijen, A. A. (1982). The overshoot layer at the base of the solar convective zone and the problem of magnetic flux storage. *Astron. Astrophys.*, 113:99.

van Ballegooijen, A. A. and Choudhuri, A. R. (1988). The possible role of meridional flows in suppressing magnetic buoyancy. *Astrophys. J.*, 333:965.

Vorontsov, S. V., Christensen-Dalsgaard, J., Schou, J., Strakhov, V. N., and Thompson, M. J. (2002). Helioseismic measurements of solar torsional oscillations. *Science*, 296:101.

Wagner, G., Beer, J., Masarik, J., Muscheler, R., Kubik, P. W., Mende, W., Laj, C., Raisbeck, G. M., and Yiou, F. (2001). Presence of the solar de Vries cycle ($\sim$205 years) during the last ice age. *Geophys. Res. Lett.*, 28:303.

Weiss, N. O. (1994). Solar and stellar dynamos. In Proctor, M. R. E. and Gilbert, A. D., editors, *Lectures on Solar and Planetary Dynamos*, chapter 2, page 59. Cambridge University Press.

Weiss, N. O. (2002). Dynamos in planets, stars and galaxies. *Astronomy and Geophysics*, 43:3.9.

Weiss, N. O., Cattaneo, F., and Jones, C. A. (1984). Periodic and aperiodic dynamo waves. *Geophys. Astrophys. Fluid Dynamics*, 30:305.

Weiss, N. O. and Tobias, S. M. (1997). Modulation of solar and stellar activity cycles. In Simnett, G. M., editor, *Solar and Heliospheric Plasma Physics*, Springer Lecture Notes in Physics, page 25. Springer.

Yoshimura, H. (1975). Solar-cycle dynamo wave propagation. *Astrophys. J.*, 201:740.

Yoshimura, H. (1978a). Nonlinear astrophysical dynamos: Multiple-period dynamo wave oscillations and long-term modulations of the 22 year solar cycle. *Astrophys. J.*, 226:706.

Yoshimura, H. (1978b). Nonlinear astrophysical dynamos: The solar cycle as a nonlinear oscillation of the general magnetic field driven by the nonlinear dynamo and the associated modulation of the differential-rotation-global-convection system. *Astrophys. J.*, 220:692.